Tidal Disruption Events and Other Nuclear Transients Discovered with eROSITA

Iuliia Grotova

München 2025

Tidal Disruption Events and Other Nuclear Transients Discovered with eROSITA

Iuliia Grotova

Dissertation
an der Fakultät für Physik
der Ludwig–Maximilians–Universität
München

vorgelegt von
Iuliia Grotova
aus Sankt Petersburg, Russland

München, den 16.12.2025

Erstgutachter: Prof. Dr. Kirpal Nandra
Zweitgutachter: Prof. Dr. Andreas Burkert
Tag der mündlichen Prüfung: 26.02.2026

Contents

List of Figures

List of Tables

Zusammenfassung

Die zeitaufgelöste Röntgenastronomie bietet einen leistungsfähigen Zugang zu einigen der energiereichsten und kurzlebigsten Phänomene im Universum. Das eROSITA-Teleskop an Bord des Spectrum-Röntgen-Gamma-Satelliten eröffnet dank seiner Empfindlichkeit, Himmelsabdeckung und Survey-Kadenz eine beispiellose Möglichkeit, den transienten und variablen extragalaktischen Röntgenhimmel zu erforschen. Diese Eigenschaften machen eROSITA besonders geeignet für die Entdeckung variabler extragalaktischer Röntgenquellen. Unter diesen findet sich die kleine, aber wissenschaftlich äußerst wertvolle Untergruppe der Tidal Disruption Events (TDEs), bei denen Sterne durch die Gravitationskräfte von supermassereichen Schwarzen Löchern (SMBH) zerrissen werden. Die Identifizierung solcher transienten Signale innerhalb der großen Zahl von anderen Röntgenquellen ist entscheidend, um unser Verständnis dieser extremen physikalischen Prozesse zu vertiefen. Diese Dissertation widmet sich der Untersuchung des variablen Röntgenhimmels mit eROSITA, mit einem besonderen Schwerpunkt auf der Identifikation und Analyse stellarer TDE-Kandidaten.

Kapitel 1 bietet einen Überblick über das eROSITA-Instrument sowie über Transienten und variable Quellen im Röntgenhimmel, darunter sowohl galaktische als auch extragalaktische Objekte. Das Kapitel enthält außerdem eine Einführung in TDEs, beginnend mit den theoretischen Grundlagen und gefolgt von einer Darstellung ihrer Beobachtungseigenschaften in verschiedenen Wellenlängenbereichen. Darüberhinaus werden bereits mit eROSITA entdeckte TDEs kurz zusammengefasst.

Kapitel 2, veröffentlicht in Grotova et al. (2025a), beschreibt die systematische Auswahl extragalaktischer Röntgentransienten, die in den ersten beiden eROSITA Himmelsdurchmusterungen (eRASS) entdeckt wurden und die vor den eROSITA-Beobachtungen nicht als AGN bekannt waren. Der präsentierte Katalog, eRO-ExTra, umfasst 304 extragalaktische eROSITA-Transienten und -Variable, von denen mehr als 90 % zuverlässige optische Gegenstücke besitzen. Jede Quelle wird anhand archivierter Röntgendaten, langfristiger eROSITA-Lichtkurven und röntgenspektraler Modellierung charakterisiert. eRO-ExTra liefert den ersten systematischen Überblick über den extragalaktischen transienten Himmel im Röntgenbereich von eROSITA und stellt einen wertvollen Datensatz zur Untersuchung seltener nuklearer Variabilitätsphänomene im Umfeld massereicher Schwarzer Löcher dar.

Die Kapitel 3 und 4 befassen sich speziell mit TDEs und umfassen sowohl kanonische Kandidaten als auch extreme Szenarien, die die unteren und oberen Grenzen des für TDEs relevanten Schwarze-Loch-Massenbereichs definieren: von einem Kandidaten um ein intermediär-massereiches Schwarzes Loch bis hin zu einem Ereignis, das mit einem über der

Hills-Masse liegenden SMBH verbunden ist. Kapitel 3, zunächst veröffentlicht in Grotova et al. (2025b), präsentiert eine systematische Populationsstudie von TDEs aus dem eRO-ExTra-Katalog. Die ausgewählte Stichprobe umfasst 30 kanonische TDEs und einen off-nuklearen TDE-Kandidaten und stellt die bislang größte einheitlich im Röntgenbereich ausgewählte TDE-Stichprobe dar. Aus dieser Stichprobe leiten wir die TDE Röntgenleuchtkraftfunktion ab und bestimmen eine volumetrische TDE-Rate. Eine Multiwellenlängenanalyse zeigt, dass ein Teil der Ereignisse optische, mittel-infrarote oder Radiovariabilität aufweist, die mit Reprozessierung oder Kollisionen von akkretierten Gasströmen vereinbar ist. Diese Arbeit demonstriert die statistische Leistungsfähigkeit von eROSITA für TDE-Studien und bildet eine Grundlage für zukünftige Analysen in kommenden Röntgenhimmelsdurchmusterungen. Kapitel 4 beschreibt die Entdeckung und Analyse von J0936, eines außergewöhnlichen Röntgentransienten, der von eROSITA in einer Fanaroff-Riley-Typ-II-(FRII)-Radiogalaxie identifiziert wurde. Die Quelle zeigt einen ultrasoften Flare, ein erneutes Aufhellen Monate später und keine nachweisbare Variabilität in anderen Wellenlängenbereichen. Das Kapitel zeigt, dass sich die Röntgeneigenschaften deutlich von denen typischer FR-II-Galaxien unterscheiden und stattdessen einem partiellen, wiederholten TDE ähneln. Mit einer geschätzten SMBH-Masse oberhalb der kanonischen Hills-Masse erfordert der Ursprung vermutlich ein schnell rotierendes Schwarzes Loch oder ein off-nukleares SMBH. J0936 stellt damit einen der exotischsten und massereichsten bekannten TDE-Kandidaten dar und erweitert die Bandbreite der Umgebungen, in denen TDEs auftreten können.

Kapitel 5 fasst die Dissertation zusammen und skizziert mögliche Richtungen für zukünftige Untersuchungen von TDEs im Röntgenbereich und bei anderen Wellenlängen. Es hebt die potenziellen Anwendungen der in dieser Arbeit entwickelten Methoden hervor und nennt mehrere offene Fragen, die eine weitere vertiefte Untersuchung erfordern.

Abstract

Time-domain X-ray astronomy provides a powerful window into some of the most energetic and short-lived phenomena in the Universe. The eROSITA telescope aboard the Spectrum-Roentgen-Gamma satellite offers an unprecedented opportunity to explore the transient and variable extragalactic X-ray sky, thanks to its sensitivity, sky coverage, and survey cadence. These capabilities make eROSITA particularly well suited for detecting variable extragalactic X-ray sources. Among these, a small but scientifically valuable subset arises from rare phenomena such as tidal disruption events (TDEs), in which stars are torn apart by the gravitational forces of supermassive black holes (SMBH). Identifying such transient signals within the vast population of X-ray sources is essential for advancing our understanding of these extreme physical processes. This thesis is dedicated to exploring the variable X-ray sky with eROSITA, with a primary focus on the identification and analysis of stellar tidal disruption event candidates.

Chapter 1 provides an overview of the eROSITA instrument as well as transients and variables present in the X-ray sky, which includes both galactic and extragalactic sources. The chapter also includes an overview of TDEs, starting with a theoretical introduction and followed by a discussion of the observational properties of TDEs in various bands and previously discovered TDEs with eROSITA.

Chapter 2, published in Grotova et al. (2025a), describes the systematic selection of X-ray extragalactic transients found in the first two eROSITA all-sky surveys (eRASS) that are not associated with known active galactic nuclei (AGN) prior to eROSITA observations. The presented catalog eRO-ExTra includes 304 extragalactic eROSITA transients and variables, with more than 90% of sources associated with reliable optical counterparts. Each source is characterized through archival X-ray data, long-term eROSITA light curves, and X-ray spectral modeling. eRO-ExTra delivers the first systematic view of the extragalactic non-AGN transient sky with eROSITA, offering a valuable dataset for investigating rare nuclear variability phenomena associated with massive black holes.

Chapters 3 and 4 relate specifically to TDE science, including canonical candidates as well as extreme scenarios that define the lower and upper bounds of the black hole mass range for TDEs: from a candidate around an intermediate-mass black hole to one associated with a SMBH above the Hills mass. Chapter 3 was initially published in Grotova et al. (2025b), and presents a systematic population study of TDEs from the eRO-ExTra catalog. The selected TDE sample contains 30 canonical TDEs and one off-nuclear TDE candidate and is the largest uniformly X-ray–selected TDE sample to date. From this

sample, we derive the TDE X-ray luminosity function and infer the volumetric TDE rate. A multiwavelength analysis reveals that a subset of events shows optical, mid-infrared, or radio variability consistent with reprocessing or stream–stream collisions. This work demonstrates the statistical power of eROSITA for TDE studies and provides a foundation for future research in upcoming X-ray surveys. Chapter 4 presents the discovery and analysis of J0936, an exceptional X-ray transient identified by eROSITA in a Fanaroff-Riley Type II (FRII) radio galaxy. The source exhibits an ultra-soft flare and a months-later re-brightening. The chapter shows how its X-ray properties differ significantly from those of typical FR II galaxies and instead resemble a partial, repeated TDE. With an inferred SMBH mass above the canonical Hills mass, its origin likely requires a rapidly spinning black hole or an off-nuclear SMBH. J0936 thus represents one of the most exotic and massive TDE candidates known, expanding the range of environments in which TDEs can occur.

Chapter 5 summarizes the thesis and outlines prospective directions for future research on TDEs in X-rays and across other wavelengths. It highlights the potential applications of the methodologies developed in this work and identifies outstanding questions for further exploration in the study of TDEs.

Chapter 1

Introduction

As a dynamic and ever-changing environment, the sky continuously fluctuates, exhibiting constant variability. Living in a "Goldilocks" era for science and cosmic research, we face the Universe with many fascinating open questions, while our observational capabilities and theoretical tools have matured enough to investigate them with increasing precision. This gives us a rare opportunity to witness and explore the wonders of the cosmos, such as the birth and death of stars, the formation of galaxies, and the evolution of supermassive black holes. The changes happen on various spatial scales, from micro worlds of atoms undergoing nuclear fusion in stars to the large-scale dynamics of galaxies and galaxy clusters, such as galaxy mergers and interactions. The interplay of various physical processes composes the dynamic and complex nature of the universe. This era of discovery, driven by advancing research technologies and a supportive global scientific community, is a gift, enabling humanity to comprehend the vastness of space, appreciate the beauty of its objects, and question our place within it.

Variable sources in space undergo changes in their brightness and spectra over time. By analyzing the patterns and mechanisms behind the variability, astronomers can probe the physical conditions, environments, and underlying processes at play. Furthermore, the study of variability can reveal life cycles of celestial objects, their evolution, and their interactions with the interstellar and intergalactic medium. Understanding variability is essential for the development of more accurate models of astrophysical phenomena and related physics, allowing us to refine our comprehension of fundamental cosmic processes.

In the context of X-ray studies, variability is particularly important because X-ray emission arises from high-energy processes such as accretion onto compact objects (black holes and neutron stars), shock waves in supernova remnants, relativistic jets from black holes, and other various phenomena, each providing unique insights into the underlying astrophysical mechanisms. The time scales and amplitudes of X-ray variability offer clues about the physical processes driving the emission. Therefore, studying X-ray variability is crucial for understanding the extreme environments where the laws of physics are tested under conditions unreachable on Earth.

A first significant milestone in studying the X-ray sky was the launch of the Uhuru (Giacconi et al., 1971; Jagoda et al., 1972) satellite in the 1970s, which was the first dedi-

cated X-ray astronomy mission. Uhuru mapped the sky in X-rays (Giacconi et al., 1972), discovering a number of X-ray sources, including the first black hole candidate, Cygnus X-1 (Oda et al., 1971). This was followed by other early missions such as EXOSAT (Taylor et al., 1981) and ROSAT (Truemper, 1992). Advancements in X-ray astronomy continued with the launch of more sophisticated telescopes and advanced instrumentation like Chandra (Weisskopf et al., 2000) and XMM-Newton (Jansen et al., 2001), which enabled high-resolution X-ray imaging and spectroscopy. These missions provided a more detailed understanding of X-ray variability, revealing complex processes such as the rapid flaring of X-ray binaries (e.g., White et al. 1986; van der Meer et al. 2005, the variability of active galactic nuclei over a broad range of time scales (e.g., Boller et al. 1996; McHardy et al. 2004), as well as the discovery of ultra-luminous X-ray sources (e.g., Swartz et al. 2004; Feng & Soria 2011), tidal disruption events of stars by black holes (e.g., Bade et al. 1996; Komossa & Bade 1999; Komossa & Greiner 1999) and numerous other astrophysical phenomena.

Today, the exploration of the variable X-ray sky has reached new heights with the launch of extended ROentgen Survey with an Imaging Telescope Array (eROSITA, Predehl et al. 2021). This PhD thesis focuses on the study of extragalactic transients and variable X-ray sources with eROSITA, with a particular emphasis on tidal disruption events (TDEs) — the disruption of stars by supermassive black holes (SMBHs). The introduction is organized as follows: In Sect.1.1, I discuss the key properties of the eROSITA telescope, the primary instrument used in this work. Sect.1.2 provides an overview of X-ray transients and variables that can be observed with eROSITA. Finally, in Sect. 1.3, I focus specifically on TDEs.

1.1 eROSITA as a tool for variability studies

eROSITA was developed at the Max Planck Institute for Extraterrestrial Physics (MPE) in the period from 2007 to 2019. Launched from Baikonur, Kazakhstan, on July 13, 2019 aboard the Russian-German Spektr-RG spacecraft (SRG, Sunyaev et al. 2021) together with ART-XC telescope (4–30 keV energy range; Pavlinsky et al. 2021), eROSITA's primary goal was to conduct an all-sky survey in X-rays in the energy range from 0.2 to 10 keV, providing insights into the physics of galaxy clusters, SMBHs, and the large-scale structure of the universe. In addition, eROSITA's capabilities allow searches for galactic and extragalactic transients. With this powerful instrument, we have entered a new era of X-ray astronomy where the study of variability not only advances our understanding of known phenomena but also uncovers new unexpected sources and processes.

The eROSITA data are shared equally between German and Russian scientists, following a split by Galactic longitude (eROSITA_DE: $359.9442^\circ > l > 179.9442^\circ$ and eROSITA_RU: $-0.0558^\circ < l < 179.9442^\circ$). eROSITA operated for 2.5 years untill February 2022, when it was put into safe mode. Overall, eROSITA completed 4.3 all-sky surveys (eRASS1–5), each lasting six months, which can be used for X-ray variability studies.

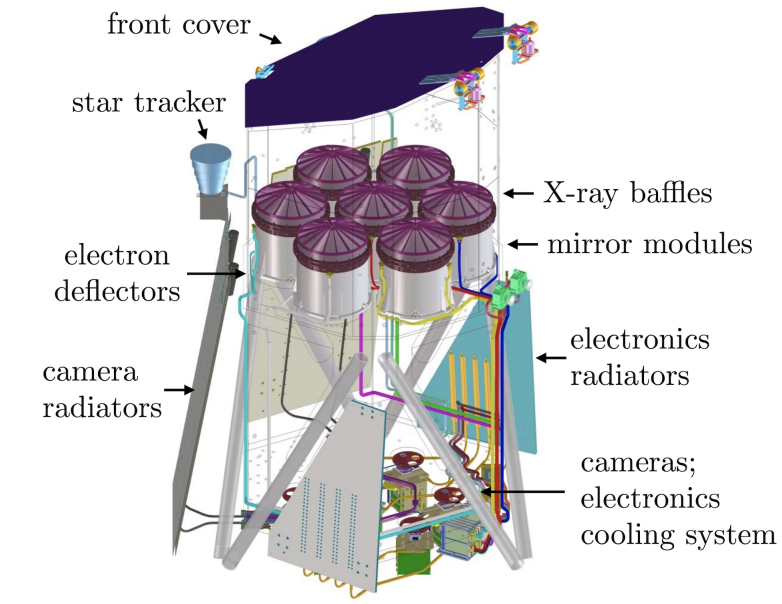

Figure 1.1: Schematic view of the eROSITA telescope. Figure from Predehl et al. (2021).

1.1.1 Instrumentation

The eROSITA telescope consists of seven individual telescope modules (TMs), arranged in a hexagonal shape. Each TM includes a mirror assembly (MA) and a camera assembly (CA). The schematic view of the eROSITA telescope in shown in Fig. 1.1.

Each MA contains 54 concentric nested mirror shells that are coated with gold to enhance X-ray reflectivity (see Fig. 1.2, left). The mirrors are arranged in a Wolter-I configuration, which focuses X-rays through grazing incidence to minimize absorption and scattering. X-ray baffles are placed in front of each mirror module to suppress undesired photons coming from single reflections from sources outside the field of view[1] (FoV), e.g., from bright sources nearby. Additionally, magnetic electron deflectors behind the mirrors help to clean the background from low-energy cosmic-ray electrons. The focused X-rays from each MA are directed onto a charge-coupled-device (CCD) camera of 384×384 pixels, with each pixel corresponding a 9.6" $\times$ 9.6" sky area. These CCDs are highly sensitive in the soft X-ray band, covering energies from 0.2 to 10 keV with a high spatial resolution. Each CA (see Fig. 1.2, right) also includes its own filter wheel, a cryogenic heat pipe system, which cools down the CCD to $-85°$C, and an electronics box for processing the camera data. eROSITA offers a resulting averaged-FoV spatial resolution of about 26", in a circular FoV with a diameter of 1.03 degrees.

eROSITA's sensitivity and sky coverage broadened our possibilities of exploring the X-ray sky in comparison to previous or still ongoing X-ray missions. Its predecessor ROSAT, launched in 1990, is about 25 times less sensitive in the soft X-ray band (0.2 to 2.3 keV),

[1] Angular area of the sky that the telescope can observe at any given time.

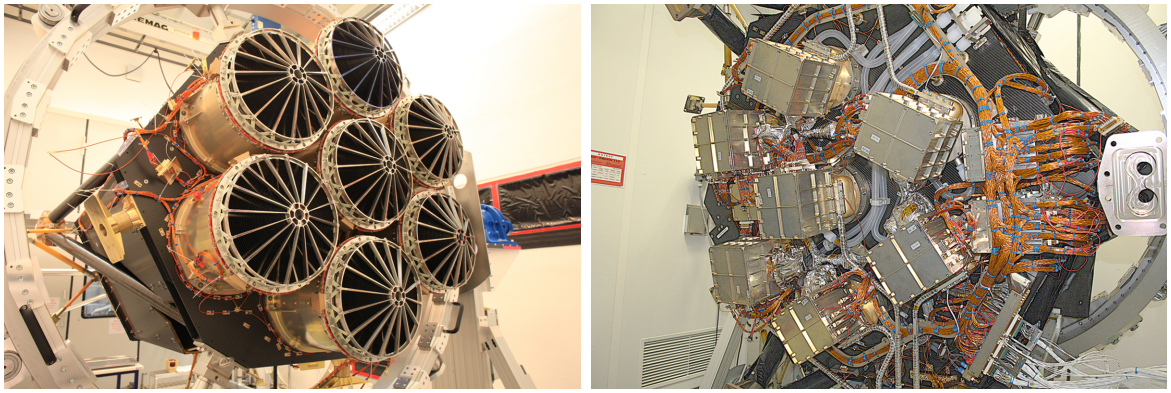

Figure 1.2: Left: Front view of the telescope with all seven TMs installed. Each TM consists of a mirror module, an X-ray baffle in front, and a magnetic electron deflector behind. Right: Rear view of the telescope with all seven CAs installed. Each CA consists of a filter wheel, a camera, and a camera electronics box. Also seen are heat pipes, purging tubes, and a harness. Figures from Predehl et al. (2021).

which restricted its ability to detect faint and distant sources. In addition, while ROSAT conducted an all-sky survey in soft X-rays, eROSITA provided the first ever imaging survey of the sky in the hard X-ray band (2.3 to 8 keV). eROSITA's energy range of 0.2 to 10 keV allows it to bridge the observational gap between ROSAT's soft X-ray range and the harder X-ray missions like NuSTAR (Harrison et al., 2013), making it well-suited to detect a broad variety of astrophysical phenomena. In comparison to Chandra and XMM-Newton, which are specialized in targeted observations, eROSITA is optimized for wide-field surveys. While Chandra has a superior angular resolution (around 0.5" compared to eROSITA's 18"), its narrower field of view and smaller collecting area affects its ability to efficiently scan large areas of the sky. XMM-Newton is close to eROSITA in survey capability but still falls short of its ability to map the entire sky with uniform sensitivity. The combined effective area[2] of the seven eROSITA telescopes is slightly higher than that of XMM-Newton in the 0.5–2 keV band (see Fig. 1.3, top). A comparison of the "grasp" (the product of the FoV multiplied and average effective area) of eROSITA with XMM-Newton, Chandra, and ROSAT is shown in the bottom panel of Fig. 1.3. The superior grasp of eROSITA in the soft X-ray band demonstrates that it is capable of detecting more X-ray photons per unit of time over a larger portion of the sky compared to the other missions, which makes it more efficient in surveying the sky. In particular, XMM-Newton and Chandra have smaller FoV ($\sim 0.2°$ for XMM-Newton and $\sim 0.04°$ for Chandra), which results in smaller grasp values given comparable effective areas. ROSAT, on the other hand, had a much smaller effective area: $\sim 200\text{cm}^2$ compared to eROSITA's $\sim 1360\text{cm}^2$ at 1 keV albeit over a larger FoV. By combining all-sky coverage with moderate resolution and sensitivity, eROSITA is uniquely positioned to complement the more focused observations of earlier missions, driving a new era in X-ray astronomy.

[2]Apparent collecting area of the telescope that is sensitive to X-ray photons at a specific energy.

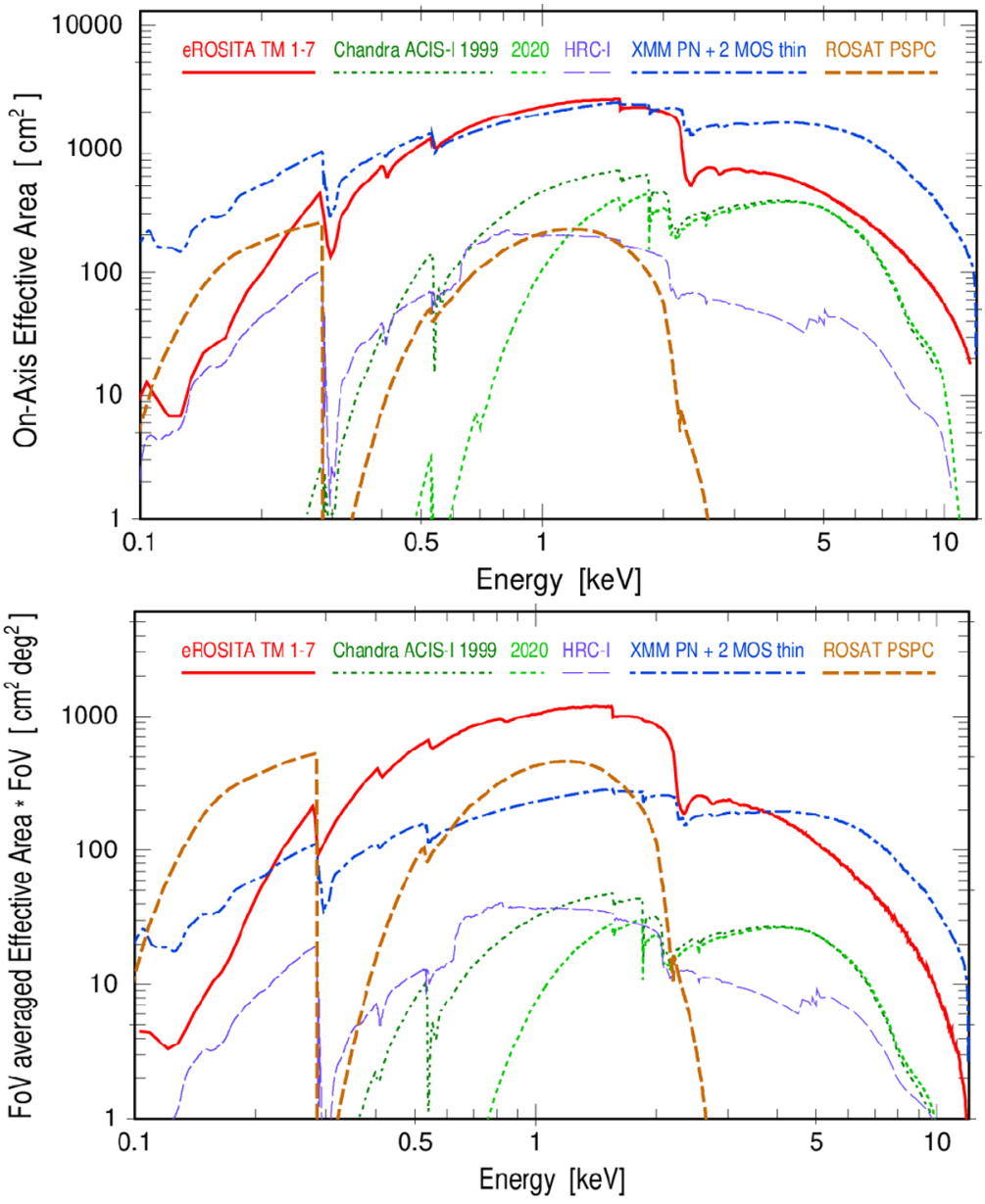

Figure 1.3: Top: Comparison of the on-axis effective areas as a function of energy for eROSITA (red), Chandra ACIS-I (in 1999, dark green, and in 2020, light green), Chandra HRC-I (purple), XMM-Newton PN + MOS (blue), and ROSAT (brown). Bottom: Comparison of the grasp, defined as the product of the field of view and the (averaged) effective area as a function of energy for eROSITA, Chandra ACIS-I, Chandra HRC-I, XMM-Newton PN + MOS, and ROSAT. Figures from Predehl et al. (2021).

1.1.2 eROSITA scanning strategy

eROSITA operates in a continuous scanning mode, utilizing the rotation of SRG and its orbital positioning in a halo orbit around the second Lagrange point (L2)[3]. The spacecraft rotates around its axis, with the instruments pointing orthogonal to the Sun direction, approximately every four hours with a scan rate of 0.025 deg s^{-1}. Thus, eROSITA's field of view sweeps across the sky in great circles, with its axis moving by approximately one degree per day following the motion of the Earth (and that of the L2 point) around the Sun. Over the course of six months, eROSITA's scanning motion covers the entire sky, completing one all-sky survey, also called an eRASS. The scanning strategy results in non-homogeneous exposure for different areas of the sky (see Fig. 1.4). Each point in the sky is typically observed around six times over a day, with each observation ("visit") lasting up to 40 seconds at the ecliptic equator. At the ecliptic poles, the scanning geometry results in significantly deeper exposure and longer visibility periods, since these regions lie along the path of successive scanning circles and are observed for many days in a row or continuously in the case of the ecliptic poles themselves. This extended exposure leads to many more than six scans, substantially improving the sensitivity and depth of observations in these areas.

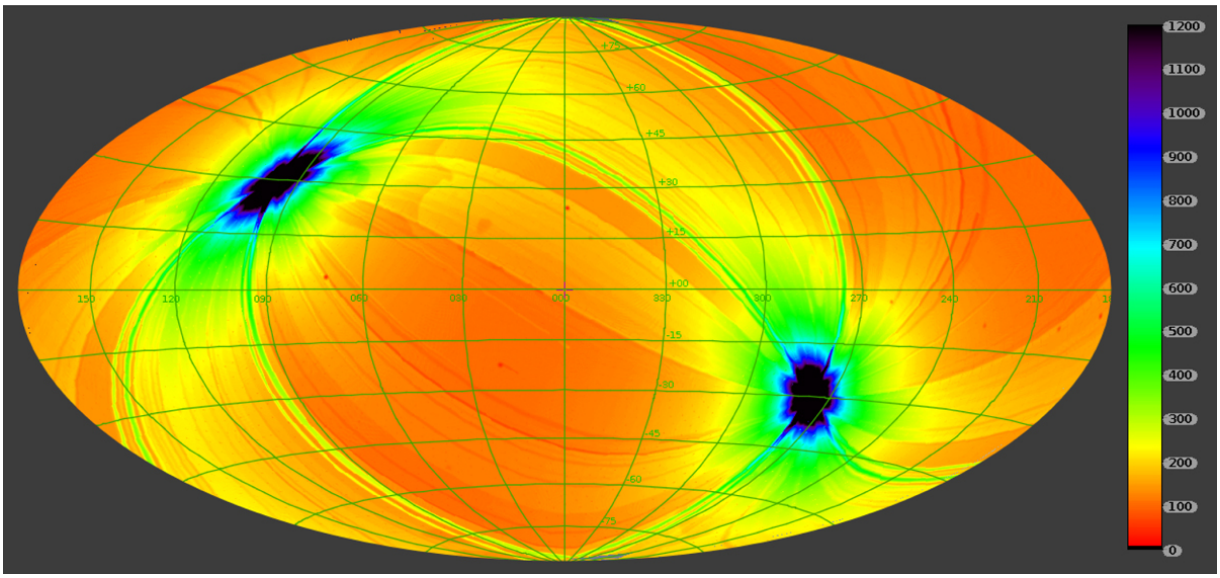

Figure 1.4: Effective exposure map of the first eROSITA all-sky survey in Galactic coordinates and Aitoff projection.The map values represent the exposure time multiplied by the average ratio of the (vignetted) effective area to the on-axis effective area within the 0.6–2.3 keV energy range. Exposure times vary from around 100 seconds at the ecliptic equator to over 10,000 seconds near the ecliptic poles. The right half of the sky corresponds to eROSITA_DE. Figure from Merloni et al. (2024).

[3]A point in space approximately 1.5 million kilometers from Earth, directly opposite the Sun, where the force from the rotation around the Sun and gravitational force balance out.

1.1.3 eROSITA X-ray sky

Being a sensitive wide-field X-ray telescope capable of delivering deep, sharp images over large areas of the sky, eROSITA has significantly enhanced our understanding of the X-ray universe, detecting numerous new sources (Merloni et al., 2024). Moreover, eROSITA's scanning strategy allows the study of a broad range of variability timescales: from tens of seconds (within a single eRASS) to years (comparing all eRASSes). This enables us to discover numerous short-term and long-term X-ray transients and variables.

Fig. 1.5 shows all 890036 sources detected in the 0.2–2.3 keV band during eRASS1 (Merloni et al., 2024), and their sky distribution. This single-band catalogue is called eRASS 1B. It contains point-like and extended, Galactic and extragalactic X-ray sources. The majority of the point sources are expected to be active galactic nuclei, powered by supermassive black holes at the centers of galaxies (e.g., Boller et al. 2022; Liu et al. 2022a; Igo et al. 2024; Iwasawa et al. 2024; Waddell et al. 2024). Other classes of sources include galaxy clusters (Bulbul et al., 2024), supernova remnants (e.g., Becker et al. 2021; Mayer et al. 2023), X-ray binary systems (e.g., Avakyan et al. 2023) and even more rare transients, e.g., TDEs. A detailed overview of variable X-ray sources to be found with eROSITA is further provided in Sect. 1.2 and Sect. 1.3.

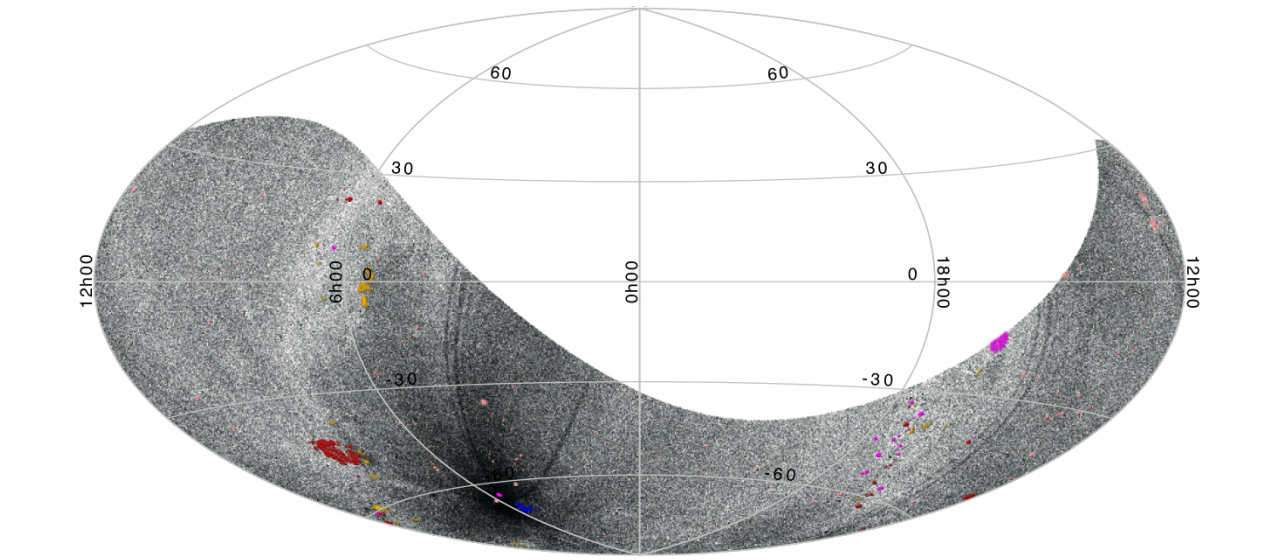

Figure 1.5: eRASS1 1B catalog in Equatorial coordinates (J2000) and Aitoff projection. Each grey point shows 1 out of 890036 detected sources in the catalog. Figure from Merloni et al. (2024).

1.2 The variable X-ray sky

The X-ray sky is dynamic and diverse, containing a broad range of transient and persistent sources. In the Galaxy, we observe accreting compact objects such as black hole (BH) and neutron star (NS) X-ray binaries, highly magnetized pulsars, cataclysmic variables, and stellar flares. On extragalactic scales, the variable X-ray sky is dominated by active galactic nuclei (AGN), TDEs, and other high-energy transients such as gamma-ray bursts and fast X-ray transients. These phenomena arise from a variety of physical processes making the X-ray sky a rich laboratory for studying extreme astrophysics.

To explore different populations of transients and variables — from the common to the extremely rare — it is crucial to be familiar with the sources in the X-ray variable sky. In this section, I describe various Galactic (see Sect. 1.2.1) and extragalactic (see Sect. 1.2.2) X-ray sources, discussing their typical properties and variability characteristics. The summary of luminosities, light curve shapes, and timescales of X-ray transients and variables is presented in Fig. 1.6, which provides a visual overview of different types of X-ray transients plotted as a function of their rest-frame time since identification and their X-ray luminosities in the 0.3–10 keV energy band. The density of observations, shown in grayscale, illustrates which regions of this parameter space have been explored more extensively. The figure highlights the vast dynamic range of X-ray transient phenomena, with luminosities spanning from $L_x \approx 10^{28} - 10^{49}$ erg s^{-1} and timescales ranging from milliseconds to years. Different source classes, such as gamma-ray bursts, AGN flares, supernova shock breakouts, magnetar flares, TDEs, and X-ray binaries, occupy distinct regions, helping to categorize new discoveries.

Since this thesis focuses on TDEs, it is essential to understand the broader context of X-ray transient and variable sources to correctly identify and classify these events. A clear distinction between TDEs and other types of X-ray variability is crucial for ensuring accurate event identification and for ruling out contaminating sources.

The eROSITA telescope, with its soft X-ray sensitivity, is well-suited to the detection of a wide range of X-ray transients. It is particularly sensitive to soft X-ray TDEs, as well as AGN variability, stellar flares, and high-energy transient events from compact objects. Its all-sky survey strategy provides an unprecedented opportunity to systematically detect and classify transient X-ray sources varying on timescales of hours (during an eROday) or months (in between eRASSes), making it an essential tool for population studies of variable astrophysical phenomena.

1.2.1 Galactic sources

Stellar flares

X-ray stellar flares arise from the magnetic reconnection events in stellar coronae, when the energy stored in twisted magnetic fields is explosively released (e.g., Haisch et al. 1991; Güdel 2004; Güdel & Nazé 2009). Therefore, flares occur in magnetic stars. Intense heating of the coronal plasma leads to the X-ray emission. As illustrated in Fig. 1.6, flares

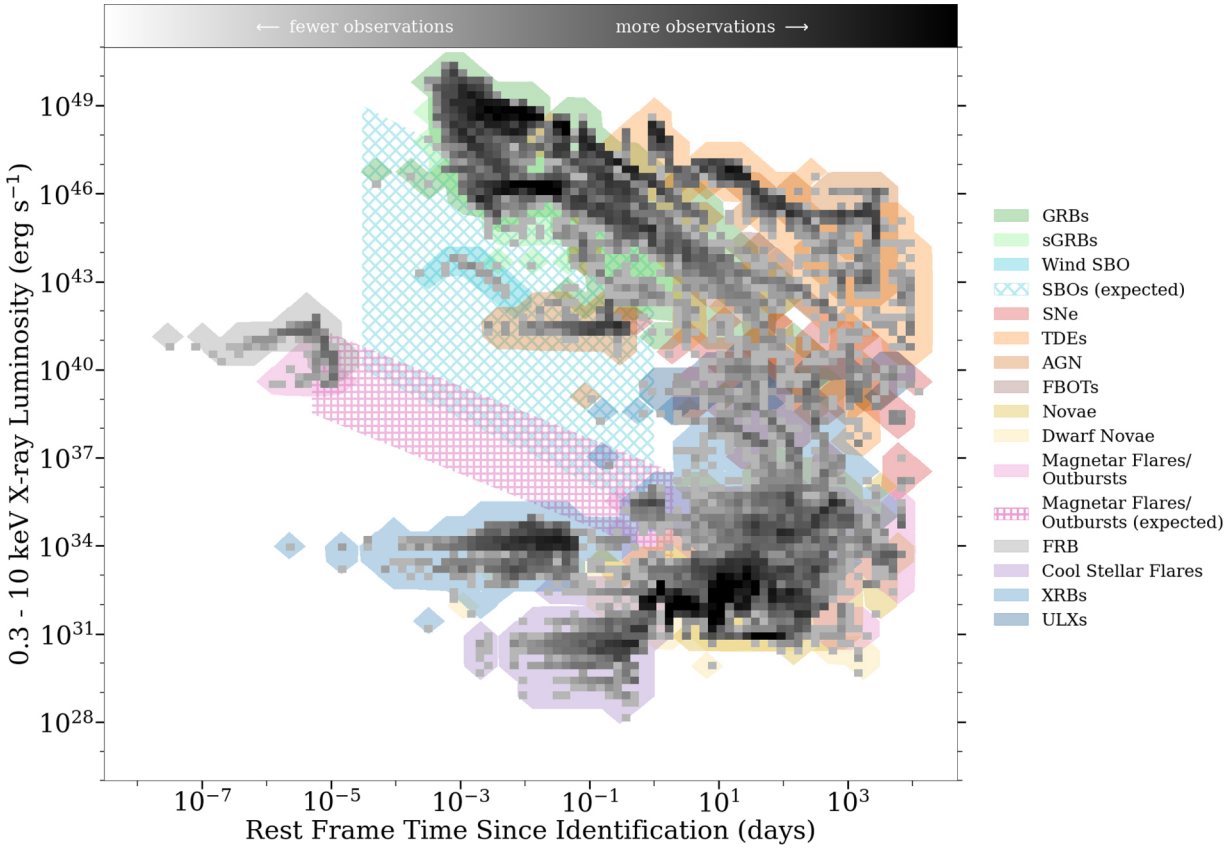

Figure 1.6: The density of light curves in X-ray luminosity vs. time since identification space, with different classes of transients overlaid. The grayscale intensity represents the number of observed light curves, highlighting which regions of parameter space are well-sampled. Most transient populations, both Galactic and extragalactic, have well-sampled light curves ranging from hours to several years after their discovery and cover an enormous range of X-ray luminosities, spanning over 20 orders of magnitude. Figure from Polzin et al. (2023).

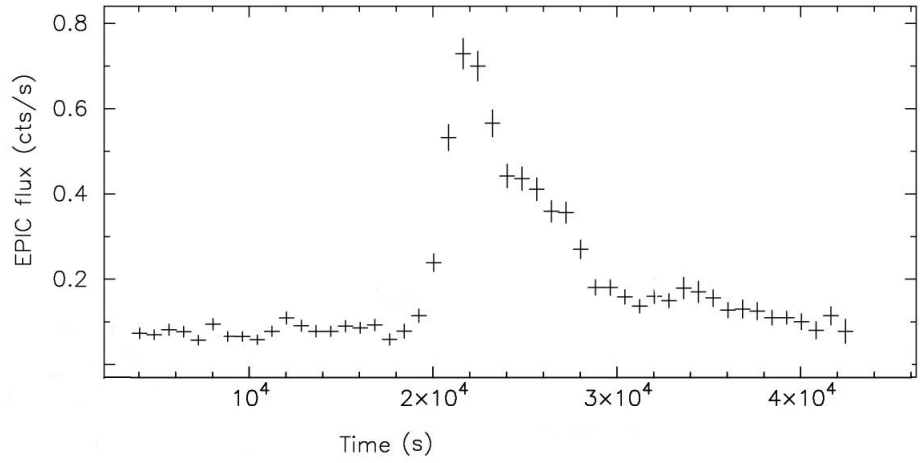

Figure 1.7: XMM EPIC X-ray light curve for the star 1RXS J231628.7+790531 in 0.2–12 keV, showing a prominent stellar flare. Figure adopted from Pye et al. (2015).

in cool low-mass stars (T < 4000K) are short, from hundreds of seconds up to ≈ 1 day, and have luminosities of $L_x \approx 10^{28} - 10^{32}$ erg s^{-1}. In cool stars, stellar flares are driven by the presence of convective zones that generate substantial surface magnetic fields, giving rise to stellar magnetic activity (Reiners, 2012). An example of an X-ray light curve of a cool star is shown in Fig. 1.7. Flares in hot stars (T > 7500K) have similar timescales and luminosities (e.g., Stelzer et al. 2005; Bhatt et al. 2014). In hot stars the energy transport is predominantly radiative and magnetic dynamo processes are ineffective. Here magnetic fields are attributed to fossil fields — a remainder of the magnetic field in the interstellar medium from which the star formed (Babel & North, 1997).

X-ray binaries

Galactic X-ray binaries (XRBs) are among the brightest objects in the X-ray sky and span luminosities $L_X \approx 10^{32} - 10^{39}$ erg s^{-1} (Polzin et al., 2023). The main source of X-ray emission in XRBs is the accretion of matter onto a compact object (NS or BH) from a companion star (Lewin et al., 1995; Remillard & McClintock, 2006).

XRBs experience extreme episodic outbursts during which the X-ray flux increases by several orders of magnitude reaching peak X-ray luminosities up to $10^{36} - 10^{39}$ erg s^{-1} over a timescale of ≈ days – months (Tanaka & Shibazaki, 1996; Yan & Yu, 2015) due to thermal-viscous instabilities in an accretion disk (Lasota, 2001). Additionally, neutron star XRBs can experience Type I X-ray bursts (see Fig. 1.8), i.e., thermonuclear flashes on the neutron star surface, lasting seconds to minutes (e.g., Wolff et al. 2005).

Cataclysmic variables

Cataclysmic variables (CVs; Warner 1995; Warner 2003) are binary star systems where a white dwarf (WD) accretes matter from a companion of a lower mass. The X-ray properties

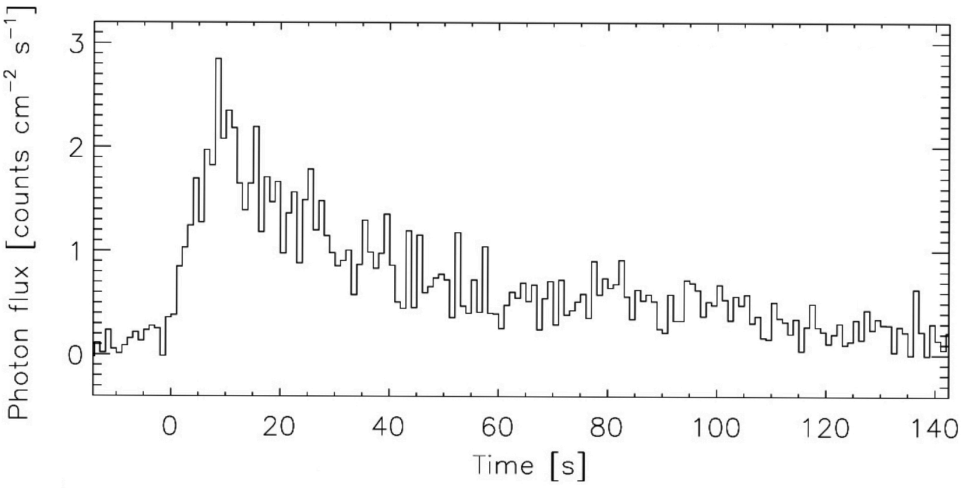

Figure 1.8: Example of Type I X-ray burst light curve of GS 1826-24 observed with INTEGRAL/JEM-X (3–25 keV). Figure from Galloway et al. (2020).

of CVs have been explored recently with eROSITA (Schwope et al., 2024; Ok et al., 2024). The origin of the X-rays in the system and its X-ray variability depends on the strength of the magnetic field. In non-magnetic CVs (with magnetic field strength $B < 0.1$ G), the WD accretes matter via a star filling the Roche Lobe and forming an accretion disk around the WD. In X-rays they exhibit distinct behavior between their quiescent and outburst states. During quiescence, hard X-ray emission arises primarily from the boundary layer where accreted material impacts the WD, with typical luminosities around $10^{30} - 10^{31}$ erg s^{-1} (e.g., Pandel et al. (2003); Nabizadeh & Balman (2020)). Outbursts, driven by thermal-viscous disk instabilities, lead to increased mass accretion rates. The boundary layer becomes optically thick, and the X-ray emission softens (e.g., Pringle & Savonije 1979; Wheatley et al. 2003), reaching $L_X \sim 10^{32} - 10^{33}$ erg s^{-1} (e.g., Baskill et al. 2005) on a scale of weeks (e.g., Coppejans et al. 2016). In magnetic CVs ($B > 10^4$ G), strong magnetic fields prevent the formation of an accretion disk and channel material directly onto the magnetic poles along the field lines. This leads to highly localized and often modulated X-ray emission, typically observed on timescales of minutes to hours (e.g., Matt et al. 2000; Bernardini et al. 2017).

An example of an X-ray transient in CVs is a nova — a dramatic eruption caused by thermonuclear runaway in hydrogen-rich material accreted onto the surface of the white dwarf. Post-outburst novae exhibit supersoft X-ray emission (Orio et al. 2001, $2.5 - 10 \times 10^5$ K, with $L_x \approx 10^{38}$ erg s^{-1}). A notable example of a nova in its "fireball" state was discovered by eROSITA by König et al. (2022b). This X-ray state (see Fig. 1.9) occurs immediately after the thermonuclear runaway, as the ejected material expands rapidly in all directions, creating a luminous and optically thick fireball.

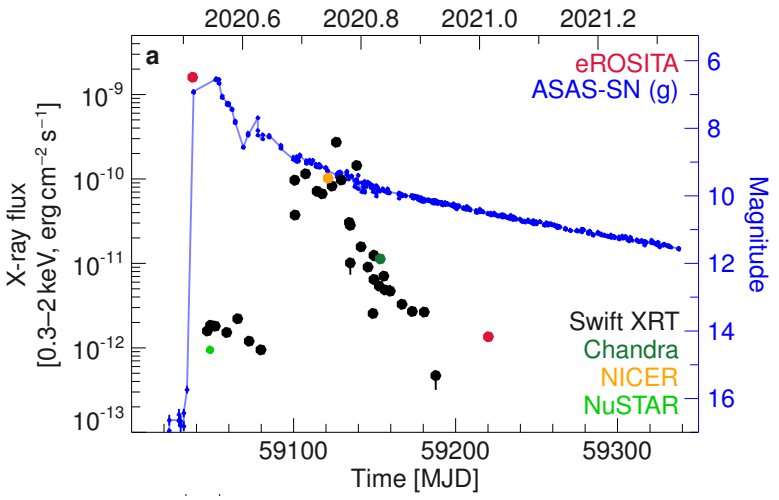

Figure 1.9: Long-term evolution of YZ Ret nova tracing the absorbed X-ray flux (using eROSITA, Swift, NICER, and Chandra data) and the optical flux (ASAS-SN data) from the flash through the supersoft state. The extrapolated NuSTAR flux is multiplied by 100 for visibility. Figure from König et al. (2022b).

1.2.2 Extragalactic X-ray transients and variables

Supernovae

Supernovae (SNe, Woosley & Weaver 1986) are among the most powerful explosions in the universe, happening in the end of stellar evolution of massive stars or white dwarfs. These events are classified broadly into two main categories based on their progenitor systems and explosion mechanisms: core-collapse supernovae (CCSNe, Janka 2012) and thermonuclear supernovae (Type Ia SNe, Nomoto et al. 1984; Hillebrandt & Niemeyer 2000). CCSNe arise from the gravitational collapse of massive stars ($M > 8M_{\odot}$) following the exhaustion of nuclear fuel in their cores, while Type Ia SNe result from the thermonuclear explosion of a carbon-oxygen white dwarf in a binary system that accretes material from a companion until it approaches the Chandrasekhar limit[4].

Initially, brief (30–3000 s) bright X-ray emission ($L_X \sim 10^{43} - 10^{46}$ erg s^{-1} with temperatures of $0.1 - 1$ keV) can appear due to the breakout of the shock wave from the stellar surface in the early moments after a SN explosion (Alp & Larsson, 2020). These thermal events are shock breakouts (SBOs). Afterwards, thermal and non-thermal X-ray emission primarily originates from shock-heated plasma in the expanding ejecta and circumstellar medium (Chevalier & Fransson, 1994; Immler & Lewin, 2003). For example, CCSNe expanding in a dense medium exhibit luminous X-ray emission ($10^{39} - 10^{41}$ erg s^{-1}, Dwarkadas & Gruszko 2011). In contrast, Type Ia supernovae, with lower circumstellar medium densities, are typically fainter in X-rays (e.g., Immler et al. 2006; Russell & Immler 2012, $L < 10^{38}$ erg s^{-1}).

[4]The maximum mass of a stable white dwarf star ($\approx 1.4M_{\odot}$).

Ultra-luminous X-ray sources

Ultraluminous X-ray sources (ULXs, Long et al. 1981; Fabbiano 1989) are extragalactic off-nuclear point sources with extraordinary high X-ray luminosities compared to X-ray binaries ($L_X > 10^{39}$ erg s^{-1}) under the assumption of isotropic emission (Kaaret et al., 2017). The ULX might originate in binaries with stellar-mass compact objects in extreme super-Eddington accretion regimes, where the possibility of super-Eddington accretion is facilitated by the presence of winds and outflows (Poutanen et al., 2007; Fabrika et al., 2015; Kosec et al., 2018) or rotating neutron stars with strong magnetic fields undergoing super-Eddington accretion (Basko & Sunyaev, 1976; Bachetti et al., 2014; Fürst et al., 2016; Israel et al., 2016). Finally, ULXs might originate from accretion onto intermediate-mass black holes (IMBHs), not exceeding the Eddington limit (Barrows et al., 2019). X-ray spectra of ULXs often display a two-component structure (e.g., Miller et al. 2003; Cropper et al. 2004). Firstly, there is a soft thermal component below 2 keV, which represents emission from an accretion disk. Additionally, a harder component above 2 keV is typically present, indicative of upscattering in a hot corona or the presence of a high-energy tail associated with the accretion flow. While some ULXs are persistent sources, others show variability over timescales of tens to thousands of days and luminosities greater than several $\times 10^{38}$ erg s^{-1} and up to 10^{40} erg s^{-1} (see Fig. 1.6). This transient behavior is often attributed to disk instabilities (e.g., Lasota et al. 2011). Periodic or quasi-periodic variability has also been observed in some ULXs, including pulsations in ULX pulsars, confirming neutron star accretors in these systems (e.g., Bachetti et al. 2014).

Gamma-ray Burst Afterglows

Gamma-ray bursts (GRBs; Klebesadel et al. 1973) are a series of intense, short-duration hard X-ray, gamma-ray flashes coming from random directions in the sky. GRBs are separated in two classes (Kouveliotou et al., 1993; Dezalay et al., 1996), according to their duration: long (LGRBs, > 2s), and short (SGRBs, < 2s). While LGRBs are associated with the core-collapse of massive stars (Woosley & Bloom, 2006), SGRBs are linked to compact object binary (NS-NS or NS-BH) mergers (Berger, 2014). Transient emission is often seen following the prompt GRB event. These GRB afterglows (Costa et al., 1997) are often X-ray bright. The afterglow emission arises from synchrotron radiation as relativistic jets interact with the surrounding medium (Kumar & Granot, 2003). Typical X-ray afterglow peak luminosities are in the range $10^{46} - 10^{49}$ erg s^{-1} in the hours following the GRB (D'Avanzo et al., 2012). Their light curves show segmented power-law decay $\propto t^{-\alpha}$ (Nousek et al., 2006). Examples of X-ray light curves of GRB afterglows are shown in Fig. 1.10. The X-ray spectra are typically hard and can be fit with a power-law with $\Gamma \approx 1 - 2.4$ (de Pasquale et al., 2006).

Fast X-ray transients

Fast X-ray Transients (FXTs) are short flashes of X-ray emission lasting from seconds to hours (e.g., Quirola-Vásquez et al. 2022). Although, their origin is still uncertain, they

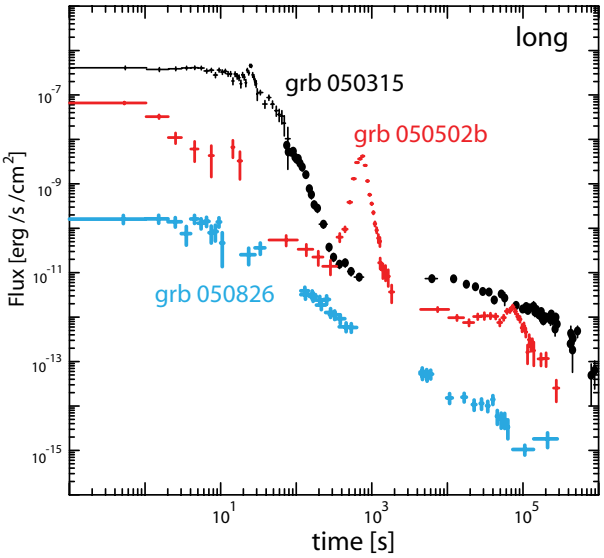

Figure 1.10: Examples of X-ray afterglow light curves of GRBs observed with Swift/XRT. Figure adopted from Gehrels et al. (2009).

are thought to be associated with strong gravitational wave sources, such as a merger of binary NS (Dai et al., 2006); a disruption of a WD by an IMBH (Maguire et al., 2020); and SBOs with compact progenitors (Waxman & Katz, 2017).

Active galactic nuclei

Active galactic nuclei (AGN) has a SMBH with a mass ranging from 10^6 to $10^9\,M_\odot$ in the centres of massive galaxies (Lynden-Bell, 1969). In the standard paradigm the SMBH is surrounded by a geometrically thin, optically thick accretion disk (Shakura & Sunyaev, 1973), extending to the innermost stable circular orbit[5] (ISCO) of the BH. This disk produces quasi-thermal emission peaking in the optical to ultraviolet (UV) energy bands (Frank et al., 2002). At higher energies, typically above $\sim 2\,\mathrm{keV}$, power-law emission is observed, which is believed to originate from a hot corona (with temperatures around $10^9\,\mathrm{K}$) situated above the disk (Galeev et al., 1979). The corona upscatters the soft photons from the accretion disk via inverse Compton scattering, producing the observed hard X-ray power-law spectrum. The AGN spectrum is typically characterized by a photon index Γ, where the power-law flux F(E) is expressed as $F(E) \propto E^{-\Gamma}$. The photon index Γ generally lies in the range 1.8–2.0 (Nandra & Pounds, 1994; Reeves & Turner, 2000; Molina et al., 2009). The X-ray luminosities of AGN span a wide range, typically from $\approx 10^{41}\,\mathrm{erg\,s^{-1}}$ for low-luminosity AGN to $\approx 10^{46}\,\mathrm{erg\,s^{-1}}$ for bright quasars (e.g., Aird et al. 2010; Fotopoulou et al. 2016).

AGN exhibit significant variability in X-rays on a wide range of timescales, from hours

[5]The innermost stable circular orbit is the smallest stable circular orbit in which a test particle can stably orbit a massive object in general relativity.

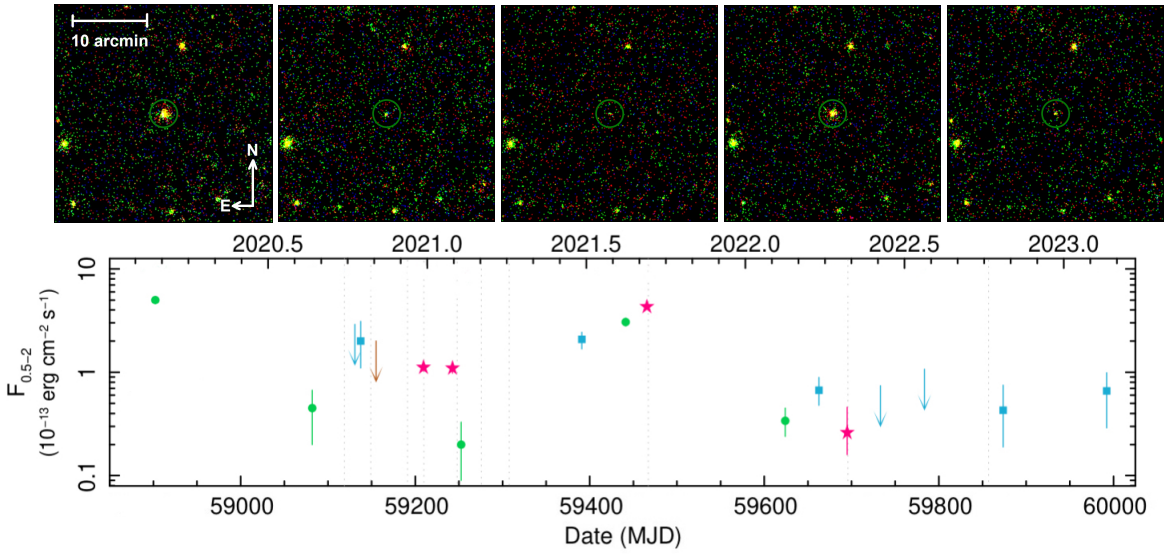

Figure 1.11: eRASS1–5 X-ray images and X-ray light curve of a changing-look AGN identified with eROSITA. The flux variability, and therefore the changes of brightness of the source, are caused by the cloud obscuration events around the SMBH. Figures adopted from Markowitz et al. (2024).

to years. On the one hand, short-term variability (hours to days) is often attributed to fluctuations in the accretion process near the SMBH, where viscous and thermal instabilities in the inner accretion disk can drive rapid changes in X-ray emission (Lyubarskii, 1997). Magnetohydrodynamic (MHD) turbulence and magnetic reconnection events in the corona may also contribute to short-term variability (e.g., di Matteo 1998). On the other hand, long-term variability (months to years) is present in a large fraction of AGN (Soldi et al. 2014, see Fig. 1.11). It may result from changes in the accretion rate (McHardy et al., 2006; Noda & Done, 2018), disk structure (Czerny, 2006), or the state of the corona (Wilkins & Gallo, 2015). The observed X-ray variability amplitude often anti-correlates with the AGN's X-ray luminosity (Nandra et al., 1997). Variability studies of AGN with eROSITA were explored in Boller et al. (2021); Homan et al. (2023); Medvedev et al. (2023); Boller et al. (2025); Krishnan et al. (2024); Prokhorenko et al. (2024).

AGN X-ray variability can be accompanied by significant spectral changes. Partial-covering absorbers or variable column densities can attenuate the soft X-rays more strongly than the hard X-rays, leading to an apparent hardening of the spectrum. Conversely, a decrease in obscuration can make the spectrum appear softer. Such effects are evident in "changing-look" AGN (Matt et al., 2003; Ricci et al., 2016), where rapid changes in obscuration significantly alter the observed spectral shape intervening material in the line of sight, such as the AGN's torus or clumpy absorbing clouds (Risaliti et al., 2002; Turner & Miller, 2009).

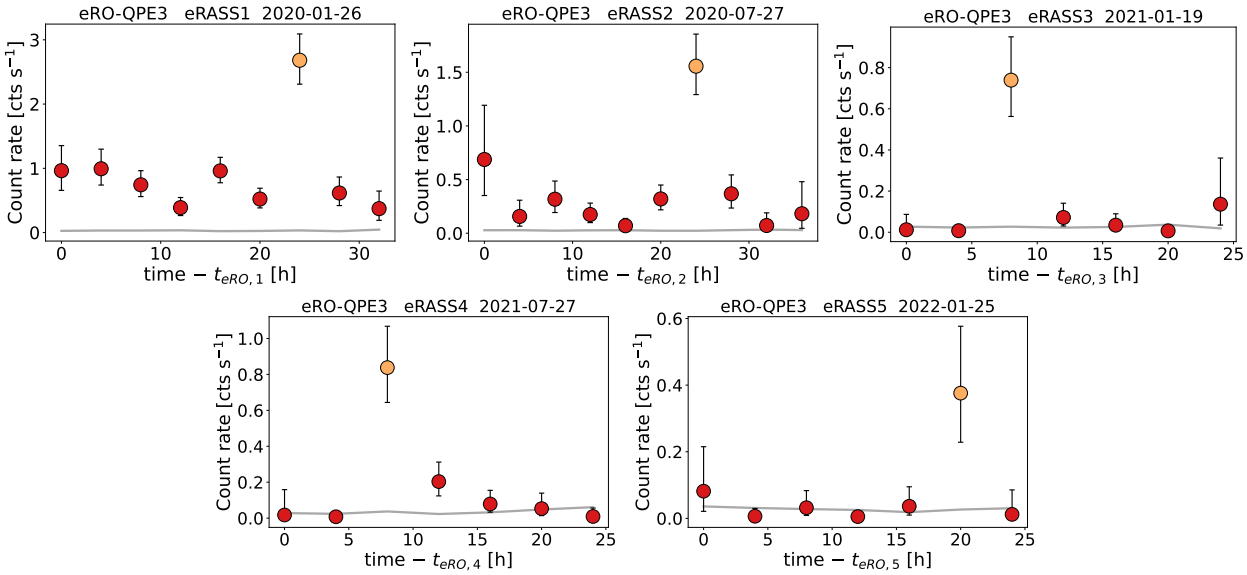

Figure 1.12: eRASS1-5 light curves of eRO-QPE3 in the 0.2–2.0 keV band. Orange data points highlight the detection of eruptions, and the gray line connects the background level across the eROdays in each eRASS. This example highlights eROSITA's capability to detect transients on the eROday timescale. Figure from Arcodia et al. (2024).

Quasi-periodic eruptions

Quasi-periodic eruptions (QPEs) are high-amplitude X-ray outbursts repeating every few hours and originating near the SMBH in a galaxy center (Miniutti et al., 2019; Giustini et al., 2020). eROSITA played a crucial role in uncovering the QPE population (Arcodia et al., 2021, 2024) by utilizing its all-sky coverage and short-term eROday light curves, suitable for searches for such flares. An example of a QPE light curve is shown in Fig. 1.12. QPEs span luminosities $10^{42}-10^{43}$ erg s^{-1} and are X-ray soft with the temperatures varying between ≈ 50 and ≈ 120 eV between the eruption and quiescence phases (Arcodia et al., 2024).

Despite the QPE origin still being unclear, the proposed scenarios include either accretion disk instabilities (e.g., Raj & Nixon 2021; Pan et al. 2023) or a binary system of a central BH and a much smaller body orbiting it (e.g., King 2022; Metzger et al. 2022). In the latter case, the disk is pierced by the orbiter, and shocks are caused by a cloud of gas ejected by the collisions (Linial & Metzger, 2024). Recent models suggest that the disk itself may originate from the debris of a tidally disrupted star (see Sect. 1.3), and that the orbiting companion may be a part of an extreme mass ratio inspiral (EMRI) system, in which a compact object spirals into a much more massive BH while accreting gas from the disk (Franchini et al., 2023; Linial & Metzger, 2024).

1.3 Tidal Disruption Events

A tidal disruption event (TDE) occurs when a star passes too close to a supermassive black hole (SMBH), so that the star's self-gravity is insufficient to withstand the tidal forces of the black hole (Rees, 1988). A schematic representation of a TDE is shown in Fig. 1.13. In the canonical scenario, the star is fully torn apart into a stream of debris. Approximately half of this stellar debris becomes gravitationally bound to the SMBH, forming an accretion flow (Evans & Kochanek, 1989). The bound material initially follows highly eccentric orbits, eventually circularizing due to stream-stream collisions, forming a hot accretion disk (Bonnerot et al., 2015). This disk emits intense radiation, predominantly in X-rays for the innermost regions near the SMBH, and optical or UV light from reprocessing in the outer layers or surrounding material (Metzger & Stone, 2016; Dai et al., 2018).

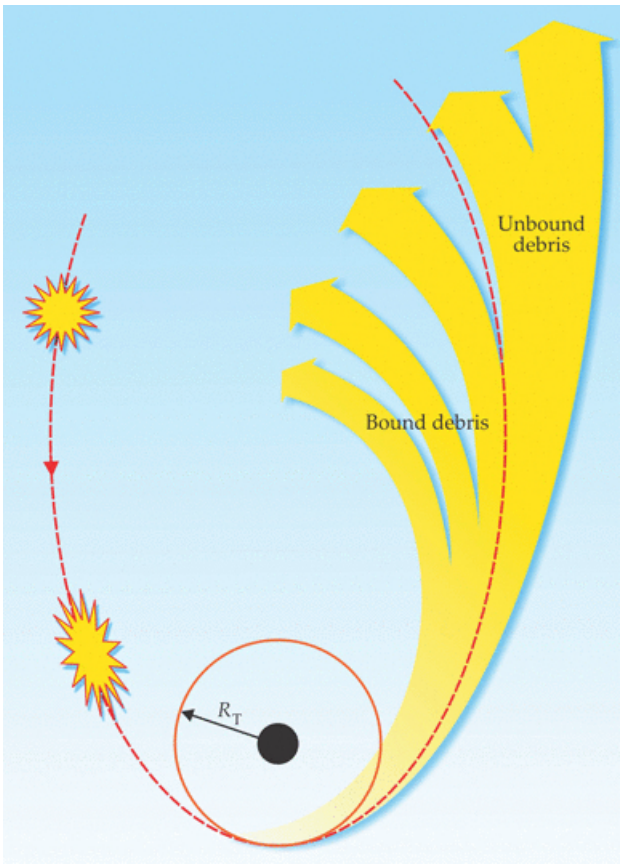

Figure 1.13: Schematic illustration of a TDE. A star approaching a SMBH is torn apart by tidal forces when it crosses the critical tidal radius, R_T, where the black hole's tidal force exceeds the star's self-gravity. Following the disruption, approximately half of the stellar debris remains gravitationally bound and eventually accretes onto the black hole, while the other half is ejected. Adapted from S. Gezari, Physics Today.

1.3.1 Physics of TDEs

The tidal radius is the characteristic distance at which tidal forces overcome a star's self-gravity. By equating the self-gravity force of a star and the tidal force from a black hole (BH), the tidal radius can be estimated:

$$R_t = R_* \left(\eta^2 \frac{M_{\rm BH}}{M_*} \right)^{1/3} \tag{1.1}$$

where R_* is the radius of the star, M_* is the mass of the star, $M_{\rm BH}$ is the BH mass, and $\eta \approx 1$, depending on the structure of the star (Evans & Kochanek, 1989). Thus, the star is disrupted if the pericentre radius[6] of the star's orbit is less than the tidal radius (Hills, 1975). For a typical Sun-like star, the tidal radius lies outside the the Schwarzschild radius[7] for non-spinning SMBHs with masses up to approximately $10^8 M_\odot$, which means that the disruption happens outside the event horizon and is observable. However, if the BH mass exceeds this threshold, the tidal radius falls within the Schwarzschild radius, and the star will be swallowed whole without producing an observable electromagnetic signature (Rees, 1988). This critical BH mass, known as the Hills mass ($M_{\rm Hills}$), can be determined by equating the tidal radius to the Schwarzschild radius (r_s):

$$M_{\rm Hills} \sim \frac{c^3}{2G} \left(\frac{R_*}{M_*} \right)^{1/2}. \tag{1.2}$$

Following Eq. 1.2, the disruption of white dwarfs (WDs; $R_* \approx 0.01 R_\odot$, $M_* \approx M_\odot$) can provide unique evidence for the presence of intermediate-mass black holes (IMBHs), since WDs can only be disrupted by BHs with masses in the range $10^3 M_\odot < M_{BH} < 10^5 M_\odot$: for lower mass BHs the tidal radius becomes similar to the stellar radius, and no disruption occurs; for larger BHs the tidal radius falls within the Schwarzschild radius, leading to the direct capture of the WD without observable emission (Maguire et al., 2020).

When a star is disrupted by tidal forces, approximately half of the stellar material is ejected from the system on hyperbolic orbits. In contrast, the other half remains bound to the black hole, and can be accreted (Rees, 1988). The distribution of specific energy ϵ across the stellar debris plays a crucial role in determining the fallback time and the evolution of the mass accretion rate onto the BH. For Keplerian orbits, the specific energy $\epsilon = -GM_{BH}/2a$, where a is the semi-major axis of the elliptical orbit. A spread of specific energies ($\Delta\epsilon$) in the debris appears since different parts are located at different positions in the BH's gravitational potential. $\Delta\epsilon$ can be computed from the gradient of the gravitational potential across the star's radius (Lacy et al., 1982), thus, at the tidal radius:

$$\Delta\epsilon \sim \frac{GM_{\rm BH}R_*}{r_t^2} = \frac{GM_{\rm BH}}{R_*} \left(\frac{M_*}{M_{\rm BH}} \right)^{2/3}. \tag{1.3}$$

[6] The closest distance between an orbiting object and the central body it orbits.

[7] The critical radius at which the escape velocity equals the speed of light, defining the event horizon of a non-rotating BH, $r_s = \frac{2GM_{\rm BH}}{c^2}$.

The fallback time is defined as the orbital period of the most bound debris that returns to the pericentre after the disruption. The orbital period of a bound debris element is related to the semi-major axis by Kepler's third law: $T = 2\pi\sqrt{a^3/GM_{\rm BH}}$. For the most bound material $\epsilon = |-\Delta\epsilon|$ determines the timescale. Therefore, substituting for a and ϵ, the fallback time is (Gezari, 2021):

$$t_{\rm fallback} \sim \frac{\pi}{\sqrt{2}}\left(\frac{R_*^3}{GM_*}\right)^{1/2}\left(\frac{M_{\rm BH}}{M_*}\right)^{1/2} = 0.11yrR_*^{3/2}M_6^{1/2}M_*^{-1}, \tag{1.4}$$

where $M_6 = M_{BH}/10^6 M_\odot$. As the fallback time scales as $M_{\rm BH}^{1/2}$, the TDE flare light curve might be used for determining the BH mass.

The fallback rate $\dot{M}_{\rm fallback}$ describes how mass returns to the BH over time: $\dot{M}_{\rm fallback} \sim dM/dt$. Since the fallback time is related to the specific energy of the debris by: $t_{\rm fallback} \propto |\epsilon|^{-3/2}$, we can express $|\epsilon|$ as a function of t: $|\epsilon| \propto t^{-2/3}$, using Eq. 1.3 and Eq. 1.4. The debris mass distribution is approximately uniform in energy, so $\frac{dM}{d\epsilon} \sim$ const. Using the chain rule for derivatives, the fallback rate is then proportional to the rate of change of ϵ with respect to time:

$$\dot{M}_{\rm fallback} \sim \frac{dM}{dt} \propto \frac{d\epsilon}{dt} \propto t^{-5/3}, \tag{1.5}$$

or writing explicitly all constants after integration from $t_{\rm fallback}$ to infinity:

$$\dot{M}_{\rm fallback} = \dot{M}_{\rm peak}(t/t_{\rm fallback})^{-5/3}, \tag{1.6}$$

where $\dot{M}_{peak} = \frac{M_*}{3t_{fallback}}$. The luminosity follows the fallback rate resulting in a light curve decay with the characteristic $t^{-5/3}$ slope. However, in the case of a partial disruption, i.e., when a star loses part of its mass due to tidal forces but remains intact after passing near a BH, a steeper power-law decline is expected ($t^{-9/4}$,e.g., Coughlin & Nixon 2019). Other free parameters of the system, such as the internal structure and spin of the star or its impact parameter, as well as the BH spin may also influence the fallback rate (Gezari, 2021).

In the canonical case of efficient disk circularization, the bound material forms an accretion disk, emitting radiation as it spirals inward, producing a bright flare that is observable across the electromagnetic spectrum, particularly in the X-ray, UV, and optical bands. The accretion rate and luminosity are often characterized using Eddington values. The Eddington luminosity is the luminosity at which the radiation pressure due to electron scattering equals the gravitational force: $L_{\rm Edd} = \frac{4\pi GMm_pc}{\sigma_T}$. The Eddington accretion rate, corresponding to the Eddington luminosity, is: $\dot{M}_{\rm Edd} = \frac{L_{\rm Edd}}{\eta c^2}$, where η is the radiative efficiency. Depending on the BH mass, the accretion geometry, and the fraction of gas ejected with an outflow, the accretion mode (Gezari, 2021) can be super-Eddington ($\dot{M}_{\rm fallback}/\dot{M}_{\rm Edd} > 1$ for $M_{BH} > 3\times10^7 M_\odot$) or sub-Eddington ($\dot{M}_{\rm fallback}/\dot{M}_{\rm Edd} < 1$ for $M_{BH} < 3\times10^7 M_\odot$).

The peak temperature of a standard, radiation-dominated thin disk can be estimated using the blackbody approximation for the inner region of the disk:

$$T_{\rm peak} \approx \left(\frac{3GM\dot{M}}{8\pi R_{\rm in}^3 \sigma} \right)^{1/4}, \tag{1.7}$$

where $R_{\rm in}$ is the inner disk radius (typically taken as a few times the Schwarzschild radius). Substituting values for an arbitrary SMBH ($M \sim 10^6 M_\odot$) and assuming an Eddington accretion rate, the resulting peak temperature is of order

$$T_{\rm peak} = 3 \times 10^5 (M^6)^{1/12} \left(\frac{R_*}{R_\odot} \right)^{-1/2} \left(\frac{M_*}{M_\odot} \right)^{-1/6} \text{K} \tag{1.8}$$

Thus, the peak of the thermal emission is in the soft X-ray band (e.g., for a solar-type star and $M_{BH} \approx 10^6 M_\odot$, $kT \approx 30$ eV), consistent with observations of many X-ray-selected TDEs (e.g., Rees 1988; Komossa 2015; more details in Sect. 1.3.2). This makes instruments like eROSITA, with its sensitivity in the soft X-ray range (0.2–2 keV), particularly well-suited to discovering and studying TDEs.

1.3.2 X-ray discovered TDEs

The first observational evidence for TDEs came from the detection of ultra-soft X-ray flares from the centers of quiescent galaxies during the ROSAT all-sky survey in 1990–1991 (NGC 5905, Bade et al. 1996; Komossa & Bade 1999; RX J1242.6–1119, Komossa & Greiner 1999; RX J1624+7554, Grupe et al. 1999; RX J1420+5334, Greiner et al. 2000). The joint X-ray light curve, remarkably consistent with theoretical predictions, is shown in Fig. 1.14. In the early 2000s, the XMM-Newton survey, utilizing its higher spatial resolution and sensitivity, as well as Swift and Chandra, detected new TDE candidates or were used to follow up ROSAT-detected TDEs (e.g., Komossa et al. 2004). Repeated coverage of some sky areas and large X-ray source catalogues, enabled the identification of new transients with prominent flares by comparing the data with previous X-ray observations, especially with the ROSAT database (e.g., Cappelluti et al. 2009; Khabibullin & Sazonov 2014; Maksym et al. 2014). While many of these detected sources were consistent with the expected properties of soft X-ray TDEs (e.g., Saxton et al. 2012b, 2017), new discoveries of non-canonical TDEs also appeared, such as jetted TDEs (which are discussed later in this section).

A comprehensive review of properties of X-ray-selected TDEs was presented in Saxton et al. (2020). Approximately 20 X-ray selected TDE candidates have been discovered before eROSITA. Overall, the canonical X-ray TDEs are characterized by:

- **Soft X-ray spectrum**: as discussed in Sect. 1.3.1, TDE spectra are usually dominated by thermal blackbody emission with temperatures kT $\approx 0.04 - 0.12$ keV (or power law indices $\Gamma \approx 3 - 5$), originating from an accretion disk formed by the stellar debris.

- **Flaring X-ray light curve**: canonical X-ray light curves usually show a fast rise (days to weeks) and a gradual decay (months to years). The decay often follows the predicted $t^{-5/3}$ power-law slope (see Sect. 1.3.1 and Fig. 1.14), consistent with the fall-back time.

- **Peak X-ray luminosities** are typically in the range $10^{42} - 10^{44}\,\mathrm{erg\ s^{-1}}$.

- **Quiescent host galaxies**: X-ray TDEs are usually identified in hosts with no previous signs of historical active galactic nuclei (AGN) X-ray emission. They are predominantly found in post-starburst or E+A galaxies, suggesting a preference for dense stellar environments where disruption rates are higher (French et al., 2016).

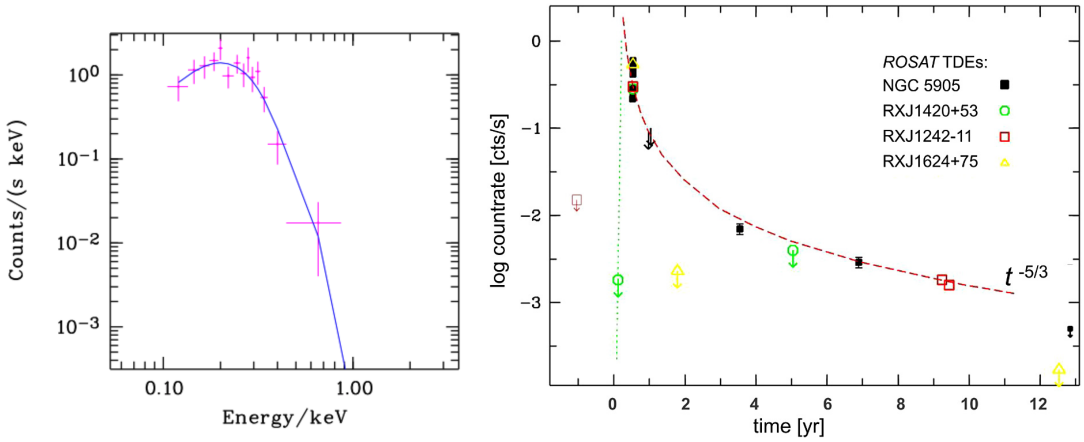

Figure 1.14: Typical observational properties of X-ray TDEs. Left: Ultra-soft ROSAT spectrum of the TDE candidate RX J1420+5334. The pink markers show the binned observed spectrum, and the blue line is the best fit blackbody model with $\mathrm{kT} = 38 \pm 10$ eV. Right: Joint X-ray light curve of four TDEs identified with ROSAT, all shifted to the same peak time. The light curve is consistent with a $t^{-5/3}$ power-law decline (dashed lined). Figures from Greiner et al. (2000) and Komossa (2015).

Beyond the standard class of soft X-ray TDEs, several subclasses exhibit deviations from the canonical properties. In some cases, the star is only partially disrupted and survives the encounter (Guillochon & Ramirez-Ruiz, 2013). These events may result in multiple flares from repeatedly stripping the star on each pericenter passage (e.g., see detailed examples in Sect. 1.3.5). Moreover, a small fraction of TDEs exhibit powerful relativistic jets that may produce hard X-ray and radio emission (see Sect. 1.3.3 for more information on radio emission of TDEs), distinguishing them from thermal soft X-ray TDEs (e.g.,Swift J164449.31573451, Bloom et al. 2011; Burrows et al. 2011; Swift J2058.4+0516, Bradley Cenko et al. 2012; Swift J1112.2-8238, Brown et al. 2015). Follow-up observations showed that these jetted TDEs have higher peak X-ray luminosities ($\mathrm{L} \approx 10^{46} - 10^{48}\,\mathrm{erg\ s^{-1}}$) and harder X-ray spectra with power-law slopes $\Gamma < 2$.

1.3.3 Observational properties of TDEs in other bands

TDEs exhibit distinctive observational signatures not only in X-rays but also in the UV (e.g., Gezari et al. 2006, 2008, 2009), optical (e.g., Hammerstein et al. 2022; Yao et al. 2023), infrared (IR; e.g., Panagiotou et al. 2023; Masterson et al. 2024), and radio bands (e.g., Alexander et al. 2020). An example of a multiwavelength light curve of an eROSITA TDE candidate, showing prominent flares in various bands is shown in Fig. 1.15.

In the UV and optical bands, TDEs are characterized by a sharp increase in brightness followed by a gradual decline over months to years. Similarly to the X-ray flares, the light curves often follow a power-law decay, typically proportional to $t^{-5/3}$ (Gezari, 2021). Spectroscopically, TDEs display broad emission lines, including, for example, hydrogen Balmer lines and helium lines, indicating high-velocity outflows and the presence of ionized gas (e.g., Gezari et al. 2012; Hammerstein et al. 2022).

In the infrared band, TDEs can exhibit emission resulting from the reprocessing of higher-energy radiation by surrounding dust (van Velzen et al., 2021). IR light curves of TDEs can show delayed peaks compared to their optical/UV counterparts, due to the time required for the dust to absorb and re-emit the radiation (e.g., Dou et al. 2017).

Radio emission in TDEs is relatively rare and typically associated with the launch of relativistic jets (e.g., Sfaradi et al. 2024) or outflows. A small fraction of TDEs (at most a few percent) have been observed to produce radio-luminous mildly relativistic jets (e.g., Bloom et al. 2011). The remainder of the population are radio quiet, producing less luminous jets, non-relativistic outflows (e.g., Alexander et al. 2017; Goodwin et al. 2023), or possibly no radio emission at all.

1.3.4 Multiwavelength view of TDEs

TDEs exhibit a wide range of observational characteristics and can appear dramatically different depending on the wavelength in which they are observed, with some TDEs even being detected only in one or two bands. Thus, the discovery of multiwavelength TDEs has raised an important question: are these variations of the same phenomenon, requiring a unified model, or do they represent distinct populations? Two main models — obscuration and stream-stream collision — have been proposed to explain the observed multiwavelength properties of TDEs.

Obscuration model

The obscuration model suggests that the observed emission in TDEs is significantly influenced by a reprocessing layer or envelope of stellar debris that absorbs and re-emits high-energy X-ray and UV radiation from the accretion disk. This layer, composed of optically thick gas and potentially dust, plays a critical role in determining the appearance of TDEs across different wavelengths, including optical, IR, and X-rays (Metzger & Stone, 2016; Dai et al., 2018).

The geometry and column density of the obscuring material are highly anisotropic,

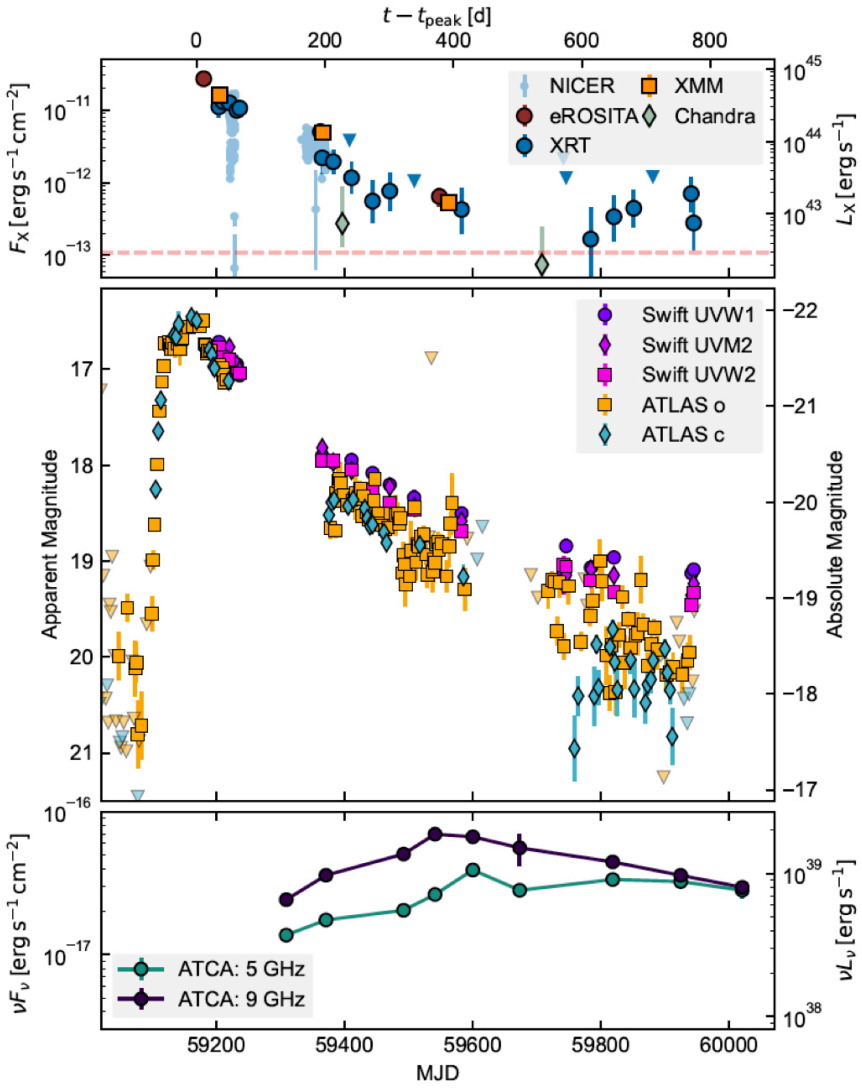

Figure 1.15: The optical, UV, X-ray and radio light curves of the eROSITA TDE candidate J2344. The source showed quasi-simultaneous flares in X-ray, optical and UV bands and later radio brightening associated with an appearance of a jet. Top panel: X-ray data are compiled from eROSITA, NICER, Swift-XRT (XRT), XMM-Newton (XMM), and Chandra telescopes. F_X and L_X denote X-ray flux and rest-frame luminosity in 0.2-2.3 keV. Middle panel: UV observations from Swift were obtained in three filters—UVW1 (260 nm), UVM2 (220 nm), and UVW2 (190 nm). Optical photometry is from ATLAS in the orange ("o") and cyan ("c") bands. Bottom panel: radio observations at 5 and 9 GHz were conducted with ATCA. Figure from Malyali (in prep.).

leading to different observational features depending on the line of sight. If an observer looks through dense regions of the obscuration layer, e.g., parallel to the disk in Fig. 1.16, X-ray emission may be heavily attenuated or even completely obscured. In this scenario, the energy absorbed by the gas is reprocessed into optical and IR emission (Dai et al., 2018). This scenario aligns with observations of X-ray faint TDEs, which are predominantly bright in optical/UV bands (Gezari et al., 2012). Conversely, lines of sight with minimal obscuration, e.g., perpendicular to the accretion disk as shown in Fig. 1.16, produce a TDE with strong X-ray signatures and relatively weak optical emission. These TDEs exhibit X-ray spectra with temperatures $\approx 10^5$–10^6 K indicative of thermal disk emission (Komossa, 2015; Dai et al., 2018). Such X-ray bright TDEs are more likely to be detected in soft X-ray surveys, such as eROSITA. Intermediate viewing angles can yield a mixture of emission features, where soft X-rays are partially absorbed and reprocessed into UV or optical wavelengths.

Additionally, dust in the surrounding environment may contribute to IR emission through reprocessing, as it absorbs high-energy photons and re-emits them thermally. Therefore, the IR emission may peak later than the optical or UV emission, consistent with delayed heating of dusty material located at larger radii (van Velzen et al., 2016).

Stream-stream collision model

In the stream-stream collision model, multiwavelength emission arises from the interaction of stellar debris streams during their infall and circularization around the SMBH. An illustration of the initial shock and following circularization is shown in Fig. 1.17. After a star is disrupted, its debris forms eccentric streams that collide before settling into an accretion disk. These collisions, occurring at relativistic speeds, dissipate energy in shocks, producing luminous thermal radiation, e.g., blackbody-like emission peaking in the optical/UV, as well as non-thermal radiation, e.g., bremsstrahlung and Compton scattering contributing to X-rays (Piran et al., 2015; Shiokawa et al., 2015; Lu & Bonnerot, 2019). Additionally, optical and IR emission may arise from the reprocessing of X-ray and UV photons by the surrounding material.

The efficiency of accretion disk circularization also affects the observational properties. If the stellar debris circularizes efficiently, strong X-ray emission may emerge quickly as the accretion disk forms and heats to temperatures capable of producing thermal X-rays. In this case, the X-ray flare would precede or coincide with optical emission, which could arise later from the reprocessing of X-rays by surrounding material or from slower outflows at larger radii (Guillochon & Ramirez-Ruiz, 2015; Dai et al., 2018). In contrast, if circularization is inefficient, the initial debris streams may experience prolonged collisions before fully settling into an accretion disk. Under these conditions, the optical flare, originating from shock-driven emission during these collisions, would dominate early on. X-ray emission would emerge only after sufficient circularization has occurred to form a hot accretion disk (Piran et al., 2015; Blagorodnova et al., 2017).

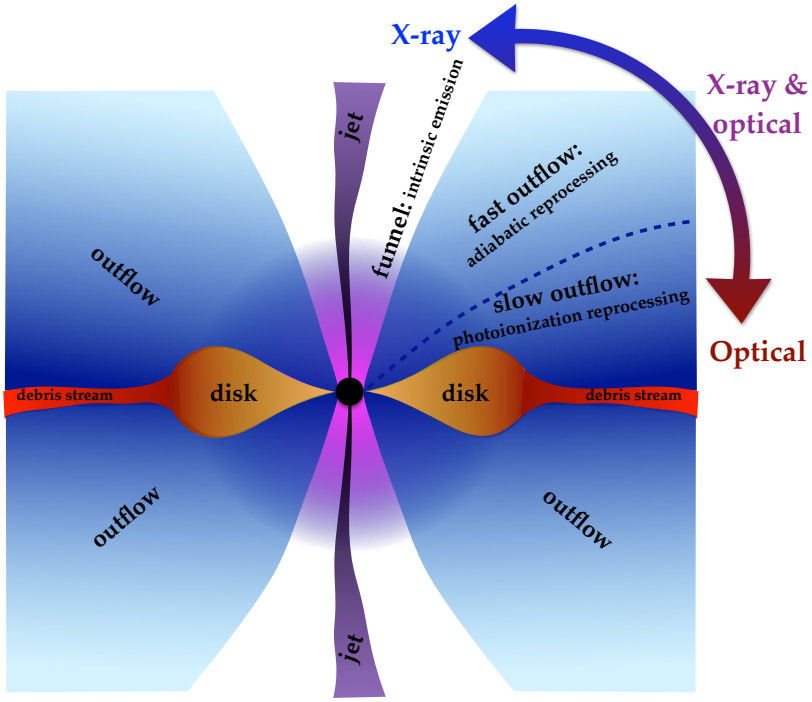

Figure 1.16: Schematic of viewing-angle dependence of observed multiwavelength TDE emission. The emission from the inner super-Eddington disk is reprocessed by an obscuring envelope. The inner region is only visible when the observer's line of sight is aligned with the optically thin funnel, exposing X-ray radiation without any obstruction. In other viewing orientations, X-rays are fully or partially reprocessed into optical and IR. A jet is shown for completeness, although jets were not detected for the majority of TDEs. Figure from Dai et al. (2018).

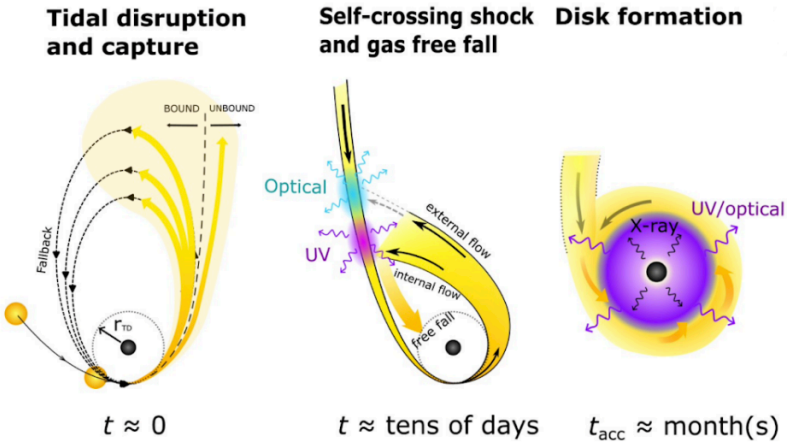

Figure 1.17: Scheme of TDE evolution in stream collision and delayed disk formation scenario. Step one: a star is torn apart at the pericenter. Around half of the stellar debris escapes while the other half remains gravitationally bound to the BH. Step two: stream-stream collision occurs producing the primary UV/optical flare and an optically thick envelope. Step three: gas falls onto the BH and forms an accretion disk, emitting X-rays. Figure adapted from Guo et al. (2025).

1.3.5 Individual TDEs discovered with eROSITA

eROSITA has enabled the discovery of numerous individual TDE candidates through a systematic, real-time search for nuclear transients during the telescope's operational phase from Nov 2019 to Feb 2022. The dedicated efforts of the TDE team at MPE, with constant monitoring shifts, led to the rapid identification of newly emerging transients and timely multiwavelength follow-up observations, essential for further study of these events. The detailed investigation of these sources uncovered non-canonical TDE behavior, broadening our objectives from merely detecting new transients to understanding the diversity and unusual properties of TDEs.

eROSITA has uncovered TDE candidates with a broad variety of light curves not necessarily consistent with a theoretically predicted $t^{-5/3}$ decline:

- TDE candidate AT2019avd was discovered in the nucleus of a previously inactive galaxy at z=0.029. The source appeared ultra-soft in X-rays (kT $\approx$ 85 eV) and 90 times brighter than the previous limits from XMM-Newton (Malyali et al., 2021). The Zwicky Transient Facility (ZTF; Bellm et al. 2019) optical light curve showed significant optical variability and was double peaked. The first optical peak preceded the first eROSITA detection by 450 days, and the rise of the second peak coincided with the eROSITA detection of the X-ray transient in eRASS1. While the X-ray properties made AT 2019avd a promising TDE candidate, its unusual optical properties gave rise to active discussions about the nature of this event, explaining it with

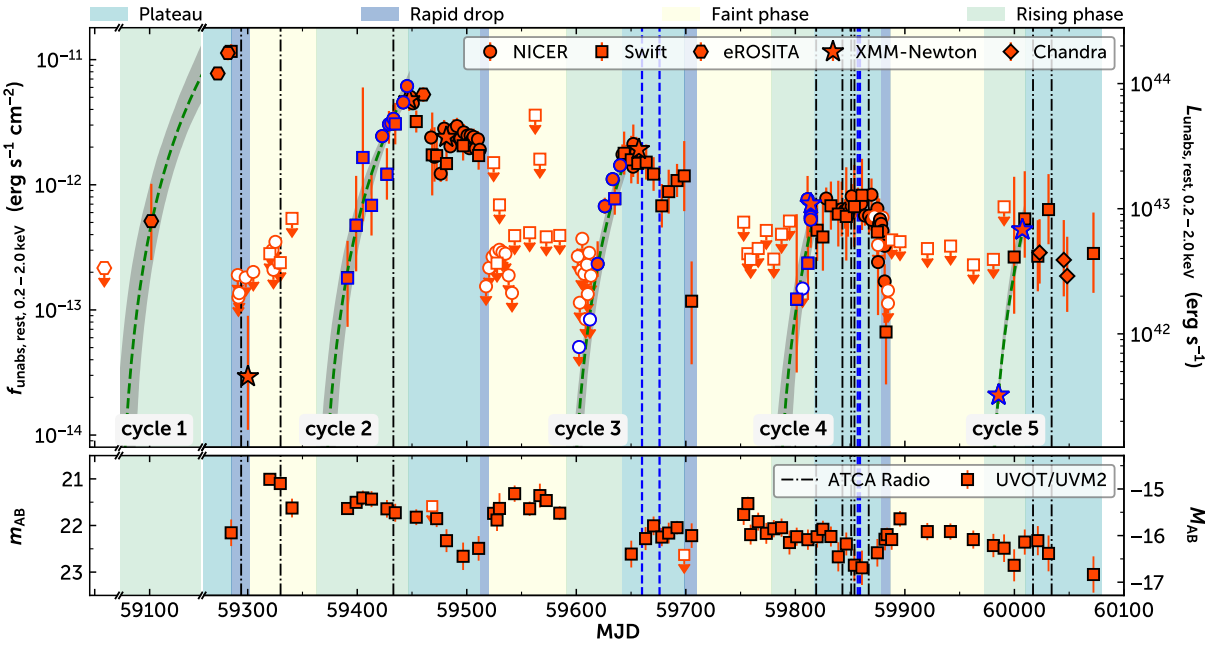

Figure 1.18: Long-term X-ray and UV light curves for J0456, a repeated partial TDE candidate discovered with eROSITA. The coloured regions represent the four phases: the plateau phase (light cyan), the rapid drop phase (light blue), the faint phase (light yellow), and the rising phase (light green). Top panel: the unabsorbed rest-frame X-ray light curve in the 0.2–2.0 keV band from eROSITA, Swift/XRT, NICER, XMM-Newton, and Chandra, with 90% uncertainties for detections and 3σ upper limits. Green dashed lines indicate the best-fitting power-law models for the five X-ray rising phases, with shaded regions representing the 1σ uncertainties. Bottom panel: Swift/UVOT UVM2 light curve with 1σ uncertainties and 3σ upper limits. Vertical lines mark the dates of ATCA radio observations; black dashed lines indicate non-detections and blue dashed lines indicate detections. Figure from Liu et al. (2024).

a stellar binary TDE candidate, or a TDE involving a supermassive black hole binary (Malyali et al., 2021). Another interpretation included a two-phase scenario in which the first optical peak was caused by disrupted stellar stream circularization, and the second phase through delayed accretion (Chen et al., 2022).

- Another eROSITA TDE candidate, eRASSt J074426.3+291606 (J0744) was discovered as a bright, ultra soft ($\Gamma \approx 4$) X-ray transient with a peak X-ray luminosity of $L_X \approx 5 \times 10^{43}$ erg s^{-1} in a dwarf galaxy (Malyali et al., 2023b). Extensive follow-up with NICER, Swift and Chandra revealed a rebrightening X-ray light curve, significantly deviating from the expected $t^{-5/3}$ decay. J0744 was accompanied by an optical-UV flare. Ultra-soft X-rays appearing only 20 days after peak optical brightness suggest the prompt formation of an accretion disc. J0744 is the faintest optical TDE observed to date, with the peak observed optical luminosity only reaching absolute g-

band magnitude of ≈ -16.8mag. Whereas other detected TDEs with similar optical peak luminosities have been characterized as "faint and fast" based on their optical decay timescale (e.g., iPTF-16fnl, Blagorodnova et al. 2017, $t_{decay} \approx 50$ days), J0744 uncovered a new class of "faint and slow" optical light curves ($t_{decay} > 100$ days).

eROSITA has also shed light on the phenomenon of repeated TDEs:

- The rebrightening of a ROSAT-selected TDE has revealed a repeating tidal disruption event occurring on a decadal timescale. RX J133157.6-324319.7 (J1331) was initially discovered in 1993 as a soft X-ray flare (kT ≈ 0.1 keV), and nearly 30 years later, eROSITA detected a second bright flare from the same source (Malyali et al., 2023a). Given that the probability of observing two independent, full TDEs from the same galaxy within a 30-year period is extremely low ($\approx 5 \times 10^{-6}$), the most plausible explanation is that J1331 underwent two partial tidal disruption events. This scenario suggests that the disrupted star is on a highly eccentric orbit around the BH, losing mass during each pericenter passage.

- Another exceptional repeating X-ray nuclear transient, eRASSt J045650.3-203750 (J0456, Liu et al. 2023), was discovered with eROSITA, exhibiting a recurrence period of ≈ 223 days. Thanks to an extraordinary prompt follow-up, J0456 is one of the best-studied repeating TDE candidates to date. Its X-ray evolution follows four distinct stages (see Fig. 1.18): a rising phase, a plateau lasting ~ 2 months, a rapid X-ray flux drop with an amplitude > 100 in just one week, and a faint state persisting for ~ 2 months. The transitions between these phases, along with the accompanying spectral evolution from soft ($\Gamma \gtrsim 3$) to hard ($\Gamma \lesssim 3$), suggest the periodic formation and subsequent destruction of a warm and hot corona with each stellar passage.

1.3.6 TDE or AGN?

The primary contaminants in TDE searches are variable AGN, given the widespread and diverse variability of the latter (see Sect. 1.2.2). Archival X-ray data can help establish pre-flare quiescence, but in many cases, the lack of deep, high-quality observations makes it difficult to confidently rule out prior emission. In this context, multiwavelength follow-up becomes essential, providing additional diagnostic tools to separate TDEs from AGN and other variable sources, ensuring more reliable classifications.

Optical spectroscopy

Optical spectroscopy is an important step to confirm the quiescence or otherwise of the host galaxy and, therefore, to identify new TDE candidates (Komossa & Greiner, 1999). AGN exhibit characteristic high-ionization narrow emission lines, such as [O III] λ5007, [N II], and [Ne III], which originate in the Narrow-Line Region (NLR) — a region of low-density gas located far from the SMBH and photoionized by the persistent radiation from a long-lived accretion disk (Osterbrock, 1989). In contrast, TDE's quiescent hosts either have no

emission lines or have low-ionization lines in cases of star-forming galaxies (e.g., Baldwin et al. 1981). However, distinguishing low-mass AGN and AGN in Low-Ionization Nuclear Emission Regions (LINERs) from TDEs can be more challenging spectroscopically (e.g., Greene 2012). In addition, unlike AGN, where the Broad-Line Region (BLR) is present continuously, TDEs can exhibit broad emission lines (e.g., Balmer and helium lines) only temporarily following disruption. These broad lines arise from the transiently forming accretion disk and outflows, and they fade over months to years, unlike AGN BLRs which persist as long as accretion is sustained (Arcavi et al., 2014; Holoien et al., 2015). A comparison of optical spectra of AGN and TDE is shown in Fig. 1.19.

Since TDE emission lines can evolve, it is essential to compare spectra before, during, and after the flare. Archival spectra, if available, help determine whether emission lines existed prior to the event, while late-time optical follow-up (months to years post-flare) can confirm whether these features fade. Relevant spectroscopic data can often be sourced from large-scale surveys such as the Sloan Digital Sky Survey (SDSS; Abdurro'uf et al. 2022), which covers a significant portion of the Northern sky; the Dark Energy Spectroscopic Instrument (DESI; Levi et al. 2019), which focuses on both Northern and equatorial fields, and the 6dF Galaxy Survey (Jones et al., 2004), targeting the Southern sky. In addition, a wide range of facilities across both hemispheres enables targeted follow-up, including instruments like ESO New Technology Telescope (NTT; Buzzoni et al. 1984) in La Silla, Magellan telecopes at the Las Campanas Observatory (Dressler et al., 2011), the Southern African Large Telescope (SALT; Buckley et al. 2006) at the South African Astronomical Observatory, and Wide field Spectrograph (WiFeS; Dopita et al. 2010) mounted on the ANU 2.3m telescope at Siding Spring Observatory, among many others.

Mid-infrared colors

Infrared colors from the Wide-field Infrared Survey Explorer (WISE; Wright et al. 2010) provide a useful diagnostic for distinguishing TDEs from AGN. AGN exhibit redder mid-infrared (mid-IR) colors than passive galaxies due to their persistent dusty torus, which reprocesses UV/X-ray radiation from the accretion disk into infrared emission. A common selection criterion for AGN is W1−W2$>$ 0.5 mag (where W1 and W2 filters are centered at 3.4 μm and 4.6 μm, respectively), with some studies using a more conservative threshold of W1−W2$>$ 0.8 mag to ensure robust AGN identification (Stern et al., 2012; Assef et al., 2013). This makes WISE color selection a valuable tool for excluding AGN contamination when identifying new TDE candidates in a systematic way. Since WISE is an all-sky survey that began prior to the launch of eROSITA, it provides a pre-flare baseline of the W1–W2 color for all sources. Specifically, the primary WISE mission (Wright et al., 2010) and the NEOWISE reactivation mission (Mainzer et al., 2011), together covering the sky from Dec. 2009 to Aug. 2024[8], offer valuable mid-infrared coverage not only before the X-ray flare, but sometimes also during and after the event.

[8] https://irsa.ipac.caltech.edu/Missions/wise.html

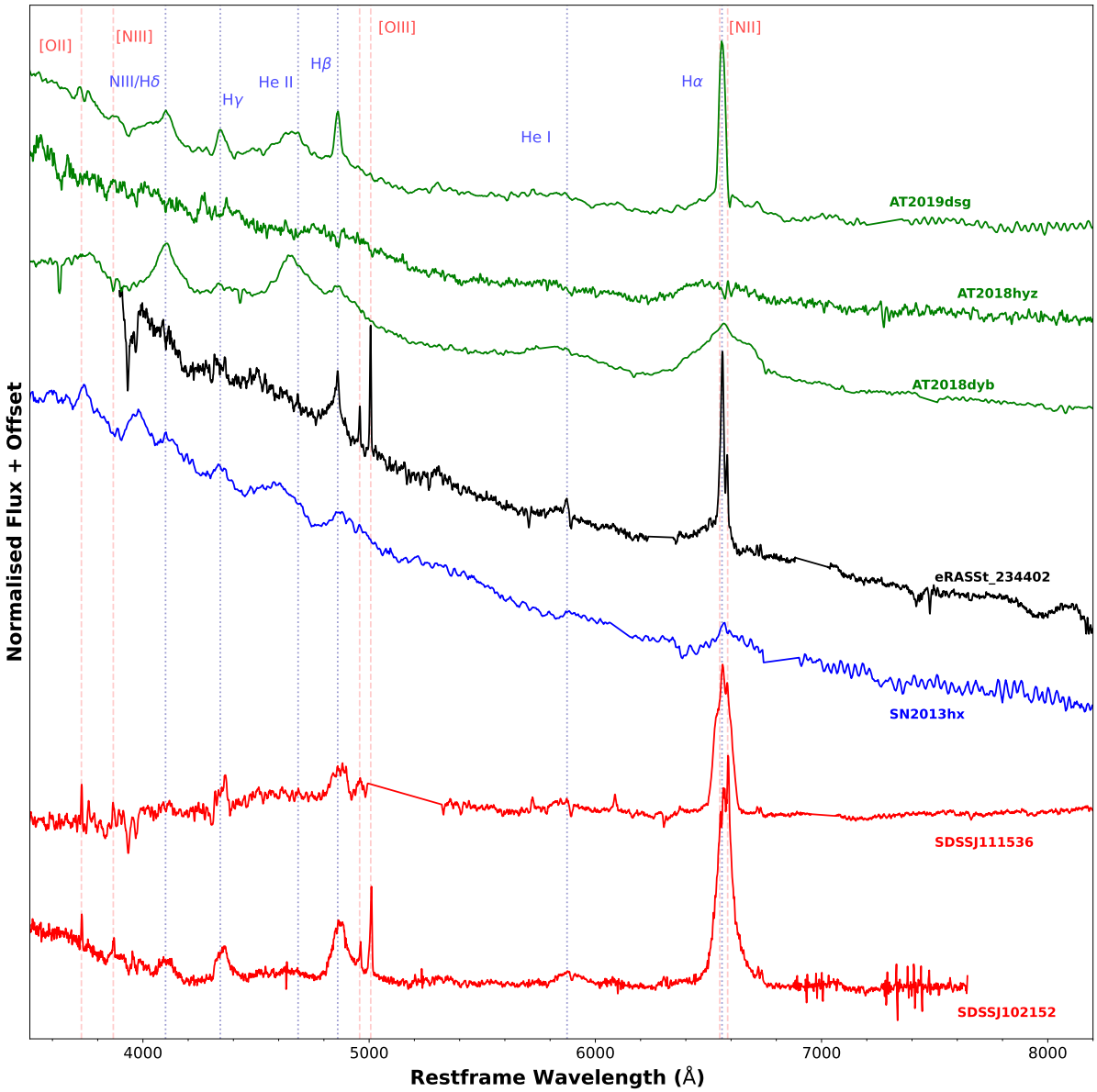

Figure 1.19: Optical spectrum of an eROSITA TDE candidate J2344 (black; Homan et al. 2023) compared with spectra of several classes of objects: TDEs (green), supernovae (blue), and changing-look AGN (red). The emission lines marked in red (dashed) are those more typically associated with AGN and the emission lines marked in blue (dotted), are those that are prominent in both AGN and TDEs. TDEs can exhibit broad emission lines (e.g., Balmer and helium lines). Sometimes, however, the difference can be very subtle (e.g., in case of J2344). Figure from Homan et al. (2023).

Radio properties

Radio observations provide a key diagnostic for identifying AGN, as radio-loud AGN exhibit long-lived strong, non-thermal synchrotron emission from relativistic jets or compact radio cores (e.g., Urry & Padovani 1995; Blandford et al. 2019). In contrast, most TDEs are initially radio-silent, as they lack persistent jets, though some can produce transient radio flares due to outflows or jet formation after the TDE (e.g., Alexander et al. 2020; Cendes et al. 2024). Thus, a long-lived compact radio core is a strong indicator of an AGN, whereas a non-detection in archival radio data followed by a delayed transient suggests a TDE. Radio data, both archival and from follow-up observations, play an important role in characterizing eROSITA TDEs and distinguishing them from AGN. Archival surveys such as the Faint Images of the Radio Sky at Twenty-Centimeters (FIRST; Becker et al. 1995) and the NRAO VLA Sky Survey (NVSS; Condon et al. 1998) provide broad coverage of the Northern sky at 1.4 GHz, offering useful pre-flare reference fluxes. In addition, there are more recent surveys such as Rapid ASKAP Continuum Survey (0.8 GHz and 1.4 GHz; McConnell et al. 2020), and the VLA Sky Survey (VLASS, 3 GHz; Lacy et al. 2020) Follow-up observations can be conducted with instruments like the Australia Telescope Compact Array (ATCA), which is well-suited for monitoring transient and variable radio emission in the Southern hemisphere.

Follow-up in X-rays

Prompt follow up of TDE candidates in X-rays and better sampling of their X-ray light curves may help to confirm the presence of only one flare, rather than persistent variability characteristic of AGN. However, one should remember that additional X-ray flares might be observed in repeating TDEs, as was shown by the examples in Sect. 1.3.5.

It is important to mention that TDEs can occur in AGN as well (e.g., Chan et al. 2019), but distinguishing them is challenging due to their similar emission mechanisms and the presence of variability in both classes (Auchettl et al., 2018). Additionally, both AGN and TDEs show exceptions to standard classification criteria, making it difficult to establish clear-cut distinctions. However, systematic multiwavelength follow-up, including well-sampled X-ray light curves, optical spectral evolution, and infrared diagnostics, can help identify strong TDE candidates. Ensuring that multiple distinguishing properties favour a TDE scenario, rather than relying on a single indicator, will undoubtedly help to create a clean TDE sample.

1.3.7 Era of population studies

eROSITA has been important for studying not only individually discovered X-ray TDEs but also in exploring systematically X-ray TDE populations. The first population study of TDEs in the Russian half of the eROSITA sky was presented by Sazonov et al. (2021). Their sample included 13 TDEs detected during the first and second all-sky surveys, selected based on their X-ray and optical properties. The criteria included X-ray amplitude cut

(> 10), removal of stellar and AGN contaminants using multiwavelength properties of hosts, as well as optical spectroscopic confirmation. The sample was used to construct a TDE X-ray luminosity function (XLF), best fit by a single power law with a slope of -0.6 ± 0.2. The function was used to estimate the total rate of 1.1×10^{-5} TDEs per galaxy per year, which is an order of magnitude less than theoretically predicted (Stone & Metzger, 2016). While Sazonov et al. (2021) investigated TDEs in the Russian half of the eROSITA sky, this thesis focuses on the study of TDEs and other non-AGN extragalactic transients in the German half.

Outside the X-ray band, a number of recent large-scale optical (e.g., ZTF and Gaia) and infrared (e.g., WISE) surveys have significantly expanded TDE samples. For example, van Velzen et al. (2020) analyzed a sample of 33 optical-UV selected TDEs and found that most of them were X-ray faint, suggesting that optical TDEs might be powered by reprocessing of high-energy radiation in surrounding debris coming or from outer shocks. Similarly, Yao et al. (2023) explored a flux-limited, spectroscopically complete TDE sample of 33 sources observed with ZTF, estimating an optical TDE rate of 3.2×10^{-5} per galaxy per year. In contrast, infrared-selected TDEs discovered using NEOWISE (e.g., Masterson et al. 2024) appear to trace a different population. These events exhibit slow-rising infrared flares, likely due to dust echoes rather than prompt emission from an accretion disk. Their rate of 2×10^{-5} per galaxy per year, is in between optical and X-ray-selected samples but differs in host galaxy demographics. The host galaxies of mid-IR-selected TDEs do not exhibit a green valley overdensity or a preference for quiescent galaxies, in contrast to those of optical and X-ray–selected samples, suggesting that infrared selection may preferentially detect TDEs in dustier environments. The majority of mid-IR TDEs are X-ray faint.

1.3.8 Open questions and motivation to study TDEs

TDEs provide a unique observational window into the physics of BHs and their environments. By revealing otherwise dormant, quiescent BHs, TDEs help trace the BH mass function at its lower end ($< 10^8\ M_\odot$), including potential IMBHs (10^3–$10^5, M_\odot$; e.g., Lin et al. 2018). What makes TDEs particularly extraordinary is that they allow us to observe the entire process of a transient event associated with a SMBH, from the initial disruption of the star to the eventual decline of the emission as the debris is fully accreted or ejected. TDEs evolve on humanly observable timescales, from weeks to years, offering a unique real-time view of the processes in the vicinity of the SMBH (Gezari, 2021), capturing the formation of a transient accretion disk as the stellar debris circularizes and the emergence of a hot corona that shapes the high-energy emission. Their transient nature and multi-wavelength emission, particularly in X-rays, make TDEs a valuable tool for probing black hole demographics, dynamics, and physical properties, especially in the innermost regions.

Open questions that can be addressed through the study of TDEs selected in X-rays include:

1. How can extragalactic non-AGN transients be systematically identified, and how can

we find populations of both canonical and non-canonical TDE candidates?

2. What are typical X-ray light curve and spectral properties of canonical TDEs, do they agree with theoretical predictions? With a growing sample, we can investigate how the diversity in X-ray light curve properties and spectral evolution of TDEs is shaped by factors such as accretion physics, obscuration, host galaxy environments, and the orbital dynamics of the disrupted star.

3. What are the luminosity function and occurrence rates of TDEs? How do these observational results compare with estimates derived from TDE samples selected in other wavebands? Do they align with theoretical expectations based on stellar loss-cone dynamics? As sample sizes grow, it will also be crucial to investigate how the TDE population evolves with redshift, and whether TDE rates and luminosities change over cosmic time.

4. Can TDEs observed in different bands (e.g., optical, IR, and X-ray) be explained within a single unified physical model? The diversity of observed properties raises questions about whether these variations stem from differences in physical processes (e.g., accretion efficiency, reprocessing, or jet production) or viewing geometry (e.g., inclination relative to the obscuring material). Also, can the unified model explain the differences in TDE rates and bring us closer to the theoretical predictions?

5. Do X-ray selected TDEs show a preference for specific host galaxy types, as observed in optically selected samples? What drives the apparent over-representation of TDEs in certain environments, and are TDEs also expected to occur in other types of host galaxies?

6. How do TDE properties differ for BHs of different masses, ranging from IMBHs to SMBHs?

eROSITA is uniquely suited to address many of these open questions. Its capability to conduct deep all-sky surveys enables the detection of a large, statistically significant sample of X-ray bright TDEs, including events in quiescent galaxies and potential IMBH hosts.

1.3.9 Outline of this thesis

This PhD thesis presents a comprehensive study of X-ray-selected non-AGN extragalactic transients discovered with eROSITA, particularly focusing on TDEs. The following overview summarizes each chapter and its contribution to addressing the key questions presented in Sect. 1.3.8.

In Chapter 2, we use the unprecedented opportunity to explore the variable X-ray sky with eROSITA to present a systematic selection of extragalactic X-ray transients detected in the first two eROSITA all-sky surveys and not associated with known AGN. The resulting catalog, eRO-ExTra, comprises 304 sources and serves as a relatively clean parent sample

of non-AGN variability phenomena linked to SMBHs. This study provides reliable optical counterparts for over 90 % of the sources and includes an analysis of their X-ray properties. Notably, more than 95 % of the sample were detected in X-rays for the first time with eROSITA, making the catalog a valuable resource for studying extragalactic transients, including rare events such as TDEs. This chapter establishes a methodological foundation for addressing the Question 1.

Chapter 3 presents an in-depth analysis of the eROSITA TDE population selected from the catalog presented in Chapter 2. We identify and characterise 31 TDE candidates, including 30 canonical TDEs and one off-nuclear candidate, which may be associated with an IMBH. This chapter provides a comprehensive analysis of their multiwavelength characteristics, including X-ray (Question 2), optical, mid-infrared, and radio, in the context of obscuration and stream-stream collision models (Question 4). Host galaxy properties are also analyzed, in order to address Questions 5 and 6. Furthermore, we derive the X-ray TDE luminosity function and estimate TDE rates (Question 3). Beyond providing significant input into the X-ray TDE population studies, this chapter highlights the capabilities of the eRO-ExTra catalog in systematically identifying and studying transient events.

Chapter 4 focuses on an exceptional TDE candidate, J0936, discovered in a Fanaroff-Riley Type II (FRII) radio galaxy. While this event exhibits the canonical X-ray properties of TDEs and is among the brightest soft nuclear transients detected by eROSITA, its host galaxy is highly unusual (Question 5). A detailed analysis of its X-ray behavior reveals that such properties are atypical for FRII galaxies, further supporting the TDE hypothesis. However, if J0936 is indeed a TDE, it would have occurred around a SMBH with a mass exceeding the Hills mass limit, making it one of the most massive SMBHs associated with a TDE to date (Question 6). Given these constraints, the BH would need to be rapidly rotating, or alternatively, the event could represent an off-nuclear TDE around a smaller BH. The possibilities are explored in detail in this chapter.

Finally, in Chapter 5, I discuss prospects for future eROSITA transient and TDE studies and summarize the main conclusions of this thesis.

Chapter 2

eRO-ExTra: eROSITA Extragalactic Non-AGN X-ray Transients and Variables in eRASS1 and eRASS2

[This work was published in Astronomy & Astrophyics in Jan. 2025:
https://doi.org/10.1051/0004-6361/202451253.
The version presented in this thesis includes minor textual revisions relative to the published article.]

The variable X-ray sky may help us uncover some of the most rare astrophysical phenomena. While previous studies showed the dominance of regular active galactic nuclei (AGN) variability (see Chapter 1.2.2), a small fraction of sources expected in an all-sky X-ray survey arise from more exotic transients such as tidal disruption events, quasi-periodic eruptions, or other short-lived events associated with supermassive black hole accretion. eROSITA provides an unprecedented opportunity to explore the X-ray sky due to the sensitivity, sky coverage, and cadence of the all-sky survey. First of all, however, it is crucial to develop robust methodologies for identifying and classifying extragalactic non-ANG X-ray transients. This chapter describes the systematic selection of extragalactic X-ray transients found in the first two eROSITA all-sky surveys that are not associated with sources known to be AGN prior to the eROSITA observations. By combining long-term X-ray light curves and spectral properties, as well as multiwavelength counterpart information, this chapter aims to create a relatively clean parent catalog of non-AGN variability phenomena associated with extragalactic sources. Furthermore, this chapter provides the groundwork for a comprehensive and systematic approach that can be applied in the subsequent chapters and in future surveys and studies.

2.1 Introduction

The X-ray sky harbors a wide variety of variable and transient sources. As discussed in Chapter 1.2.1, in our Galaxy and nearby galaxies, the detected populations predominantly consist of stellar phenomena and compact objects, such as flaring coronal stars, cataclysmic

variables, and X-ray binaries. The extragalactic X-ray variable and transient sky (see Chapter 1.2.2) is dominated by events associated with accretion onto supermassive black holes (SMBHs). Perturbations in the persistent accretion flow in active galactic nuclei (AGN) (Hawkins, 2002; Noda & Done, 2018), corona instabilities (Di Matteo, 1998; Wilkins & Gallo, 2015; Ricci et al., 2020), and obscuration (Risaliti et al., 2002; Matt et al., 2003; Markowitz et al., 2024) can lead to variability with a wide range of timescales and amplitudes. In short-term accretion events such as tidal disruption events (TDEs, see Chapter 1.3), on the other hand, the X-ray transient is thought to be the result of a star being disrupted in the gravitational potential of a SMBH (Hills, 1975; Rees, 1988; Komossa & Bade, 1999; Saxton et al., 2020). In some cases a star is only partially disrupted, called a partial TDE (pTDE), resulting in repeating flares on scales from months (Liu et al., 2023) to decades (Malyali et al., 2023a). Most recently, quasi-periodic eruptions (QPEs, see Sect. 1.2.2) have been added to the list (Miniutti et al., 2019; Giustini et al., 2020; Arcodia et al., 2021, 2024). The origin of these quasi-periodic X-ray flares with timescales from hours to days is still debated, but an observational link to TDEs has been found in some events (Chakraborty et al., 2021; Miniutti et al., 2023; Quintin et al., 2023; Evans et al., 2023; Arcodia et al., 2024).

Systematic studies of the variable X-ray sky have been performed previously. For example, Fuhrmeister & Schmitt (2003) classified 1207 variable sources in the *ROSAT* all-sky survey. Long-term variability studies of large samples of AGN have been performed in the *Chandra* Deep Field-South and the COSMOS field using *XMM-Newton*, revealing the ubiquitous variability of AGN (Lanzuisi et al., 2014; Paolillo et al., 2017). The first systematic look at the variable X-ray sky with eROSITA was performed in the 140-square-degree final Equatorial-Depth Survey (eFEDS) field by Boller et al. (2022). Having explored variability on a timescale of days, 65 significantly varying sources were identified, most of which are consistent with originating from Galactic stellar flares or variable AGN. A continuation of this study for the whole eROSITA_DE sky was performed in Boller et al. (2025) for the first eROSITA all-sky survey, who identified more than a thousand variable sources. Similarly to the eFEDS field, the majority of objects were associated with flaring stars, and 10 % of sources were associated with AGN.

In this chapter, we present a systematically selected sample of extragalactic X-ray transients and variables discovered in eROSITA-DE during the first two all-sky surveys (eRASS1: 12 December 2019–11 June 2020 and eRASS2: 11 June 2020–14 December 2020). We specifically focus on sources that are not associated with known AGN prior to the detection of X-ray variability with eROSITA, do not show AGN-typical multiwavelength properties, and are not associated with X-ray binaries in nearby, well-resolved galaxies. However, there might still be a fraction of AGN in the sample, in particular, low-luminosity AGN, about which previous knowledge was not available. Based on the selection criteria, sampled volume, luminosities, and timescales probed by the eROSITA data, the majority of the selected events are expected to originate from accretion events onto otherwise inactive SMBHs in the centers of galaxies.

The chapter is structured as follows: in Sect. 2.2 we present the selection of the eRO-ExTra catalog, including the primary selection of the eROSITA X-ray variability catalog,

the optical counterpart identification and exclusion of galactic and AGN contaminants. In Sect. 2.3 we present the eROSITA light curve and X-ray archival data analysis, X-ray spectral modeling and redshift compilation. We report on radio properties of the catalog in Sect. 2.4 and several included sources detected as transients at other wavelengths in Sect. 2.5. We conclude with a discussion in Sect. 2.7 and a summary in Sect. 2.8. We adopt a flat ΛCDM cosmology throughout this chapter, with $H_0 = 67.7\,\mathrm{km\ s^{-1}\ Mpc^{-1}}$ and $\Omega_m = 0.309$ (Planck Collaboration et al., 2016). Most uncertainties quoted in the chapter are based on 68 % confidence intervals.

2.2 The selection of extragalactic transients and variables

2.2.1 The eRASS1 – eRASS2 X-ray variability sample

To build the sample of extragalactic transients, we first compiled the sample of variable sources selected based on the amplitude and the significance of the variability between eRASS1 and eRASS2. This allows the selection of all sources that brightened or faded significantly between eRASS1 and eRASS2. The flowchart of the included selection steps is presented in Fig. 2.1 and is described in more detail in the following.

First, we crossmatched the eRASS1 catalog (Merloni et al., 2024) with the eRASS2 single band catalog, which is available within the eROSITA collaboration but not publicly released (0.2–2.3 keV, version 221031). The eRASS2 catalog contains sources with DET_LIKE > 6 and was processed with an updated version of the eROSITA standard data processing pipeline (version 020), whereas eRASS1/DR1 was based on version 010 (Merloni et al., 2024). The updated data processing version includes updates on the pattern and energy tasks, an improved boresight correction, a change in flaregti (flare filtering) parameters, improved low-energy detector noise suppression, and a better computation of the subpixel position. We performed the crossmatch with a 15" radius and defined three subsamples of sources: detected in both eRASS (C12), only in eRASS1 (C1), and only in eRASS2 (C2). The crossmatching radius was chosen based on eROSITA's typical positional uncertainty (see Merloni et al., 2024, Fig. 5). After the crossmatch, we applied a detection likelihood cut DET_LIKE > 15 on the brighter detection of a source in either eRASS1 or eRASS2 to minimize spurious events. The chosen threshold corresponds to ≈ 0.03% of false positives (see Seppi et al., 2022, Fig. 3). Extended sources were removed using the extension likelihood cut EXT_LIKE = 0. A comprehensive description of the source detection parameters is provided in Brunner et al. (2022). Provided that a brighter detection has a detection likelihood of at least DET_LIKE = 15, and that of a fainter detection can be as low as DET_LIKE = 6, the chosen radius accounts for the combination of the eRASS1 and eRASS2 positional errors for more than 90 % of point sources. Since we searched for the closest match, we checked if there are cases in C12 where the crossmatch would have multiple counterparts within 15" and found 98/348,000 sources. After applying the selection cuts (DET_LIKE > 15, EXT_LIKE = 0, SEP cut, see Fig. 2.1), there

remained only four potential spurious matches, for which we visually confirmed that the closest match is correct.

eROSITA's scanning strategy (Merloni et al., 2024) results in a nonuniform exposure across the sky (see Fig. 2.2, left) with the highest exposure being reached near the ecliptic poles and the lowest near the ecliptic equator. For this study, we removed sources within 3 deg from the South Ecliptic Pole (SEP). At the SEP, the significantly larger exposure (up to 30 ks in each eRASS compared to $\sim$ 100 s near the equator) and depth, leads to high source density and potentially source confusion, requiring a very different data analysis from the rest of the sky. Results of the variability analysis of the SEP sources are presented in Bogensberger et al. (2024). To reduce the number of spurious detections, we also excluded regions in selected overdensities in the eRASS source catalogs. This includes, for example, regions near supernova remnants, very bright point sources, stellar clusters, and large local galaxies. The summary of the flagging procedure is provided in Merloni et al. (2024) in their Table 5. Regions around nearby galaxy clusters were not excluded, since eROSITA's angular resolution is sufficient to distinguish X-ray point sources from diffuse cluster emission. Additionally, cluster member galaxies can still host extragalactic transients and variable sources.

For sources in the C1 and C2 samples, we calculated the 3σ upper limits for the flux in the survey in which the source is not detected (eRASS1 or eRASS2) at the X-ray detection positions in the 0.2–2.3 keV band, assuming the same spectral model as used to calculate the flux in the eRASS catalogs (absorbed power law with $\Gamma = 2$, $N_H = 3 \times 10^{20}\,cm^{-2}$). The details of the upper limit computation can be found in Appendix A.1.

To characterize the variability, we determined the fractional amplitude, A, and significance of the variability S for each source as:

$$A = F_{max}/F_{min} \tag{2.1}$$

$$S = \frac{F_{max} - F_{min}}{\sqrt{F\_ERR^2_{max} + F\_ERR^2_{min}}}, \tag{2.2}$$

where F_{max} and F_{min} are the maximum and minimum fluxes, corresponding to the integrated fluxes either in eRASS1 or eRASS2, and F_ERR_{max} and F_ERR_{min} are their 1σ symmetric errors. For detections we used the catalog fluxes and their uncertainties. For sources for which the catalogs did not include error estimates (see the discussion in Merloni et al. 2024 for details), we assigned the median of the count error of all sources with counts and exposure time within 10 % of those of the source. This approach provided at least 20 similar sources for each error estimation, with the exception of one high-count source, for which we assumed a $\sqrt{N}$ error. To calculate the flux uncertainties in both cases, count rates were converted to fluxes using the standard catalog energy conversion factor ($ECF = 1.074 \times 10^{12}$ for $\Gamma = 2$ and $N_H = 3 \times 10^{21} cm^{-2}$). For the nondetections in C1 and C2, F_{min} is the 3σ upper flux limit and $F\_ERR_{min} = 0$. The final sample includes 2331 variable sources (C12: 1927; C1+C2: 404), which vary with $A > 4$ and $S > 4$, where 6 % (i.e., 147) have both amplitude and significance higher than 10.

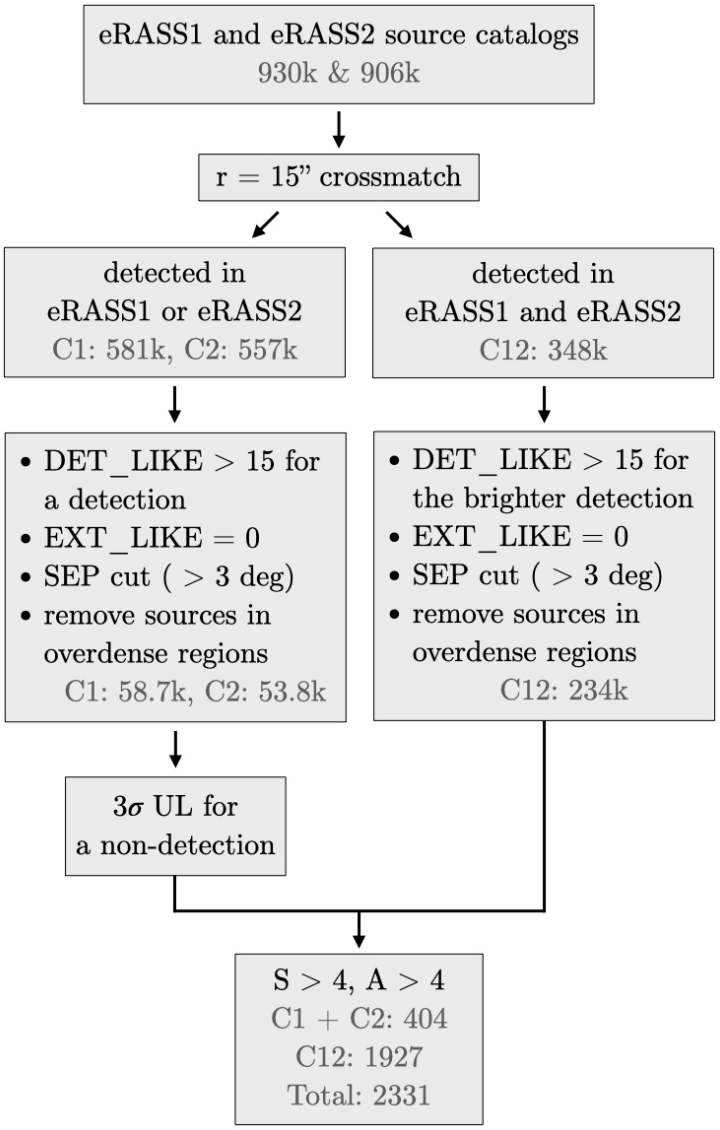

Figure 2.1: eRASS1 – eRASS2 variability sample selection steps. First, the eRASS1 and eRASS2 source catalogs are crossmatched to identify sources detected in both (C12) or only in one eRASS (C1, C2). Then, cuts are applied to exclude spurious and extended sources. Next, 3σ upper limits for nondetections are calculated for C1 and C2 subsamples. Finally, the variability significance, S, and fractional amplitude, A, are computed. In total, 2331 sources (C1+C2: 404; C12: 1927) with $S > 4$ and $A > 4$ remain.

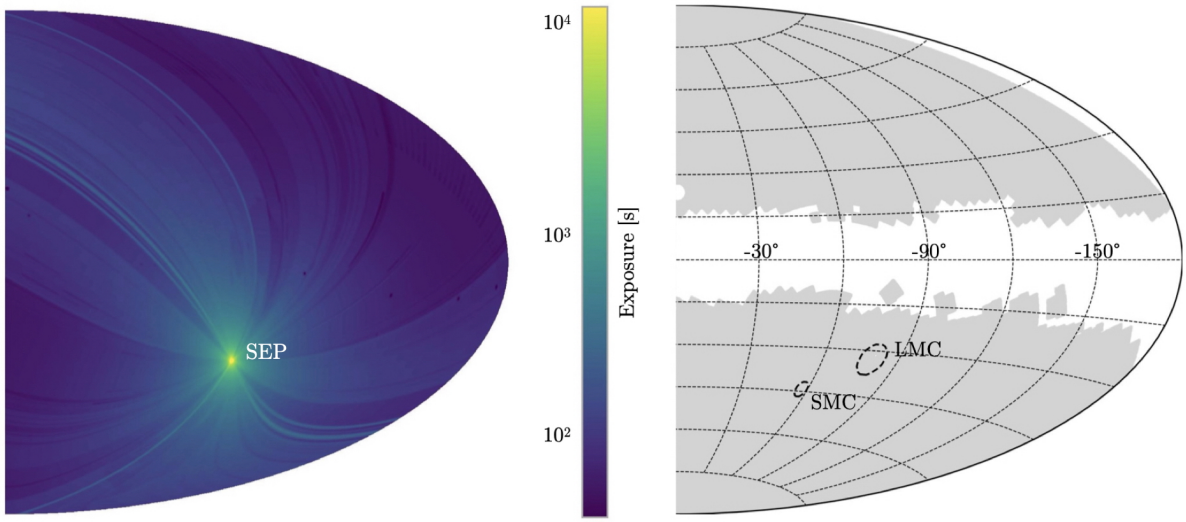

Figure 2.2: Representation of eROSITA_DE sky in Aitoff projection in Galactic coordinates. The left panel shows the (vignetted) effective eRASS1 exposure map with values ranging from ≈ 100 s (blue) at the ecliptic equator to more than 10,000 s (yellow) close to the south ecliptic pole (SEP). The right panel shows the LS10 footprint in the same projection and coordinates, covering 76 % of eROSITA_DE. The locations of Large Magellanic Cloud (LMC) and Small Magellanic Cloud (SMC) are shown for illustrative purposes.

2.2.2 Counterpart identification

An important step to determine the extragalactic nature of an X-ray transient is to identify its multiwavelength counterpart. In this section, we describe the criteria by which optical counterparts were associated with the X-ray detections. The flowchart of the selection steps is shown in Fig. 2.3.

For the identification of the optical and near-infrared counterparts, we concentrated on the Legacy Survey DR10 area (LS10[1]; Dey et al. 2019), since it provides extensive coverage of the eROSITA_DE sky (76 %) except in the Galactic Plane and several other small sky regions (see Fig. 2.2, right). From the 2331 sources in the variability sample, 1613 (≈ 70 %) are within the LS10 footprint. Sources not covered by the LS10 footprint are primarily concentrated in the Galactic Plane ($|b| < 15°$, ≈ 25% of the eROSITA_DE sky) and were excluded from further study. As variability for sources in the Galactic Plane is heavily dominated by stellar phenomena, the exclusion of this region is expected to have minor impact on identifying the extragalactic transient and variable population presented in this chapter.

LS10 provides deep and homogeneous photometry in the *g, r, i, z* and WISE W[1,2,3,4] bands. For sources located in areas within the LS10 footprint but where catalog data are not yet available in this data release, we used Gaia DR3 (Gaia Collaboration et al.,

[1] `https://www.legacysurvey.org/dr10/`

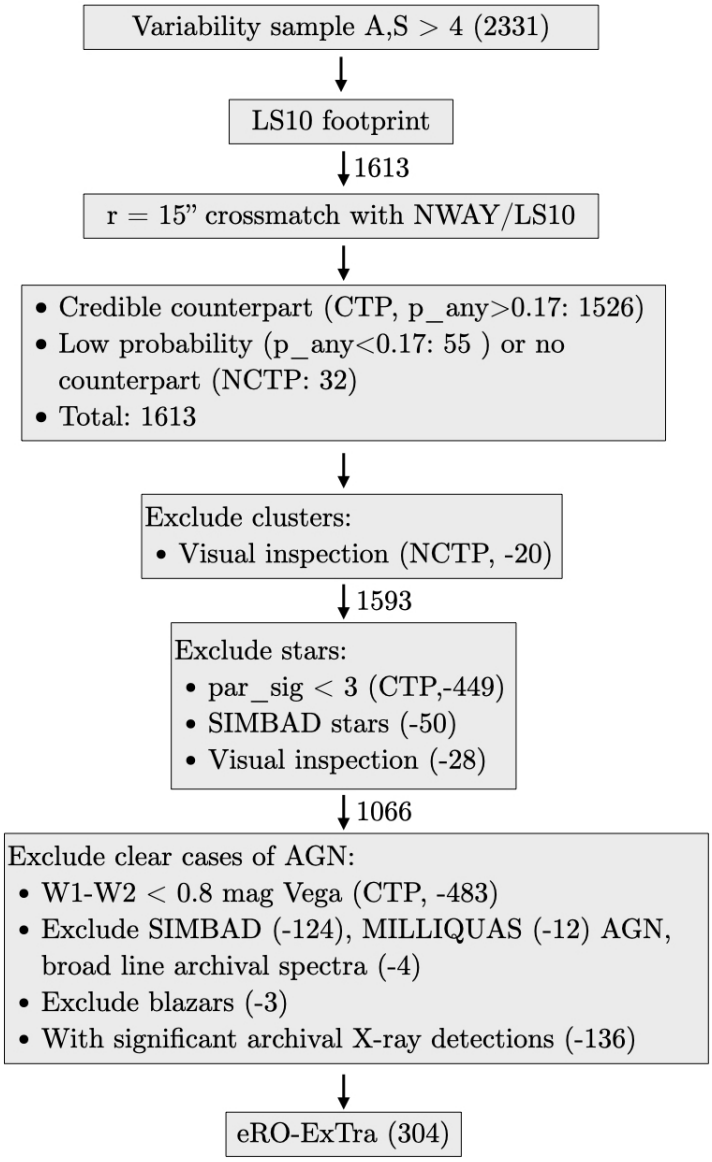

Figure 2.3: Selection of extragalactic transients from variability sample. Firstly, we assign NWAY LS10 optical counterparts: 1526/1613 have a credible counterpart within 15"; 87/1613 are not associated with an NWAY/LS10 optical source or do not have a credible NWAY/LS10 counterpart. Then we apply numerous cuts to exclude contaminating clusters, stars and known pre-eROSITA AGN. The final catalog of Extragalactic X-ray transients (eRO-ExTra) includes 304 sources. All eRO-ExTra sources are associated with an optical LS10 counterpart, 93 % of those are credible (`p_any` > 0.17).

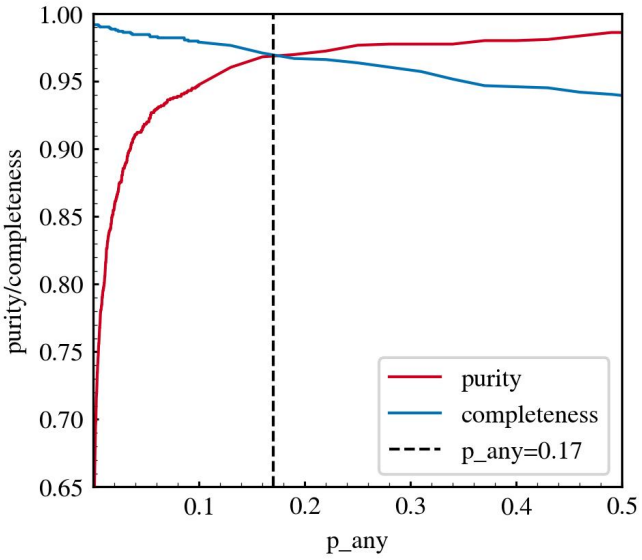

Figure 2.4: Functions of purity and completeness vs. `p_any`. The functions were calculated for our sample after the NWAY match, given detection likelihood values of DET_LIKE > 15. The value of `p_any`=0.17 at the intersection of purity and completeness functions at 0.97 is chosen as the optimal minimum probability value for the selection of reliable NWAY counterparts for eRO-ExTra.

2016, 2023) and CatWise2020 (Marocco et al., 2021) independently to replace missing photometry results. However, we note that Gaia (G < 20 mag) is shallower than LS10 and is biased against extended sources, such as nearby galaxies. While Catwise2020 is deeper than the LS10 W[1,2,3,4] bands (six times as many exposures), it suffers from blending. The counterparts were identified using NWAY (Salvato et al., 2018) by applying the procedure as described for the eROSITA eFEDS field (see Salvato et al., 2022, Sect. 3.1). Specifically, the geometrical distribution of sources (i.e., the distance from the X-ray position and positional uncertainty, the number density, and the similarity of their SEDs compared to those in a training sample) are taken into account. For details on the priors for LS10, Gaia DR3, and CatWise2020 and the agreement between the three surveys see Salvato et al. (in prep.), where the counterpart identification process for eRASS1 is described. The training sample was not specifically selected for the counterpart identification of X-ray transients and variables, but rather for typical X-ray emitters, due to the lack of previously discovered sources with suitable properties. The most complete to-date version of the NWAY/LS10 counterpart catalog for eROSITA is eRASS:5, a not-yet-published stacked source catalog for all eRASS. We associated NWAY/LS10 counterparts with the sources in the variability sample by crossmatching the X-ray position of the brighter detection in eRASS1 or eRASS2 with the eRASS:5 X-ray position with a radius of r = 15", which is used as an X-ray eROSITA position in the NWAY/LS10 counterpart catalog.

Of the 1613 sources within the LS10 footprint, 1581 ($\approx 98\,\%$) have at least one possible

counterpart in the NWAY catalog within 15". The probability that for a given X-ray source one or more counterparts with properties typical for an X-ray emitter were found, is defined by the p_any parameter (Salvato et al., 2018). The optimal minimal value of p_any = 0.17 was determined as the intersection of purity and completeness functions calculated for various p_any for our sample after the NWAY match (Fig. 2.4). Henceforth, the counterparts with p_any > 0.17 are considered reliable. As shown in Fig. 2.4, the threshold of p_any> 0.17 corresponds to chance coincidences of < 5 %. There are 1526 (97 % of the 98 % of sources with a counterpart) sources with a counterpart with p_any>0.17; the remaining 55 sources (3 %) have a potential counterpart with a lower probability (0<p_any<0.17). The p_any values are provided in our final catalog, and users are advised to consider the association probability for their analysis.

NWAY identified multiple counterparts in LS10 for 14/1581 sources. Multiple potential counterparts were kept during all further selection steps. For simplicity, we cited the numbers of X-ray sources in the description of the selection flow and in Fig. 2.3, without the numbers of potential optical counterparts. After all cuts were applied, 11/14 X-ray sources were excluded as either stars or AGN (see Sect. 2.2.3 and Sect. 2.2.4). For another source, one LS10 counterpart was excluded as an AGN and another one remained in the catalog, based on a higher relative probability (NWAY_p_i, see Table A.2) of the eROSITA/LS10 match. For two remaining sources, multiple matches were associated with LS10 duplicates, which pointed to the same galaxy. In these cases, the closest match was selected for the catalog.

For 32 sources, no NWAY counterpart was found within 15" from the X-ray position. Three of those had reliable NWAY/LS10 counterparts with p_any>0.17 using a larger crossmatching radius (16" < r < 20"); 20 sources were associated with extended emission initially missed in the EXT_LIKE cut of the detection epoch but clearly identified in the eRASS:5 data. Removing the latter sources from the sample resulted in 1593 unique X-ray sources.

2.2.3 Exclusion of Galactic objects

To further reduce the contamination of the sample by Galactic objects, we made use of (1) the parallax significance estimates from Gaia DR3 (if p_any > 0.17) and (2) available classifications provided in the SIMBAD database (Wenger et al., 2000). The summary is shown in the sixth box in Fig. 2.3. First, the parallax significance cut of par_sig < 3 was applied, where par_sig = parallax $\times \sqrt{\text{parallax\_ivar}}$ with parallax_ivar being the inverse-variance of the parallax. This cut removed 449 sources.

Next, we excluded known stars by crossmatching the remaining sources with SIMBAD, which contains names, positions, and known properties of more than 16 million objects and provides their classifications. For sources with reliable NWAY/LS10 counterparts (p_any> 0.17), we searched for SIMBAD sources within 15" of the LS10 counterpart position; otherwise (p_any< 0.17), we searched within 15" of the X-ray position. In both cases, 50 sources were excluded due to the presence of a star in SIMBAD within this radius. Finally, we visually inspected the LS10 images and excluded 28 obvious stellar contami-

nants such as saturated bright stars and sources in densely populated stellar fields. One of these sources was identified as a Galactic nova in a fireball phase (König et al., 2022b, MGAB-V207). In total, 527 ($\approx 30\%$) sources were removed from the eRASS1 – eRASS2 variability sample as likely to be stars (see Fig. 2.3 for step-by-step numbers). At this step 1066 variable X-ray sources were left in the sample.

2.2.4 Exclusion of AGN

A large contribution to the extragalactic X-ray variable sky comes from AGN. In this section, we describe the identification of sources with properties matching those of regular AGN and how they were excluded. The applied selection criteria are shown in the second to last step of the flowchart in Fig. 2.3.

Firstly, we removed sources with major AGN contribution by applying a mid-IR color cut ($\mathrm{W1} - \mathrm{W2} < 0.8\,\mathrm{mag_{Vega}}$) from Stern et al. (2012) for sources with reliable counterparts. This discarded 483 sources ($\approx 30\,\%$ of all sources in LS10 footprint).

Secondly, we excluded sources classified as active galaxies in SIMBAD (124 sources), using the crossmatch described in Sect. 2.2.2. In addition, The Million Quasars Catalog (Milliquas; Flesch 2023) helped us to identify more contaminating AGN and QSOs in the sample. Milliquas contains 907,144 type-I QSOs and AGN, largely complete from the literature to 30 June 2023. We crossmatched our catalog and Milliquas using the same approach as for the SIMBAD catalog and excluded an additional 12 AGN. To ensure the non-AGN nature of sources based on archival pre-flare data, we also visually inspected available archival optical spectra and excluded four sources which show characteristics of broad-line AGN. Finally, we crossmatched our sample with the eROSITA blazar catalog[2] (Haemmerich et al., 2025) and excluded three sources. At this step, a total of 626 AGN were excluded, reducing the sample to 440 sources.

2.2.5 Historical variability from X-ray archives

Archival X-ray observations helped us further to exclude possible AGN which were not removed in previous steps. In particular, sources with significant archival X-ray detections are likely to have flaring caused by long-term AGN variability. To characterize the history of the eROSITA transients and variables, we explored the archives of previous and operating X-ray missions. We used the web-based High-Energy light curve Generator (HILIGT[3]; Saxton et al., 2022; König et al., 2022a) to retrieve flux and upper limit values estimated via aperture photometry with the Bayesian approach of Kraft et al. (1991) for archival observations from Neil Gehrels *Swift* X-ray Telescope (XRT; Burrows et al. 2005), *ROSAT* (Voges et al., 1999), and for the *XMM* Slew Survey (Saxton et al., 2008). For the flux

[2]The eRASS1 blazar catalog includes known sources from the 4FGL (Ballet et al., 2023), ROMA BZCAT (Massaro et al., 2015), 3HSP (Chang et al., 2019), HighZ (Sbarrato et al., in prep), Milliquas (Flesch, 2023), KDEBLLACS and WIBRaLS2 (D'Abrusco et al., 2019), ABC (Paggi et al., 2020), and BROS (Itoh et al., 2020) catalogs, found within 8" from the eROSITA position.

[3]`https://xmmuls.esac.esa.int/upperlimitserver`

estimation in the energy band 0.2–2.0 keV we chose a uniform spectral model of an absorbed power law with $\Gamma = 2$ (same as in the eROSITA source catalogs) and $N_H = 10^{21} cm^{-2}$, and a confidence interval (CL) of 99.87 %, corresponding to a one-sided 3σ level.

All presented eROSITA transients and variables were covered by at least one of the above missions. Only upper limit estimates could be derived for 296 out of 440 sources. For each source, we compared the archival upper limit, F_{ul}, with the peak flux measured by eROSITA, F_{peak}, taking the flux uncertainty, $(F_{err})_{peak}$, into account. If $F_{ul} \leq (F - F_{err})_{peak}$, the source was assigned arch_flag = 1 ("constraining") in our catalog. Otherwise, it was assigned arch_flag = 0 ("not constraining"). In total 144 sources have archival detections. These detections can also constrain whether a source shows long-term variability or the eROSITA detection marks a brightening from a previously lower flux level. Archival detections performed at least one year before the eROSITA peak indicate X-ray long-term variability if one of the following criteria is true:

1) the significance of the source variability S (Eq. 2.2) between the archival detection and the fainter of the eRASS1 or eRASS2 flux constraints is ≥ 3;

2) the significance of the variability S between the archival detection and the eROSITA peak is ≤ 3;

3) the archival detection is brighter than the eROSITA peak.

A source that fulfills at least one of these conditions received arch_flag = −1 ("variable") in the catalog. Otherwise, the sources are flagged with arch_flag = 2 ("not variable"). The latter group includes sources with archival detections fainter or comparable with the eROSITA minimum since they might indicate the pre-flare quiescent state of the system.

Overall, 136 sources identified as variable (arch_flag = −1) were excluded from the extragalactic variability catalog. Whereas all of these excluded sources were in the *ROSAT* footprint, 86 % of sources were also covered by *XMM-Newton* and 23 % by *Swift* pointed or slew observations. Although some bright archival detections might indicate a repeating transient, for example, as shown in Malyali et al. (2023a), with a TDE candidate re-brightening on a time scale of decades, a more likely explanation is long-term AGN variability. One the other hand, some AGN which do not have significant archival detections might have been missed in the archival variability cut due to the limitations in sensitivity and coverage of previous missions. By combining this cut and the cuts discussed in Sect. 2.2.4, 762/1066 sources were classified as AGN and were excluded to form a sample of 304 extragalactic non-AGN sources.

Table 2.1: Summary of source classification based on X-ray-archival data.

Detected		Not Detected	
Variable	Not variable	Constraining	Not constraining
136	8	68	228

A summary of the historical light curve classification is presented in Table 2.1. The archival fluxes with their uncertainties, instruments, and observing dates are provided in the catalog. Overall, 296/304 sources are not detected in archival observations and have

only archival upper limits and, therefore, can be considered as genuinely new eROSITA transients.

2.2.6 The final catalog

The resulting catalog eRO-ExTra contains 304 transients and variables without a known pre-eROSITA AGN origin. All sources are associated with an extragalactic optical LS10 counterpart. Since this study is focused on non-AGN sources, all further analysis was performed for the eRO-ExTra catalog. The summary of the catalog and its properties are discussed further in Sect. 2.6.

2.3 X-ray light curve and spectral analysis

2.3.1 eROSITA light curves

The eROSITA X-ray light curves of the eRO-ExTra sample were analyzed to characterize the long-term flux evolution. Each survey observes a source's position multiple times ("visits") with a cadence of ≈ 4 hours (referred to as one "eroday"). The number of visits, hence the accumulated exposure, depends on the proximity to the survey poles. It ranges from at least six visits near the survey equator to several tens near the poles. The long-term behavior can be assessed using the data of all four complete all-sky surveys (eRASS1 – eRASS4) and eRASS5, if available. With each successive eRASS being ≈ 6 months after the previous one, this provides a coverage of 1.5–2 years.

To analyze the long-term eROSITA behavior, we first crossmatched the eRASS:5 X-ray position (see Sect. 2.2.2) with the detections in the eRASS3, eRASS4, and eRASS5 (v.221031, v.221031 and v.21101, respectively, unpublished, 1B: 0.2-2.3 keV, processing version 020) source catalogs using a matching radius of r=15". The eRASS:5 coordinates are used for the crossmatch since the accumulated catalog contains the most accurate X-ray positions. Upper limits were computed following the procedure described in Appendix A.1 if a source was not detected in an eRASS.

The light curves were then divided into four classes: "flare," "decline," "brightening," and "other," using an automated procedure considering general light curve trends and variability significance across eRASS measurements. The decision tree for the light curve classification is detailed in Fig. 2.5.

Sources peaking in eRASS1 are classified as either decline or other. The decline class includes sources which peak in eRASS1 and decay onward. The light curve (or its part) is considered decaying if one of the following condition is satisfied (i.e., decay condition): for each pair of light curve points (m,n) after the peak, where m < n: (1) flux(m) > flux(n); or (2) flux(n) and flux(m) are consistent within $2S$, where S is defined by Eq. 2.2. Also, we require $S_{\rm decay}$, defined as the significance of the total decay from the peak to the last light curve point eRASS4(5), to be larger than two. Otherwise, the source is classified as other.

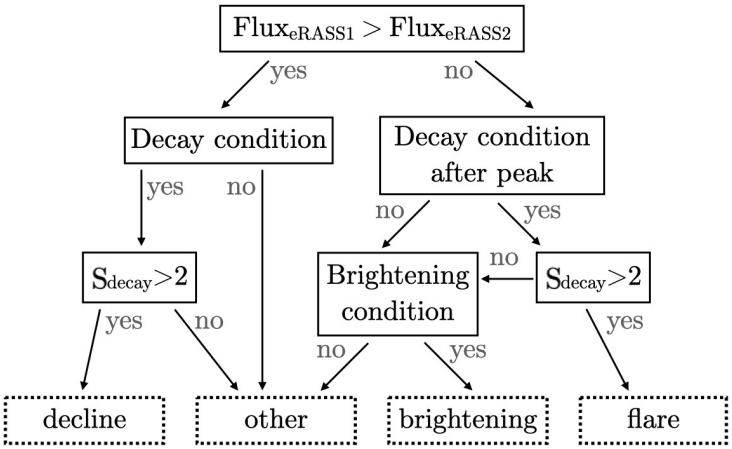

Figure 2.5: Decision tree of light curve classification into four classes: decline, flare, brightening, and other.

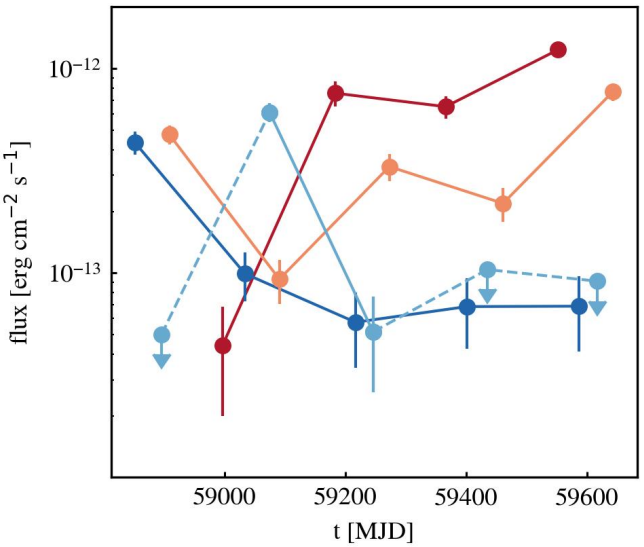

Figure 2.6: Light curve class examples: decline (dark blue), flare (light blue), brightening (red), and other (orange). Solid lines connect detections. Dashed lines connect to upper limits.

Sources peaking in eRASS2 or in later epochs belong to either brightening, flare or other light curve class. The brightening class shows a flux rise from eRASS1 to eRASS2 and then continues brightening, in agreement with the following condition (i.e., brightening condition): for each pair of light curve points (m,n), where m < n: (1) flux(m) < flux(n); or (2) flux(n) and flux(m) are consistent within $2S$. Otherwise, the source is classified as other. The light curve has a flare if it first brightens from eRASS1 to eRASS2 and later decays. In order to have a flare class, the source should satisfy the decay condition after

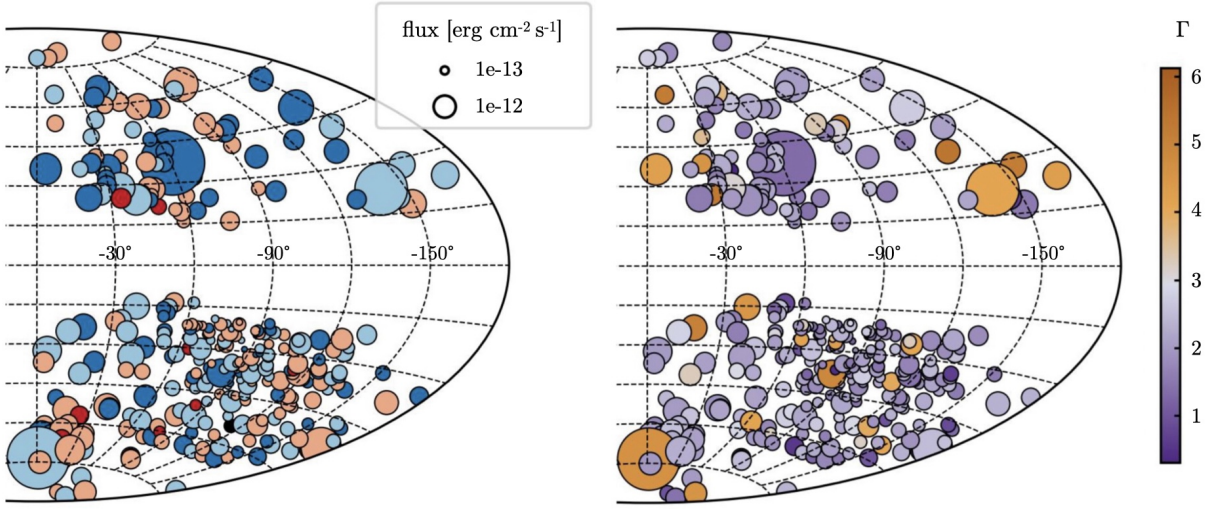

Figure 2.7: eRO-ExTra catalog in Aitoff projection in Galactic coordinates. Left: sources color-coded by light curve type: dark blue – decline, light blue – flare, red – brightening, orange – other (see Fig. 2.6). Right: sources color-coded by the peak photon index from the hardest (purple) to the softest (orange). In both plots, the symbol size is scaled by the peak flux. The higher concentration of faint sources in the southern hemisphere is caused by higher exposure times near the SEP.

the peak epoch as well as have $S_{\rm decay} > 2$. If the latter condition is not satisfied (in other words if light curve decay is not sufficient) the source is classified as either brightening or other, depending on the agreement with the brightening condition.

Table 2.2 provides the light curve classification summary. Examples for each class are shown in Fig. 2.6. The light curve classification is included as flag LC_type in the final catalog. The distribution of sources in the sky color coded by their light curve class and scaled by their peak eRASS1 or eRASS2 flux is shown in the left panel of Fig. 2.7. A noticeable concentration of sources, including faint transients, in the southern Galactic hemisphere is caused by higher eROSITA exposure times near the SEP.

We separately searched for available X-ray observations by other missions, performed slightly earlier or during eROSITA epochs. The information about these observations is included in the catalog as well. Detections within a year before the eROSITA peak may have already been associated with the start of the event later found by eROSITA: 1eRASS J004058.3-683816 and 1eRASS J132252.1+182253 were detected by the XMM-Newton Slew Survey a few days before the eROSITA peak, with the archival points being in agreement within $1.5 \times$ S (see Eq. 2.2) with the eROSITA peak flux and the light curve decay trend. The archival classification of these sources (arch_flag = 0) in Sect. 2.2.5 is based on their earlier archival observations. The X-ray mission archives contained 150 eRO-ExTra sources where detections or upper limits constrain the behavior during or after the eROSITA observations. Mostly, additional points during or after eROSITA observations are non-constraining upper limits. In addition, several detections and constraining upper limits are

consistent with the expectations from the eROSITA light curve and their classifications. Only two sources should belong to a different light curve class taking into account the additional data, namely, 1eRASS J045457.8-652846 changes from a flare to other, and 1eRASS J102851.3+251439 – from decline to flare. For consistency, the catalog includes light curve classification based on the eROSITA points only.

Table 2.2: Summary of the eROSITA-based light curve classification for 304 sources in eRO-ExTra.

Flare	Decline	Brightening	Other
101	79	8	116

2.3.2 eROSITA spectral modeling

For each source, we extracted spectra for the peak eRASS epoch using the `eSASS` task `SRCTOOL` (version eSASSusers_211214) with circular source and annular background regions centered on the X-ray positions. Utilizing `SRCTOOL`'s AUTO mode, the radii of the source and background regions were selected taking into account the source counts, the level of the background map model at the source position, the best fitting source extent model radius, as well as a model of the effective eROSITA PSF at the source position (averaged over the integration, and summed over all operating telescope modules).

X-ray spectra were analyzed using the Bayesian X-ray Analysis software (BXA; Buchner et al., 2014), which connects the nested sampling algorithm UltraNest (Buchner, 2021) with the fitting environment XSPEC (Arnaud, 1996). The spectra were fitted unbinned using C-statistic (Cash, 1976), and the eROSITA background was modeled using the principal component analysis (PCA) technique described in Simmonds et al. (2018) and Liu et al. (2022a). Each extracted eROSITA spectrum, which contains a contribution from both the source and background emission, was jointly fitted. The background spectrum was modeled with the fixed derived background model, and the source spectrum was modeled with a chosen source model convolved with the X-ray responses plus the background model convolved with a diagonal matrix response. Here, an absorbed power law model `tbabs` $*$ `powerlaw` was used with fixed Galactic equivalent neutral hydrogen column density ($N_{\rm H,gal}$) extracted from the HI4PI survey (HI4PI Collaboration: et al., 2016) individually for each source. In addition to the free parameters of the source model (photon index and normalization), the background model has a free normalization parameter, which should be equal to unity in the simultaneous source and background fitting. We assumed wide flat priors on the photon index and the logarithm of the normalization. The best-fit values of the photon index gamma Γ and the corresponding 0.2–2.3 keV fluxes were both derived as medians from the BXA posterior distributions with uncertainties calculated as 68% percentile interval around the median (1σ). An example is shown in Fig. 2.8. The values of $\rm N_{H,gal}$, Γ, fluxes with errors and goodness of fit can be found in the eRO-ExTra catalog.

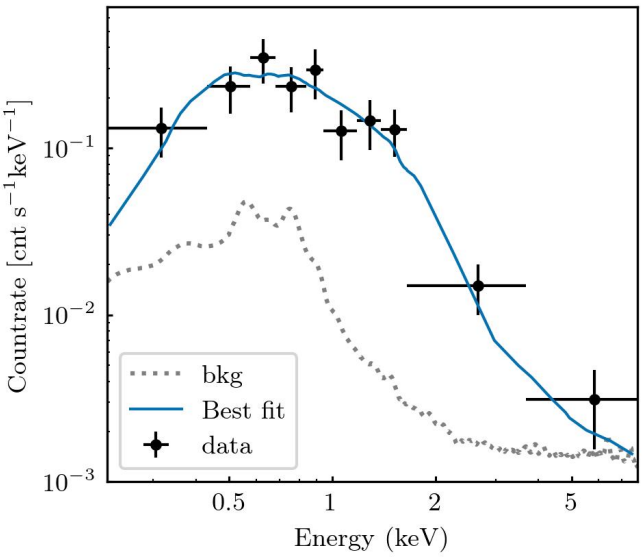

Figure 2.8: Example BXA fit to the eRASS2 data of 1eRASS J143045.4-332705. This is a typical source from the sample with A = 8.2 and S = 7, peak flux f = 5.05×10^{-13} erg cm^{-2} s^{-1} and the best fit value of photon index $\Gamma = 1.97 \pm 0.24$. Black markers are the observed data (binned for illustration purposes only). The blue line shows the best-fit convolved model for an absorbed power law. The background model is shown as a black dotted line.

The sample includes sources with photon indices in the range $0.3 < \Gamma < 6.1$ (see Fig. 2.9) and a mean of $\Gamma = 2.2$, dominated by 85 % of sources having $1 < \Gamma < 3$. The soft tail of the distribution includes 33 sources (11 %) with $\Gamma > 3$, based on the mean posterior values. It is important to note that the best-fit results of the hard tail of the distribution with $\Gamma < 1$ (4 % of sources) may be affected by the choice of the spectral model, particularly an underestimation of the intrinsic obscuration introduced by using a fixed $N_{H,gal}$. However, due to the low photon counts for most sources, a more complex spectral modeling cannot be performed consistently. Similarly, the extremely steep photon index, namely, $\Gamma > 6$, for one faint source (1eRASS J064449.4-603704), is due to the simple spectral model assumption. The distribution of sources in the sky color coded by Γ is shown in the right panel of Fig. 2.7, illustrating how sources with various photon indexes are homogeneously distributed.

2.3.3 Redshifts

Spectroscopic redshifts are available for 79 sources, 27 of which are archival and 52 were obtained in our dedicated follow-up campaign of eROSITA X-ray transients. The summary of the follow-up observations is provided in Appendix A.2. For sources without spectroscopic redshifts, the eRO-ExTra catalog includes photometric redshifts (photo-z), which

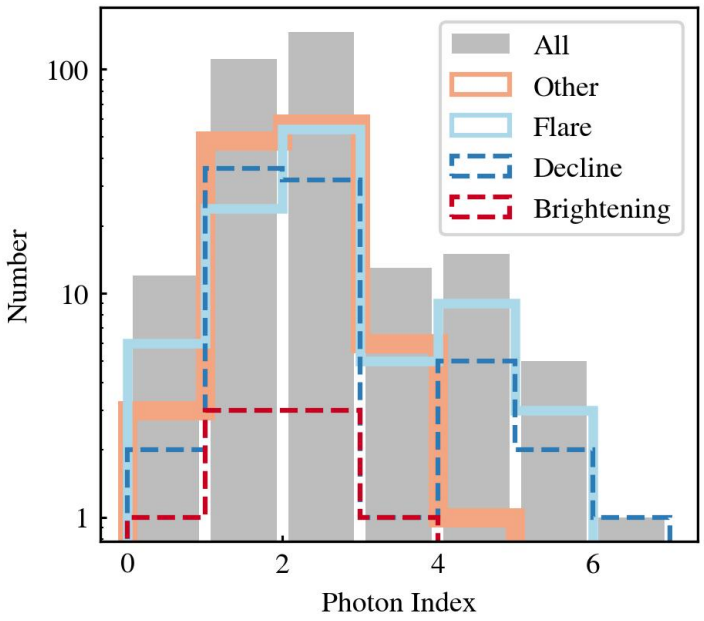

Figure 2.9: Distribution of best fit photon indices for peak X-ray spectrum of each source in eRO-ExTra. The different histograms show the distributions separated by light curve class.

have accuracy 6 % with a fraction of outliers estimated to be around 12 %, provided by the eROSITA collaboration (Salvato et al., 2025). In this chapter, to consider a photo-z reliable, we additionally required all LS10 photometry bands (*griz*) to be available. For even more accuracy, one could also filter photo-z using LS10 parameters ANYMASK and ALLMASK, which denote sources that touch bad pixels; however, we did not exclude such photo-z from consideration in this chapter. Also the values for sources `p_any`< 0.17 should be used only after confirming the counterpart. As a result, using only spectroscopic redshifts or reliable photo-z of sources with credible counterparts, the redshift completeness of the sample reaches 84 %.

Fig. 2.10 shows the total, spectroscopic, and photometric redshift distributions. The majority of sources are at $z < 0.3$ (64 %), and several sources (1 %) have $z > 1$. As shown in Fig. 2.10, sources with photometric redshifts typically lie at higher redshifts than those with spectroscopic measurements. This difference arises from the limitations of optical spectroscopic follow-up, as more distant sources appear fainter and are therefore more challenging to observe spectroscopically.

2.4 Radio properties

We investigated the radio properties of the eRO-ExTra sources using the Rapid Australian Square Kilometre Array Pathfinder (ASKAP; Hotan et al. 2021) Continuum Sur-

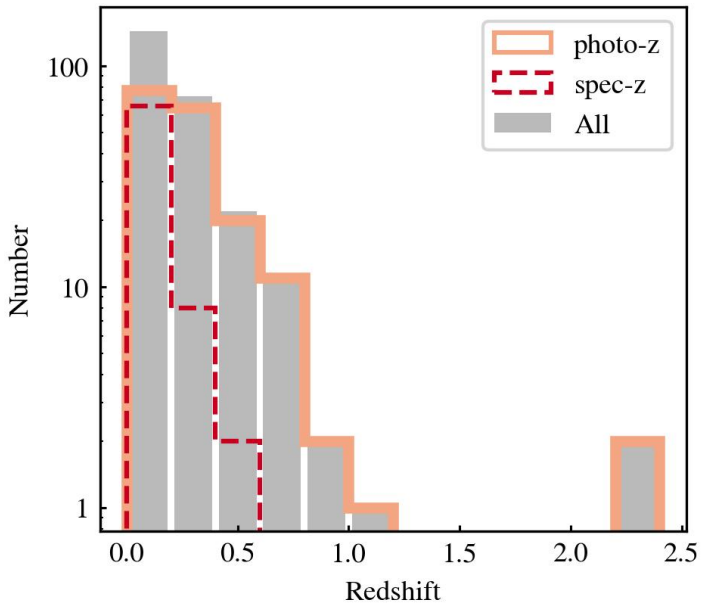

Figure 2.10: Distribution of reliable spectroscopic and photometric redshifts available for 255 eRO-ExTra sources.

vey (RACS; McConnell et al. 2020) and the Karl G. Jansky Very Large Array Sky Survey (VLASS; Lacy et al. 2020). RACS is the first large-area radio survey completed with the full 36-dish ASKAP radio telescope, which is part of the Australia Telescope National Facility (ATNF). It provides detections and upper limits at 0.88 GHz (RACS-low) and 1.39 GHz (RACS-mid). VLASS is a high angular resolution (2.5", high sensitivity (rms $\approx 120\,\mu$Jy/bm) survey of the sky visible to the VLA (Dec> -40 deg) at a central frequency of 3 GHz. Overall, three VLASS epochs are foreseen, each 32 months apart. VLASS 1 began in 2017, and thus, most eRO-ExTra sources visible to the VLA were observed before the eRASS scans in VLASS 1 and after/during the eROSITA surveys in VLASS 2. This makes the catalogs complementary for radio transient searches associated with the eRO-ExTra sources.

Crossmatching the eRO-ExTra catalog with RACS-low resulted in 30 matches. A radius of 5" (based on the typical RACS positional uncertainty, McConnell et al. 2020) was used for crossmatching radio sources and optical reliable LS10 counterparts from eRO-ExTra. For sources with non-reliable counteparts, the X-ray position from eRO-ExTra and a larger radius of 15" (see Sect. 2.2.1) were used for the crossmatch. Additionally, we crossmatched the catalog with VLASS 2.1. We found eight matches using a radius of 2.5" based on the positional uncertainty of VLASS for sources with reliable counterparts and 15" in other cases. All eRO-ExTra sources with a VLASS detection overlap with sources in the RACS catalog, providing spectral information between 0.8–3 GHz. We used RACS images to perform visual morphology checks of the radio sources. All sources are compact point sources consistent with both non-AGN and AGN hypotheses. In addition, we searched for

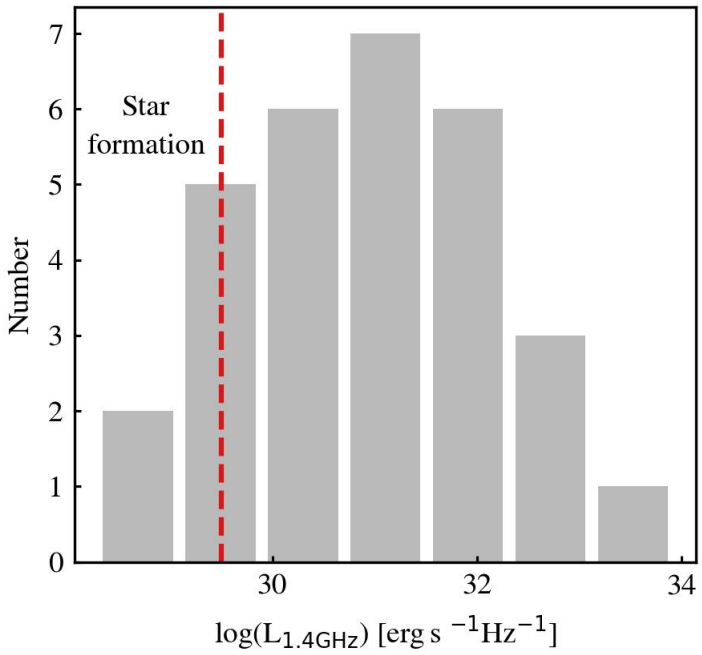

Figure 2.11: Radio luminosity distribution at 1.4 GHz for 30 RACS-detected sources. The dashed red line shows the radio luminosity corresponding to star formation rate SFR = 20 $M_{\odot}yr^{-1}$. Radio emission of $\approx 20\,\%$ of sources can be explained by star formation, while higher luminosities for remaining sources suggest other emission processes.

radio variability between VLASS 1 and VLASS 2. One source, 1eRASS J092753.8+162005, showed a significant brightening from VLASS 1 to VLASS 2. No significant variability was detected for the remaining objects.

Overall, the eRO-ExTra catalog contains 31 known radio sources, including one source not in RACS or VLASS for which a radio detection is reported in SIMBAD. To explore the origin of the radio emission, we compared the RACS radio luminosities with the typical luminosities associated with star formation (see Appendix A.4 for details; the results for the VLASS detections are consistent with those from RACS). As can be seen in Fig. 2.11, the large majority of the eRO-ExTra sources have radio luminosities significantly above the expectation from star formation rates $< 20\ M_{\odot}yr^{-1}$ (Kennicutt, 1983), suggesting another dominating emission mechanism. This can be, for example, underlying activity of the SMBH, or may be directly related to the transient event detected by eROSITA. As a result of the overlap of the radio and eROSITA observing periods, it is challenging to distinguish between these scenarios without further radio observations. Therefore, radio properties were not used as a selection criterion for the eRO-ExTra catalog.

2.5 Known transients

Consistent with the selection criteria, eRO-ExTra includes three previously reported eROSITA TDE candidates: 1eRASS J082336.8+042303 (AT2019avd, Malyali et al. 2021), eRASSt J074426.3+291606 (Malyali et al., 2023b), and eRASSt J234403.1-352640 (Homan et al., 2023; Goodwin et al., 2023). These transients show no archival X-ray detections, a flaring light curve and a soft X-ray spectrum at the peak, as expected from canonical TDEs (Gezari, 2021). In addition, 1eRASS J123822.2-253210 was reported in Wilms et al. (2020) as a bright, transient X-ray source with no identified origin.

To further explore the nature of unknown X-ray events, we crossmatched eRO-ExTra with Transient Name Server[4] (TNS). We found 17 (6 %) sources reported in TNS as new optical transients. Two of have been classified as AGN (1eRASS J141904.3-215330[5], 1eRASS J082336.8+042303[6]), while the remaining are unclassified. The TNS entry information is provided in the catalog.

2.6 The eRO-ExTra catalog

The eRO-ExTra catalog includes 304 transient and variable sources varying with $S > 4$ and $A > 4$ between eRASS1 and eRASS2. Following the meticulous selection procedure described in Sect. 2.2, the sample was cleaned from known AGN and Galactic objects and predominantly comprises events of, at this stage, unconstrained origin. A fraction of AGN unknown to-date might still be present in the catalog. The example columns of the eRO-ExTra catalog are shown in Table A.3, and the full catalog column description is provided in Table A.2. The eRO-ExTra sample includes 31 radio-detected sources (Sect. 2.4) and three previously reported eROSITA TDE candidates (Sect. 2.5).

Fig. 2.12 shows the distribution of all eRO-ExTra sources with a reliable counterpart (`p_any` > 0.17) in the g-r vs. z-W1 photometry plane. The overplotted lines are the division between Galactic and extragalactic objects (Salvato et al., 2022), and several representative tracks of different classes of extragalactic objects: QSO, obscured Seyfert, and inactive galaxies (S0, SB, Elliptical). The computation of the theoretical color-redshift tracks and used SED templates for each object type are discussed in Salvato et al. (2022). The plot testifies to the successful removal of Galactic sources from the sample, with only four falling below the dashed black separation line. Visual inspection of the LS10 images confirmed that these sources are galaxies, as indicated by their characteristic extended morphology in the optical. The majority of the eRO-ExTra population is located in the area where active and inactive galaxies can be found.

Most of the sources in the catalog have a reliable (`p_any` > 0.17) NWAY/LS10 optical counterpart. The remaining 7 % with less reliable associations may include hostless transients, or events originating from higher-redshift or faint galaxies.

[4] `https://www.wis-tns.org`

[5] `https://www.wis-tns.org/object/2020csk/`

[6] `https://www.wis-tns.org/object/2019avd`

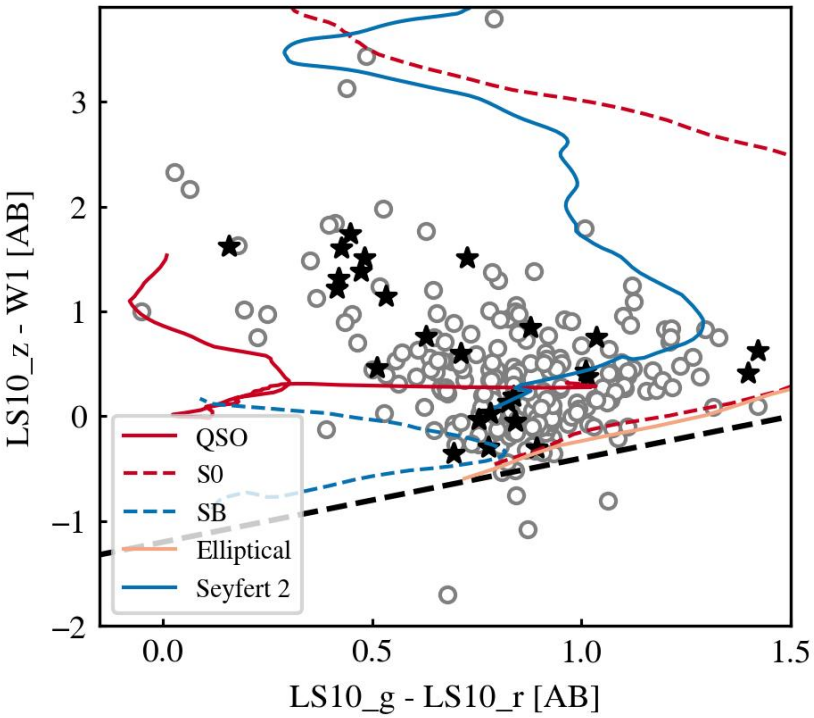

Figure 2.12: Distribution of 226 eRO-ExTra sources with reliable counterparts (p_any > 0.17) and accurately measured LS10 fluxes in the z–W1 vs. g–r plane. Black stars indicate the radio-detected sources. Tracks of active and inactive galaxies are included and described in the figure legend. The black dashed line ($z-\mathrm{W1}-0.8\times(g-r)+1.2=0$) marks the division between Galactic (below) and extragalactic (above) sources. The theoretical tracks and the marked division between Galactic and extragalactic sources are both from Salvato et al. (2022).

2.7 Discussion

A detailed classification of all sources included in the eRO-ExTra catalog is beyond the scope of this chapter, and the reader is encouraged to use the catalog to explore the nature of the sources. The eRO-ExTra catalog probes the non-AGN extragalactic population at X-ray energies to an extent not reached by previous studies, due to the eROSITA sensitivity, all sky coverage and consistent cadence over 2.5 years. The catalog is suitable for studying long-term transients and variables thanks to the presented multistep selection: only ≈0.001 % of all eRASS1 and eRASS2 significant detections (306/389k sources with DET_LIKE > 15) remain. With the sky density of unknown X-ray variables reaching 0.03 source $\deg^{-2}$ year^{-1}, the catalog can be used to find rare astronomical events as well as to perform systematic population studies. A systematic study of the eROSITA canonical TDE population using eRO-ExTra is presented in Chapter 3.

While the eRO-ExTra sample selection took great care to minimize the contamination by AGN, a fraction of the remaining sources is likely to be associated with regular accretion events onto SMBHs. Future multiwavelength follow-up is needed to confirm the classification of the sources. As can be seen in the photon index distribution (Fig. 2.9), 41 % of eRO-ExTra sources have a spectral slope of $\Gamma < 2$. Although AGN typically have similar values of Γ and some $\Gamma < 2$ sources in the sample might have this origin, hard X-ray spectra are also not uncommon in other source populations. For example, the accretion onto the SMBH during a TDE can lead to the formation of a corona (Guolo et al., 2024) while the TDE is still X-ray bright. Due to the time sampling of eROSITA observations (one visit per 6 months), such events may be detected only in the phase when the source is X-ray hard. Another example is eROSITA TDE candidate eRASSt J045650.3-203750 (Liu et al., 2023). This source had a hard spectrum during the X-ray plateau phase, reaching $\Gamma = 2.5$, compared to the typically softer TDE spectra with $\Gamma > 3$ (Saxton et al., 2020). Other subclasses of TDE candidates often show harder spectra as well. In a recent mid-infrared-selected TDE sample (Masterson et al., 2024), representing a new population of dusty TDEs, WTP15abymdq showed $\Gamma = 0.7 - 2.0$ across all presented epochs. Another class of hard sources are jetted TDEs, for example, Swift J164449.3+573451 (Burrows et al., 2011; Saxton et al., 2012a) and Swift J2058.4+0516 (Cenko et al., 2012) which both had hard ($\Gamma < 2$) spectra even at peak.

Similarly to the spectral slope not being a decisive criterion to select against AGN, the X-ray light curve class (see Sect. 2.3.1) cannot be used directly to exclude AGN. A decline or flare light curve is expected for a variety of non-AGN transient source populations. Sources with brightening or other light curves may look like variable AGN. However, given the limited temporal coverage provided by the eROSITA data alone, also transients such as TDEs or partial TDEs with X-ray flares, rebrightenings, or even QPEs can appear different than monotonically decaying (Malyali et al., 2021; Liu et al., 2023; Malyali et al., 2023b). Therefore, non-AGN transients can belong to any presented light curve class.

Next, we compared the eRO-ExTra catalog with previously performed studies of the X-ray variable sky. Fuhrmeister & Schmitt (2003) performed a systematic study of the X-ray variability in the *ROSAT* all-sky survey. Among the 1207 sources in their sample,

they identified more than 60 % with stars, 10 % with an extragalactic origin, while 25 % remained without a counterpart association. In the eRASS1-eRASS2 variability sample within the LS10 footprint (Fig. 2.3), the fraction of stars was only 33 %, likely as a result of the removal of the Galactic Plane. Only 4 % of the sources have no reliable counterpart, thanks to NWAY and the available multiwavelength data. Moreover, within the LS10 footprint, 66 % of the sources are extragalactic, which can be attributed to eROSITA's significantly higher sensitivity. In addition, the eRO-ExTra catalog was thoroughly cleaned from AGN contamination, which lets us identify rare non-AGN extragalactic transients.

Another long-term (3.5 years) extragalactic variability study was performed by Lanzuisi et al. (2014) with *XMM-Newton*. This study focused on the AGN population in the COSMOS field and, therefore, cannot be directly compared with the eRO-ExTra catalog. It showed that the majority of AGN are X-ray-variable, which is in line with the large fraction of AGN (70 %) that was removed from the eRASS1 – eRASS2 variability sample for the selection of the eRO-ExTra catalog.

A first variability study of the X-ray sky with eROSITA was performed within the eROSITA final Equatorial-Depth Survey (eFEDS) field in November 2019 (Boller et al., 2022). The majority of 65 sources (82 %) found in this study were of Galactic origin, while only 18 % were extragalactic sources. The extragalactic sample included seven previously known AGN and 5 galaxies detected in X-rays with eROSITA for the first time. For the whole eROSITA_DE sky, an analysis of the short-term variability was performed in Boller et al. (2025) and identified 1307 variable sources out of a subset of 128,669 sources from eRASS1, exhibiting a net count exceeding ten. The majority of sources are located in the galactic plane or are consistent with stellar objects, including flare stars, young stars and active binaries, and only about 10 % of variable sources are extragalactic. The timescales probed by the eFEDS survey and eRASS1 variability studies are significantly shorter than the ones presented in the eRO-ExTra catalog. The eFEDS observations were performed over the course of a few days and were thus primarily sensitive for identifying short-term variability, such as stellar flares. The eRASS1 variability study was performed analysing the 4 hr cadence light curves. eRO-ExTra, in contrast, probes the long-term variability over a 1–2 year period.

Fig. 2.13 presents the flux distribution of the eRO-ExTra sample compared with those of the X-ray variability studies discussed above. Using WebPIMMS[7], the fluxes from Fuhrmeister & Schmitt (2003) (0.1–2.4 keV) and Lanzuisi et al. (2014) (0.5–2 keV) were converted into the eROSITA energy band (0.2–2.3 keV) assuming the same spectral model as described in Sect. 2.2.1. Since the eRO-ExTra catalog probes the extragalactic population, we selected 403 sources from the Fuhrmeister & Schmitt (2003) catalog not associated with Galactic objects, according to the provided classification. Due to multiple selection steps (Sect. 2.2), eRO-ExTra provides a much cleaner selection of extragalactic transients, compared to Fuhrmeister & Schmitt (2003) as can be seen by the excess of high flux sources, which are likely associated with a remaining population of Galactic sources. Additionally, thanks to eROSITA's sensitivity, the eRO-ExTra sample extends to fainter objects. To

[7] `https://heasarc.gsfc.nasa.gov/cgi-bin/Tools/w3pimms/w3pimms.pl`

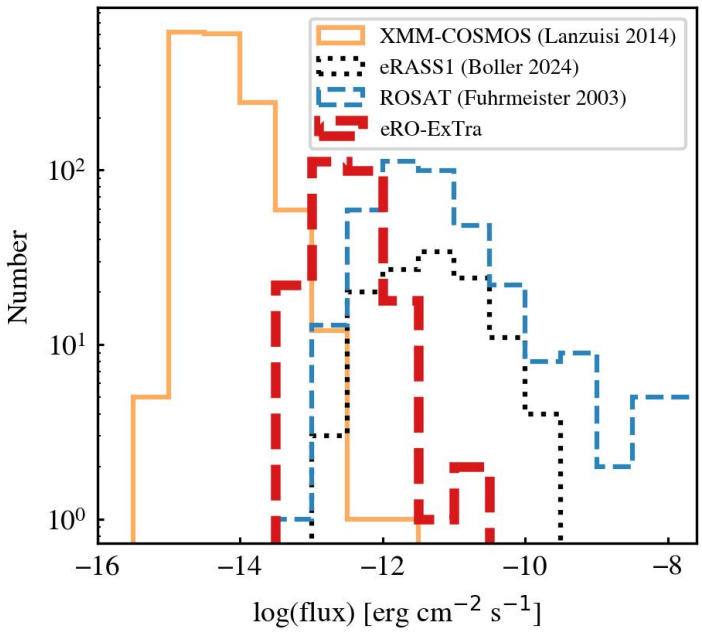

Figure 2.13: Comparison of 0.2–2.3 keV flux distributions of eRO-ExTra with those of variable or transient extragalactic sources in previous studies. The dashed red line shows this study, the orange line shows XMM-COSMOS (Lanzuisi et al., 2014), the dotted black line shows eRASS1 (Boller et al., 2025), and the dashed blue line shows ROSAT (Fuhrmeister & Schmitt, 2003).

compare with the extragalactic population of the eRASS1 variability catalog (Boller et al., 2025), we selected only sources within the LS10 footprint in their sample and further applied a cut to their parameter C_gal_ex > 0. The C_gal_ex parameter is calculated based on parallax, proper motion, optical and infrared photometry, and X-ray information, such that positive values correspond to extragalactic sources (see Salvato et al. 2025 for more details). This results in 123 objects. Only six of those are also included in the eRO-ExTra sample, emphasizing the very different and complementary selection criteria. The *XMM*-COSMOS sample probes significantly lower fluxes than eRO-ExTra as a result of the deeper (pencil-beam) exposure compared to the all-sky survey of eROSITA. Overall, eRO-ExTra fills the flux gap of X-ray-detected transients and variables lying between the *XMM*-COSMOS and *ROSAT* studies.

Fig. 2.14 shows the luminosity vs. spectroscopic or photometric redshift of the sources in the eRO-ExTra catalog compared to the *XMM*-COSMOS and *ROSAT* variability samples. For eRO-ExTra we used a subsample of 261 sources with reliable counterparts and redshifts. The X-ray luminosity range probed by eRO-ExTra covers 10^{42} to 10^{45}erg s^{-1}, compatible with the typical luminosities of TDEs (Gezari, 2021) but also low and moderate- luminosity AGN. A particularly luminous TDE in the sample (eRASSt J234403.1-352640, Homan et al. 2023; Goodwin et al. 2023) is highlighted with a star. The *XMM*-COSMOS sample

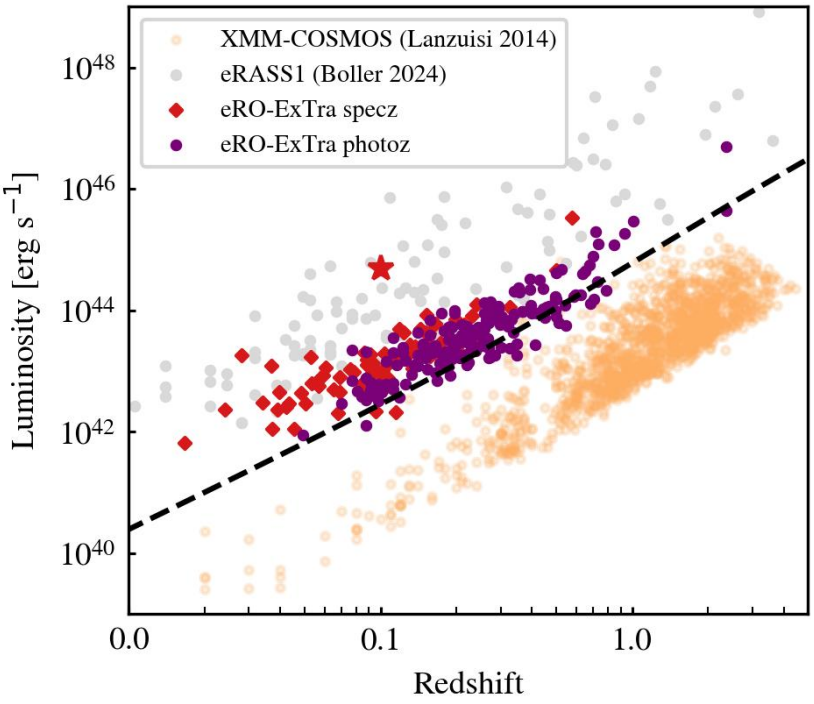

Figure 2.14: Luminosity 0.2–2.3 keV vs. redshift for all eRO-ExTra sources with reliable spectroscopic (red) or photometric (violet) redshifts. The black dashed line shows the approximate limit where a source would satisfy the eRO-ExTra selection criteria (detection likelihood, amplitude and significance cuts) at $b_{ecl} = 30°$. A star highlights a known luminous TDE candidate eRASSt J234403.1-352640. The eRASS1 (gray, Boller et al. 2025) and *XMM-COSMOS* (orange, Lanzuisi et al. 2014) variability samples are shown for comparison.

covers a comparable luminosity range to eRO-ExTra, but at higher redshift. In contrast, the extragalactic eRASS1 variability sample is on average more luminous. This can be attributed to their higher flux detection limit necessary to probe shorter timescales within one eroDay (4 hr). In addition, the eRASS1 sample includes known AGN and quasars at higher luminosities.

Using a subsample of sources with credible optical counterparts (`p_any`=0.17) and reliable redshifts (see Sect. 2.3.3), we estimated the integrated volumetric rate of eRO-ExTra transients and variables equal to $1.8^{+0.5}_{-0.4} \times 10^{-7}\mathrm{Mpc}^{-3}\mathrm{year}^{-1}$. The rate corresponds to the number of eRO-ExTra sources found according to the presented selection criteria. A direct comparison of this rate with previously published rates of specific transient populations (e.g., TDEs) cannot be done due to the heterogeneous nature of the eRO-ExTra sample. The occurrence rates of canonical TDEs from eRO-ExTra are presented in Chapter 3. The computation details of the eRO-ExTra X-ray luminosity function and the rate are detailed in Appendix A.5.

2.8 Summary

eROSITA has allowed us to explore systematically the variability of the X-ray sky over 2.5 years and discover numerous transients. In this chapter, we have presented a catalog of 304 extragalactic transients and variables (eRO-ExTra) in the western Galactic hemisphere and contained within the LS10 footprint, without clear infrared AGN signatures ($\mathrm{W1} - \mathrm{W2} < 0.8\,\mathrm{mag_{vega}}$) or known pre-eROSITA AGN classification. The catalog includes sources with a variability significance and a fractional amplitude larger than 4 in the first two eROSITA all-sky surveys (Nov 2019–Nov 2020). All eRO-ExTra X-ray sources are identified with optical LS10/NWAY counterparts, with 93 % having a reliable counterpart. The catalog includes eROSITA X-ray positions, discovery dates, fluxes or upper limits for eRASS1 – 4(5), as well as counterpart optical LS10 coordinates and photometry.

We presented the analysis of the X-ray properties of the sample, which is useful for further classification of the sources. Firstly, we reported on the archival X-ray data from *Swift*, *XMM-Newton* and *ROSAT* for the sample to explore the long-term variability of the sources. More than 95 % of the transients have no archival detection and were discovered in X-rays with eROSITA for the first time. The archival X-ray detections and upper limits are provided in the catalog. Secondly, we analyzed the long-term X-ray eROSITA light curves and provided a classification into four categories: decline, flare, brightening and other. Finally, for the light curve peak eROSITA epoch (eRASS1 or eRASS2, depending on the light curve class), we presented the results of the X-ray spectral modeling with a power law model. The catalog includes the best-fit values of Γ. Furthermore, the catalog includes archival and follow-up spectroscopic or photometric redshifts, providing a redshift completeness of >80 % for the sample.

A selection of databases, including SIMBAD, TNS, RACS and VLASS, was used to classify already known sources. There are 31 sources showing archival radio detections, which can be either a sign of AGN, star formation or a newly launched jet. Several

sources are already published transients, namely, the TDE candidates AT2019avd, eRASSt J074426.3+2916066 and eRASSt J234403.1-352640.

The catalog provides the first glimpse into the eROSITA X-ray transient sky and lets us systematically study the variability of various astronomical phenomena on months/year timescales. Looking forward, the eRO-ExTra catalog can be used to disentangle the nature of still unclassified sources via in-depth analysis and multiwavelength follow-up and to perform population studies of X-ray transients. It can furthermore guide the transient selection and identification approach to new and future X-ray surveys, such as Einstein Probe (Yuan et al., 2022).

2.9 Data availability

The eRO-ExTra catalog is presented in Table A.3 and is available in electronic form at the CDS via anonymous ftp to `cdsarc.u-strasbg.fr` (`130.79.128.5`) or via `https://cdsarc.cds.unistra.fr/viz-bin/cat/J/A+A/693/A62`. The reduced optical spectra listed in Appendix A.2 can be downloaded here: `https://github.com/grotova/eRO-ExTra`.

Chapter 3

The Population of Tidal Disruption Events Discovered with eROSITA

[This work was published in Astronomy & Astrophyics in May 2025:
https://doi.org/10.1051/0004-6361/202553669.
The version presented in this thesis includes minor textual revisions relative to the published article.]

The eROSITA all-sky survey has opened a data-rich era to conduct population studies of tidal disruption events (TDEs) and other X-ray transients. The careful selection of extragalactic transients and variables, described in Chapter 2, provides a strong foundation for the exploration of various subgroups of sources. This chapter presents a systematic study of X-ray-selected canonical TDEs (see Chapter 3.2) from the eRO-ExTra catalog (see Table A.3). With eROSITA, we not only significantly increase the number of X-ray discovered TDE candidates to date but also enable a deep statistical analysis of the canonical TDE population. Using the selected eROSITA TDE sample, this chapter examines rates, host galaxy characteristics, and multiwavelength properties of X-ray selected TDEs. In addition, it highlights how the eRO-ExTra catalog can serve as a valuable resource for studying other classes of nuclear transients in the future.

3.1 Introduction

The first TDE candidates were discovered in X-rays by the *ROSAT* all-sky survey (e.g., Bade et al. 1996; Grupe et al. 1999; Komossa & Greiner 1999; Greiner et al. 2000, see Sect. 1.3.2). They showed large amplitude soft X-ray flares (with characteristic black body temperature of $\approx$ few $\times 10^5$K) in the centers of otherwise inactive galaxies and a theoretically predicted decline in flux ($\propto t^{-5/3}$; Komossa 2015) on timescales of months to years (see Chapter 1.3 for more details). Further X-ray-selected TDE candidates came from the *XMM-Newton* Slew survey, *Chandra*, and the Neil Gehrels *Swift* Observatory. A comprehensive review of 21 X-ray-discovered TDE candidates reported in the literature by mid-2019 is provided in Saxton et al. (2020). eROSITA has revealed numerous canonical TDEs and uncovered more exotic TDE scenarios (see Sect. 1.3.5). For exam-

ple, in eROSITA_DE repeating and partial TDEs (pTDEs) exhibiting repeating flares on timescales of weeks (e.g., eRASSt J045650.3-203750; Liu et al. 2023, Liu et al. 2024) to decades (e.g., RX J133157.6-324319.7; Malyali et al. 2023a) were discovered. The eROSITA all-sky coverage and higher sensitivity have also enabled the first systematic X-ray TDE population studies. For example, a study of a sample of 13 TDE candidates found between Jun 2020 and Dec 2020 in eROSITA_RU was presented in Sazonov et al. (2021).

Thanks to the advent of large wide-field optical surveys (e.g., Zwicky Transient Facility, Bellm et al. 2019, ASAS-SN, Shappee et al. 2014; Kochanek et al. 2017, see Sect. 1.3.7) the discovery rate of TDEs in the optical band has significantly increased in the last years (e.g., see a review of 56 TDE candidates in Gezari 2021), enabling the first population studies (van Velzen et al., 2021; Yao et al., 2023; Guolo et al., 2024). Population studies have also been performed in the mid-infrared (mid-IR; Masterson et al. 2024) and radio bands (Dykaar et al., 2024; Goodwin et al., 2025a). The growing samples of events demonstrate that the underlying population of TDEs is very heterogeneous, a conclusion supported by observed differences in the TDE luminosity functions and rates. For example, not all X-ray-selected TDEs show optical or IR emission and vice versa; many show notable deviations from the expected monotonically-decaying light curve evolution, including combinations of missing or altered multiwavelength signatures (van Velzen et al., 2020; Masterson et al., 2024). The apparent dichotomy in the multiwavelength emission of TDEs (see Sect. 1.3.4), reflected in differing characteristic radii and temperatures, can be attributed to distinct physical processes and emission regions. The X-ray emission, consistent with thermal emission, is expected to trace the formation of the accretion disk around the supermassive black hole (SMBH). Conversely, the optical emission is thought to arise from collisions of the debris stream at large radii during the circularization process (Piran et al., 2015; Jiang et al., 2016; Bonnerot et al., 2017). Alternatively, optical and IR emission may come from reprocessing of the X-ray emission by an optically thick envelope (Roth et al., 2016; Dai et al., 2018; Thomsen et al., 2022). In the latter scenario, the observed differences between the optical and X-ray emission properties are explained by the observer's viewing angle (Dai et al., 2018; Parkinson et al., 2022) and patchy obscuration (van Velzen et al., 2020). It is an open question which scenario is preferential for describing the observed properties of TDEs, and whether several processes co-exist during different stages of TDE evolution. Moreover, recent samples of X-ray (Sazonov et al., 2021) and optically (Yao et al., 2023) selected TDEs uncovered lower TDE rates ($\approx 10^{-5}\mathrm{year}^{-1}\mathrm{galaxy}^{-1}$) comparing to the theoretical rates predicted by loss-cone dynamics (Brockamp et al., 2011; Mageshwaran & Mangalam, 2015; Stone & Metzger, 2016), which are of order $10^{-4}\mathrm{year}^{-1}\mathrm{galaxy}^{-1}$. Population studies involving systematic all-sky studies will shed more light on the missing TDE problem, whether it arises from observational effects, such as selection biases of TDEs in different energy bands, or the physical interpretation of multiwavelength TDE emission.

Another puzzle about TDE host galaxies is that optical and X-ray TDEs are mostly identified in the "green valley" of the galaxy color-mass space (e.g., Law-Smith et al. 2017; Hammerstein et al. 2021; Sazonov et al. 2021; Yao et al. 2023), which is associated with galaxies between starforming ("blue") and passive ("red") states (Martin et al., 2007). Whereas the larger TDE rate in green valley galaxies may be explained by an efficient loss

cone filling after a recent star formation period or a galaxy merger (French et al., 2020a; Hammerstein et al., 2021), it is still unclear if the overpopulation is biased against redder hosts wherein the TDEs can be obscured by dust (Roth et al., 2021).

In this chapter, we present a sample of the 31 most prominent TDE candidates selected from the first two eROSITA all-sky surveys in the western Galactic hemisphere. The presented sample is the largest systematically X-ray-selected TDE sample to date due to the unprecedented sensitivity, six-month cadence and all-sky coverage of eROSITA. The sample includes 30 canonical TDEs and one off-nuclear TDE candidate. We provide a statistical study of the population, using in-depth X-ray analysis as well as multiwavelength data in the mid-IR, optical and radio bands. The study focuses on improving existing X-ray TDE rate estimates, inspecting the TDE host population and black hole (BH) mass distribution, and exploring a multiband view of TDEs on a timescale of years.

The chapter is structured as follows: in Sect. 3.2 we outline the selection of the TDE sample; in Sect. 3.3 we overview the final sample, its X-ray properties, and optical counterparts; in Sect. 3.4 we explore the multiwavelength variability of the selected TDEs, and in Sect. 3.5 we analyze the host galaxy properties of the sample. We provide a discussion in Sect. 3.6, including the computation of the TDE X-ray luminosity function and rates in Sect. A.5; and conclude with a summary in Sect. 3.7.

We adopt a flat ΛCDM cosmology throughout this chapter, with $H_0 = 67.7\,\mathrm{km\ s^{-1}\ Mpc^{-1}}$ and $\Omega_m = 0.309$ (Planck Collaboration et al., 2016). The uncertainties quoted in this chapter are based on 68% confidence intervals, and upper limits (ULs) are reported at 3σ, unless stated otherwise.

3.2 Selection of TDE candidates

X-ray emission is a direct probe of BH accretion and, therefore, a robust way of identifying accretion-driven flares. This chapter focuses on canonical X-ray TDEs, i.e., events characterized by an X-ray light curve showing a single flare lasting months to years with a soft ($\Gamma > 3$) spectrum. The parent sample is the catalog of extragalactic non-AGN X-ray transients and variables eRO-ExTra[1], presented in Chapter 2 and Grotova et al. (2025a). The following subsections detail the TDE selection process based on X-ray light curve and spectral properties.

3.2.1 Parent catalog: eRO-ExTra

As described in Chapter 2, eRO-ExTra is a systematically selected catalog of 304 X-ray transients and variables discovered in the first two eROSITA_DE all-sky surveys (Merloni et al., 2024, eRASS1 and eRASS2; Nov 2019–Nov 2020) and contained within the Legacy survey DR10 (LS10[2]; Dey et al. 2019) footprint. Starting from more than two thousand sources that vary between eRASS1 and eRASS2 with significance and fractional amplitude

[1] https://cdsarc.cds.unistra.fr/viz-bin/cat/J/A+A/693/A62
[2] https://www.legacysurvey.org/dr10/

larger than four, eRO-ExTra was thoroughly cleaned from contaminants, such as stars and traditional Active Galactic Nuclei (AGN). The eRO-ExTra catalog made use of available archival photometric and spectroscopic data to exclude AGN contaminants. In particular, a mid-IR cut $W1 - W2 < 0.8\,\mathrm{mag_{Vega}}$ (Stern et al., 2012) was applied to exclude typical AGN, based on their mid-IR color indicative of hot dust emission. Moreover, available pre-flare archival spectra were inspected, and sources with typical AGN emission lines were removed. Other applied criteria included a parallax cut, visual inspection as well as utilizing previous classification from the literature, including SIMBAD, Milliquas, and eROSITA blazar catalogs (see Sect. 2.2). Archival X-ray data were used to help to distinguish new transients from long-term X-ray variables such as AGN. Specifically, the eRO-ExTra catalog has been cleaned from sources showing significant archival X-ray detections at the level of eROSITA peaks, using *XMM-Newton* Slew Survey (Saxton et al., 2008), *Swift* (Burrows et al., 2005) and *ROSAT* (Voges et al., 1999) archival data.

All eRO-ExTra sources are associated with optical LS10 counterparts using NWAY (Salvato et al. 2018; Salvato et al. 2022, see Sect. 2.2.2). Based on the assigned NWAY counterpart probability (`p_any` > 0.17), more than 90% of the counterparts are considered reliable. Moreover, reliable spectroscopic or photometric redshifts (Saxena et al., 2024) are provided for more than 80% of the sample.

The systematic selection of eRO-ExTra as well as the provided long-term eROSITA light curve classification and X-ray spectral modeling at the peak epoch let us identify strong candidate canonical TDE.

3.2.2 eROSITA light curves

The eROSITA X-ray light curves can help further differentiate TDEs from variable AGNs and AGN ingition events. As described in Chapter 1.3.1, the canonical X-ray light curve of a TDE exhibits a rapid rise, reaching luminosities between 10^{42} and a few times $10^{44}, \mathrm{erg, s^{-1}}$ within several weeks to a few months after the disruption event, followed by a decline over months to years. The goal of this work is to systematically select canonical TDE candidates following this predicted single flare behavior. eROSITA TDE candidates that show larger diversity in X-ray light curves (e.g., Guolo et al. 2024) are left to future work.

The eROSITA light curves include fluxes of all four complete all-sky surveys (eRASS1 – eRASS4) and eRASS5, if available, henceforth, eRASS4(5). This provides the coverage of 1.5–2 years, with each eRASS being $\approx$ 6 months after the previous one. Although the eROSITA sampling of light curves is too sparse to constrain precisely rise and decay times and slopes and provides only a lower limit for the peak flux, it allows us to differentiate canonical TDE candidates from other sources which vary repeatedly or stay consistently bright on a longer time scale. We used the light curve classification from the eRO-ExTra catalog (see Sect. 2.3.1), which divides the sample into four classes using eRASS1-4(5) data: decline, flare, brightening and other. Canonical TDEs are selected from the flare and decline classes. The former class implies that eROSITA has covered the rise and decay phases of the event, and sources in the latter class were only observed from/after their peak. In this chapter, we infer the overall rising or declining behavior of each source

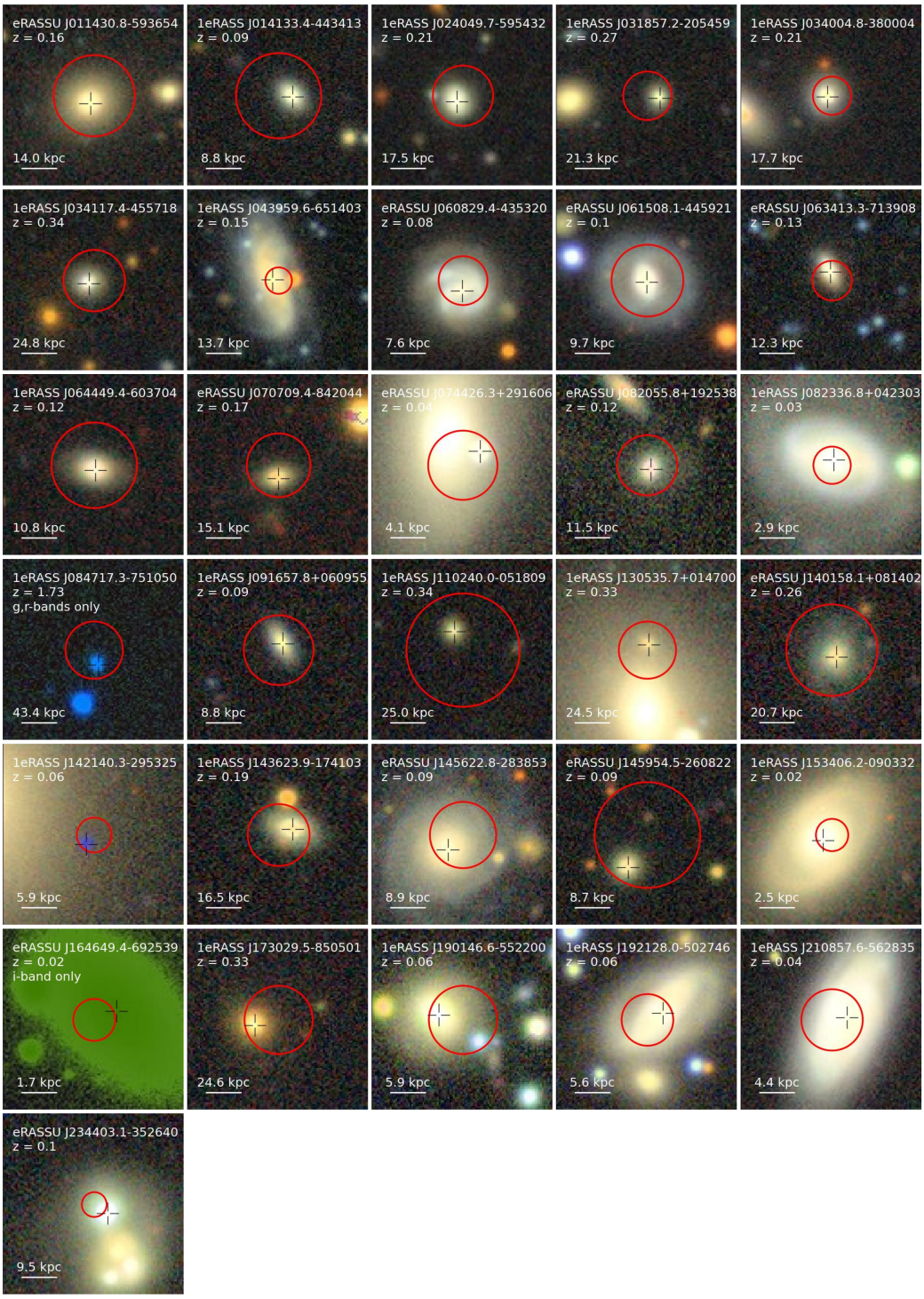

Figure 3.1: LS10 *griz*-color images (100 × 100 pixels) of the host galaxies of the X-ray TDE sample (see Table 3.1). Black crosses denote the LS10 counterpart positions, and the red circles show the eROSITA X-ray positions with their 3σ errors. Images for eRASSU J164649.4-692539 and 1eRASS J084717.3-751050 were taken only in i and g,r bands, respectively. The counterpart of 1eRASS J142140.3-295325 appears blue, since it was detected only in the g-band (see Appendix B.2).

based solely on the eROSITA data points, which are separated by about six months. We note, however, that short-term variability may occur between eRASS epochs, as has been observed in other TDE candidates (e.g., Liu et al. 2023). Similarly, in this chapter we do not consider the short term variability within a single eRASS to identify canonical TDEs.

3.2.3 eROSITA spectral modeling

The X-ray spectra at peak luminosity let us highlight TDE candidates from the eRO-ExTra catalog. All our sources are modeled with fixed Galactic absorption (`tbabs`) components with equivalent neutral hydrogen column densities ($N_{H,gal}$) extracted from the HI4PI survey (HI4PI Collaboration: et al., 2016) at their sky position. The eRO-ExTra catalog provides best-fit values with a power law model `tbabs*powerlaw`. To identify canonical X-ray soft TDEs, we select sources with photon indexes $\Gamma > 3$, so that the 68% confidence lower limit exceeds $\Gamma = 3$. This threshold was chosen based on the typical observational properties of previously X-ray-selected TDEs ($\Gamma = 3 - 5$; Saxton et al. 2020). We note that this threshold selects again only the canonical X-ray soft population of TDEs and not the entire class of possible X-ray TDEs, as several evolution scenarios may cause the spectra to be harder. For example, hard spectra can arise from Comptonization of disk photons in a newly-formed corona (Guolo et al., 2024) or in jetted TDEs, which have harder spectra with $\Gamma < 2$ even at the light curve peak (Burrows et al., 2011; Saxton et al., 2012a; Cenko et al., 2012).

In addition to the peak eROSITA epoch, for each source we also modeled the spectra of the other eROSITA epochs with sufficient counts (`DET_LIKE`> 15). For all epochs, we extracted spectra using the `eSASS` (Brunner et al., 2022) task `SRCTOOL` (version eSASS-Susers_211214) with circular source and annular background regions centered on the X-ray positions. A redshifted blackbody model `tbabs*zbbody` was used for the additional fits. Utilising `SRCTOOL`'s AUTO mode, the radii of the source and background regions were selected taking into account the source counts, the level of the background map model at the source position, the best fitting source extent model radius, and model of the effective eROSITA PSF at the source position (averaged over the exposure, and summed over all operating telescope modules). The spectra were fit unbinned using the Bayesian X-ray Analysis software (BXA; Buchner et al., 2014), which connects the nested sampling algorithm UltraNest (Buchner, 2021) with the fitting environment XSPEC (Arnaud, 1996). The C-statistic (Cash, 1976) was used, and the eROSITA background was modeled using the principal component analysis (PCA) technique described in (Simmonds et al., 2018). Each extracted eROSITA spectrum, which contains a contribution from both the source and background emission, was jointly fitted using the source and background models. We assume wide flat priors on the blackbody temperature and the logarithm of the normalization. Best-fitting parameters for the peak epochs are listed in Table 3.2, with results for all epochs given in Table B.1 in the Appendix.

Table 3.1: Excerpt of X-ray properties of 31 TDE candidates selected from eRO-ExTra catalog. The table includes eROSITA names with the X-ray detection coordinates (RA, Dec) and their positional uncertainties (poserr) from eRASS:5, a cumulative catalog of 4(5) eRASSes; the peak date (MJD_{peak}); and the light-curve class (LC), where LC = 1 corresponds to a declining light curve and LC = 2 corresponds to a single-flare light curve (see Sect. 2.3.1 for more details on light-curve classes). The additional properties of these sources can be found in the eRO-ExTra catalog.

Name	RA [deg]	Dec [deg]	poserr [arcsec]	MJD_{peak} [days]	LC
eRASSU J011430.8-593654	18.62827	-59.6148	2.0	59176	2
1eRASS J014133.4-443413	25.38988	-44.5706	2.1	59008	1
1eRASS J024049.7-595432	40.20569	-59.9088	1.5	59190	2
1eRASS J031857.2-205459	49.73930	-20.9142	1.2	59061	2
1eRASS J034004.8-380004	55.02058	-38.0005	0.9	59057	2
1eRASS J034117.4-455718	55.32153	-45.9552	1.5	59046	2
1eRASS J043959.6-651403	69.99796	-65.2342	0.6	58830	1
eRASSU J060829.4-435320	92.12252	-43.8888	1.2	59130	2
eRASSU J061508.1-445921	93.78363	-44.9892	1.7	59133	2
eRASSU J063413.3-713908	98.55552	-71.6521	0.9	59094	2
1eRASS J064449.4-603704	101.20532	-60.6175	2.1	58974	1
eRASSU J070709.4-842044	106.78928	-84.3454	1.5	59120	2
eRASSU J074426.3+291606	116.10968	29.2682	1.7	59143	2
eRASSU J082055.8+192538	125.23252	19.4271	1.5	59150	2
1eRASS J082336.8+042303	125.90327	4.3837	0.9	59153	2
1eRASS J084717.3-751050	131.82708	-75.1808	1.4	59078	2
1eRASS J091657.8+060955	139.24081	6.1655	1.7	58977	1
1eRASS J110240.0-051809	165.66691	-5.30382	2.7	58999	1
1eRASS J130535.7+014700	196.39949	1.7835	1.4	59025	2
eRASSU J140158.1+081402	210.49221	8.2339	2.2	59038	2
1eRASS J142140.3-295325	215.41512	-29.8892	0.8	59066	2
1eRASS J143623.9-174103	219.09953	-17.6847	1.5	58881	1
eRASSU J145622.8-283853	224.09512	-28.6481	1.6	59076	2
eRASSU J145954.5-260822	224.97715	-26.1395	2.5	59076	2
1eRASS J153406.2-090332	233.52573	-9.0591	0.8	58897	1
eRASSU J164649.4-692539	251.70577	-69.4274	1.0	59115	2
1eRASS J173029.5-850501	262.60794	-85.0842	1.6	59125	2
1eRASS J190146.6-552200	285.44438	-55.3663	1.6	58948	1
1eRASS J192128.0-502746	290.36772	-50.4654	1.2	59138	2
1eRASS J210857.6-562835	317.24352	-56.4754	1.5	59149	2
eRASSU J234403.1-352640	356.01296	-35.4445	0.6	59180	2

Table 3.2: X-ray modeling results for the TDE sample using power-law (`tbabs*powerlaw` from the eRO-ExTra catalog, see Chapter 2) and blackbody (`tbabs*bbody`, see Sect. 3.2.3) models. The table lists the Galactic hydrogen column density ($N_{H,gal}$) from the HI4PI survey, fixed in both models; the photon index for the peak eROSITA epoch (Γ_{peak}) from the power-law fit and the corresponding 0.2–2.3 keV flux at the peak eRASS ($F_{peak,0.2-2.3,keV}$); and the blackbody temperature (kT) from the blackbody fit.

Name	N_H $[10^{20}cm^{-2}]$	Γ_{peak}	$F_{peak,0.2-2.3\,keV}$ $[10^{-13}$ erg cm^{-2}s$^{-1}]$	kT_{peak} [eV]
eRASSU J011430.8-593654	2.4	4.11 ± 0.29	6.37 ± 0.88	0.10± 0.01
1eRASS J014133.4-443413	1.6	4.15 ± 0.46	3.11 ± 0.64	0.08 ± 0.01
1eRASS J024049.7-595432	2.6	2.86 ± 0.30	2.78 ± 0.42	0.20 ± 0.02
1eRASS J031857.2-205459	2.2	4.07 ± 0.26	4.18 ± 0.54	0.09 ± 0.01
1eRASS J034004.8-380004	1.4	2.93 ± 0.18	4.50 ± 0.46	0.17 ± 0.01
1eRASS J034117.4-455718	1.2	2.65 ± 0.39	1.15 ± 0.23	0.17 ± 0.04
1eRASS J043959.6-651403	4.8	4.89 ± 0.08	13.17 ± 0.44	0.081 ± 0.002
eRASSU J060829.4-435320	9.0	4.09 ± 0.23	6.51 ± 0.61	0.11 ± 0.01
eRASSU J061508.1-445921	5.7	3.24 ± 0.38	1.97 ± 0.35	0.14 ± 0.02
eRASSU J063413.3-713908	10.1	4.25 ± 0.15	2.34 ± 0.14	0.12 ± 0.01
1eRASS J064449.4-603704	11.7	6.13 ± 0.62	0.61 ± 0.12	0.08 ± 0.01
eRASSU J070709.4-842044	15.4	4.14 ± 0.26	2.44 ± 0.24	0.14 ± 0.01
eRASSU J074426.3+291606	4.3	4.25 ± 0.27	12.34 ± 1.49	0.10 ± 0.01
eRASSU J082055.8+192538	5.0	5.17 ± 0.33	10.66 ± 1.39	0.08 ± 0.01
1eRASS J082336.8+042303	2.6	4.12 ± 0.09	100.83 ± 4.27	0.087 ± 0.002
1eRASS J084717.3-751050	12.3	2.75 ± 0.46	0.69 ± 0.13	0.32 ± 0.06
1eRASS J091657.8+060955	3.5	5.40 ± 0.40	8.89 ± 1.35	0.06 ± 0.01
1eRASS J110240.0-051809	4.3	4.92 ± 0.44	5.27 ± 0.96	0.08 ± 0.01
1eRASS J130535.7+014700	1.9	3.68 ± 0.25	7.71 ± 1.01	0.11 ± 0.01
eRASSU J140158.1+081402	2.1	5.19 ± 0.43	4.34 ± 0.72	0.06 ± 0.01
1eRASS J142140.3-295325	7.1	3.10 ± 0.12	15.74 ± 0.95	0.17 ± 0.01
1eRASS J143623.9-174103	8.2	4.55 ± 0.30	5.04 ± 0.61	0.10 ± 0.01
eRASSU J145622.8-283853	12.6	5.30 ± 0.30	6.30 ± 0.67	0.09 ± 0.01
eRASSU J145954.5-260822	14.9	2.94 ± 0.54	1.78 ± 0.39	0.18 ± 0.04
1eRASS J153406.2-090332	12.5	4.24 ± 0.12	17.96 ± 0.87	0.118 ± 0.004
eRASSU J164649.4-692539	10.8	4.47 ± 0.19	10.47 ± 0.72	0.096 ± 0.004
1eRASS J173029.5-850501	11.3	3.00 ± 0.40	1.93 ± 0.34	0.24 ± 0.03
1eRASS J190146.6-552200	8.2	5.05 ± 0.29	10.24 ± 1.17	0.09 ± 0.01
1eRASS J192128.0-502746	6.8	2.81 ± 0.25	9.09 ± 1.02	0.20 ± 0.02
1eRASS J210857.6-562835	4.0	3.24 ± 0.28	6.66 ± 0.89	0.13 ± 0.01
eRASSU J234403.1-352640	1.2	4.62 ± 0.08	189.75 ± 7.21	0.075 ± 0.002

3.2.4 Host photometry

In addition to the LS10 values of W1-W2 provided in eRO-ExTra, we explored the available mid-IR light curves (see Sect. 3.4.1) to confirm that the pre-TDE value of W1-W2 is less than 0.8 and to exclude possibly missed AGN varying in the mid-IR. Finally, one source was excluded since its potential optical counterpart is compact and very faint[3]; therefore, inconsistent with a typical TDE host in the low-redshift universe.

3.3 The final sample of golden TDE candidates

The sample of canonical TDE candidates selected from eRO-ExTra includes 31 sources that: 1) have a single decline or a single flare eROSITA light curve; 2) have $\Gamma > 3$, accounting for errors; 3) have a clear host galaxy counterpart without known AGN signatures. The sample and some key X-ray properties from the eRO-ExTra catalog are presented in Tables 3.1 and 3.2.

3.3.1 Optical counterparts for the TDE sample

To meet the criteria just described, each TDE candidate is associated with an LS10 optical counterpart. Using the counterparts identified in Chapter 2 and applying the same reliability criterion (`p_any` > 0.17), 28 out of 31 sources have a reliable counterpart. However, it is important to note that three optical counterparts[4] of sources with low `p_any` < 0.17 are still likely genuine, since the optical counterpart position is in agreement with the X-ray position within 3σ. The low `p_any` indicates that the multiwavelength properties of the counterparts do not entirely match the properties of typical X-ray emitters. This is not surprising, as no TDE was included in the training sample used in Salvato et al. (2018). LS10 image cutouts of the host galaxies are shown in Fig. 3.1 and the counterpart properties are listed in Table 3.3.

Spectroscopic redshifts are available for 19 sources from either archival data or a dedicated follow-up program (see the summary provided in Chapter 2); photo-z for the remaining sample were computed following the procedure described in (Salvato et al., 2025) using CIRCLEZ (Saxena et al., 2024) with LS10 photometry (*griz*, W1,W2,W3,W4). Fig. 3.2 shows the sample in the redshift-luminosity plane. Overall, the TDE sample spreads over the range of redshifts of $0.02 < z < 0.34$ and luminosities of $5.7 \times 10^{41} < \mathrm{L_X} < 5.3 \times 10^{44}$ erg s^{-1} in the rest frame $0.2 - 6.0$ keV band.

Several sources from the sample have been previously reported in individual papers: 1eRASS J082336.8+042303 (AT2019avd, Malyali et al. 2021), eRASSt J074426.3+291606 (Malyali et al., 2023b), and eRASSt J234403.1-352640 (Homan et al., 2023; Goodwin et al.,

[3] r = 24.5mag, corresponding to the luminosity of $\nu \mathrm{L}_\nu \approx 8 \times 10^{40}$ergs^{-1} at z=0.1 (the mean redshift in the sample) and the stellar mass of $\approx 5 \times 10^6 \mathrm{M}_\odot$ consistent with a dwarf galaxy

[4] See Appendix B.2 for more details on the optical counterpart of J1421.

Table 3.3: LS10 counterparts of TDE candidates with their identification probabilities (p_any) and reshifts (z). Photometric redshifts are noted with their 1σ (68% confidence level) errors, others are spectroscopic. The origin of the redshifts as well as more counterpart properties can be found in the eRO-ExTra catalog. The photo-z for J0847 is not-reliable, since two optical photometry *griz* points were missing in the calculation, and is, therefore, not listed. The p_any value for J0744 is omitted, since the counterpart was identified in Malyali et al. (2023b).

	Name	p_any	LS10_RA [deg]	LS10_Dec [deg]	z
1	J0114	0.43	18.6286	-59.6152	0.16
2	J0141	0.38	25.3891	-44.5707	0.09
3	J0240	0.99	40.2062	-59.9091	$0.21^{+0.07}_{-0.04}$
4	J0318	0.32	49.7388	-20.9143	$0.27^{+0.13}_{-0.09}$
5	J0340	0.99	55.0208	-38.0005	$0.21^{+0.06}_{-0.05}$
6	J0341	0.99	55.3219	-45.9553	$0.34^{+0.08}_{-0.11}$
7	J0439	0.98	69.9986	-65.2342	0.15
8	J0608	0.77	92.1226	-43.8892	0.08
9	J0615	0.92	93.7837	-44.9893	$0.10^{+0.03}_{-0.03}$
10	J0634	0.70	98.5558	-71.6518	0.13
11	J0644	0.58	101.2052	-60.6178	0.12
12	J0707	0.24	106.7895	-84.346	$0.17^{+0.23}_{-0.02}$
13	J0744	-	116.1089	29.2688	0.04
14	J0820	0.95	125.2324	19.427	0.12
15	J0823	0.99	125.9032	4.384	0.03
16	J0847	0.99	131.8265	-75.1814	-
17	J0916	0.16	139.2407	6.1658	0.09
18	J1102	0.26	165.6673	-5.3031	$0.33^{+0.10}_{-0.09}$
19	J1305	0.06	196.3994	1.7837	$0.33^{+0.07}_{-0.08}$
20	J1401	0.96	210.492	8.2337	$0.26^{+0.06}_{-0.05}$
21	J1421	0.12	215.4155	-29.8896	0.06
22	J1436	0.85	219.0989	-17.6845	$0.19^{+0.06}_{-0.03}$
23	J1456	0.95	224.0958	-28.6487	0.09
24	J1459	0.02	224.978	-26.1409	0.09
25	J1534	0.99	233.5261	-9.0593	0.02
26	J1646	0.21	251.7032	-69.4271	0.02
27	J1730	0.88	262.6191	-85.0844	$0.33^{+0.07}_{-0.05}$
28	J1901	0.9	285.4461	-55.3662	0.06
29	J1921	0.97	290.3667	-50.4652	0.06
30	J2108	0.98	317.2424	-56.4753	0.04
31	J2344	0.49	356.0123	-35.4449	0.10

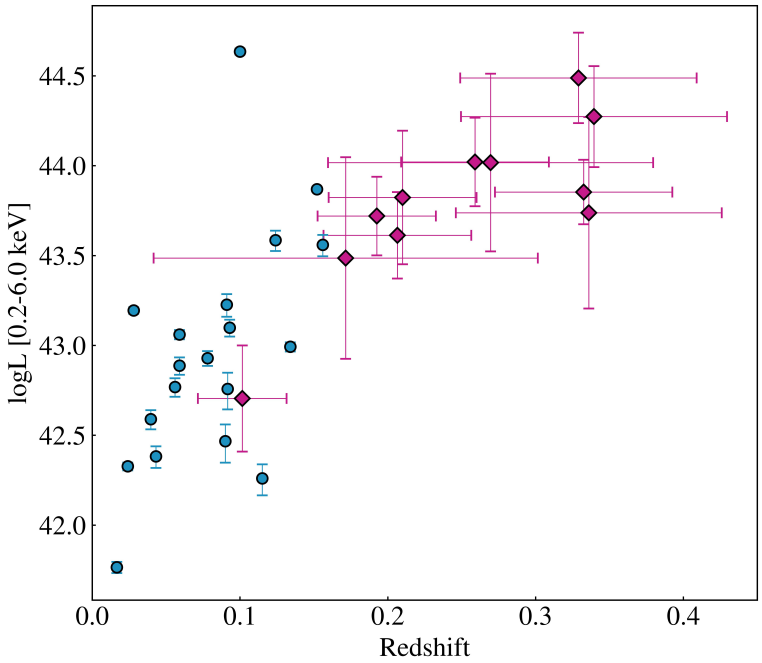

Figure 3.2: Rest-frame luminosity in 0.2–6.0 keV vs. redshift. The blue circles denote sources with spectroscopic redshifts and the pink diamonds show those with photometric redshifts. The most luminous source in the sample is J2344.

2023). The TDE nature of the candidates was also strengthened by the presence of TDE-like emission in optical, mid-IR, and radio bands (see Sect.3.4 for more details). This demonstrates the reliability of the methodology used in the presented selection.

3.3.2 X-ray properties of the TDE sample

This subsection provides insights into the X-ray properties of the selected TDEs, particularly light curve shapes, rise and decay timescales, and spectral evolution.

Most sources in the sample do not show significant X-ray spectral variability, with their blackbody temperature staying consistent within 3σ in all detected epochs (see Table B.1). Therefore, the vast majority of selected TDEs remain X-ray soft throughout the event. Only two candidates, namely, J2344 and J0439, show kT evolution with 6σ (from eRASS1 to eRASS2) and 9σ (from eRASS2 to eRASS3) significance, respectively. Where J2344 shows even further spectral softening from 80 eV to 40 eV within a year (from eRASS2 to eRASS4), J0439 exhibits a significant temperature increase from 80 eV to 210 eV. The observed spectral hardening might be associated with the formation of a hot corona (e.g., Wevers et al. 2021; Liu et al. 2023), similar to a transition from a soft disc-dominated state

to a hard corona-dominated state observed in X-ray binary systems with stellar mass BH (Wang et al., 2022).

X-ray light curves based on the eRASS4(5) surveys in the soft 0.2–2.3 keV energy band with 6-month cadence are provided in the Appendix in Fig. B.1. By selection, all sources in the sample peaked either in eRASS1 (P1) or eRASS2 (P2). The P1 candidates show a decaying light curve, and the P2 candidates have a flare light curve. After the peak, the sources declined monotonically or declined after a $0.5 - 1$ year plateau phase. It is important to note that the peak flux and amplitudes of the events are lower limits only, since the actual peak could happen between eROSITA scans.

The sample contains more P2 sources (23 objects) than P1 sources (8). This difference in identification numbers reflects the selection criteria of the eRO-ExTra parent catalog, namely, amplitude ($A > 4$) and significance ($S > 4$) cuts between eRASS1 and eRASS2. Whereas P2 sources are selected based on their rise, between eRASS1 and eRASS2, P1 sources are chosen based on their decay between eRASS1 and eRASS2. We find that the rise timescales for the sample (possible to estimate only for P2) is, on average, shorter than the decay timescales. Namely, all P2 sources rise within ≈ 6 months. However, the decay time for a fraction of TDEs is longer, with 30 % of P2 sources decaying at least over $1 - 1.5$ years. To verify the selection favoring P2 sources over P1, we tested whether P2 sources would be selected based on their decline amplitude: only 9 out of 24 sources would be kept after applying the $A > 4$ and $S > 4$ cuts in the decay phase between eRASS2 and eRASS3, consistent with the number of P1 sources.

As mentioned before, the estimation of rise, decay, and plateau time scales is limited by the sparsity of the eROSITA light curve sampling. Therefore, further timescales are provided only for assessing general trends, omitting possible variability between eRASSes. For the P2 sources, the rising timescale does not exceed 6 months (or 1 year if we assume that the peak can also be between eRASS2 and eRASS3). This aligns with the expected rise time for TDEs (Gezari, 2021). Three P2 sources show a plateau phase at the peak level lasting $\approx 0.5 - 1$ year. The majority of sources (21/31) decay within half a year in agreement with the TDE light curve trends from Sazonov et al. (2021). The remaining sources decay over two-three eRASSes ($1 - 1.5$ years).

The majority of pre-eROSITA archival X-ray data for the sample provided in the eRO-ExTra catalog[5] is not constraining and includes only upper limits either shallower than the brightest eROSITA detection or significantly above eROSITA's detected minimum. There are constraining measurements only for 4 sources in the sample. An archival upper limit by *XMM-Newton* revealed a large amplitude of more than a factor of 50 for the flare in J0823, whereas the eRASS1/2 amplitude was only a factor of 6. Deep archival *ROSAT* upper limits for 1eRASS J091657.8+060955 and eRASSU J164649.4-692539 reinforce the archival X-ray quiescence of the candidates. Moreover, in the case of 1eRASS J091657.8+060955 it supports the presence of a TDE flare, since eROSITA has observed only the decline phase. In addition, 1eRASS J024049.7-595432 has a constraining *XMM-Newton* detection.

[5]No data is available for J0744+29: the archival X-ray detection belongs to the bright galaxy nearby, while the real host is a X-ray quiet dwarf galaxy (Malyali et al., 2023b) .

The flux is comparable to the detected eROSITA minimum and can be interpreted as underlying host emission being consistent with the luminosity expected from star-forming galaxies (Schober et al., 2014). The archival constraints are shown in the light curve plots in Fig. B.1.

3.4 Multiwavelength variability

In this section, we describe the optical, mid-IR and radio properties of the sample.

3.4.1 Mid-infrared variability

Mid-IR flares in TDEs are thought to arise from reprocessing of optical, ultraviolet (UV), and X-ray photons by dust within a few parsecs of the SMBH. They can last for years (Jiang et al., 2016; Dou et al., 2017; van Velzen et al., 2021), peak at 3–10 μm, and reach luminosities of 10^{42-43} erg s^{-1} (Lu et al., 2016).

To study the mid-IR properties of the eROSITA TDE sample, we use data from WISE during the NEOWISE reactivation mission (NEOWISE-R, Mainzer et al. 2011) which covered the entire sky every half year from Sep. 2014 to Aug. 2024 in the W1 (3.4 μm) and W2 (4.6 μm) bands. Light curves were extracted using the NASA/IPAC Infrared Science Archive within 5" from the position of optical counterparts. The photometry was rebinned to one data point per NEOWISE-R all-sky scan using a weighted mean. The W1 and W2 light curves for all sources are shown in the Appendix in Fig. B.3 and Fig. B.4.

Approximately 30 % of the eROSITA TDE sample shows mid-IR variability. Sources with significance $\sigma_{\mathrm{W1,max}} > 3$ and amplitude ΔW1 > 0.3mag are summarized in Table 3.4. For five of these, we found flares with $\Delta \mathrm{W1} \approx 0.9 - 1.5$ mag (see Fig. 3.3). Most mid-IR flares show a fast rise within six months, followed by a slow decay over several years. The exception is J0644 with its $\approx$ 1-year brightening and $\approx$ 6-month fading time. The "fast rise and slow decay" trend resembles the one found for mid-IR selected TDEs and is consistent with dust reprocessing of the intrinsic TDE flare (Masterson et al., 2024).

Seven sources with mid-IR flares have well-sampled light curves in both W1 and W2 bands to explore the W1-W2 evolution, which can trace the developent of temporary accretion-driven activity during the TDE accretion phase. For all seven sources the mid-IR brightening was accompanied by a significant reddening (see Table 3.4), with the most significant changes in W1-W2 observed for J0823 (from 0.1 mag to 0.8 mag) and J2108 (from 0.1 mag to 0.7 mag).

3.4.2 Optical variability

Next, we explored how many sources in our sample of TDEs are accompanied by optical transient emission, using data from Gaia (Gaia Collaboration et al., 2016), ATLAS (Tonry et al., 2018) and ZTF light curves (Bellm et al., 2019). ZTF host-subtracted light curves in the g-band were extracted at the position of the optical counterpart using the ZTF

Table 3.4: Properties of prominent mid-IR flares (W1, W2) of TDE candidates observed with WISE. The column Δ_{W1} [mag_{Vega}] is the amplitude of variability in the W1 band (in Vega magnitudes); σW1 is the 68% photometric uncertainty in W1; $MJD_{W1,peak}$ is the Modified Julian Date of the W1-band peak; $W1 - W2_{pre}$ denotes the W1–W2 color measured before the TDE flare; and $W1 - W2_{flare}$ is the W1–W2 color measured at the time of the TDE flare peak.

Name	Δ_{W1} [mag_{Vega}]	σ_{W1}	$MJD_{W1,peak}$	$W1 - W2_{pre}$	$W1 - W2_{flare}$
J0439	1.0	99.4	59021	0.4	0.7
J0644	1.5	58.3	57499	-	-
J0823	1.4	78.0	59151	0.1	0.8
J2108	1.3	152.4	58229	0.1	0.7
J2344	0.9	79.0	59365	0.3	0.7
J0141	0.4	3.8	59184	-	-
J0608	0.3	17.2	59276	0.3	0.5
J0615	0.6	38.0	59121	0.2	0.6
J0847	0.4	6.0	59255	-	-
J1436	0.3	9.2	59250	0.3	0.6

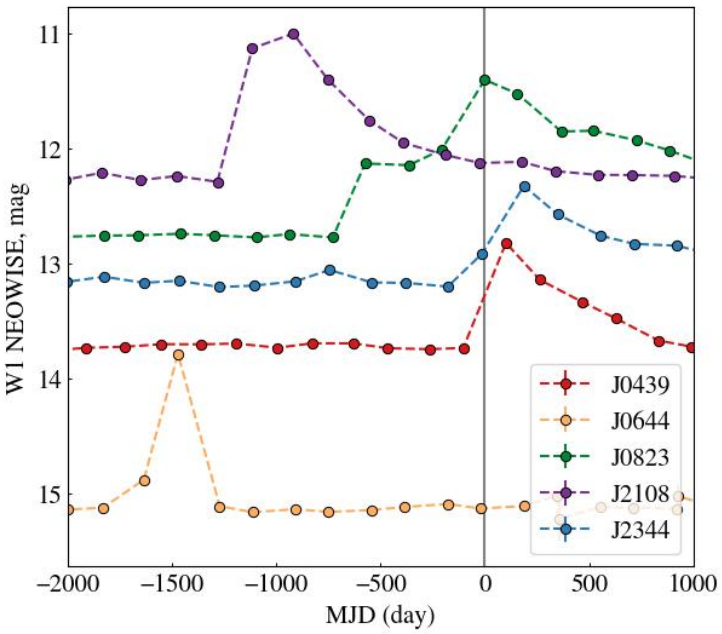

Figure 3.3: W1 NEOWISE light curves of 5 TDE candidates with significant IR flares of more than 0.9 mag. The X-axis is shifted so that x=0 corresponds to the peak eROSITA detection for each source. The magnitudes are given in the Vega system.

forced photometry service (Masci et al., 2019). We applied a signal to noise threshold of S/N > 3, scisigpix < 10, zpmaginpscirms < 0.1 to filter out noisy images (more information on the data quality parameters is provided in the ZTF manual[6]). Gaia *g*-band light curves were extracted from the Gaia Alerts web server[7]. Since the service does not provide host-subtracted light curves, we estimated the flare magnitudes by subtracting the provided pre-flare historical magnitudes of the hosts. ATLAS light curves were obtained from publicly available photometric data in the cyan (420–650 nm) and orange (560–820 nm) filters. They were extracted by forced photometry on the difference images and rebinned to 24 hr. To remove epochs of low-quality photometry, we discarded data points with the semi-major axis of the fitted PSF model greater than 3 pixels.

Flares with flux amplitudes larger than two were found in the ZTF and Gaia data for six sources (see the summary in Table 3.5). Their single-band non host-subtracted light curves are compiled in Fig. 3.4, while more detailed plots of host-subtracted light curves are available in Fig. B.5. Detailed discussions of the optical properties of J0744, J0823, and J2344 were presented already elsewhere (Malyali et al., 2023b, 2021; Homan et al., 2023).

The majority of prominent flares discussed above are also clearly detected with ATLAS. Although ATLAS provides coverage for all sources not covered by Gaia or ZTF, the remaining TDE candidates either did not have accompanying optical flares or the ATLAS data are too noisy to identify additional fainter statistically significant flares. For these sources, we estimated ATLAS ULs for potentially undetected flares using mean five-sigma limit magnitude in the orange filter. The UL values are presented in the Table B.2 and span from 18.2 to 19.1 mag. The shallow level of ATLAS upper limits, in comparison, for example, to the ZTF typical limiting magnitude of $\approx 20.5 - 21$ in the *g,r* bands, shows a currently existing observational bias against detecting fainter optical transients in the eROSITA_DE sky. Given the variety of the timing of optical and X-ray flares (from around -600 to 0 days, see Fig. 3.4), deeper all-sky optical surveys would be required to systematically identify optical flares for X-ray selected TDEs. As an example of an observational bias, the LS10 optical transient J1421 was detected in the *g*-band with 19.21 mag due to accidental fortunate timing of LS10 epochs (see Appendix B.2) and would be missed otherwise, if we used an ATLAS UL equal to 18.3 mag. The transient is off-center and is a strong candidate for an off-nucleus TDE (more details in Sect. 3.5.2).

Finally, we estimated $L_{opt,peak}/L_{x,peak}$ at the optical flare peak time for the quasi-simultaneous X-ray and optical flares (J0439, J0744, J2344). The value ranges in $L_{opt,peak}/L_{X,peak} \in (4 - 11)$. This is in agreement with the L_{opt}/L_x estimates from Guolo et al. (2024). Upper limits for $L_{opt,peak}/L_{X,peak}$ were calculated for the remaining sample. The resulting values, ranging between 5 and 140, are consistent with the expectations (Guolo et al., 2024). This confirms that although optical flares were not detected for the majority of the sample, this might be due to observational limitations.

[6] `https://irsa.ipac.caltech.edu/data/ZTF/docs/forcedphot.pdf`
[7] `http://gsaweb.ast.cam.ac.uk/alerts/home`

Table 3.5: Properties at peak of optical flares of eROSITA TDE candidates.

Name	g-band [$\mathrm{mag_{AB}}$]	$\mathrm{L_{g,peak}}$ $\times 10^{44}[\mathrm{ergs^{-1}}]$	$\mathrm{Date_{peak}}$ [MJD]
J0318	20.3 ± 0.1	$5.0^{+7.1}_{-3.6}$	58430
J0439	18.41 ± 0.12	$7.97^{+0.93}_{-0.83}$	58975
J0744	19.6 ± 0.1	$0.16^{+0.01}_{-0.01}$	59126
J0823	17.13 ± 0.04	$0.86^{+0.03}_{-0.03}$	58538
J1102	19.8 ± 0.3	$13.54^{+17.46}_{-8.48}$	58619
J2344	16.50 ± 0.11	$18.74^{+1.99}_{-1.80}$	59135
J1421	19.21 ± 0.05	$0.53^{+0.02}_{-0.03}$	58643

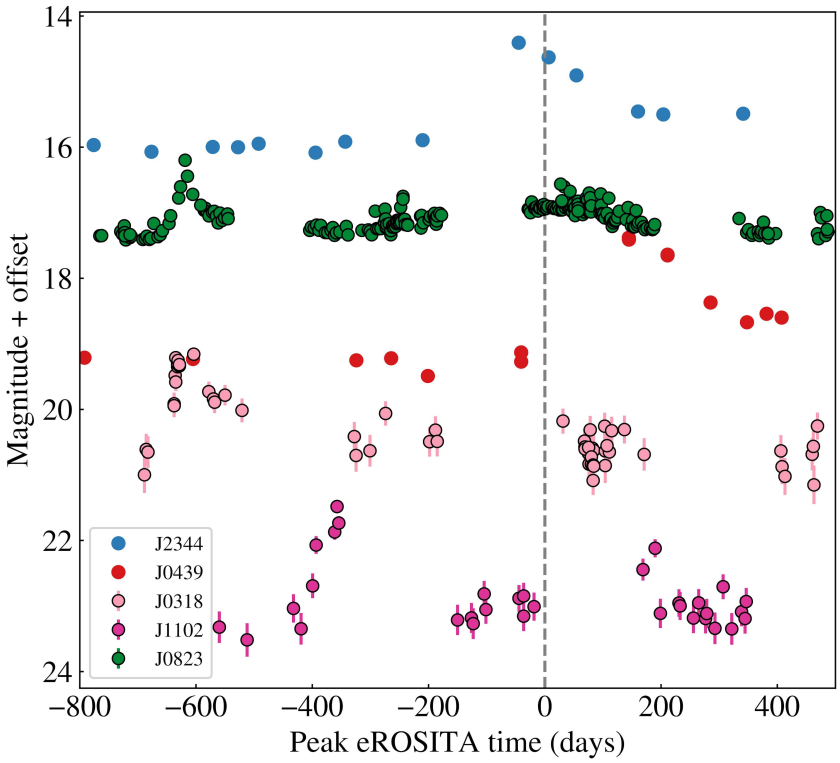

Figure 3.4: Non-host subtracted g-band light curves of five TDE candidates showing significant optical flares. The x-axis shows time after eROSITA peak in days, so that x=0 corresponds to the peak eROSITA detection for each source. The summary of observational information is provided in Table B.2. The individual host subtracted light curves are showin in Fig. B.5. The optical flare of J0744 is too faint to be distinguished in a non host-subtracted light curve and is shown in the host-subtracted plot only.

3.4.3 Radio variability

To search for potential radio counterparts, the LS10 positions of the eROSITA TDEs were cross-matched with the Rapid ASKAP Continuum Survey (RACs, McConnell et al., 2020; Duchesne et al., 2023, 2024) source catalog with a radius of 25". We choose this cross-matching radius as it represents the resolution of the RACs images (the full width at half maximum of the PSF is 25", McConnell et al. 2020). Four radio counterparts out of the 31 TDE candidates were found. For these four sources, we then searched the CASDA Data Portal for all publicly available RACs observations covering their sky locations. Flux densities in the image plane were derived by fitting an elliptical Gaussian with the size of the synthesized beam. The results are reported in Table 3.6.

Table 3.6: RACS radio detections of eROSITA TDEs.

Name	MJD [day]	Frequency [GHz]	Flux Density [μJy]
J0823	59232	1.4	862±221
	60310	0.9	1335±277
J1305	58970	0.9	4280±241
	60326	0.9	4110±332
J1646	58935	0.9	1888±162
	59211	1.4	1221±160
	59231	1.4	2222±860
J2108	58610	0.9	1330±220
	58936	0.9	989±251
	59220	1.4	952±167
	60330	0.9	1170±150

Each of the detected four sources has between two and four RACs observations at central observing frequencies of 0.9 GHz or 1.4 GHz, allowing a search for radio variability. The TDE candidates J1646, J2108, and J1305 show indications of radio variability across the RACs observations spanning 2019–2024. J1646 was detected at 0.9 GHz with a luminosity of $L_{9GHz} = 1.7 \times 10^{28}$ erg s^{-1} Hz^{-1} already 539 d before the eROSITA discovery, suggesting that the emission originates from the host galaxy rather than from the event that generated the X-ray flare. The inferred luminosity is consistent with star formation (in agreement with the star-formation-rate threshold and estimation approach described in Appendix A.4), supporting the non-TDE interpretation. Variability at 1.4 GHz was detected between 62 and 82 d after the eROSITA peak, in agreement with expectations from a newly launched outflow. J2108 showed constant (within the errors) radio emission before and after the eROSITA peak date at a luminosity of $L_{9GHz} = 5.1 \times 10^{30}$ erg s^{-1} Hz^{-1}. Also, in this case, the radio emission is very likely unrelated to the X-ray flare, given its constant level prior to the TDE and the absence of variability or increased flux following the X-ray event. The centroid of the radio source associated with J1305 is 11" away from

the optical position of the galaxy the event is associated with, so this radio source may be unrelated to the host galaxy. Due to the resolution of the RACs images and the fact that this radio source falls within one beam of the optical counterpart, higher resolution radio observations are required to determine if this radio source is associated with the optical counterpart. For the fourth source, J0823, only single-epoch RACs measurements in different bands are available; therefore, variability cannot be evaluated. However, we note that Wang et al. (2023) reported the detection of radio variability in this source from VLA and VLBA interpreted as evidence for a radio-emitting outflow launched by the transient event. The remaining 27 TDE candidates in the sample were undetected by RACs, with typical 3σ upper limits of $\approx$500–1000 μJy. A detailed analysis of the radio properties of these events, including more sensitive dedicated radio follow-up observations of 22 TDE candidates in this sample, is presented in Goodwin et al. (2025b). In addition, a summary of the radio flare properties of J2344 was presented in Goodwin et al. (2023).

3.5 Host galaxy properties

3.5.1 SED modeling

To infer the host galaxy properties of our TDE candidates, we model the spectral energy distributions (SEDs) using the photometry provided by LS10. This includes optical photometry in *griz* bands from DECam and mid-IR photometry W1-4 from NEOWISE. Fluxes were corrected for the Galactic foreground extinction. In addition to the inverse flux variance FLUX_IVAR provided in the LS10 catalog, we introduced systematic uncertainties equal to 0.05 mag for *griz* filters and 0.2 mag for W1-4 filters (Salvato et al., 2022), which account for such factors as source variability and different extraction radii. The modeling was not performed for J0847, J1646, and J1421 since two or more optical photometry bands are missing.

We applied the same methodology and models as used in several previous systematic TDE studies (Sazonov et al., 2021; van Velzen et al., 2021; Hammerstein et al., 2023; Yao et al., 2023; Masterson et al., 2024). We fit models from the Flexible Stellar Population Synthesis (FSPS) framework (Conroy & Gunn, 2010) with the Prospector software (Johnson et al., 2021). We assumed a delayed, exponentially declining star formation history with a Chabrier initial mass function (Chabrier, 2003). The model has five free parameters: the galaxy's stellar mass, the age of the stellar population, the e-folding timescale of star formation, metallicity, and dust optical depth, for which we used the extinction law from Calzetti et al. (2000). To derive uncertainties, we applied MCMC sampling using the emcee package (Foreman-Mackey et al., 2013). The MCMC chains were initialized with 100 walkers, starting from the maximum likelihood fit with a burn-in phase of 500 steps per walker and 1000 iterations of the MCMC sampling.

We used MCMC fits to evaluate the host stellar masses and rest frame ${}^{0.0}u - r$ colors, where 0.0 denotes the rest-frame values. As in previous studies, we reported a surviving stellar mass obtained by multiplying the total mass by the factor "mfrac" obtained from

the model. The surviving mass is defined as a mass that survived throughout the galaxy's evolution, accounting for mass loss due to stellar winds or supernovae. The SED fitting results are shown in the Appendix in Table B.3.

A comparison of the stellar masses and colors of this TDE sample with other X-ray, optical or mid-IR selected TDE samples is shown in Fig. 3.5. The eROSITA TDE sample shows an overdensity in the green valley, with more than half of the modeled sample (18/28 sources) falling in this conservatively defined area. Previous studies also have found that X-ray and optically selected TDE populations are preferentially located in the green valley (e.g., Arcavi et al. 2014; van Velzen et al. 2021; Sazonov et al. 2021; Yao et al. 2023; Hammerstein et al. 2023). The higher TDE occurrence rate in the green-valley galaxies is considered to be due to the higher concentration of stars scattered into the loss cone because of a recent merger (Prieto et al., 2016; Hammerstein et al., 2021) or a starburst (French et al., 2016; Stone et al., 2018; Stone & Metzger, 2016). However, it was recently shown that higher central stellar concentration increases the rate of strong scattering that may lead to the decrease of the TDE rate scattered into the loss cone (Teboul & Perets, 2025). While X-ray and optically selected TDEs are concentrated in the green valley, the mid-IR TDE population consists of redder and more massive galaxies, which was explained by the selection bias of choosing the brightest IR flares (Masterson et al., 2024). However, X-ray TDEs with mid-IR flares in this chapter do not follow this trend, with their stellar masses being homogeneously distributed within $\log(M_{gal}/M_{sun}) \approx 9.6 - 11$.

We note that the selection of the extinction model influences the stellar mass and color results. Using the extinction law from Prevot et al. (1984), the stellar masses reduce on average by 50 % and ${}^{0,0}u - r$ increases by ≈ 0.1 mag. This results in a small movement toward the upper left corner of the diagram; however, the qualitative result of an overdensity in the green valley is not changed. In addition, it is worth pointing out that the training sample used for computing the photo-z via machine learning was tuned for AGN (Saxena et al., 2024). A direct comparison between the photo-z and the spec-z for the sources with spectroscopic redshifts available suggests that the photoz tends to be higher than they should be, resulting in bluer colors. The increasing sample size with available spectroscopy will allow the computation of the photo-z to be optimized for TDEs in the near future.

We used the scaling relation from Reines & Volonteri (2015) to estimate the BH masses from the host stellar masses, taking into account the 0.5dex scatter of the relation. The BH mass distribution vs. redshift is shown in Fig. 3.6, ranging from $\log(M_{BH}/M_{\odot})$=5.4 to 7.6 with a peak $\approx 6 \times 10^6 M_{\odot}$. This is below the Hills-mass for the $1\,M_{\odot}$ star and a non-spinning BH (Hills, 1975) and is, thus, consistent with the TDE interpretation. The lack of BHs with masses less than $2 \times 10^5 M_{\odot}$ might be due to an increasingly smaller volume in which TDEs can still be detected around low mass black holes (Wevers et al., 2017), the BH occupation fraction in low mass galaxies (Stone & Metzger, 2016) or inefficient circularization (Dai et al., 2015).

It is evident from Fig. 3.6 that eROSITA TDEs accompanied by mid-IR flares are preferentially located at lower redshifts ($z < 0.2$), with 60 % of mid-IR bright sources being below the X-ray luminosity median of the TDE sample ($L_{median} = 2.4 \times 10^{43} ergs^{-1}$).

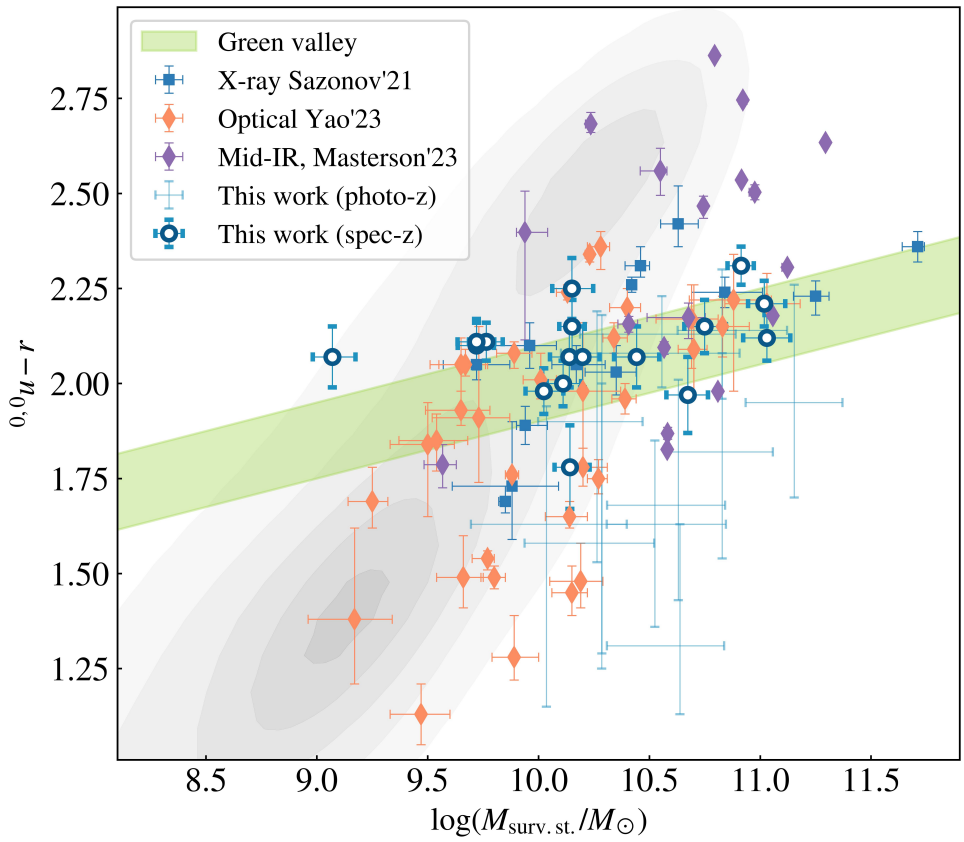

Figure 3.5: Host galaxy color vs. surviving stellar mass of the eROSITA TDE sample in comparison to other TDE samples selected in X-rays, optical and mid-IR. Gray contours denote a sample of SDSS galaxies within the same redshift range ($z < 0.34$) from Mendel et al. (2014). The green area shows the green valley defined in Yao et al. (2023). The blue circles show the eROSITA TDEs presented in this chapter with spec-z and sources with photo-z are shown with blue errorbars. The errors for sources with photo-z are calculated accounting for 1σ photo-z errors. The orange and purple diamonds, and blue squares denote TDE samples selected in optical (Yao et al., 2023), mid-IR (Masterson et al., 2024) and X-rays (Sazonov et al., 2021), respectively.

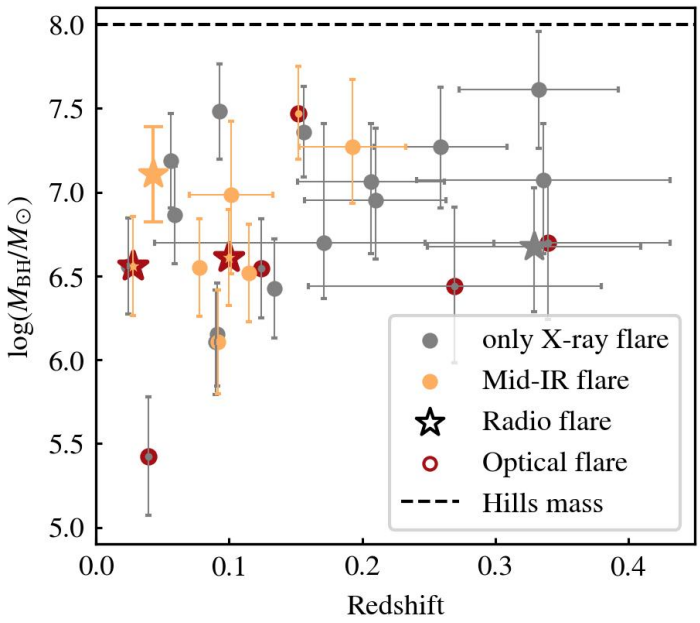

Figure 3.6: Black hole mass vs. redshift for the eROSITA TDE sample. Gray circles mark sources detected only in X-ray. Orange circles show sources which also had mid-IR flares, while red outlined circles show those that have optical flares. Sources with radio detections are denoted with stars. The dashed black line shows Hills mass for a solar-type star and a non-spinning SMBH.

This might be associated with the obscuring envelope scenario (see Sect. 3.6.3), which would make TDEs that are at larger distances less likely to be discovered in X-rays due to obscuration. The lack of sources with mid-IR flares at higher redshifts also comes from the limited sensitivity of WISE. Although optically bright TDEs from the sample are more concentrated in the low BH mass regime, this is likely related to selection effects only (see Sect. 3.4.2). Indeed, comparing the BH mass distributions of our sample and optically selected samples (Yao et al., 2023; Guolo et al., 2024), we find a very similar mean BH mass supporting the argument that the detection of X-ray emission is independent of the BH mass and and may be affected by external factors such as system geometry or obscuration.

3.5.2 J1421: an off-nuclear TDE candidate

No SED modeling was performed for the source J1421. This TDE candidate differs from the rest of the sample as its optical counterpart was detected only as a transient in a single photometric band in two LS10 epochs (see Appendix B.2 for more details). The optical position is located $\approx$ 18 arcsec (21 kpc) and $\approx$ 24 arcsec (28 kpc), respectively, from the centers of two merging galaxies at z = 0.06 (see Fig. B.2). There is no separate underlying quiescent host detected at the position of the transient. An order-of-magnitude estimate

of the corresponding BH mass can be obtained from the integrated energy released during the X-ray flare.

Integrating the X-ray flare from eRASS1 to eRASS4 (see Fig. B.1) provides a total energy release (in the X-ray band) of $\approx 2.5 \times 10^{50}$erg. The emitted energy originates from accretion and can be roughly estimated as:

$$E_{tot} = \frac{f\eta G M_{BH} M_*}{R_t}, \tag{3.1}$$

where R_t is the tidal radius, η is radiative efficiency and f is the fraction of stellar mass accreted. Thus, solving for the BH mass for a Sun-like star with typical $\eta = 0.1$ and $f = 0.5$, we obtain $M_{BH} \approx 5 \times 10^4 M_\odot$. Although the estimated mass may indicate that the X-ray flare could be linked to an off-nuclear TDE around an intermediate mass black hole (IMBH), this calculation provides only a lower limit on mass. A better-sampled X-ray light curve and multiwavelength observations would be required to test this hypothesis to estimate the total energy of the flare and provide better mass constraints.

Recent simulations showed that gravitational recoils or disruption of satellite galaxies caused by recent galaxy mergers could lead to a population of IMBHs out to ≥ 100 kpc (Untzaga et al., 2024). Such off-nuclear transients may represent promising IMBH TDE candidates in the future.

3.6 Discussion

3.6.1 X-ray luminosity function and TDE occurrence rates

The 31 eROSITA candidates presented here form the largest systematically X-ray-selected sample of TDEs to date. The sample can be used to statistically describe the unobscured thermal population of TDEs with a canonical decaying light curve. We use the classical maximum observable volume ($1/V_{max}$) approach (Schmidt, 1968) to estimate the X-ray Luminosity Function (XLF). The calculation is based on the steps detailed in Appendix A.5, which take into account eROSITA's inhomogeneous sensitivity, the selection criteria of the parent catalog eRO-ExTra, spectral shapes, luminosities, and redshifts of the sources. To calculate the XLF, we summed the derived $1/V_{max}$ values of individual TDEs into seven equally spaced luminosity bins between 5×10^{41}ergs^{-1} and 1×10^{45}ergs^{-1}.

The uncertainty contribution for each spec-z source (i) was estimated as $(1/V^2_{max})_i$. For sources with large non-Gaussian photo-z errors (j), a more detailed approach was used to account for their L_X and V_{max} probability distributions. For each photo-z source we performed Monte Carlo sampling for 100 values of $(V_{max})_j$, randomly drafted from the photo-z probability distribution functions. Then, for each bin, we calculated the mean of $\Sigma(1/V_{max})_j$ and its standard deviation $STD_{photo-z}$ across all Monte Carlo realizations. The uncertainty, $\sqrt{STD^2_{photo-z} + \Sigma(1/V_{max})^2_i}$, takes into account the spec-z and photo-z errors of sources in each bin.

As discussed in Sect. 3.3.2, the selection is biased against sources peaking in eRASS1 due to the different typical rise and decay time scales and the primary selection cuts in the eRO-ExTra catalog. This results in potentially missing a significant fraction of sources peaking in eRASS1, which do not decay in six months by a factor of more than four. Therefore, each source in the sample should be carefully weighted to account for this bias. For that, we identified 14/23 TDEs peaking in eRASS2, which would not have been selected if the amplitude and significance cuts were applied to the light curve decay between eRASS2 and eRASS3. To account for this effect, we increased the weight of these 14 sources by a factor of two for the statistical completeness of the XLF. Thus, the final sample includes eight P1 sources with weight w=1, nine P2 sources with w=1 and 14 P2 sources with w=2. Accounting for the introduced weights, this results in 45 sources to be found per year.

Since the photo-z of J0847 is unreliable due to two missing bands, we do not use this source in the computation and implement a correction factor of 45/43 as this source has a double weight. In addition, the function is multiplied by a factor of 2.6 to account for the whole sky area, since the sample was selected from the LS10 covered area (76 % = 1/1.3, see Chapter 2) in the eROSITA_DE hemisphere (1/2). Following the approach presented in Sazonov et al. (2021), we introduced an additional factor of 3 to account for sources missed due to the typical duration of a TDE. Overall, the total correction factor equals 8.16. The final XLF as well as other luminosity functions from Sazonov et al. (2021) and Yao et al. (2023) are presented in Fig. A.1.

Fitting the XLF function with a single power law, we obtain:

$$\frac{\mathrm{dN_{TDE}}}{\mathrm{dlogL_X dVdt}} = \mathrm{B} \times \left(\frac{\mathrm{L_X}}{10^{43}\mathrm{ergs^{-1}}}\right)^{-\beta} \mathrm{Mpc^{-3}yr^{-1}}, \tag{3.2}$$

where $\mathrm{B} = (0.18 \pm 0.05) \times 10^{-7}$ and $\beta = 1.2 \pm 0.08$. The XLF function can be also fit with a double power-law function:

$$\mathrm{f(L)} = \mathrm{A} \times \left(\left(\frac{\mathrm{L}}{\mathrm{L_{br}}}\right)^{-\alpha_1} + \left(\frac{\mathrm{L}}{\mathrm{L_{br}}}\right)^{-\alpha_2}\right)^{-1} \mathrm{Mpc^{-3}yr^{-1}}, \tag{3.3}$$

where $\mathrm{A} = (0.8 \pm 0.2) \times 10^{-7}$, $\alpha_1 = 0.7 \pm 0.1$, and $\alpha_2 = 2.3 \pm 0.4$. Here, we fixed the break luminosity to $\mathrm{L_{br}} = 1 \times 10^{44}\,\mathrm{ergs^{-1}}$. This value corresponds to the Eddington-limiting prediction of an observable change of the XLF (Mummery, 2021), consistent with the significant decrease in detected sources with luminosities above this threshold. The value is also similar to $\mathrm{L_{br}}$ found in previous studies (e.g., Yao et al. 2023; Guolo et al. 2024). The double power-law significantly improves the fit to the data ($\chi^2_{\mathrm{red}} = 0.82$) compared to the single power-law fit ($\chi^2_{\mathrm{red}} = 3.05$).

By integrating the XLF from Eq. 3.3 over the luminosity range $5 \times 10^{41} < \mathrm{L_X} < 1 \times 10^{45}\,\mathrm{ergs^{-1}}$ we can estimate the average TDE volumetric rate to be $(2.3^{+1.2}_{-0.9}) \times 10^{-7}\,\mathrm{Mpc^{-3}yr^{-1}}$. Using an estimation of the total galaxy volume density of $\approx 2 \times 10^{-2}\,\mathrm{Mpc^{-3}}$ (Bell et al., 2003), the TDE rate per year and per galaxy equals to $\approx 1.2 \times 10^{-5}\,\mathrm{yr^{-1}galaxy^{-1}}$.

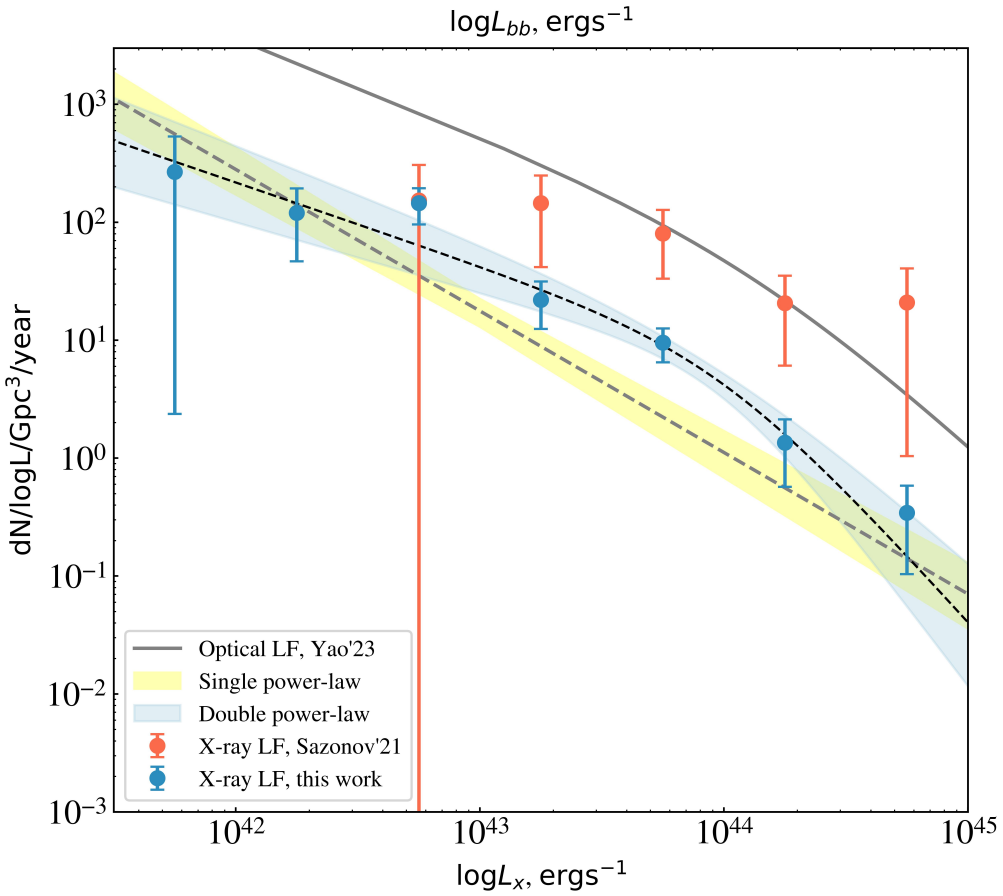

Figure 3.7: TDE XLF function in the 0.2–6.0 keV band. The blue points show the function obtained in this chapter, and the gray dashed line with the yellow region denotes its best fit with a power law (see Eq.3.2), and the blue region with a black dashed line shows the best fit with a double power law (see Eq.3.3). The orange points show the TDE XLF for eROSITA_RU from Sazonov et al. (2021). The gray solid line shows the double power law fit of a TDE optical luminosity function from Yao et al. (2023); its corresponding blackbody optical/UV luminosity ($\log L_{bb}$) values are given on the top x-axis, which differs from the bottom axis of the plot.

Table 3.7: Compilation of computed TDE rates. The top section shows the summary of X-ray TDE rates with step-by-step growing samples over two decades. The bottom section shows examples of recent TDE rates computed in other bands. The values are presented for summary purposes, with the caveat that different luminosity thresholds and selection criteria must be considered before making any direct comparison.

Band	Rate $[\mathrm{yr}^{-1}\mathrm{gal}^{-1}]$	Reference	Sample size
X-ray	9×10^{-6}	Donley et al. (2002)	3
X-ray	2×10^{-4}	Esquej et al. (2008)	2
X-ray	3×10^{-5}	Khabibullin & Sazonov (2014)	4
X-ray	1×10^{-5}	Sazonov et al. (2021)	13
X-ray	1.2×10^{-5}	This work	31
Optical	3.2×10^{-5}	Yao et al. (2023)	33
Mid-IR	2×10^{-5}	Masterson et al. (2024)	12

Pre-eROSITA X-ray TDE rates were derived from ROSAT and XMM-Newton observations (see Table 3.7). The first XLF based on eROSITA was presented in Sazonov et al. (2021) using 13 sources from eROSITA_RU. This sample included eRASS2 sources out to $z < 0.6$ with an amplitude larger than 10 and without AGN signatures, and covered the brighter end of the luminosity function ($\mathrm{L_X} = 10^{42.5} - 10^{45}\mathrm{ergs}^{-1}$). Since we applied a lower amplitude cut in our approach, our XLF spans over a lower range of luminositites down to 5×10^{41} erg s^{-1}, and lets up probe the fainter end of the TDE population. Whereas both functions are consistent in the mid-luminosity regime ($\approx 10^{43}$ erg s^{-1}), the slopes clearly diverge at higher luminosities. The discrepancy is due to different selection criteria used in defining the samples. The TDE sample used in this chapter contains purely canonical TDEs with decaying or flaring light curves, whereas TDEs in Sazonov et al. (2021) include also sources ($\approx 30\%$) brightening at later eRASSes. The exclusion of these sources from the latter sample makes the resulting function less steep and comparable with our XLF. Also selecting sources with amplitude larger than 10 may contribute to finding a flatter slope. The TDE rate of $(2.1 \pm 0.1) \times 10^{-7}\mathrm{Mpc}^{-3}\mathrm{year}^{-1}$ presented in Sazonov et al. (2021) is comparable with the one in this chapter. While the XLF from Sazonov et al. (2021) is slightly higher than that derived in this chapter (see Fig. A.1), the inclusion of a broader X-ray luminosity range leads to a similar integrated TDE rate.

The slopes of our XLF broken double power-law fit are consistent with those obtained for optically-selected TDE samples. In the X-ray sample of optically selected TDEs, Guolo et al. (2024) found $\alpha_{1,\mathrm{Guolo}} = 0.96^{+0.21}_{-0.24}$ and $\alpha_{2,\mathrm{Guolo}} = 2.65^{+1.1}_{-0.9}$, which agree with values presented in this study within the error bars. The slope values derived for the optical TDE luminosity function from Yao et al. (2023), $\alpha_{1,\mathrm{Yao}} = 0.84^{+0.30}_{-0.36}$ and $\alpha_{2,\mathrm{Yao}} = 1.93^{+0.32}_{-0.27}$, also align with our results. In addition, the single power law fit of TDE XLF reproduced using first-principles relativistic disk theoretical approach in Mummery & van Velzen (2025) corroborates our findings. There the inferred XLF is scaled with luminosity as $\propto \mathrm{L_X^{-1.15}}$, which is very similar to results obtained in our single power-law fit.

The normalization of our eROSITA TDE XLF is about a factor of ten lower (see Fig. A.1) than that of optical TDEs from Yao et al. (2023). Here, it is important to note that X-ray and optical emissions of TDEs are generated by different physical processes (see Chapter 1.3). Although the shapes of the luminosity functions are similar, the X-axes are different for both functions and therefore, they cannot be directly compared. Re-normalization of the two functions is challenging: it was demonstrated that for different TDE candidates, the difference between optical/UV and X-ray luminosities can lay within a very broad range of values with $L_{BB}/L_X \in (0.5, 3000)$ at early times and $L_{BB}/L_X \in (0.5, 10)$ at late times (Guolo et al., 2024). This results in the optical TDE rate being slightly higher than the X-ray rate. The similar rate difference was also found in previous X-ray studies (see Table 3.7). The possible reasons for smaller X-ray rates comparing to the theoretical estimates and missing a fainter TDE population might be: 1) not including all possible X-ray TDE types in our canonical sample (see Sect. 3.6.4), 2) missing some X-ray TDEs due to obscuration or geometry effects (see Sect. 3.6.3), 3) sensitivity limitations of current X-ray all-sky surveys, leading to not detecting fainter events, or 4) primary selection criteria of the eRO-ExTra catalog not picking up events with $A < 4$. These factors should be explored in the future to confirm if optically and X-ray selected populations of TDEs are indeed drawn from the same BH mass distribution (Mummery & van Velzen, 2025).

3.6.2 Multiwavelength flares of TDE candidates

The presented TDE sample shows a wide variety of multiwavelength behaviors in the X-ray, optical, mid-IR, and radio bands. The diversity spans from TDE candidates detected only in X-rays to sources emitting in all four bands. The summary of the TDE multiwavelength flares is provided in Table 3.8, and the multiwavelength light curves are shown in Appendix B.3.

Mid-IR flares were detected both before and around the time of the X-ray peak. E.g., in J0644 and J2108, mid-IR flares were found $\approx$ 1500 and $\approx$ 1000 d before the X-ray detection. Also, in J0823, the mid-IR emission developed more than a year before the X-ray flare, consistent with the early optical peak. A detailed analysis of the multiwavelength properties of J0823 is provided in Malyali et al. (2021). J0439-65 and J2344-35 (more details in Homan et al. 2023) peaked in the X-rays and mid-IR around the same time. However, the precise timing cannot be constrained, given the sparsity of the eROSITA and NEOWISE data. Similarly, optical outbursts come noticeably earlier (e.g., J0318, J1102) or quasi-simultaneously (e.g., J0439) compared to X-ray peaks. Further discussion on the origin of mid-IR and optical flares in connection to X-ray flares is provided in Sect. 3.6.3.

3.6.3 Driving mechanisms of multiwavelength emission

The order of the multiwavelength flares, their realtive time lag or the total absence of observational features in certain bands have made it challenging to distinguish or unify X-ray, optical and IR TDEs. Currently, two leading models are used explain the observed multiwavelength TDE scenarios.

Table 3.8: Summary of peak times for TDE candidates showing multiwavelength flares. The Δt in days is to the time of the brightest detection in the X-ray band. P1 group includes sources with a single decline light curve peaking in eRASS1, and P2 includes those with a flare light curve peaking in eRASS2.

Name	LC type	Δt_{mid-IR} [days]	$\Delta t_{optical}$ [days]	Δt_{radio} [days]
J0141	P1	+175	-	-
J0318	P2	-	-631	-
J0439	P1	+191	+145	-
J0608	P2	+146	-	-
J0615	P2	-12	-	-
J0644	P1	-1475	-	-
J0744	P2	-	-17	-
J0823	P2	-2	-615	+79
J0847	P2	+177	-	-
J1102	P1	-	-381	-
J1305	P2	-	-	-55
J1421	P2	-	-423	-
J1436	P1	+369	-	-
J1646	P2	-	-	-181
J2108	P2	-920	-	-539
J2344	P2	+185	-45	+129

Firstly, the obscuration model states that a newly formed TDE accretion disk is surrounded by an optically thick envelope formed from stellar debris. The envelope can reprocess soft X-rays from accretion onto the BH and produce optical and IR emission (Roth et al., 2016; Dai et al., 2018). Particularly, the reprocessing layer can appear from winds from the accretion disk (Strubbe & Quataert, 2009; Lodato & Rossi, 2010; Miller, 2015) or stellar debris remaining in the vicinity of the black hole (Loeb & Ulmer, 1997; Guillochon et al., 2014; Metzger & Stone, 2016). For X-ray fluxes high enough to sufficiently ionize the surrounding envelopes, the intrinsic X-ray emission can be observed simultaneously with the optical emission. This pattern can be seen in sources J2344, and J0439, where the X-ray and optical flares occured quasi-simultaneously within the observationally available cadence. On the other hand, a critically low intrinsic X-ray flux may lead X-rays to be completely absorbed. Indeed, numerous studies have identified optical TDEs without any X-ray signatures (e.g., van Velzen et al. 2020). Scenarios between these two extremes (due to lack of X-ray emission or envelope thickness) may lead to delayed observed X-ray emission, for example, as we see in sources J1102 and J0318. Similarly, the mid-IR emission may precede X-ray emission due to dust reprocessing in the galaxy center - once the envelope becomes sufficiently ionised and/or the optical depth decreases, the intrinsic X-ray emission can escape and become observable, giving rise to a delayed X-ray emission relative to the IR event (see more details in Chapter 1.3.4).

The geometry of the surrounding envelope may also impact the observable properties of TDEs (Guillochon et al., 2014; Dai et al., 2018; Parkinson et al., 2022). Depending on

the viewing angle and the thickness of the obscuring material, we may either directly see the X-ray emission from the galactic center, or have a partially or fully obstructed view, looking perpendicularly through the envelope. Several factors, e.g., critical absorption or orientation of the surrounding envelope, can lead to extreme cases of X-ray non-detections. Whereas we still would detect TDE candidates in optical or IR bands, where the emission originates from reprocessing, this observational restriction can lead to underestimating TDE rates in X-rays.

Alternatively, TDEs can be described by the stream-stream collision model (Piran et al., 2015; Jiang et al., 2016; Svirski et al., 2017). In this scenario, the optical and X-ray photons originate in different locations. While X-rays appear in the case of efficient circularization of stellar debris and accretion onto the black hole, optical emission can be produced earlier by shocks of stellar debris streams at larger distances. The effect can be even more prominent in the presence of magnetic stresses acting on the streams and strengthening self-crossing shocks (Bonnerot et al., 2017). The stream-stream collision model describes TDEs with optical emission significantly preceding X-ray emission, by explaining delayed X-ray emission with inefficient circularization of the debris (Gezari et al., 2017; Liu et al., 2022b). Some TDE candidates are better described with a stream-stream collision model. In particular, in the case of the multipeak optical light curve of J0823, the first peak was explained by a stream self-intersection, and the second peak was described by an accretion disk formation (Malyali et al., 2021; Chen et al., 2022).

In the presented sample, only a relatively small fraction of X-ray TDEs is detected in either mid-IR ($\approx 30\%$), optical ($\approx 20\%$), or both ($\approx 10\%$). The fractions should be considered only as lower limits due to significant observational limitations (see Sect. 3.4.2). For comparison, similar fractions were reported in the mid-IR population study by Masterson et al. (2024) with $\approx 30\%$ of sources detected in X-rays, and an optical population study by Guolo et al. (2024), in which $\approx 40\%$ of optically selected TDEs were detected in X-rays. While these fractions are wrought with uncertainties from differences in multiwavelength observing strategies, they can help elucidate the geometry and physics of the underlying accretion flow.

3.6.4 Non-canonical X-ray TDEs to be found

Whereas this work focused on the selection of canonical TDEs (with a soft spectrum, a single decline light curve and a non-AGN quiescent host galaxy), future studies will explore more complex scnearios, e.g., using the eRO-ExTra catalog or other surveys. Considering the non-canonical population will surely impact the rate and XLF prediction and help with the understanding of the unified picture of TDEs.

Firstly, recent discoveries (e.g., RX J133157.6-324319.7 Malyali et al. 2023a; AT2018fyk Wevers et al. 2023; eRASSt J045650.3-203750 Liu et al. 2023, 2024) showed that X-ray TDEs can be repeating and pTDEs, namely, in which a star loses only a fraction of its mass and survives its initial encounter with the BH, afterwards proceeding for another cycle of disruption during the next orbital pass. The expectation of an impact on the X-ray TDE rate is strengthened by the fact that the pTDE rate is predicted to be larger

or comparable to full TDEs (e.g., Bortolas et al. 2023) since their encounter cross-sections are larger. The eRO-ExTra catalog contains potential pTDE candidates: 13 sources with a light curve class other and one source with a brightening light curve have soft spectra at peak with $\Gamma > 3$.

Secondly, the selection against sources with hard spectra may lead to missing some TDEs. For example, the accretion onto the SMBH during a TDE can lead to the formation of a corona (Guolo et al., 2024; Liu et al., 2023) while the TDE is still X-ray bright. Due to the time sampling of eROSITA observations (one visit per 6 months), such events may be detected only in the phase when the source is X-ray hard. Other TDE subclasses such as jetted TDEs (Burrows et al., 2011; Saxton et al., 2012a; Cenko et al., 2012) also were found to have X-ray spectra at peak with $\Gamma < 2$. In addition, intrinsically absorbed sources may also appear harder when modeled with a simple power law. The eRO-ExTra catalog contains 146 sources with $\Gamma < 3$ and flaring or declining light curves. Further investigation is needed to determine whether some of them are missed TDE candidates. Due to such factors as sparse eROSITA coverage and unknown/low-luminosity AGN contamination, it is challenging to perform a systematic selection of a clean sample of non-canonical TDEs from eRO-ExTra. However, additional multiwavelength follow-up may help to confirm the TDE origin of individual events.

Finally, TDEs are expected to occur not only in quiescent galaxies but also in AGN at higher rates (Karas & Šubr, 2007). However, it is challenging to identify a TDE in an AGN due to its low-contrast emission in comparison with the bright accretion disc, and long-lived AGN variability caused by instabilities in the accretion flow (Komossa, 2015). Several X-ray and UV outbursts in AGN were considered TDE candidates (e.g., Ricci et al. 2020).

3.7 Summary

We have presented a sample of canonical TDE candidates discovered in the eROSITA_DE sky during its first and second all sky surveys (Dec. 2019 - Dec. 2020). This is the largest systematically X-ray-selected sample of TDEs to date, which includes 31 TDE candidates. The sources are selected from the catalog of extragalactic non-AGN X-ray transients and variables eRO-ExTra (see Chapter 2), out to $z < 0.34$, with a single decline or a flare X-ray lighcurve, a soft X-ray spectrum with $\Gamma > 3$ and no known long-term variability or AGN association. The sample includes 30 canonical TDEs and one off-nuclear TDE candidate. All sources remained X-ray soft throughout the evolution, except for J0439, in which the observed spectral hardening might be associated with the formation of a hot corona.

We computed the TDE XLF, which is well fit with a double power law with where we fixed the luminosity break fixed at $10^{44}\mathrm{ergs}^{-1}$, a value motivated by the Eddington-limiting prediction for an observable change in the TDE luminosity function (Mummery, 2021). From this we inferred a TDE rate of $\approx 1.2 \times 10^{-5}\,\mathrm{yr}^{-1}\mathrm{galaxy}^{-1}$, comparable to the estimate for the previous eROSITA X-ray TDE sample of Sazonov et al. (2021), and lower than the optical rate from Yao et al. (2023). The presented rate of X-ray-selected

canonical TDEs does not consider missed events due to obscuration or geometry effects or non-standard behavior (e.g., repeated or pTDEs), which may explain the discrepancy. The SED modeling of host galaxies revealed an overdensity in the green valley, as found in previous TDE studies. The BH masses of the canonical TDEs in the sample span from $\log(M_{BH}/M_{\odot})$=5.4 to 7.6.

A fraction of TDEs in the sample showed multiwavelength variability in the optical (20%), mid-IR (30%) and radio (15%) bands, with optical and mid-IR outbursts either preceding or being quasi-simultaneous with the X-ray peak. We discussed the origin of multiwavelength flares in the context of the obscuring envelope model and the stream-stream collision model. Both scenarios can be used equally well to describe the observational data.

The exploration of TDEs with eROSITA should be continued to include events discovered in eRASS3–eRASS5. Furthermore, future studies should include non-canonical TDEs (e.g., from the eRO-ExTra catalog), which will improve the estimation of XLF and TDE rates, and shed more light on understanding TDE host population and multiwavelength properties. The methodology of the TDE identification presented in this chapter may also be applied in new X-ray surveys such as Einstein Probe, which is expected to detect several tens to hundreds of events per year (Yuan et al., 2016, 2022).

Chapter 4

eRASSt J093641.9+111347: a TDE in an FRII Radio Galaxy?

The unique sensitivity and all-sky view of eROSITA can reveal a wide range of exotic extra-galactic transients. Following the population study of canonical X-ray-selected tidal disruption events (TDEs), this chapter focuses on one particularly unusual TDE candidate identified in the third eROSITA all-sky survey (eRASS3). While non-canonical TDEs are becoming increasingly common (e.g., see Sect. 1.3.5), their systematic analysis remains challenging due to their diverse multiwavelength properties. Investigating individual, unconventional TDEs offers valuable insights into the underlying physics, helping to expand our understanding of the broader TDE population. In this chapter, I present the analysis of a TDE candidate in a Fanaroff-Riley Type II (FRII) radio galaxy that hosts a supermassive black hole whose mass likely exceeds the Hill's mass.

4.1 Introduction

With the population of TDEs actively growing (e.g., see Sect. 1.3.2,1.3.5,1.3.7), the typical environments of their host galaxies remain an open question. The host galaxy distribution of TDEs spans a wide range of galaxy types — from early-type, quiescent galaxies (e.g., French et al. 2020b) to late-type, star-forming galaxies (e.g., Bloom et al. 2011). Observations have revealed a distinct population of TDEs in galaxies located within the so-called "green valley" (e.g., Hammerstein et al. 2021; Wang et al. 2023; Yao et al. 2023), a region of post-starbursts galaxies in the color-magnitude diagram between the blue cloud of star-forming galaxies and the red sequence of quiescent systems (Arcavi et al., 2014; French et al., 2016). The green valley overdensity was also found for canonical X-ray TDEs in Chapter 3. On the other hand, recent findings have also highlighted the occurrence of TDEs in more unusual host galaxies, such as active Seyfert galaxies (e.g., Blanchard et al. 2017) or galaxies ongoing a major starburst (Tadhunter et al., 2017). In addition, a hot topic in the field remains the search for off-nuclear TDEs (e.g., Yao et al. 2025), potentially around intermediate-mass black holes (IMBHs) wandering in the galaxy outskirts.

Typically, TDEs are identified in quiescent galaxies (see Sect. 1.3.2), as detecting them in active galaxies is more challenging due to the high levels of background emission from the active nucleus (see Sec 1.2.2), which can obscure the transient signal (Gezari, 2021). Among the most unusual hosts for TDEs would be Fanaroff-Riley Type II (FRII) radio galaxies (Fanaroff & Riley, 1974), characterized by their powerful, extended radio lobes and typically associated with large elliptical galaxies. Such systems generally harbour very massive SMBHs (e.g., Kozieł-Wierzbowska & Stasińska 2011), often approaching or exceeding the Hills mass for solar-type stars (see Sect. 1.3.1), making them less likely hosts of observable TDEs. Low-excitation radio galaxies (LERGs; Laing et al. 1994) are a subset of these galaxies, known for their weak optical and X-ray emission, which suggest the presence of a radiatively inefficient active galactic nucleus (AGN). Because of low levels of intrinsic X-ray emission, unlike more typical AGN, the detection of an X-ray TDE in a LERG might be possible due to reduced background noise from the nucleus.

In this chapter, I report on the discovery and a set of multiwavelength observations of the TDE candidate eRASSt J093641.9+111347 (hereafter, J0936), associated with an FRII radio galaxy at $z = 0.127$. The chapter is structured as follows: In Sect. 4.2, I report on the X-ray discovery of J0936 with eROSITA and follow-up observations with *NICER*, *Chandra* and *Swift*. I present the host galaxy properties in Sect. 4.3, and summarize the multiwavelength follow-up of the transient in Sect. 4.4. I discuss the possible origin of the transient in Sect. 4.5, by analyzing X-ray properties of the FRII galaxy population and testing the TDE hypothesis. Finally, I conclude with a summary in Sect. 4.6.

4.2 X-ray observations

4.2.1 eROSITA discovery

J0936 was first detected by the eROSITA source detection pipeline as a new ultra-soft X-ray source in eRASS3 observations performed on 13th May 2021, located at RA(J2000) = 09:36:41.99, Dec(J2000) = +11:13:50.96 with an estimated positional uncertainty of ≈ 5" radius (including systematics). The source detection pipeline was developed by the MPE team for the systematic search of new X-ray sources not detected in earlier eRASS[1] scans, while eROSITA was still operating in its regular survey mode. First, all source catalogues updated since the previous check were stacked into a single merged catalogue, with duplicate sources in overlapping regions between neighboring sky tiles removed. Each week, newly obtained eROSITA scans were compared against this merged catalogue to identify new sources. Transients were then flagged based on whether they had previous detections by eROSITA. Counterparts of newly identified transients were examined to remove sources associated with galaxy nuclei that showed no prior indication of hosting an AGN (see Chapter 3 for the selection criteria of extragalactic non-AGN transients). Since

[1]eROSITA all-sky survey (see Sect. 1.1)

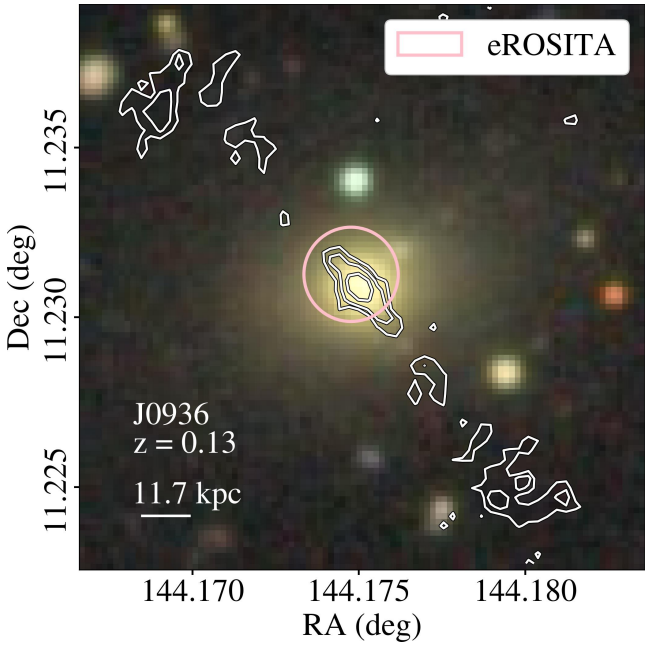

Figure 4.1: LS10 image of the host galaxy SDSS J093641.99+111350.9, coincident with the X-ray position of J0936. The pink circle (radius 5") indicates the eROSITA positional uncertainty. White VLASS radio contours at 2σ, 3σ, and 5σ highlight the FRII double-lobe morphology.

J0936 was not detected by eROSITA before eRASS3[2], the pipeline flagged it as a potential candidate.

The discovery was initially published in an Astronomer's Telegram (No. 14668; Grotova et al. 2021). The eROSITA position coincides with the center of SDSS J093641.99+111350.9, a galaxy with a spectroscopic redshift of $z = 0.127$ (see Fig. 4.1), suggesting J0936 to be a nuclear transient. The 0.2–2.3 keV eRASS3 flux of the transient was $\approx 8.7 \times 10^{-13}$ erg cm^{-2} s^{-1}, which is a factor of 13 brighter than the 3σ upper limit of 6.6×10^{-14} erg cm^{-2} s^{-1} in the same band, derived from earlier observations of the same region in eRASS1 (May 2020) and eRASS2 (November 2020). J0936 was also later detected by eROSITA during eRASS4 on November 13th, 2021. The eRASS1 – eRASS4 X-ray images of J0936 are shown in Fig. 4.2, highlighting the notable appearance of the bright transient.

4.2.2 X-ray follow-up

The nuclear transient search pipeline allowed for the prompt follow-up of J0936 by the MPE team on a timescale of weeks. X-ray observations by *NICER* and *Swift*, described further in this section, helped us better constrain the X-ray light curve evolution and

[2]As it was detected in eRASS3, the source is not included in the systematic nuclear transient and TDE studies presented in Chapters 2 and 3.

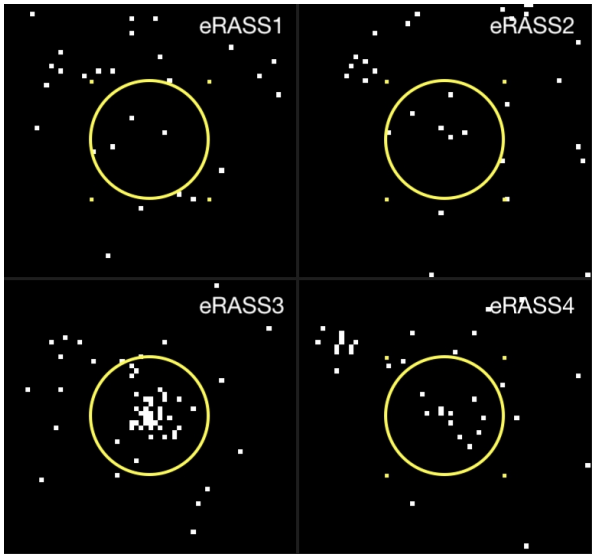

Figure 4.2: eROSITA X-ray images of the sky at the position of J0936 in eRASS1-4. The source was not detected in eRASS1 and eRASS2, brightened significantly by eRASS3, and subsequently faded again in eRASS4. The yellow circles represent the eROSITA position with a 5" uncertainty radius. Each white dot corresponds to a single detected X-ray photon, including background events.

provided important probes of the transient energetics. The full log of X-ray observations is shown in Table 4.1.

Table 4.1: Log of X-ray observations of J0936, along with their 0.2-2.3 keV fluxes and best fit kT values. For eROSITA, the mid-date of the coverage in each eRASS is given.

Date	Instrument	ObsID	Exposure [s]	flux, 0.2-2.3 keV $[10^{-13} \times \mathrm{erg\,cm^{-2}\,s^{-1}}]$	kT [eV]
13.05.2021	eROSITA	eRASS3	132.6	8.7±1.5	70±6
26.05.2021	NICER	4202180101	2829	15.0±1.5	40±2
02.06.2021	Swift/XRT	15765-1	1630	1.8±0.8	110±10
09.06.2021	Swift/XRT	15765-2	1920	2.1±0.8	142±20
06.10.2021	Swift/XRT	16375	2850	5.0±0.3	91±6
11.11.2021	Chandra/HRC-I	26189	3012	1.9±0.1	-
13.11.2021	eROSITA	eRASS4	142.7	3.0±0.9	60±12
15.10.2022	Swift/XRT	17964	2020	0.3±0.2	270±115

Follow-up DDT observations with *NICER* (PI: Z. Liu) were performed on 26–27 May 2021, shortly after the eRASS3 detection. Afterwards, several follow-up observations were performed with *Swift* (PI: I. Grotova) until the source went back to its pre-flare flux level. Another *Swift* observation was made after the transient rebrightening in eRASS4. The

Swift/XRT observations were performed in photon counting mode. Observations with the Ultraviolet and Optical Telescope (UVOT; Roming et al. 2005) were obtained simultaneously with the XRT observations in UVW1 and UVW2 filters, and did not show any signs of variability. A follow-up *Chandra* observation (PI: A. Malyali) was performed on 10 November 2021 using the HRC-I instrument to better constrain the X-ray position of the transient.

4.2.3 X-ray data reduction and spectral fitting

For the eRASS3 and eRASS4 observations of J0936, spectra were extracted using the `eSASS` task `SRCTOOL` in AUTO mode with circular source and annular background regions centered on the X-ray positions. The eROSITA spectra were analyzed using the Bayesian X-ray Analysis software (BXA; Buchner et al., 2014). The spectra were fitted unbinned using the C-statistic (Cash, 1976), and the eROSITA background was modeled using the principal component analysis (PCA) technique (Simmonds et al., 2018; Liu et al., 2022a). The source and background eROSITA spectra were jointly fitted. The eRASS3 spectrum (net count rate $0.3\mathrm{cts\,s^{-1}}$) is best fit by an absorbed blackbody model `tbabs*bbody` with $\mathrm{kT} = 70 \pm 6\mathrm{eV}$ and $\mathrm{N_H} = (1.6 \pm 0.5) \times 10^{20}\mathrm{cm^{-2}}$ (see Fig. 4.3). The inferred $\mathrm{N_H}$ is consistent with the Galactic foreground value along the line of sight. The same model with fixed Galactic column density was used for all further observations. An alternative fit, with a slightly higher C-statistic per bin, was performed using an absorbed power-law model `tbabs*pow`, yielding a photon index of $\Gamma = 5.2 \pm 0.4$. The very soft spectrum, with $\Gamma > 3$, is consistent with the canonical TDE selection criterion (see Chapter 3).

The *Swift*/XRT data were reduced using the `xrtpipeline`. Spectra for each epoch were extracted using the `xrtproducts` task. The *NICER* data were analyzed using HEASoft (version `6.34`) along with the *NICER* data analysis software (version `13`) and calibration files (version `20240206`). The `nicerl2` task was used to produce cleaned X-ray events, during which events having an overshoot (high-energy particle events[3]) greater than 1.5 or an undershoot (detector reset due to optical loading[4]) exceeding 300 were excluded. Subsequently, the `nicerl3-spec` task was utilized to generate the X-ray spectrum for the *NICER* observation (Observation ID: 4202180101). The X-ray spectrum was rebinned to ensure a minimum of one count per bin. I implemented the SCORPEON[5] model to create a background model for the *NICER* observation. Additionally, the `nicerarf` and `nicerrmf` tasks were used to generate the response matrix and ancillary file. *Swift* and *NICER* spectra were modeled with `XSPEC` software (Arnaud, 1996) using the C-statistic. The summary of the modeling results is provided in Table 4.1.

The *Chandra* source detection was performed with the `wavdetect` command in `Ciao` using the reduced data downloaded from the *Chandra* X-ray Center archive[6] with the binning parameter set to 4, energy = 1.4967 and ecf = 0.393. Overall, six sources were detected

[3] `https://heasarc.gsfc.nasa.gov/docs/nicer/analysis_threads/overshoot-intro/`

[4] `https://heasarc.gsfc.nasa.gov/docs/nicer/analysis_threads/undershoot-intro/`

[5] `https://heasarc.gsfc.nasa.gov/docs/nicer/analysis_threads/scorpeon-overview/`

[6] `https://cxc.harvard.edu/cgi-bin/op/op_status_table.cgi?field=ObsId&id=26189&out=long&tab_del=HTML`

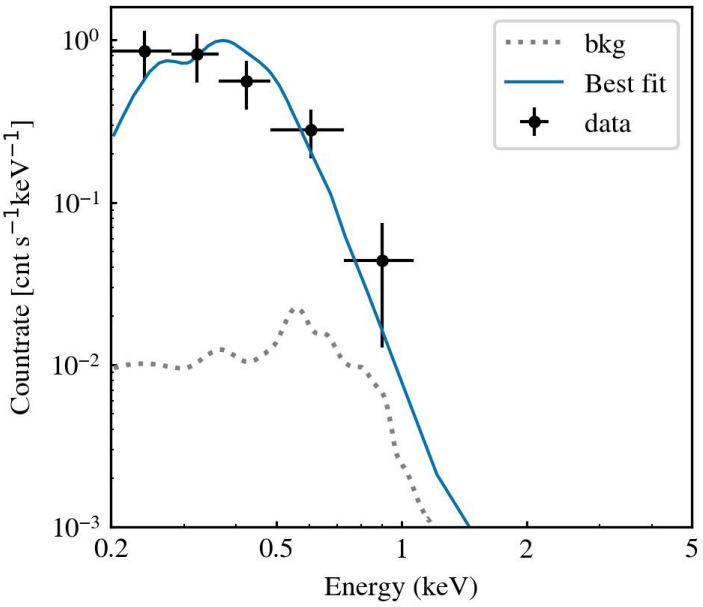

Figure 4.3: BXA fit to the eRASS3 data of J0936. Black markers are the observed data (binned for illustration purposes only). The blue line shows the best-fit convolved model for an absorbed blackbody. The background model is shown as a black dotted line. The best fit eRASS3 kT value is 70 ± 6 eV.

Table 4.2: Sources detected during the *Chandra*/HRC-I follow-up (ObsID 26189). The projected physical offset from the LS10 coordinates of the J0936 host galaxy is calculated assuming a redshift of z = 0.127.

Source	RA [deg]	Dec [deg]	Offset [kpc]
1 (J0936)	144.174966	11.230681	1.17
2	144.197233	11.247635	231.12
3	144.157816	11.263417	308.19
4	144.076701	11.295702	975.76
5	144.275987	11.091878	1432.36
6	144.304804	11.485498	2390.32

in the observed field (see Table 4.2). Based on 56 detected source counts, the *Chandra* position of J0936 was determined to be RA = 144.174966 deg and Dec = 11.230681 deg with the positional error of 0.65" dominated by 1σ systematic uncertainties[7]. The *Chandra* detection, along with the LS10 image of the host galaxy overlaid with the *Chandra* source position and uncertainty, are shown in Fig. 4.4. The flux was extracted using the `srcflux`

[7] `https://cxc.harvard.edu/cal/ASPECT/celmon/`

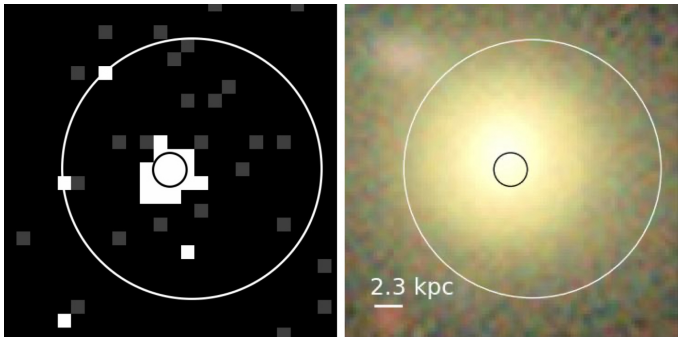

Figure 4.4: Left: *Chandra* X-ray image of J0936. Right: LS10 optical image of the J0936 host galaxy. In both images, the black circle marks the *Chandra* detection of the transient with 0.65" uncertainty, and the white circle indicates the eROSITA detection with 5" uncertainty.

command at the detection position, assuming an absorbed power-law model `tbabs*pow` with the same fixed N_H and $\Gamma = 3$ — the value closest to the Γ of the eRASS4 detection performed only three days earlier. The Γ estimate for eRASS4 was obtained using the same modeling procedure as described in Sect. 2.3.2.

4.2.4 X-ray light curve evolution

The X-ray light curve of J0936 covering ≈ 600 days is shown in the top panel of Fig. 4.5. After the initial discovery in eRASS3, the source reached its peak flux of 1.5×10^{-12}erg cm^{-2} s^{-1} as observed with *NICER* on 26.05.2021, corresponding to a luminosity of $L_{peak} = 5.3 \times 10^{43}$ erg s^{-1} and amplitude > 23 comparing with its eRASS1+2 upper limit. After the peak, the source has significantly faded by a factor of ten within a week. Following the first flare, a moderate re-brightening in X-rays was detected in eRASS4 half a year later. Later, the source was detected below the pre-flare upper limits.

The blackbody temperature of J0936 varies from ≈ 40 keV in its brightest peak state to ≈ 150 keV at the light curve decline (see the bottom panel of Fig. 4.5). The eRASS4 re-brightening is accompanied by a spectral softening as well. Overall, as can be seen in Fig. 4.6, the data show an apparent anti-correlation between flux and kT, with lower temperatures observed at higher fluxes.

4.3 Host galaxy properties

4.3.1 Multiwavelength properties

As illustrated in Fig. 4.1, the host galaxy of J0936 is an elliptical galaxy at z=0.127. The archival SDSS optical spectrum (see Fig. 4.7, binned to the SDSS spectral resolution[8])

[8] R ≈ 2000, `https://classic.sdss.org/dr7/instruments/spectrographs/`

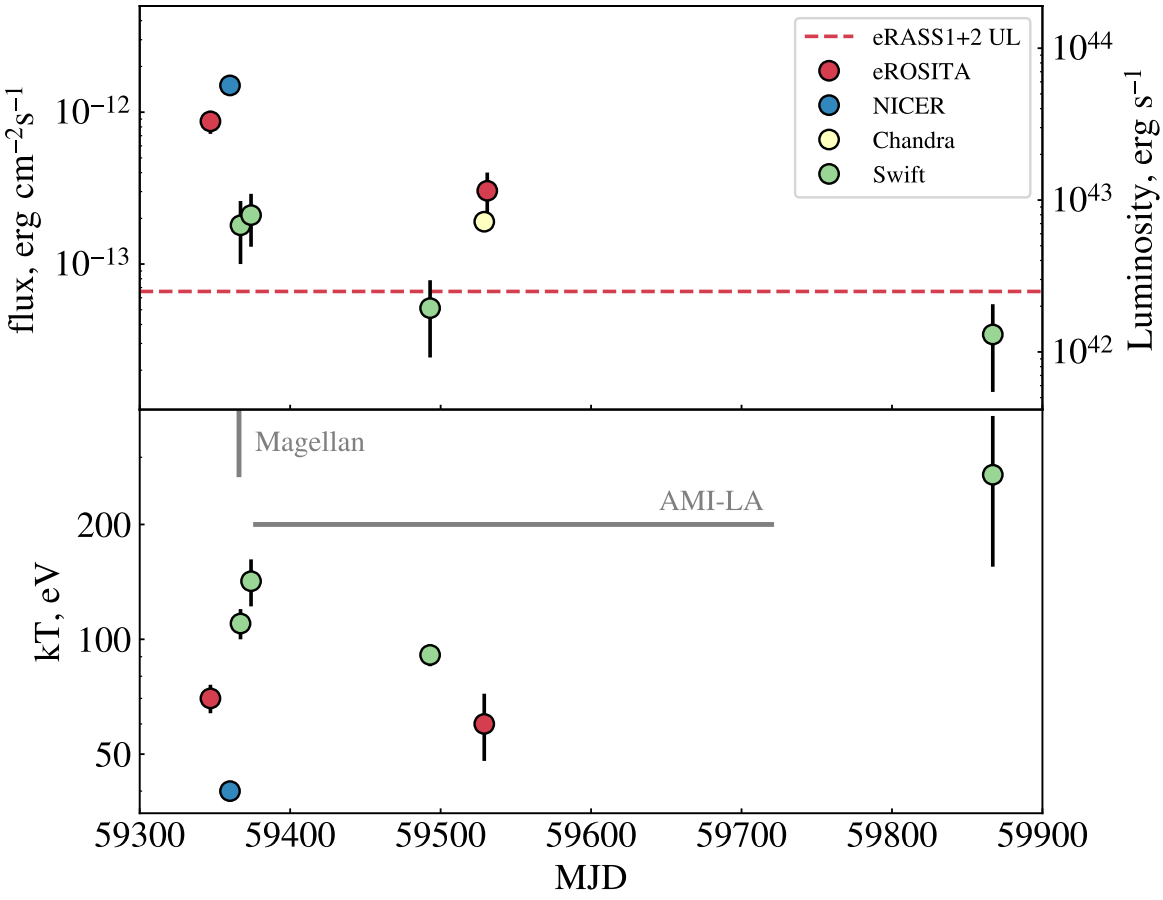

Figure 4.5: Top: X-ray light curve of J0936 in the 0.2–2.3 keV band, showing a flare with a later re-brightening. The red points show the eROSITA detections, and the red dashed line corresponds to the eRASS1+2 3σ upper limit. Blue, green and yellow points show *NICER*, *Swift* and *Chandra* detections, respectively. Bottom: Blackbody temperature evolution. The *Chandra* observation is omitted as HRC-I does not provide spectral information. The gray lines denote times of radio and optical follow up observations (more details in Sect. 4.4).

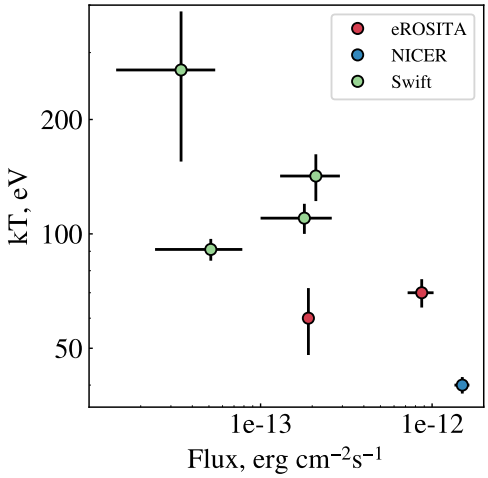

Figure 4.6: Blackbody temperature (kT) versus X-ray flux in the 0.2–2 keV band for J0936. Measurements correspond to the epochs shown in the X-ray light curve in Fig. 4.5 and Table 4.3.

is consistent with a quiescent galaxy, showing no emission lines and no signature of nuclear activity. Similarly, the WISE color of the galaxy (WISEA J093642.00+111351.0) of $W1 - W2 = 0.15$ mag is consistent with a quiescent host rather than an actively accreting AGN (e.g., Stern et al. 2012).

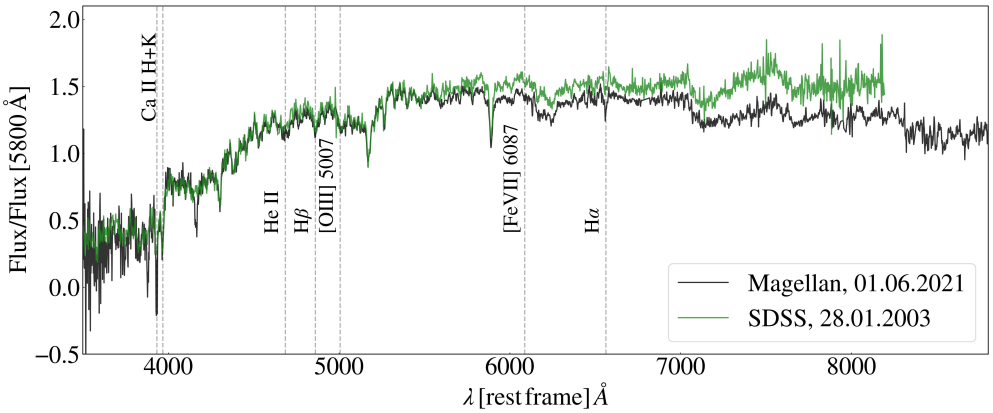

Figure 4.7: Optical spectra of the host galaxy SDSS J093641.99+111350.9. The archival SDSS spectrum taken in 2003 is shown in green, while the follow-up Magellan spectrum, obtained shortly after the X-ray flare in 2021, is shown in black. Both spectra are consistent and do not show signs of optical variability. The discrepancies at long wavelengths are likely due to calibration and/or different extraction regions. A narrow, single-pixel spike near [OIII] is present in the SDSS spectrum; it is likely a noise artifact (cosmic ray or sky-subtraction residual) and is not seen in the higher-resolution Magellan spectrum, so I do not consider it astrophysical.

On the other hand, the galaxy was classified as an FRII radio galaxy in van Velzen et al. (2015) based on its strong radio symmetrical jets (see radio contours in Fig. 4.1). Given the combination of its radio properties and the optical spectrum without emission lines, the source is classified as a Low-Excitation Radio Galaxy (LERG) in Best & Heckman (2012). LERGs are thought to host relatively inactive AGNs, with low accretion rates compared to higher-excitation systems such as Seyfert galaxies. Along with the optical spectrum consistent with that of a quiescent galaxy, they also usually have non-AGN WISE colors ($W1 - W2 < 0.5$mag, e.g., Grandi et al. 2021; Mingo et al. 2022). In the X-ray regime, LERGs typically show faint, non-thermal emission from their jets and may exhibit a hard X-ray spectrum (e.g., Evans et al. 2006). Indeed, the host galaxy of J0936 was undetected in the archival observations performed by ROSAT in 1990 with an upper limit of 1.6×10^{-13}erg cm^{-2}s^{-1} in 0.2–2.0 keV, and an even tighter eRASS1/2 upper limit of 6.6×10^{-14} erg cm^{-2} s^{-1} in 0.2–2.3 keV, corresponding to an X-ray luminosity limit of $L_{\rm X} \lesssim 2.8 \times 10^{42}$ erg s^{-1} (assuming a photon index $\Gamma = 2$, standard for the eROSITA catalogs; Merloni et al. 2024).

4.3.2 X-ray transient location within the host galaxy

The position of the X-ray transient was examined in the context of the host galaxy and its radio morphology. The eROSITA detection is consistent with the central region of the FRII radio structure, which is dominated by the core and the base of the jets (see Fig. 4.8, left). This central radio region is aligned with the optical center of the host galaxy (see Fig. 4.1), suggesting a nuclear origin. The *Chandra* detection provides a significantly more accurate localization than eROSITA, with a positional uncertainty of 0.65". It coincides closely with the optical galaxy center and also overlaps with the densest part of the central radio emission (see Fig. 4.8, right). This suggests that the X-ray transient likely originated from the nuclear region, associated with the supermassive black hole in the galaxy center.

Based on the *Chandra* position, I estimated the projected distance between the X-ray position of J0936 and the optical galaxy nucleus to be $1.17^{+1.52}_{-1.17}$ kpc, consistent with a nuclear origin. Assuming the positional uncertainties of both the X-ray and optical measurements, I place an upper limit of 2.7 kpc on any potential offset from the nucleus. Other sources detected by *Chandra* (see Table 4.2) are located at projected distances $\gtrsim 200$ kpc from the optical position of the host galaxy and are therefore unlikely to be physically associated with it.

4.4 Multiwavelength follow-up

Optical follow-up was performed shortly after the X-ray discovery on 1st June 2021 with the 6.5 m Baade Magellan Telescope located at Las Campanas Observatory, Chile (PI: Stefano Ciroi). The spectrum was obtained with the IMACS Short Camera (Dressler et al., 2011), and was reduced with IRAF[9] following the usual procedure of overscan subtraction, flat-

[9] `https://iraf.net`

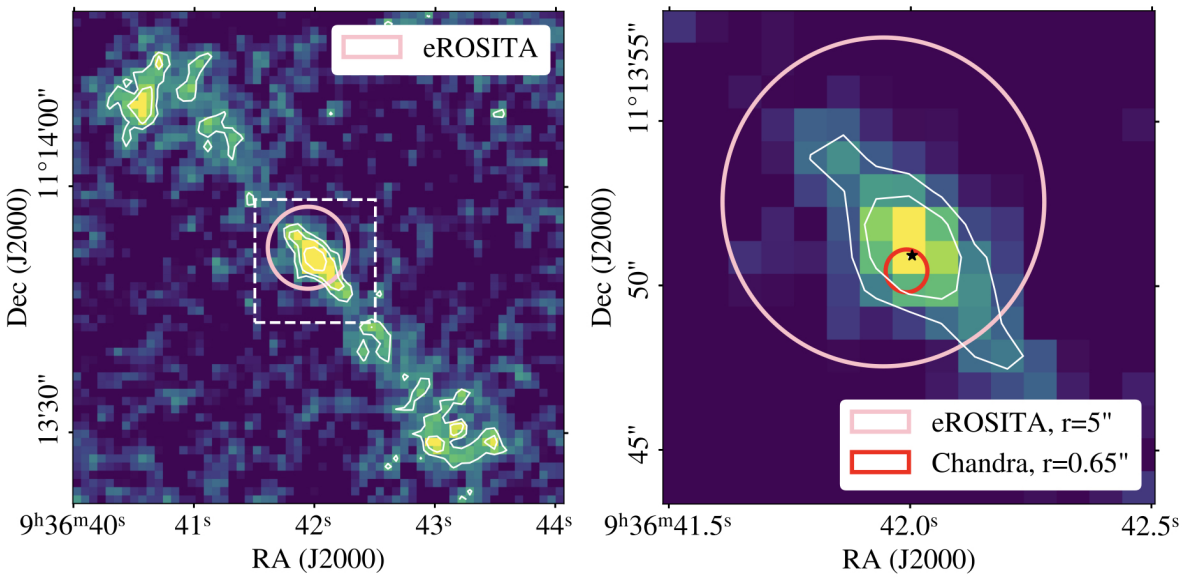

Figure 4.8: Left: VLASS radio image of the host galaxy in the S-band (2–4 GHz), obtained with a 2.048 GHz bandwidth and centered around 3 GHz, displaying the characteristic FR II double-lobe jet morphology. The white contour levels correspond to 2σ, 3σ, and 5σ above the background. The pink circle indicates the eROSITA position of J0936 with a 5" uncertainty. Right: Zoom-in of the boxed region from the left panel. The red circle shows the Chandra position of J0936 with 0.65" uncertainty, and the black star marks the optical center of the galaxy. The white contour levels correspond to 2σ, 3σ above the background.

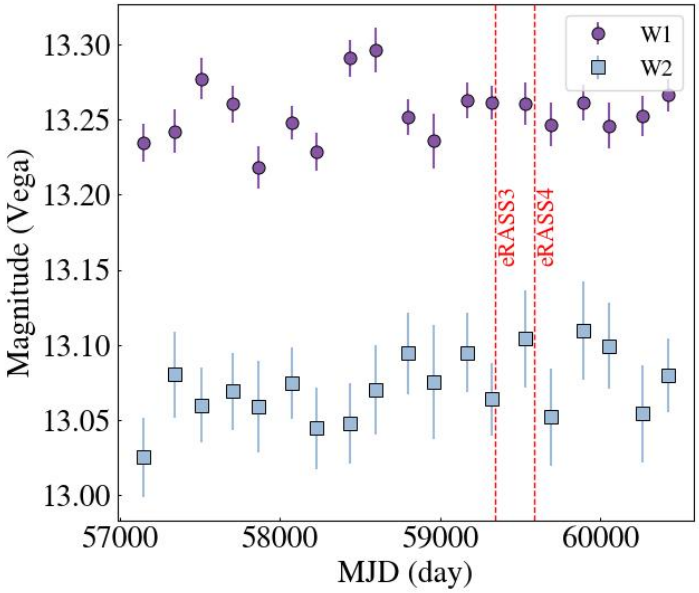

Figure 4.9: NEOWISE W1 and W2 light curves, binned in ten-day intervals, for J0936. Purple circles denote W1 data points, and blue squares show W2 data points. The red dashed lines indicate the times of the eRASS3 and eRASS4 eROSITA observations, corresponding respectively to the first detection of the TDE flare and the subsequent detection of the second flare.

field correction, and wavelength calibration by means of a He-Ne-Ar lamp. As illustrated in Fig. 4.7, the spectrum taken after the flare shows no emission lines and is consistent with the archival spectrum. No significant variability is present in the optical light curve as observed by ATLAS (Tonry et al., 2018) and ASAS-SN[10] (Kochanek et al., 2017).

The NEOWISE long term W1 and W2 light curves, obtained as described in Sect. 3.4.1, are presented in Fig. 4.9. The W1 and W2 light curves of J0936 show only marginal variability (amplitude < 0.1 mag) not correlated between the two bands. With average systematic errors mostly exceeding 0.1mag for W1 and W2 in NEOWISE[11], the light curves are fully consistent with constant flux. Additionally, genuine mid-IR variability from a TDE would produce correlated changes in W1 and W2 due to dust reprocessing (e.g., see WISE light curves of TDE candidates from Chapter 3 in Fig. B.3). Thus, J0936 is not variable in mid-IR both historically and around the time of the X-ray flare.

Since the host of J0936 is a strong radio emitter with powerful jets, a radio follow-up campaign was performed with the Arcminute Microkelvin Imager Large-Array (AMI-LA; Zwart et al. 2008; Hickish et al. 2018; PIs: David Williams and Rob Fender) to test if the X-ray flare is accompanied by radio variability. AMI-LA is a radio interferometer made up of eight 12.8 m antennas, creating 28 baselines ranging from 18 m to 110 m in length. It

[10] `https://asas-sn.osu.edu/sky-patrol/coordinate/3d153a5a-4edd-4fe5-ba01-38529ba59d86`

[11] see Figures 4 and 5 of the documentation at `https://irsa.ipac.caltech.edu/data/WISE/docs/release/NEOWISE/expsup/sec3_2.html`

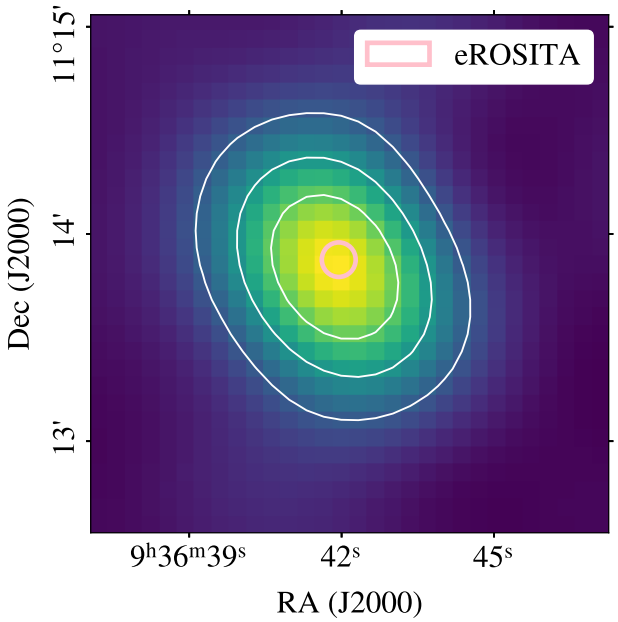

Figure 4.10: Example of an AMI-LA radio image of J0936 (2.5' cutout). The pink circle indicates the eROSITA position with a 5" uncertainty, coinciding with the center of the extended radio source. White contours correspond to 2σ, 3σ, and 5σ above the background. Data provided by L. Rhodes, University of Oxford.

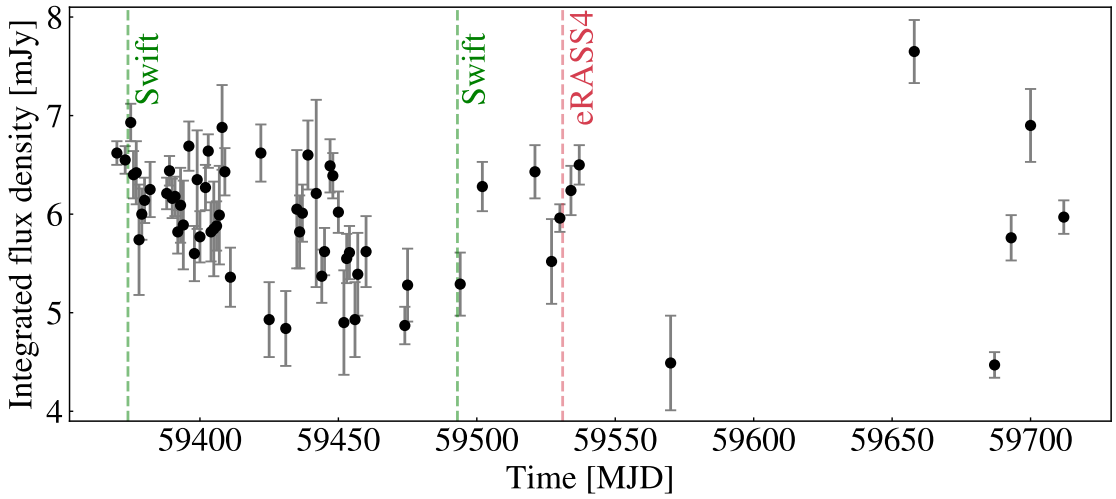

Figure 4.11: AMI-LA radio light curve of J0936. Black points show the integrated flux density of the source. Green dashed lines mark the *Swift* detections of J0936 on 09.06.2021 and 06.10.2021, when the source was in the faint state after the first X-ray flare. The red dashed line marks the eRASS4 detection of J0936 during the second flare on 13.11.2021. Figure provided by L. Rhodes, University of Oxford.

operates with a 5 GHz bandwidth, split into eight channels, centered around a frequency of 15.5 GHz. Regular observations were conducted over ≈ 350 days, starting on 12 June 2021 — about one month after the first eROSITA detection of the X-ray flare. Fig. 4.10 shows an example of an AMI-LA image, displaying an extended radio source with the eROSITA position coinciding with its center.

Modest, day–week scale fluctuations were detected in the integrated AMI-LA flux of this FRII (see Fig. 4.11). Following the approach of Rhodes et al. (2023), we confirm that the observed variability is statistically significant, with a fractional variability of $8.7 \pm 0.9\,\%$. Instrumental calibration errors are unlikely because the calibrator behavior and typical systematics were corrected for, and interstellar scintillation (Cordes & Lazio, 2002) was considered and found inconsistent with the observed properties. Given the large, unresolved morphology in our images (see Fig. 4.10), the most straightforward interpretation is that a compact, variable core (or a compact jet component embedded in the extended lobe) dominates the short-timescale variability. Such a core can produce high variability brightness temperatures and can appear in the integrated flux even when the source is overall lobe-dominated. The brightness temperature, estimated from Eq.6 in Rhodes et al. (2023), is of order 10^{11}K, consistent with synchrotron radiation (Kellermann & Pauliny-Toth, 1969). The variability may be caused by a late-time activity related to the TDE candidate J0936, similar to behavior seen in other TDEs (e.g., Goodwin et al. 2023; Rhodes et al. 2023). Definitive discrimination would require higher-resolution imaging or multi-frequency monitoring to isolate the compact component, which is not possible with the current dataset.

4.5 Discussion

4.5.1 X-ray variability of FRII galaxies

To determine if X-ray variability is common in FRII galaxies, I explored a systematically selected sample of FRII galaxies, called FRIICAT, compiled by Capetti et al. (2017). The catalogue contains 122 FRII radio galaxies with $z \leq 0.15$, obtained by utilizing observations from the NVSS, FIRST, and SDSS surveys. To be classified as an FRII galaxy, each source must have an edge-brightened radio morphology and at least one of the radio emission peaks located farther than 30 kpc from the center of the host. Overall, 47/122 FRIICAT sources are located in the German half of the eROSITA sky ($359.9442^\circ > l > 179.9442^\circ$). It is noteworthy that J0936 is included in FRIICAT, making it a very suitable sample for comparing its X-ray variability with that of the rest of the FRII population.

I used the eROSITA eRASS:5 catalog (ver.240620, processing c030; unpublished, available for the eROSITA collaboration), to analyse the X-ray variability of the covered subsample. eRASS:5 is a compiled catalog of all available eROSITA epochs and is suitable for identifying X-ray sources down to the faintest possible eROSITA limit. I crossmatched eRASS:5 with the FRIICAT using a radius of 15", and excluded extended X-ray sources, following the selection detailed in Chapter 2. Eight point sources, in addition to J0936,

Table 4.3: FRII radio galaxies from FRIIcat detected in eROSITA_DE (excluding J0936). The eRASS:5 fluxes and luminosities are provided in the 0.2–2.3 keV energy band, estimated using a power law model with fixed $\Gamma = 2.0$ and $N_H = 3 \times 10^{20}$ cm^{-2}, as adopted in the eROSITA catalogs.

Name	RA [deg]	Dec [deg]	z	flux [$\times 10^{-14}$erg cm^{-2} s^{-1}]	L [$\times 10^{42}$erg s^{-1}]
J024558.54-064900.6	41.493916	-6.816833	0.139	1.2	0.62
J080158.09+175152.6	120.492041	17.864611	0.147	5.1	2.4
J091153.61+372413.3	137.973375	37.403694	0.104	6.1	1.4
J093215.91+180419.9	143.066291	18.072194	0.147	2.3	1.34
J094124.02+394441.8	145.350083	39.744944	0.108	4.7	1.2
J095640.77-000124.0	149.169875	0.023333	0.139	2.0	1.03
J125222.61+031554.0	193.094208	3.265000	0.099	2.1	0.52
J141247.44+045431.5	213.197666	4.908749	0.136	2.0	0.98

were detected with DET_LIKE > 6 (see Table 4.3). The sources are detected only in the compiled catalog with luminosities $\approx 10^{42}$ erg s^{-1} and are not detected in each individual eRASS. The luminosities were derived assuming a power-law spectrum with fixed photon index $\Gamma = 2.0$ and $N_H = 3 \times 10^{20}$ cm^{-2}, consistent with the eROSITA catalog convention (Merloni et al., 2024). The eROSITA detections of these FRII galaxies are too faint to provide spectral modeling constraints. For the 38 FRIIs not detected in eRASS:5, I computed single-eRASS 3σ ULs (Tubín-Arenas et al., 2024; Merloni et al., 2024) using eRASS1 to constrain the maximum luminosity within an eRASS. The computed luminosity upper limits are below 10^{43} erg s^{-1}, with a median value of 5×10^{42} erg s^{-1}. In contrast, J0936 is much brighter, with its peak luminosity reaching 5×10^{43} erg s^{-1}.

Although the spectra of the eROSITA-detected FR II galaxies could not be modeled, previous studies have found FR II galaxies to exhibit generally hard X-ray spectra. For example, Evans et al. (2006) explored a sample of FR I and FR II galaxies from the 3CRR catalog[12] selected based on their low-frequency emission characteristics to avoid orientation-dependent effects of relativistic beaming. The study found that all FR II galaxies in the sample exhibited much harder X-ray spectra ($\Gamma < 2$ and/or kT > 200 eV), which were also heavily obscured ($N_H > 10^{23}$ cm^{-2}). Additionally, strong obscuration could explain the general eROSITA non-detection. In contrast, the X-ray spectra of J0936 are much softer for all detections and are best fit with $\Gamma > 4$.

The X-ray variability and spectral properties of J0936 are unique. Thus, I conclude that the X-ray properties of J0936 do not resemble other FRII galaxies and require an alternative explanation.

[12] `https://3crr.extragalactic.info`

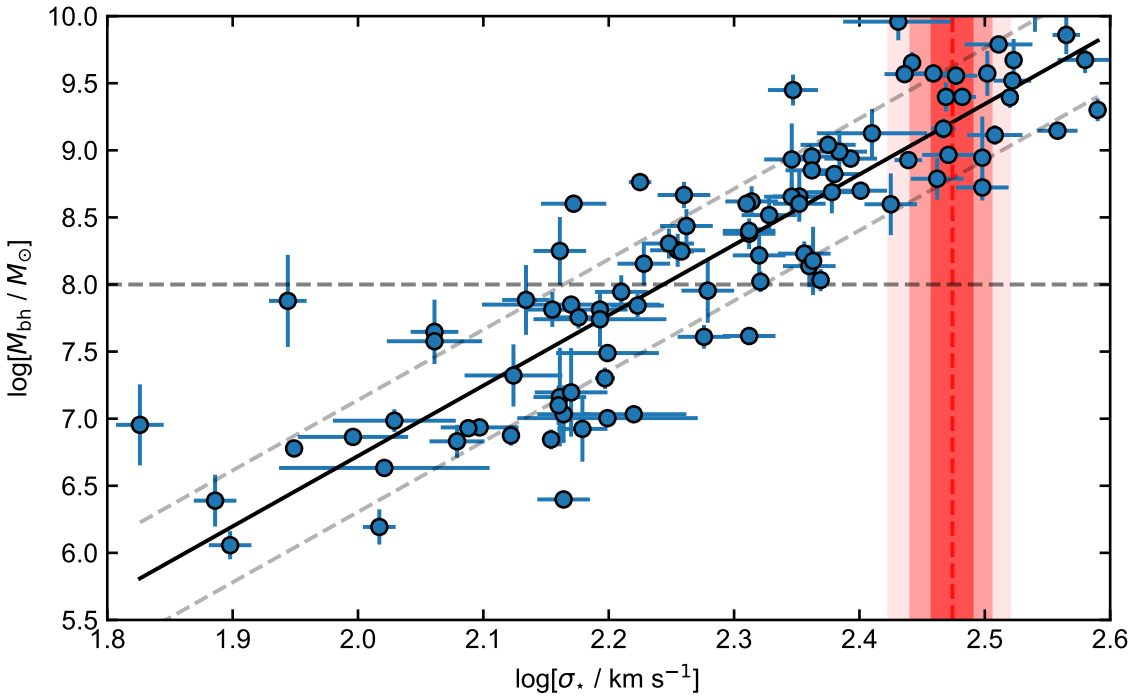

Figure 4.12: $M_{BH} - \sigma$ relation illustrating the SMBH mass of the J0936 host. The black line shows the best fit model from Saglia et al. (2016) and the grey dashed line marks the Hills mass for a non-spinning BH. The galaxy sample shown with blue points, which was used to derive this relation, is also from Saglia et al. (2016). The three red shaded bands enclose the 1, 2 and 3-sigma uncertainties on the host stellar velocity dispersion, showing that the J0936 SMBH mass is significantly above the Hills mass. Although the scatter in the relation is large, the black hole mass for J0936 must be an extreme outlier if the disrupting BH lies below the Hills mass. Figure by A. Malyali, MPE.

4.5.2 TDE around a rapidly rotating SMBH

The association of the X-ray flare with the nuclear region of the host galaxy suggests that the transient could have been caused by a TDE from the central SMBH. Indeed, the X-ray properties of J0936 align well with the TDE hypothesis. In particular, its ultra-soft X-ray spectrum and a flaring light curve evolving on a scale of weeks are typical for TDEs (Saxton et al., 2020; Gezari, 2021). A moderate rebrightening observed in eRASS4 (see Fig. 4.5) may indicate that J0936 is a partial repeating TDE, as seen other in X-ray TDEs (e.g., Malyali et al. 2023a; Liu et al. 2023).

To further test the TDE hypothesis, I estimated the accreted mass corresponding to the energy released during the first flare. Given that I detected no transient or variable optical or UV emission for J0936, I obtained an estimate of the lower limit of the total released energy from the X-ray light curve only. By integrating the X-ray light curve (0.2–2.3 keV) from MJD 59347 to 59374 over a period of 27 days, I obtained a total radiated energy

2.3×10^{50} erg, and, therefore, an accreted mass M_{accr} of $1.5 \times 10^{-3} M_{\odot}$. It is important to note that the provided value is only a lower limit as due to the sparsity of the X-ray light curve I do not have the coverage of the whole flare. The low M_{accr} agrees with the partial TDE scenario and has been seen in previous TDE studies (e.g., Gomez et al. 2020). Moreover, the mass accreted during partial TDEs is highly sensitive to the system parameters, including the impact parameter, and may constitute less than 1% of the stellar mass (e.g., Miles et al. 2020).

I estimated the SMBH mass for J0936 using the standard $\mathrm{M_{BH}} - \sigma$ relation from Saglia et al. (2016):

$$\log_{10} M_{\mathrm{BH}} = 5.246 \log_{10} \sigma - 3.77.$$

For the host galaxy, I adopted a stellar velocity dispersion of $\sigma = 298 \pm 11$ km s^{-1} (Capetti et al., 2017). Taking the 99.7% confidence interval, σ spans 265–331 km s^{-1}, leading to a BH mass of $\log \mathrm{M_{BH}} \approx 9.2^{+0.2}_{-0.3}$. Including the intrinsic scatter of the relation (± 0.417 dex, see Table 11 in Saglia et al. 2016) gives a range of $\log_{10} M_{\mathrm{BH}} \sim 8.51 - 9.87$ or $M_{\mathrm{BH}} \sim 3 \times 10^8 - 7 \times 10^9\ M_{\odot}$.

However, due to the limitations imposed by the Hill's mass (see Sect. 1.3.1), SMBHs in the TDE host galaxies typically are in the mass range of $(10^6 - 10^8) \times M_{\odot}$ (Stone & Metzger, 2016; Wevers et al., 2017). For BH masses in the derived range, tidal disruption of a main-sequence star becomes increasingly difficult because the Hills mass rises only weakly with stellar mass (see Eq. 1.2). In practice, increasing the stellar mass while staying on the main sequence can make disruption possible only for the lower end of the calculated BH mass range. For example, a $30\,\mathrm{M_{\odot}}$ O-star with $\mathrm{R} \approx 10\,\mathrm{R_{\odot}}$ can be disrupted outside the Schwarzschild radius of a BH with mass of a few $\times 10^8\,\mathrm{M_{\odot}}$. At the upper end of the non-spinning BH range ($\mathrm{M_{BH}} > 10^9 \mathrm{M_{\odot}}$) only giant or supergiant stars with radii of tens to hundreds of $\mathrm{R_{\odot}}$ can be disrupted outside the event horizon (e.g., MacLeod et al. 2012). Such stars are also more prone to partial tidal stripping, as potentially observed in J0936, where only their extended envelope is removed while the core survives to potentially experience multiple tidal encounters (e.g., Navarro Navarro & Piran 2025).

Given that the implied SMBH mass of J0936 exceeds the Hills mass for TDEs of a main sequence star by a non-spinning black hole (see Fig. 4.12), the SMBH may also rotate rapidly for a TDE scenario to be possible. A larger Hills mass is allowed for a rotating (Kerr) BH, since as the spin increases the ISCO decreases, and the tidal disruption radius is altered. The Hills mass for a Kerr BH is $M_{\mathrm{Hills,\ Kerr}} \sim M_{\mathrm{Hills,\ Schwarzschild}} \cdot \left(1 + \frac{a}{M_{\mathrm{BH}}}\right)^{3/2}$ (Rees, 1988) and can reach $7 \times 10^8 M_{\odot}$. Indeed a small subset of TDEs have been discovered around exceptionally massive black holes and hypothesized to be highly spinning: AT 2021lwx is a TDE candidate around BH with $M_{BH} \approx 10^8 M_{\odot}$ (Subrayan et al., 2023); another example is ASASSN-15lh, originating from a rapidly spinning black hole with $M_{BH} \approx 10^9 M_{\odot}$ (Mummery & Balbus, 2020); AT 2022cmc is a jetted TDE with a highly spinning BH with potential mass up to $5 \times 10^8 M_{\odot}$ (Andreoni et al., 2022).

Another possible scenario is that the BH is undermassive and in reality lies lower in the $\mathrm{M_{BH}} - \sigma$ than predicted by its velocity dispersion. As can be seen from Fig. 4.12, there are sources lying beyond the relationship scatter, including an extreme outlier NGC 3079.

NGC 3079 is a well-known outlier below the $M - \sigma$ relation because it hosts a pseudo-bulge rather than a classical bulge. In such galaxies, secular evolution builds the central stellar component without efficiently growing the SMBH, so the black hole is smaller than predicted for its velocity dispersion (e.g., Kormendy & Ho 2013). This behavior is typical for late-type galaxies and pseudo-bulges, which show larger scatter and systematic offsets below the canonical $M - \sigma$ relation. However, J0936 has a very high Sersic index ($n \approx 7.4$; Simard et al. 2011), indicating a classical bulge or elliptical morphology. Classical bulges have tightly coupled SMBH and stellar growth, so the mechanism that produces NGC 3079's and similar galaxies' offset does not apply. Any deviation of its SMBH mass from $M - \sigma$ would therefore more likely reflect measurement uncertainties or intrinsic scatter rather than morphological effects.

The X-ray spectral and multiwavelength properties of J0936 are also consistent with the TDE scenario. As it was shown in Chapter 3, a lot of promising TDE candidates are found without optical or mid-IR flares and with a quiescent spectrum of the host galaxy. This behavior can be explained, for example, by minimal obscuration along the line of sight, leading to little or no reprocessed emission at other wavelengths (see Chaper 1.3.4). In this case, the soft to hard transition of the X-ray spectrum corresponding to the bright and faint states (see Fig. 4.6), respectively, can be attributed to the formation of a hot corona and its further destruction, as discussed in Chapter 3.

The detection of a TDE in an FRII LERG represents a remarkable and unusual addition to the variety of known TDE host galaxies. Such a discovery could provide crucial insights into the relationship between SMBH activity and tidal disruption processes, expanding our understanding of the diverse environments in which TDEs can occur.

4.5.3 TDE around a wandering BH?

Although, J0936 could have come from an FR II radio galaxy with a spinning BH of $\log(M_{BH}/M_{\odot}) \approx 8.8$, the transient may also originate from an SMBH binary in the galactic center, where the disruption could involve a lower-mass black hole. Alternatively, the TDE could be off-nuclear around a smaller mass BH. Assuming that the source is not radiating above the Eddington limit and that the TDE emission is dominated by the observed X-rays, the measured bolometric luminosity value at the light curve peak implies a minimum BH mass of $\approx 1.5 \times 10^6 M_{\odot}$. Recent studies suggests that a significant fraction of TDEs may be produced by wandering BHs in the host galaxy (e.g., Ricarte et al. 2021). To test this hypothesis, a dedicated *Chandra* follow up (PI: A. Malyali) was performed, allowing to resolve the location of the X-ray transient with the accuracy of 0.65" (see Fig. 4.4). The *Chandra* results remain consistent with both nuclear and off-nuclear scenarios, with a maximum offset of 2.7 kpc from the galactic center, and cannot be used to definitively distinguish between these origins. A more detailed analysis of the *Chandra* data will be performed in the future studies in order to better constrain the X-ray position, using, e.g., MARXS simulations (Günther et al., 2017).

4.6 Summary

This chapter presents the discovery of an exceptional X-ray transient, J0936, associated with an FRII radio galaxy, the main observational features of which are as follows:

- eROSITA detected an ultra-soft X-ray brightening ($kT = 70$ eV, $A > 13$) from a previously X-ray quiet galaxy at $z = 0.127$ (Sect. 4.2.1).
- *Swift* and *NICER* follow-up, as well as a further eROSITA observation revealed an X-ray flare lasting at least 26 days, with a re-brightening occurring approximately six months after discovery (Sect. 4.2.4). The peak flux reached 1.5×10^{-12} erg cm^{-2} s^{-1}, corresponding to a luminosity of 3.15×10^{43} erg s^{-1}.
- No multiwavelength variability was found in UV and optical bands (Sect. 4.4). The optical spectrum is consistent with that of a quiescent galaxy before and after the X-ray flare. Modest short-term radio fluctuations were detected on timescales of days to weeks, possibly originating from the compact variable core.
- The X-ray flare is associated with an FR II radio galaxy characterized by large-scale jets extending over tens of kpc, with emission primarily concentrated in the lobes. The FR II nucleus hosts an inefficiently accreting AGN, which are often heavily obscured. The galaxy is classified as a LERG due to absence of optical emission features. The BH mass of the host is $M_{BH} \sim 3 \times 10^8 - 7 \times 10^9$ $M_\odot$.

By analyzing a sample of FR II radio galaxies from FRIICAT, it was found that the X-ray properties of J0936 differ significantly from those observed in other FR II galaxies in terms of duration, spectral softness and luminosity (Sect. 4.5.1). On the other hand, J0936 is strongly consistent with being a partial repeated TDE based on its X-ray properties and absence of detectable emission in optical and UV. Being identified in an FR II radio galaxy hosting a SMBH with an estimated mass of $M_{BH} \approx 10^9 M_\odot$, J0936 is a TDE candidate with one of the most massive BHs to date. However, the SMBH mass exceeding the Hills mass suggests that additional conditions must be met for a TDE to be observable in this system. One possibility is that the BH is rapidly rotating (Sect. 4.5.2), therefore, increasing the critical mass threshold for disruption. Alternatively, the event could be associated with an off-nuclear wandering SMBH or a black hole binary within the galaxy center (Sect. 4.5.3). The current precision of the X-ray position is consistent with both scenarios. The unusual nature of the host galaxy and its high BH mass make J0936 a valuable addition to the non-canonical TDE population and one of the most exotic TDE candidates known, offering new insights into the diverse environments capable of hosting TDEs.

Chapter 5

Conclusion

5.1 Summary

This thesis provides a detailed exploration of the variable extragalactic X-ray sky, leveraging the rich dataset of the eROSITA all-sky survey, which is well suited for population studies. In this work, I developed a new methodology for identifying extragalactic transients and provided a systematically selected catalog, focusing on sources not associated with active galactic nuclei. Serving as a valuable resource for studying unique nuclear transients, the catalog was used to discover a rare population of tidal disruption event candidates. Thus, this thesis offers a comprehensive statistical analysis of the largest systematically selected sample of canonical X-ray TDE candidates to date. Additionally, it reveals potential unconventional TDE candidates, including one associated with an intermediate-mass black hole and another with a supermassive black hole exceeding the Hills mass.

In Chapter 2, I presented the catalog of 304 extragalactic non-AGN transients and variables, eRO-ExTra. Starting with over two thousand variable sources detected in the first two eROSITA all-sky surveys, a careful selection was implemented to exclude stellar and AGN-related transients, resulting in a clean parent sample of variability phenomena associated with massive BHs. eRO-ExTra provides reliable optical counterparts, redshifts, light curve classifications and X-ray spectral modeling results. The rigorous selection and detailed analysis make eRO-ExTra an ideal resource for studying a variety of extragalactic transient classes. Furthermore, this chapter has laid a strong methodological foundation for identification of non-AGN transients and variables in other X-ray missions (more details in Sect. 5.2).

Before the launch of eROSITA in 2019, hundreds of new TDEs were expected to be discovered during its four-year all-sky survey (Khabibullin & Sazonov, 2014), allowing a transition from the study of individual TDEs to population studies. This thesis presents the first systematic search of TDEs in the eROSITA_DE, as detailed in Chapter 3. The sample of 31 TDE candidates, selected from the eRO-ExTra catalog, nearly doubles the number of known X-ray selected TDEs (Saxton et al., 2020; Sazonov et al., 2021). Being the largest systematically selected sample to date, it enables a reliable estimate of the

TDE X-ray luminosity function, yielding a rate of $\approx 1.2 \times 10^{-5}$ events per galaxy per year. The analysis of host galaxy properties revealed an overdensity in the green valley and indicated BH masses ranging from $\approx 2.5 \times 10^5\,M_\odot$ to $\approx 4.0 \times 10^7\,M_\odot$ for canonical TDEs. Notably, one candidate off-nuclear TDE was found, potentially associated with an IMBH, in line with eROSITA detection predictions (Malyali et al., 2019). The multiwavelength analysis of the sample showed that only a fraction of X-ray-selected TDEs is accompanied by optical or mid-IR flares, with the absence of variability in other bands being typical for this population. The chapter discusses how the observed diversity in multiwavelength characteristics can be explained by obscuration or stream-stream collision models.

In addition to canonical TDEs, recent studies (see references within Sect. 1.3.5) have shown that a significant fraction of TDE candidates exhibit non-canonical X-ray properties or reside in unusual host galaxies. This thesis has contributed to the study of this unconventional subpopulation by investigating a TDE candidate eRASSt J093641.9+111347 located in an FRII radio galaxy, as presented in Chapter 4. The atypical host galaxy and its extremely high SMBH mass, exceeding Hill's mass for a non-rotating supermassive BH, make this event a valuable addition to the diverse TDE population and provide new insights into potential TDE environments. The chapter examines the X-ray variability of the FRII galaxy population and concludes that the transient exhibits unique X-ray properties compared to the typical FRII. The observational data support the possibility of a TDE occurring either around a rapidly rotating BH or as an off-nuclear event.

5.2 Future research

This thesis introduces the methodology and presents the initial results of a systematic investigation of the transient and variable sky using eROSITA, with a particular emphasis on the tidal disruption event population. The developed methods and the resulting catalogs provide a valuable foundation for future research in time-domain astrophysics, especially in the context of high-energy transients.

While this study concentrated on transients observed during the first year of the eROSITA mission, a natural extension of this work is the application of the developed methodology to the remaining eROSITA data. This would involve identifying non-AGN transients and reliable canonical TDE candidates in eRASS3 and eRASS4. Such an extension has the potential to significantly expand the current samples, possibly doubling their sizes.

The eRO-ExTra catalog, along with its potential extension, represents a valuable resource for identifying and characterizing a wide variety of non-AGN transient phenomena associated with massive black holes. While Chapter 3 focused on detailed studies of canonical TDEs, comprising approximately 10% of the catalog's sources, the majority remain unexplored and represent an exciting avenue for future work. A thorough investigation of the remaining sources will be instrumental in identifying new transient classes and refining our understanding of their physical properties. For example, this thesis primarily focused on canonical TDEs, but the eRO-ExTra catalog likely contains other classes of TDEs, such

as repeated or partial events (more details in Chapter 1.3.5). By comparing these events with canonical TDEs, we can gain a deeper understanding of how different factors such as BH spin, stellar structure, and orbital dynamics affect the disruption process. In addition, uncovering the population of non-canonical TDEs could shed more light on the missing TDE problem (see references in in Chapter 3).

On the other hand, the current sample of X-ray detected TDEs remains limited, and extending this sample is crucial for providing better constraints on such key astrophysical parameters as the X-ray luminosity function, TDE rates, and host galaxy properties. A larger, more diverse sample would allow for the statistical refinement of these parameters. In addition, it could also yield a more comprehensive understanding of the differences in TDE characteristics across various host types at different redshifts, potentially revealing new trends that could shape our understanding of the properties of nuclear stellar populations.

In addition to the initial findings discussed in this thesis, the study of TDE candidates can be continued through late-time multiwavelength follow-up observations, including optical, UV, X-ray, and radio bands.

- Late time UV plateau emission can be observed years after the initial flare of a TDE. Following the fundamental scaling relation by Mummery et al. (2023), the UV tail can serve as an effective proxy for estimating the mass of the central BH. By obtaining long-term UV data for TDEs presented in this work (and TDEs identified in future projects), e.g., with *Swift*, we can directly test and refine this scaling relation, providing more precise measurements of BH masses in TDE hosts. While the thesis presents the estimation of BH masses from SED, this modern method may provide better estimates based directly on TDE properties. Additionally, the nature of the far UV emission remains uncertain. While some models attribute this emission to the viscous spreading of an unobscured accretion disk (van Velzen et al., 2019), alternative explanations, such as emission from the disrupted star's remnants or an extended reprocessed emission from the surrounding debris, should also be considered (Piran et al., 2015; Metzger & Stone, 2016). Further UV monitoring of TDEs can help distinguish between these models and provide a clearer picture of the accretion processes in play at late times.

- TDEs are known to produce late-time radio emission on the timescale of years after the X-ray flare, originating from the synchrotron emission from the interaction of the ejected TDE debris with the circumnuclear medium (Alexander et al., 2020). A successful follow-up campaign performed with ATCA resulted in the detection of nearly half of eROSITA TDEs presented in this thesis (Goodwin et al., 2025b). The TDE radio spectra were found to be consistent with optically thin synchrotron emission. This systematic approach allowed for the development of the first hypothesis suggesting that TDE radio outflows are launched at or near the peak X-ray luminosity. Radio monitoring with ATCA and other facilities should continue to explore the evolution of radio emission and provide deeper insights into the TDE nuclear environment.

- X-ray observations at late times are essential for identifying re-brightening TDEs, or probing X-ray spectral hardening, associated with the formation of the corona. Additionally, late-time light curves are the perfect laboratory for discovering new QPE candidates and testing the TDE-QPE connection (e.g., Miniutti et al. 2019). The Einstein Probe proposal (PIs: A. Rau, P. Baldini) was accepted to follow up the presented sample of eROSITA TDEs ≈ 5 years after their initial discovery. The results of the Einstein Probe campaign will be discussed in forthcoming publications.

- The presented X-ray selected TDE sample is a valuable reference for future multi-band TDE studies. While this thesis provides the systematic comparison of host galaxy properties and event rates, further investigations from other angles, such as co-evolution of multiwavelength properties, are necessary to deepen our understanding of the dichotomy between X-ray, IR, and optical TDE populations. Future large-scale surveys, e.g., LSST (Ivezić et al., 2019), are expected to identify a significant number of TDEs, allowing more detailed statistical comparisons.

- In the optical band, follow-up observations are essential for improving the accuracy of redshift estimates for sources with photometric redshifts. Accurate redshift values are crucial for tightening the constraints on the TDE XLF and for providing more precise measurements of the host galaxy properties. Moreover, the spectroscopic redshifts will comprise a robust training set for machine learning algorithms aimed at predicting photometric redshifts for this specific source population.

Looking beyond the eROSITA mission, the methodology developed in this thesis can be applied to new all-sky X-ray surveys, such as Einstein Probe, in operation since 2024, and NewAthena (Cruise et al., 2025), planned for launch in 2037. These missions will enable the detection of a larger number of TDEs and other high-energy transients in the nearby future. In parallel, the increased number of TDE candidates could open new avenues for studying still uncertain neutrino production mechanisms in these events. Neutrinos are hypothesized to be linked to various processes, for example, to jets (e.g., Wang et al. 2011; Liu et al. 2020) or interactions with ejecta, external medium, or obscuring dust clouds (e.g., Fang et al. 2020; Wu et al. 2022). Several high-energy neutrino alerts from IceCube (Aartsen et al., 2017) have already been associated with optically discovered TDEs (Stein et al., 2021; Reusch et al., 2022; van Velzen et al., 2024), and it is crucial to extend this search to the X-ray population to further explore the connection between these extreme astrophysical phenomena. Undoubtedly, by combining the efforts of multi-messenger astronomy, the TDE era is only starting, promising to uncover new mysteries and encourage collaborations for decades to come.

Appendix A

Additional information for eRO-ExTra catalog

A.1 Upper limit calculation

The eROSITA data was reduced using the eROSITA Science Analysis Software (`eSASS`) version 020 (Brunner et al., 2022). We used Eventfiles merged for all seven telescopes in the full band "0" (0.2–10.0 keV) and other necessary files (images, background images, exposure maps, and detection masks) in the energy band "4" (0.2–2.3 keV) also merged for all seven telescopes. The upper limit was then computed at the position of the brightest detection in another eRASS.

First, we used the task `apetool` to generate PSF maps for the energy band "4", which were used to calculate aperture photometry as well as sensitivity maps and obtain total photon counts in the source region and background counts. The extraction apertures are defined in units of Encircled Energy Fraction (EEF), namely, a radius that includes a certain fraction of the total source photons. We set the source region radius to re = 0.8. The estimation of the expected background level within the extraction region was done using SourceMap products generated by `ERMLDET`, which are the images of the model background plus a model of the detected sources. In addition, in cases where the local background is contaminated, `apetool` removes model sources from the SourceMap if an input position is closer than radius rr = 0.7.

Second, to calculate the upper limits, we used the Bayesian approach by Kraft et al. (1991) to estimate the photon count upper limit at a given confidence level. We chose a single-side confidence level of 0.9987 (Ruiz et al., 2022), corresponding to a double-side confidence level of 0.997, to estimate the 3σ upper limit. The measurement was considered an upper limit if the Poisson false probability that measured gross counts in the source region are due to the background noise being more than 4×10^{-6} (a typical value for eROSITA). Otherwise, the measurement was considered a detection, and we used 1σ lower and upper limit to estimate the detection counts with an error. We extracted the vignetting corrected exposure time at the X-ray position from the exposure map in the energy band

0.2–2.3 keV and calculated the count rate and subsequently correct for the EEF.

Finally, the source photon count rate was converted into flux. We used the standard energy conversion factor (ECF = 1.074×10^{12}) from 1B eROSITA source catalog for 0.2–2.3 keV for the straightforward comparison with the source catalog fluxes. The spectral model assumed for ECF is an absorbed power law model with fixed $\Gamma = 2$, $N_H = 3 \times 10^{20}$ cm^{-2}. A similar approach of the eROSITA upper limit computation is described in Tubín-Arenas et al. (2024), which published upper limits for the public DR1 data release.

A.2 Optical follow-up of X-ray transients

The optical follow-up of eRO-ExTra sources was performed with NTT/EFOSC2, ANU/WiFeS, LCO/FLOYDS, Las Campanas/IMACS, and SALT. The summary of the observations and measured redshifts are presented in Table A.1, where (RA, Dec) are coordinates of observed optical counterparts.

NTT: The sources were observed with the ESO Faint Object Spectrograph and Camera v.2 (EFOSC2; Buzzoni et al. 1984) mounted on the ESO New Technology Telescope (NTT) in La Silla, Chile (proposal IDs: 109.23JL.001 and 108.225J.001, PI Grotova; 106.21RU.001, 110.2465.001/002 PI Malyali). We used grism 13 and the 1.2" slit, providing a wavelength range of $3685 - 9315$Å with a dispersion of 2.77Å/pixel. The data were reduced and calibrated using the esoreflex pipeline (Freudling et al., 2013, v2.11.5). The He+Ar arcs were used to obtain the wavelength calibration, and the standard stars were used for flux calibration, which were observed with the same grism and the same slit oriented along the parallactic angle at corresponding observation nights.

SALT: The spectra were obtained using the RSS instrument (Burgh et al., 2003) on the Southern African Large Telescope (SALT; Buckley et al. 2006). The PyRAF-based PySALT package[1] (Crawford et al., 2010) was used for spectral reduction, which includes corrections for gain and cross talk and performs bias subtraction. The spectrum was extracted using standard IRAF[2] tasks, including wavelength calibration (neon and argon calibration lamp exposures were taken, one immediately before and one immediately after the science spectra, respectively), background subtraction, and one-dimensional spectrum extraction. The pupil (i.e., the view of the mirror from the tracker) moves during all SALT observations, causing the effective area of the telescope to change during exposures. Therefore, no absolute flux calibration is possible. However, by observing spectro-photometric standards during twilight, we were able to obtain relative flux calibration, allowing the recovery of the correct spectral shape and relative line strengths.

WiFeS: We obtained spectra with the Wide field Spectrograph (WiFeS; Dopita et al. 2010) mounted on the ANU 2.3m telescope at Siding Spring Observatory on (proposal ID 1210124, 2210131 PI: Miller-Jones). The data were reduced using the PyWiFeS reduction pipeline (Childress et al., 2014). The pipeline produces three-dimensional sets consisting of spatially resolved, bias subtracted, flat-fielded, wavelength- and flux-calibrated spectra

[1] `https://astronomers.salt.ac.za/software/pysalt-documentation`
[2] `https://iraf.net`

for each slitlet. We then extracted background-subtracted spectra from the slitlets that provided the most significant flux using the task apall in IRAF.

FLOYDS: We obtained spectra with FLOYDS spectrographs (Brown et al., 2013) mounted on the Las Cumbres Observatory 2m telescopes at Haleakala, Hawaii, and Siding Spring, Australia. The spectra were reduced using PyRAF[3] tasks as described in (Valenti et al., 2013).

Magellan: We obtained spectra with the IMACS Short Camera (Dressler et al., 2011) mounted on the 6.5m Baade Magellan Telescope located at Las Campanas Observatory, Chile. The spectra were reduced with IRAF following the usual procedure of overscan subtraction, flat-field correction, and wavelength calibration by means of a He-Ne-Ar lamp.

A.3 Description of columns of the eRO-ExTra catalog

The full description of columns of the eRO-ExTra catalog is provided in Table A.2. Example columns for the eRO-ExTra catalog are shown in Table A.3.

A.4 Radio luminosity calculation

To estimate radio luminosities at 1.4GHz, firstly, we calculated K-corrected radio luminosity at a frequency available in used radio surveys ($\nu_{\rm RACS} = 0.88$GHz, $\nu_{\rm VLASS} = 3.0$GHz):

$$\mathrm{L}_\nu = 4\pi \mathrm{D}_\mathrm{L}^2 \mathrm{S}_\nu (1+\mathrm{z})^{-\alpha-1}, \tag{A.1}$$

where radio spectral index $\alpha = -0.7$ for galaxies (Eckart et al., 1986), $\mathrm{D_L}$ is luminosity distance, z is redshift and S_ν is flux density. Then, we converted L_ν to $\mathrm{L}_{1.4\mathrm{GHz}}$:

$$\mathrm{L}_{1.4\mathrm{GHz}} = \mathrm{L}_\nu (1.4\mathrm{GHz}/\nu)^\alpha. \tag{A.2}$$

Finally, the threshold for a radio luminosity corresponding to the expectation from star formation ($< 20\ \mathrm{M_\odot yr^{-1}}$; Kennicutt 1983) was estimated using the $\mathrm{SFR} - \mathrm{L}_{1.4\mathrm{GHz}}$ relation from Murphy et al. (2011):

$$\frac{\mathrm{L}_{1.4\mathrm{GHz}}}{\mathrm{ergs^{-1}Hz^{-1}}} = 1.5 \times 10^{28} \frac{\mathrm{SFR}_{1.4\mathrm{GHz}}}{\mathrm{M_\odot yr^{-1}}}. \tag{A.3}$$

A.5 X-ray luminosity function and rates

The selected sample can be used to statistically describe the population of non-AGN transients and variables. We used the classical maximum observable volume ($1/\mathrm{V_{max}}$) approach (Schmidt, 1968) to estimate the X-ray luminosity function (XLF).

[3] `https://lco.global/documentation/data/FLOYDS-pipeline`

Table A.1: Optical spectroscopic follow-up summary of eRO-ExTra catalog. RA and DEC are coordinates of the optical counterpart [deg].

ERO_NAME	RA	DEC	Redshift	Date	Telescope	Instrument
eRASSU J001308.6-462524	3.2844	-46.4220	0.198	2022-07-03	La Silla/NTT	EFOSC2
1eRASS J004058.3-683816	10.2434	-68.6388	0.151	2023-12-25	La Silla/NTT	EFOSC2
eRASSU J011430.8-593654	18.6292	-59.6156	0.156	2020-12-12	Las Campanas/Baade	IMACS
1eRASS J014133.4-443413	25.3891	-44.5706	0.091	2021-12-06	La Silla/NTT	EFOSC2
1eRASS J015752.7-520716	29.4716	-52.1208	0.499	2023-12-23	La Silla/NTT	EFOSC2
1eRASS J022756.0-840730	36.9827	-84.1246	0.102	2022-12-31	Siding Spring/LCO	FLOYDS
1eRASS J024140.3-422435	40.4171	-42.4102	0.214	2023-02-03	La Silla/NTT	EFOSC2
1eRASS J024930.1-274958	42.3771	-27.8327	0.089	2023-12-23	La Silla/NTT	EFOSC2
eRASSU J030334.1-544438	45.8917	-54.7442	0.091	2020-10-14	Sutherland/SALT	RSS
eRASSU J034425.8-332719	56.1084	-33.4553	0.092	2020-08-22	Siding Spring/ANU 2.3m	WiFeS
eRASSU J040131.8-512541	60.3834	-51.4278	0.088	2020-09-07	Sutherland/SALT	RSS
1eRASS J042703.1-261156	66.7628	-26.1968	0.173	2023-12-25	La Silla/NTT	EFOSC2
1eRASS J043541.5-702302	68.9224	-70.3840	0.067	2023-12-23	La Silla/NTT	EFOSC2
1eRASS J043959.6-651403	69.9985	-65.2342	0.152	2023-12-24	La Silla/NTT	EFOSC2
1eRASS J045816.7-425956	74.5698	-42.9991	0.146	2023-12-23	La Silla/NTT	EFOSC2
1eRASS J051041.0-384512	77.6701	-38.7533	0.088	2022-12-10	Siding Spring/LCO	FLOYDS
1eRASS J051902.9-512630	79.7624	-51.4424	0.106	2023-02-02	La Silla/NTT	EFOSC2
1eRASS J052001.1-561254	80.0066	-56.2151	0.095	2023-02-02	La Silla/NTT	EFOSC2
1eRASS J053952.9-272523	84.9711	-27.4215	0.231	2023-02-03	La Silla/NTT	EFOSC2
1eRASS J054236.2-591856	85.6504	-59.3154	0.1	2023-12-25	La Silla/NTT	EFOSC2
1eRASS J055648.8-211921	89.2050	-21.3207	0.050	2023-02-04	La Silla/NTT	EFOSC2
1eRASS J055701.1-451409	89.2556	-45.2360	0.248	2023-12-24	La Silla/NTT	EFOSC2
eRASSU J060829.4-435320	92.1226	-43.8892	0.076	2022-11-28	Siding Spring/LCO	FLOYDS
eRASSU J063413.3-713908	98.5558	-71.6518	0.134	2021-03-28	La Silla/NTT	EFOSC2
eRASSU J064402.2-574247	101.0098	-57.7123	0.207	2023-02-03	La Silla/NTT	EFOSC2
1eRASS J064449.4-603704	101.2052	-60.6178	0.115	2023-04-03	La Silla/NTT	EFOSC2
1eRASS J065708.6-682354	104.2875	-68.3975	0.097	2023-12-24	La Silla/NTT	EFOSC2
1eRASS J071217.2-703056	108.0719	-70.5160	0.037	2023-12-25	La Silla/NTT	EFOSC2
eRASSt J074426.3+291606	116.1089	29.2688	0.039	2021-03-31	La Silla/NTT	EFOSC2
1eRASS J075031.8+093330	117.6331	9.5588	0.060	2023-12-24	La Silla/NTT	EFOSC2
1eRASS J080622.8+070247	121.5952	7.0468	0.053	2023-02-02	La Silla/NTT	EFOSC2
eRASSU J082055.8+192538	125.2324	19.4270	0.124	2023-04-02	La Silla/NTT	EFOSC2
1eRASS J082336.8+042303	125.9042	4.3842	0.028	2021-02-18	Siding Spring/ANU 2.3m	WiFeS
1eRASS J083748.4-062335	129.4516	-6.3937	0.094	2023-12-23	La Silla/NTT	EFOSC2
1eRASS J091657.8+060955	139.2407	6.1659	0.091	2021-12-10	La Silla/NTT	EFOSC2
1eRASS J093546.2-835823	143.9404	-83.9732	0.100	2023-02-04	La Silla/NTT	EFOSC2
1eRASS J103656.4-144922	159.2351	-14.8228	0.076	2023-04-04	La Silla/NTT	EFOSC2
1eRASS J110936.6-083725	167.4021	-8.6241	0.24	2023-04-02	La Silla/NTT	EFOSC2
1eRASS J121115.1-223501	182.8138	-22.5835	0.084	2023-02-03	La Silla/NTT	EFOSC2
1eRASS J122529.2-215250	186.3716	-21.8800	0.034	2023-02-02	La Silla/NTT	EFOSC2
1eRASS J130804.7+040128	197.0196	4.0246	0.164	2023-02-03	La Silla/NTT	EFOSC2
1eRASS J142140.3-295325	215.4210	-29.8880	0.058	2021-03-29	La Silla/NTT	EFOSC2
1eRASS J143308.1-772938	218.2832	-77.4949	0.102	2023-02-04	La Silla/NTT	EFOSC2
1eRASS J143915.1-270227	219.8133	-27.0413	0.065	2023-02-04	La Silla/NTT	EFOSC2
eRASSU J145622.8-283853	224.0958	-28.6487	0.093	2021-02-18	Siding Spring/ANU 2.3m	WiFeS
eRASSU J145954.5-260822	224.9780	-26.1409	0.090	2023-04-02	La Silla/NTT	EFOSC2
eRASSU J164649.4-692539	251.7043	-69.4272	0.016	2021-06-05	Siding Spring/ANU 2.3m	WiFeS
1eRASS J190146.6-552200	285.4461	-55.3661	0.059	2021-03-27	La Silla/NTT	EFOSC2
1eRASS J192128.0-502746	290.3667	-50.4651	0.056	2021-03-31	La Silla/NTT	EFOSC2
1eRASS J201206.8-442838	303.0293	-44.4783	0.119	2021-06-05	Siding Spring/ANU 2.3m	WiFeS
1eRASS J231004.4-453925	347.5210	-45.6575	0.056	2020-08-25	Siding Spring/ANU 2.3m	WiFeS
eRASSt J234403.1-352640	356.0126	-35.4450	0.1	2021-05-05	Siding Spring/ANU 2.3m	WiFeS

In order to estimate the comoving volume V_{max}, first, we estimated the maximum observable luminosity distance D_{max} for each source, corresponding to the maximum distance at which a given transient can be detected. Several factors affect the detectability of sources in the eROSITA all-sky survey, such as the position in the sky, spectral shape, redshift and intrinsic luminosity.

eROSITA has a nonhomogeneous sensitivity, which reaches the maximum at the ecliptic poles, as shown in Fig. 2.2. Therefore, the detectability depends on the ecliptic latitude (b_{ecl}). To account for this, for each candidate, we computed the minimum flux $F_{min}(b_{ecl})$ required for a detection at a certain latitude according to the applied selection criteria, namely, amplitude cut ($A > 4$) and detection likelihood cut (det_like > 15). For this, we created sensitivity maps using eSASS command `ersensmap` in the energy band 0.2–2.3 keV for det_like = 15 and also det_like = 5, which is the minimum detection likelihood of sources included in eROSITA source catalogs. The former map was directly used to extract the minimum flux for a source to be detected with det_like = 15. The minimum flux needed to satisfy the amplitude cut was estimated as $A \times F_{min}(b_{ecl})_{det\_like=5}$ for sources with detections in both eRASS1 and eRASS2, and $A \times F(b_{ecl})_{UL}$, where $F(b_{ecl})_{UL}$ is the upper limit of eRASS1 or eRASS2. The minimum flux required for the amplitude cut is more constraining than that for the detection likelihood cur for all sources, and was, therefore, used for further steps.

Next, we estimated the maximum redshift z_{max} and the resulting D_{max}, at which a TDE with a given intrinsic L (rest-flame 0.2–6.0 keV) in an X-ray spectral shape could be detected according to the selection criteria. With pyxspec, we faked a spectrum with the best-fit parameters of the `tbabs*zpow` model of the peak eROSITA epoch with the corresponding redshift, ARF and RMF files. We fixed the intrinsic luminosity using the normalization of the model to find the largest z_{max} for a detection above F_{min}. For a fraction of sources, only photometric redshifts are available (see Sect. 2.3.3). Therefore, it is necessary to account for their errors and photo-z probability distribution function (PDZ) shapes, as they may significantly affect the values of the intrinsic luminosity used in the computation. For this, for each source we drew a sample of 100 redshift values from the corresponding PDZ and performed the $D_{max,z}$ estimation for each value. The final D_{max} was calculated as a mean of $D_{max,z}$.

Finally, to calculate the XLF, we summed the derived $1/V_{max}$ values of individual sources into luminosity bins. We chose 10 equal bins between 41.5 and 46.5. The uncertainty for each bin is estimated as $\sqrt{\Sigma(1/V_{max})_i^2}$ with the summation over the objects in a particular bin. Finally, the function should have been corrected by a factor of 2.6, since the sample was selected from the LS10 covered area (76%, see Fig. 2.7) in the eROSITA_DE hemisphere. The search identified sources peaking in eRASS1 or eRASS2, which accounts for a year of observations. Therefore, no correction was needed to evaluate the volume per year.

The final XLF was computed for the eRO-ExTra subsample of 281 sources, which have credible counterparts (p_any > 0.17) and photo-z measurements with at least 2 LS10 parameters ANYMASK_X $= 0$, where X = *g,r,i,z*. The XLF is presented in Fig. A.1.

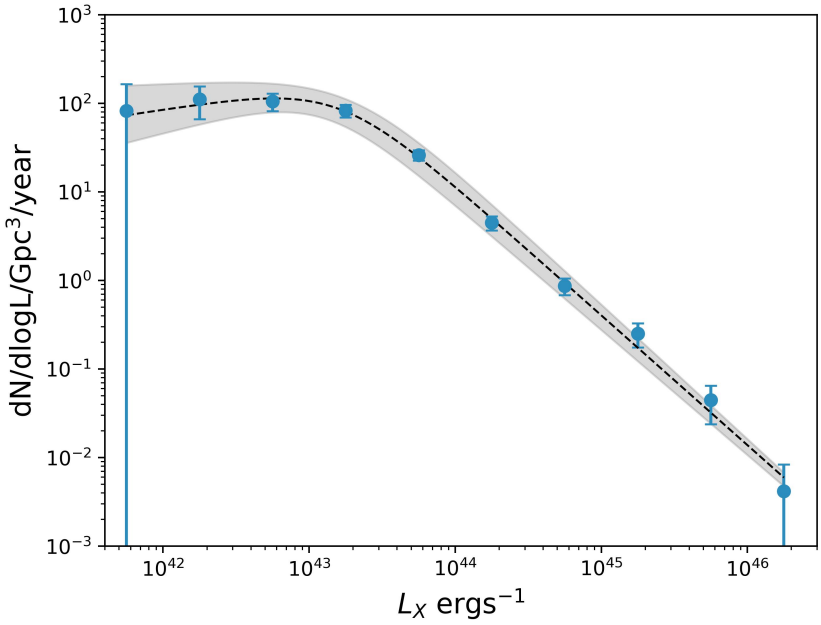

Figure A.1: XLF function for eRO-ExTra catalog in terms of rest frame 0.2–6.0 keV luminosity. The dashed black line shows the double power law fit (Eq. A.4) with the 1σ uncertainty shown in gray.

Fitting the XLF with a double power law model, we obtained:

$$f(L) = (1.7^{\pm 0.4})10^{-7} Mpc^{-3} year^{-1} \times \left(\left(\frac{L}{L_{\rm br}} \right)^{-0.25^{\pm 0.18}} + \left(\frac{L}{L_{\rm br}} \right)^{1.47^{\pm 0.05}} \right)^{-1}, \qquad \text{(A.4)}$$

where $L_{\rm br} = (1.6 \pm 0.4) \times 10^{43} {\rm ergs}^{-1}$. Using the equation above, the integrated volumetric rate of eRO-ExTra transients and variables is $1.8^{+0.5}_{-0.4} \times 10^{-7} {\rm Mpc}^{-3} {\rm year}^{-1}$.

Table A.2: eRO-ExTra catalog column description.

Column	Unit	Description
ERO_NAME		source name from DR1 or in the format eRASSU Jhhmmss.s-ddmmss
ERO_RA	deg	eROSITA Right Ascension (ICRS) from eRASS:5
ERO_DEC	deg	eROSITA Declination (ICRS) from eRASS:5
ERO_FLUX_ERASS<N>	erg/cm^2/s	source flux in 0.2–2.3 keV in eRASSN, N =1,2,3,4,(5, if available)
ERO_FLUX_ERR_ERASS<N>	erg/cm^2/s	error flux (68 %) in 0.2–2.3 keV in eRASSN, N =1,2,3,4,(5, if available); −1 = flux upper limit (99.7 %)
Amplitude		amplitude of variability between eRASS1 and eRASS2
Significance		significance of variability between eRASS1 and eRASS2
ERO_LCCLASS		eROSITA light curve class: 1 =decline, 2 =flare, 3 =brightening, 4 =other
ERO_DATE	mjd	dates of eROSITA observations: (MJD_1,..,MJD_<N>), N =1,2,3,4,(5, if available)
NH	cm^{-2}	Galactic equivalent neutral hydrogen column density in the line of sight
ERO_GAMMA		photon index for the peak eRASS
ERO_GAMMA_ERR		error photon index (68 %) for the peak eRASS
ERO_CSTAT_DOF		C-statistic per degree of freedom, used to assess the goodness of fit
ERO_FLUX_MOD	erg/cm^2/s	source flux in energy band 0.2–2.3 keV for the peak eRASS
ERO_FLUX_MOD_ERR	erg/cm^2/s	error flux (68 %) in energy band 0.2–2.3 keV for the peak eRASS
ARCH_FLAG		archival X-ray constraints: 0 =not constraining UL, 1 =constraining UL, 2 =previously detected
ARCH_DATE	mjd	dates of N archival observations: (X_1,..,X_<N>)
ARCH_FLUX	erg/cm^2/s	source flux of N archival observations:(F_1,..,F_<N>) in 0.2–2.0 keV
ARCH_FLUX_ERR	erg/cm^2/s	error flux (68 %) of N archival observations:(F_err_1,..,F_err_<N>) in 0.2–2.0 keV; −1=flux upper limit (99.7 %)
ARCH_INSTRUMENT		instruments of N archival observations (Instrument_1,..,Instrument_<N>)
NWAY_bias_LS10_Xray_proba		probability weighting intruduced by Xray_proba prior (Salvato et al., 2018)
NWAY_dist_bayesfactor		logarithm of the ratio of the prior and posterior from separation, positional error, and number density (Salvato et al., 2018)
NWAY_dist_post		distance posterior probability comparing this association vs. no association (Salvato et al., 2018)
NWAY_p_single		same as dist_post, but weighted by the prior (Salvato et al., 2018)
NWAY_p_any		for each entry in the X-ray catalog, the probability that there is a counterpart (Salvato et al., 2018)
NWAY_p_i		relative probability of the eROSITA/LS8 match (Salvato et al., 2018)
LS10_RELEASE		integer denoting the camera and filter set used in LS10, which is unique for a given processing run of the data
LS10_BRICKID		LS10 Brick ID
LS10_OBJID		catalog object number within this LS10 brick
LS10_RA	deg	J2000 Right Ascension of the LS10 counterpart
LS10_DEC	deg	J2000 Declination of the LS10 counterpart
LS10_RA_IVAR	1/deg^2	inverse variance of RA , excluding astrometric calibration errors
LS10_DEC_IVAR	1/deg^2	inverse variance of DEC, excluding astrometric calibration errors
LS10_FLUX_<X>	nanomaggy	LS10 model flux <X>, where X= *g,r,i,z*,W1,W2
LS10_FLUX_IVAR_<X>	1/nanomaggy^2	Inverse variance of flux <X>, where X= *g,r,i,z*,W1,W2
LS10_MW_TRANSMISSION_<X>		Galactic transmission in <X> filter in linear units [0, 1], where X= *g,r,i,z*,W1,W2
LS10_TYPE		morphological model from LS10
Z_REDSHIFT		redshift
Z_TYPE		redshift type: photoz = photometric, specz = spectroscopic
Z_REFERENCE		redshift origin
SIMBAD_NAME		SIMBAD source ID
SIMBAD_RA	deg	SIMBAD J2000 Right Ascension
SIMBAD_DEC	deg	SIMBAD J2000 Declination
SIMBAD_TYPE		SIMBAD main type
TNS_NAME		Transient Name Server (TNS) source name
TNS_RA	deg	TNS Right Ascension
TNS_DEC	deg	TNS Declination
TNS_DATE	mjd	TNS discovery date
VLASS_NAME		The Very Large Array Sky Survey (VLASS) source name
VLASS_RA	deg	VLASS Right Ascension
VLASS_DEC	deg	VLASS Declination
VLASS_FLUX	mJy	VLASS total flux density at 3GHz
RACS_NAME		Rapid ASKAP Continuum Survey (RACS) source name
RACS_RA	deg	RACS Right Ascension
RACS_DEC	deg	RACS Declination
RACS_FLUX	mJy	RACS total flux density at 0.88GHz

Table A.3: Example selection of columns for the eRO-ExTra catalog. The table includes eROSITA names (NAME) with the X-ray detection coordinates (RA, DEC), eRASS1 and eRASS2 fluxes (FLUX ERASS1/2 in the units of 10^{-13} erg cm^{-2}s^{-1}) and significance (S) and amplitude (A) of variability between eRASS1 and eRASS2. The table also shows light curve class (LCCLASS) and best fit photon index (GAMMA). For convenience, the "ERO" prefix in the column names is omitted, and fluxes and photon indices are combined with their corresponding errors in a single column. Triangles represent 3σ ULs. The full list of columns and their description can be found in Table A.2. The eRO-ExTra catalog is also available in electronic form at the CDS via `https://cdsarc.cds.unistra.fr/viz-bin/cat/J/A+A/693/A62`.

NAME	RA	DEC	FLUX ERASS1	FLUX ERASS2	S	A	LC CLASS	GAMMA
1eRASS J000258.3-401950	0.7411	-40.3309	1.7 ± 0.44	7.95 ± 0.86	6.5	4.7	4	1.9 ± 0.2
1eRASS J001053.3-334021	2.7223	-33.6725	6.01 ± 0.83	1.21 ± 0.46	5.1	5.0	1	2.0 ± 0.2
eRASSU J001308.6-462524	3.2856	-46.4232	$0.64^{\triangledown}$	5.85 ± 0.86	6.1	9.1	2	2.0 ± 0.3
1eRASS J003902.6-611323	9.7615	-61.2233	0.39 ± 0.17	2.41 ± 0.45	4.2	6.2	2	2.4 ± 0.3
1eRASS J004058.3-683816	10.2425	-68.6382	6.47 ± 0.64	0.58 ± 0.22	8.7	11.1	1	2.1 ± 0.2
1eRASS J005609.5-312511	14.0397	-31.4195	2.67 ± 0.48	0.38 ± 0.2	4.4	7.1	4	1.0 ± 0.3
1eRASS J005747.1-563122	14.4483	-56.5230	3.43 ± 0.51	0.65 ± 0.24	4.9	5.3	4	2.9 ± 0.3
1eRASS J010142.6-372919	15.4264	-37.4908	1.04 ± 0.3	4.7 ± 0.64	5.2	4.5	2	2.0 ± 0.3
1eRASS J010809.3-281358	17.0382	-28.2348	0.49 ± 0.22	4.81 ± 0.65	6.3	9.8	2	1.4 ± 0.2
eRASSU J011430.8-593654	18.6283	-59.6149	$0.57^{\triangledown}$	5.36 ± 0.67	7.1	9.4	2	4.1 ± 0.3
eRASSU J012026.7-292730	20.1112	-29.4582	$0.63^{\triangledown}$	4.75 ± 0.65	6.4	7.6	4	4.6 ± 0.3
1eRASS J013026.1-833548	22.6092	-83.5970	2.01 ± 0.32	0.39 ± 0.16	4.5	5.1	1	1.5 ± 0.3
1eRASS J014122.2-443615	25.3434	-44.6041	4.18 ± 0.57	0.47 ± 0.21	6.1	9.0	4	2.5 ± 0.3
1eRASS J014133.4-443413	25.3899	-44.5707	2.36 ± 0.43	0.37 ± 0.18	4.2	6.4	1	4.1 ± 0.5
1eRASS J014135.0-524620	25.3961	-52.7721	2.48 ± 0.43	$0.61^{\triangledown}$	4.3	4.1	4	2.0 ± 0.4
eRASSU J014402.3-431800	26.0097	-43.2999	$0.45^{\triangledown}$	4.0 ± 0.58	6.1	8.8	4	2.5 ± 0.3
1eRASS J015156.3-171139	27.9848	-17.1945	1.12 ± 0.3	5.05 ± 0.66	5.4	4.5	2	2.4 ± 0.2
1eRASS J015752.7-520716	29.4704	-52.1214	4.46 ± 0.54	0.68 ± 0.24	6.4	6.6	1	2.0 ± 0.2
1eRASS J020004.8-560357	30.0205	-56.0655	2.61 ± 0.42	0.39 ± 0.17	4.9	6.7	4	1.7 ± 0.3
1eRASS J020754.5-531225	31.9757	-53.2096	0.35 ± 0.17	2.01 ± 0.37	4.1	5.7	3	3.2 ± 0.6
1eRASS J021244.7-704948	33.1843	-70.8303	0.56 ± 0.17	2.73 ± 0.38	5.2	4.9	2	2.7 ± 0.3
1eRASS J021537.9-481511	33.9064	-48.2529	2.79 ± 0.42	0.5 ± 0.19	5.0	5.6	4	1.8 ± 0.3
1eRASS J022756.0-840730	36.9837	-84.1250	0.49 ± 0.16	3.4 ± 0.42	6.5	7.0	2	2.3 ± 0.3
1eRASS J023114.1-583040	37.8096	-58.5110	5.72 ± 0.51	$0.44^{\triangledown}$	10.4	13.1	4	2.8 ± 0.2
1eRASS J024049.7-595432	40.2057	-59.9089	0.38 ± 0.14	2.6 ± 0.36	5.7	6.8	2	2.9 ± 0.3
1eRASS J024140.3-422435	40.4171	-42.4096	4.16 ± 0.47	0.58 ± 0.19	7.1	7.2	1	0.6 ± 0.2
1eRASS J024509.8-371224	41.2918	-37.2044	0.27 ± 0.13	2.28 ± 0.31	5.9	8.4	2	2.4 ± 0.3
1eRASS J024800.5-323357	42.0029	-32.5665	2.11 ± 0.33	0.43 ± 0.15	4.6	4.9	4	1.2 ± 0.3
1eRASS J024930.1-274958	42.3767	-27.8330	2.16 ± 0.35	0.22 ± 0.11	5.4	9.8	1	1.7 ± 0.2
1eRASS J025408.3-470020	43.5341	-47.0058	1.65 ± 0.28	0.32 ± 0.15	4.2	5.2	1	1.9 ± 0.3
1eRASS J025412.2-251615	43.5510	-25.2710	1.64 ± 0.3	0.27 ± 0.13	4.2	6.0	4	1.5 ± 0.4
1eRASS J025436.8-361046	43.6541	-36.1795	2.18 ± 0.33	0.37 ± 0.13	5.1	5.8	4	2.3 ± 0.3
1eRASS J025830.7-182224	44.6277	-18.3732	3.41 ± 0.43	$0.43^{\triangledown}$	6.9	7.8	1	1.0 ± 0.2
1eRASS J030327.4-253122	45.8645	-25.5227	1.76 ± 0.29	0.34 ± 0.14	4.4	5.1	1	2.2 ± 0.4
eRASSU J030334.1-544438	45.8923	-54.7439	$0.45^{\triangledown}$	8.45 ± 0.59	13.5	18.7	2	2.2 ± 0.1
1eRASS J030352.2-084141	45.9677	-8.6949	3.3 ± 0.48	$0.69^{\triangledown}$	5.5	4.8	1	1.7 ± 0.3
1eRASS J030513.5-331016	46.3076	-33.1702	0.86 ± 0.21	4.19 ± 0.43	7.0	4.9	2	2.1 ± 0.2
1eRASS J030522.6-062334	46.3443	-6.3929	41.26 ± 1.55	1.33 ± 0.29	25.3	31.0	4	2.5 ± 0.1
1eRASS J030559.9-125118	46.4995	-12.8564	0.59 ± 0.2	3.63 ± 0.45	6.2	6.2	2	2.3 ± 0.3
1eRASS J031208.3-591947	48.0332	-59.3300	0.21 ± 0.09	1.44 ± 0.26	4.5	7.0	3	2.0 ± 0.3
1eRASS J031257.7-403312	48.2402	-40.5540	1.43 ± 0.24	0.29 ± 0.12	4.2	4.9	4	1.6 ± 0.3
1eRASS J031405.8-053658	48.5229	-5.6165	0.52 ± 0.19	2.58 ± 0.43	4.4	5.0	2	2.5 ± 0.4
1eRASS J031424.3-484313	48.6010	-48.7193	0.33 ± 0.13	2.11 ± 0.33	5.0	6.5	2	2.7 ± 0.3
1eRASS J031857.2-205459	49.7393	-20.9142	0.62 ± 0.19	2.9 ± 0.38	5.3	4.7	2	4.1 ± 0.3
1eRASS J031924.8-695936	49.8542	-69.9936	1.84 ± 0.24	0.31 ± 0.13	5.6	5.8	4	2.8 ± 0.3
1eRASS J032142.4-281925	50.4266	-28.3248	1.68 ± 0.28	0.34 ± 0.14	4.3	4.9	4	3.2 ± 0.4
1eRASS J032253.0-231515	50.7210	-23.2540	1.79 ± 0.32	0.38 ± 0.14	4.0	4.7	1	2.3 ± 0.3
1eRASS J032518.8-663857	51.3290	-66.6494	0.29 ± 0.11	1.63 ± 0.25	4.9	5.5	2	1.8 ± 0.3
1eRASS J032614.0-153910	51.5573	-15.6516	0.68 ± 0.21	4.13 ± 0.51	6.3	6.1	4	1.9 ± 0.3
1eRASS J033128.1-713723	52.8685	-71.6230	1.98 ± 0.25	0.42 ± 0.13	5.4	4.7	1	2.1 ± 0.3
1eRASS J033233.2-403905	53.1367	-40.6518	0.28 ± 0.12	1.92 ± 0.27	5.6	6.9	4	2.1 ± 0.3

NAME	RA	DEC	FLUX ERASS1	FLUX ERASS2	S	A	LC CLASS	GAMMA
1eRASS J033337.8-581432	53.4061	-58.2435	0.3 ± 0.11	1.24 ± 0.2	4.2	4.2	2	2.2 ± 0.3
1eRASS J033552.2-081122	53.9676	-8.1893	2.09 ± 0.31	0.49 ± 0.19	4.4	4.3	1	1.3 ± 0.3
1eRASS J034004.8-380004	55.0206	-38.0005	0.86 ± 0.18	4.04 ± 0.38	7.5	4.7	2	2.9 ± 0.2
1eRASS J034117.4-455718	55.3215	-45.9552	0.28 ± 0.1	1.17 ± 0.19	4.1	4.2	2	2.6 ± 0.4
1eRASS J034255.0-230116	55.7286	-23.0187	0.39 ± 0.15	2.5 ± 0.37	5.2	6.4	2	2.1 ± 0.3
eRASSU J34425.8-332719	56.1075	-33.4552	$0.77^{\triangledown}$	4.03 ± 0.4	8.2	5.2	4	4.0 ± 0.2
1eRASS J034459.0-104958	56.2468	-10.8328	0.34 ± 0.18	2.37 ± 0.39	4.7	6.9	2	0.8 ± 0.3
1eRASS J034833.6-722417	57.1379	-72.4052	1.14 ± 0.19	0.25 ± 0.09	4.3	4.5	4	1.2 ± 0.3
1eRASS J034945.3-190555	57.4395	-19.0989	1.64 ± 0.23	0.34 ± 0.14	4.8	4.8	1	2.2 ± 0.3
1eRASS J035035.8-653935	57.6499	-65.6588	0.72 ± 0.16	2.99 ± 0.29	7.0	4.1	2	1.8 ± 0.2
1eRASS J035219.2-340632	58.0784	-34.1083	0.33 ± 0.12	1.53 ± 0.24	4.4	4.6	4	1.9 ± 0.3
1eRASS J035405.6-500542	58.5242	-50.0953	1.88 ± 0.22	0.28 ± 0.09	6.7	6.7	4	2.2 ± 0.2
1eRASS J035709.6+053752	59.2913	5.6315	4.11 ± 0.62	0.83 ± 0.25	4.9	4.9	1	2.3 ± 0.4
1eRASS J035715.7-311118	59.3182	-31.1894	0.34 ± 0.12	1.76 ± 0.29	4.4	5.1	2	1.0 ± 0.3
1eRASS J035946.3-574126	59.9436	-57.6903	1.25 ± 0.17	0.2 ± 0.09	5.5	6.4	4	1.8 ± 0.3
eRASSU J040131.8-512541	60.3826	-51.4280	$0.22^{\triangledown}$	6.14 ± 0.39	15.3	28.2	2	2.2 ± 0.1
1eRASS J040310.7-023207	60.7970	-2.5355	0.41 ± 0.2	8.53 ± 0.75	10.4	20.9	4	2.3 ± 0.2
1eRASS J040552.5-672638	61.4701	-67.4442	0.32 ± 0.1	1.32 ± 0.2	4.4	4.1	2	2.4 ± 0.3
1eRASS J040557.4-314606	61.4897	-31.7688	1.69 ± 0.22	0.36 ± 0.15	5.1	4.7	4	2.3 ± 0.3
1eRASS J041209.5-535539	63.0396	-53.9277	0.14 ± 0.06	0.72 ± 0.13	4.0	5.2	2	1.9 ± 0.4
1eRASS J041306.6-473040	63.2766	-47.5110	1.28 ± 0.19	0.26 ± 0.09	4.8	5.0	4	1.4 ± 0.3
1eRASS J041307.6-522048	63.2824	-52.3463	0.76 ± 0.14	0.15 ± 0.07	4.0	4.9	4	2.1 ± 0.3
1eRASS J041641.2-302031	64.1723	-30.3420	1.47 ± 0.23	0.36 ± 0.14	4.1	4.0	4	2.6 ± 0.4
1eRASS J042052.9-495002	65.2243	-49.8349	0.27 ± 0.09	1.33 ± 0.17	5.4	4.9	2	2.3 ± 0.2
1eRASS J042204.8-324526	65.5210	-32.7572	0.58 ± 0.19	2.76 ± 0.35	5.5	4.8	4	2.2 ± 0.2
1eRASS J042258.1-583151	65.7415	-58.5309	0.16 ± 0.06	0.66 ± 0.11	4.1	4.0	2	1.0 ± 0.3
1eRASS J042703.1-261156	66.7625	-26.1969	0.32 ± 0.16	3.52 ± 0.43	7.0	10.9	4	2.3 ± 0.2
1eRASS J042938.4-585619	67.4105	-58.9390	0.74 ± 0.11	$0.18^{\triangledown}$	4.9	4.1	1	2.6 ± 0.3
eRASSU J043057.9-631958	67.7411	-63.3327	$0.29^{\triangledown}$	1.29 ± 0.15	6.5	4.4	2	1.7 ± 0.2
1eRASS J043129.6-333756	67.8732	-33.6304	0.28 ± 0.14	1.51 ± 0.26	4.2	5.4	4	2.2 ± 0.3
1eRASS J043337.3-353652	68.4054	-35.6143	2.88 ± 0.4	0.41 ± 0.14	5.9	7.0	4	1.7 ± 0.3
1eRASS J043358.3-391636	68.4935	-39.2777	1.92 ± 0.31	$0.47^{\triangledown}$	4.6	4.1	1	2.3 ± 0.3
1eRASS J043536.6-761117	68.8995	-76.1881	0.32 ± 0.11	1.42 ± 0.21	4.7	4.5	2	2.6 ± 0.3
1eRASS J043541.5-702302	68.9235	-70.3841	1.85 ± 0.19	0.16 ± 0.07	8.5	11.8	1	2.1 ± 0.2
1eRASS J043826.0-190150	69.6096	-19.0309	3.12 ± 0.43	$0.7^{\triangledown}$	5.7	4.4	1	1.6 ± 0.2
1eRASS J043921.6-523244	69.8423	-52.5454	0.56 ± 0.11	4.04 ± 0.29	11.2	7.1	2	1.7 ± 0.1
1eRASS J043959.6-651403	69.9980	-65.2342	10.63 ± 0.35	1.03 ± 0.14	25.6	10.3	1	4.9 ± 0.1
1eRASS J044305.2-244525	70.7720	-24.7572	0.25 ± 0.12	1.56 ± 0.29	4.1	6.2	2	2.1 ± 0.4
1eRASS J044415.9-563449	71.0668	-56.5803	0.14 ± 0.05	0.63 ± 0.1	4.4	4.6	2	2.2 ± 0.3
1eRASS J044759.1-521548	71.9972	-52.2630	0.19 ± 0.06	0.95 ± 0.15	4.9	5.0	4	1.7 ± 0.3
1eRASS J045029.9-230350	72.6239	-23.0636	2.25 ± 0.36	0.4 ± 0.19	4.5	5.6	4	2.4 ± 0.3
1eRASS J045150.9-711236	72.9636	-71.2102	0.76 ± 0.12	0.18 ± 0.07	4.1	4.1	4	1.7 ± 0.4
1eRASS J045211.4-102216	73.0466	-10.3709	2.31 ± 0.41	0.45 ± 0.19	4.1	5.1	1	1.5 ± 0.4
1eRASS J045453.2-284814	73.7212	-28.8027	0.69 ± 0.2	3.28 ± 0.43	5.4	4.7	4	2.2 ± 0.2
1eRASS J045457.8-652846	73.7439	-65.4788	0.17 ± 0.04	0.91 ± 0.13	5.4	5.3	2	0.4 ± 0.2
1eRASS J045501.4-471046	73.7571	-47.1791	1.41 ± 0.23	0.22 ± 0.09	4.8	6.3	4	2.2 ± 0.4
1eRASS J045638.8-332545	74.1623	-33.4291	1.5 ± 0.26	0.31 ± 0.13	4.0	4.9	1	1.8 ± 0.4
1eRASS J045816.7-425956	74.5698	-42.9990	3.06 ± 0.33	0.32 ± 0.11	7.8	9.5	4	4.0 ± 0.2
1eRASS J045839.6-590808	74.6657	-59.1355	0.88 ± 0.11	0.15 ± 0.05	6.2	5.8	1	1.8 ± 0.2
1eRASS J045924.8-830250	74.8495	-83.0473	0.4 ± 0.15	1.73 ± 0.28	4.3	4.3	3	1.0 ± 0.3
1eRASS J045925.3-262538	74.8568	-26.4285	0.33 ± 0.15	2.12 ± 0.35	4.7	6.5	2	1.8 ± 0.3
1eRASS J050159.2-634604	75.4957	-63.7679	0.45 ± 0.07	0.1 ± 0.04	4.6	4.7	4	1.9 ± 0.4
1eRASS J050201.7-242614	75.5069	-24.4377	2.46 ± 0.37	0.37 ± 0.16	5.2	6.6	1	2.0 ± 0.3
1eRASS J050237.3-360203	75.6560	-36.0340	0.46 ± 0.15	2.21 ± 0.34	4.7	4.8	2	2.5 ± 0.3
1eRASS J050317.3-545908	75.8247	-54.9863	1.07 ± 0.14	4.29 ± 0.27	10.8	4.0	2	2.7 ± 0.1
1eRASS J050429.0-481029	76.1226	-48.1775	0.24 ± 0.1	1.06 ± 0.17	4.2	4.3	2	2.4 ± 0.3
1eRASS J050452.7-610218	76.2212	-61.0379	0.15 ± 0.08	0.6 ± 0.08	4.1	4.0	2	2.2 ± 0.3
eRASSU J050710.9-245808	76.7954	-24.9689	$0.46^{\triangledown}$	2.45 ± 0.37	5.4	5.3	2	0.7 ± 0.3
1eRASS J050921.3-650257	77.3404	-65.0485	0.84 ± 0.08	0.15 ± 0.04	7.2	5.5	4	1.7 ± 0.2
1eRASS J051041.0-384512	77.6705	-38.7539	7.51 ± 0.54	1.11 ± 0.22	11.0	6.7	4	1.4 ± 0.1
1eRASS J051351.1-322908	78.4623	-32.4859	2.6 ± 0.36	$0.46^{\triangledown}$	6.0	5.6	1	0.6 ± 0.2
1eRASS J051353.9-410434	78.4742	-41.0758	2.24 ± 0.29	0.43 ± 0.14	5.6	5.2	4	2.3 ± 0.2
1eRASS J051409.4-622838	78.5392	-62.4769	0.14 ± 0.04	0.55 ± 0.07	5.4	4.0	2	2.1 ± 0.2
1eRASS J051653.0-600957	79.2215	-60.1661	1.49 ± 0.11	0.34 ± 0.06	8.7	4.3	4	1.8 ± 0.1

NAME	RA	DEC	FLUX ERASS1	FLUX ERASS2	S	A	LC CLASS	GAMMA
1eRASS J051750.4-424231	79.4609	-42.7093	1.12 ± 0.2	0.2 ± 0.09	4.1	5.5	1	2.0 ± 0.4
1eRASS J051826.2-330104	79.6093	-33.0179	2.33 ± 0.35	0.53 ± 0.17	4.7	4.4	4	2.5 ± 0.2
1eRASS J051832.7-412701	79.6355	-41.4490	0.35 ± 0.12	1.5 ± 0.23	4.4	4.3	3	2.0 ± 0.4
1eRASS J051840.6-643637	79.6694	-64.6105	0.64 ± 0.07	3.6 ± 0.16	16.9	5.6	2	2.0 ± 0.1
1eRASS J051902.9-512630	79.7622	-51.4422	0.18 ± 0.07	2.58 ± 0.25	9.2	14.1	2	2.1 ± 0.2
1eRASS J051919.6-624734	79.8327	-62.7944	0.17 ± 0.04	0.68 ± 0.07	6.6	4.1	2	2.0 ± 0.2
1eRASS J052001.1-561254	80.0063	-56.2151	0.11 ± 0.05	1.05 ± 0.13	6.9	9.8	2	2.7 ± 0.3
1eRASS J052609.5-620733	81.5400	-62.1263	1.12 ± 0.09	0.1 ± 0.03	10.8	11.7	4	1.5 ± 0.2
1eRASS J052645.2-514658	81.6876	-51.7819	0.28 ± 0.09	1.69 ± 0.19	6.6	6.0	2	1.5 ± 0.2
1eRASS J053016.3-412535	82.5691	-41.4258	0.86 ± 0.19	4.89 ± 0.41	8.9	5.7	4	1.7 ± 0.2
1eRASS J053353.0-344210	83.4706	-34.7025	1.69 ± 0.29	0.38 ± 0.14	4.0	4.4	1	2.4 ± 0.4
1eRASS J053414.8-261057	83.5638	-26.1806	0.27 ± 0.14	1.84 ± 0.31	4.6	6.8	2	1.5 ± 0.3
1eRASS J053604.1-785423	84.0147	-78.9067	1.26 ± 0.19	6.32 ± 0.44	10.5	5.0	2	2.6 ± 0.1
1eRASS J053952.9-272523	84.9703	-27.4219	0.37 ± 0.17	4.69 ± 0.48	8.5	12.5	2	2.6 ± 0.2
1eRASS J054236.2-591856	85.6509	-59.3151	0.6 ± 0.08	3.26 ± 0.19	13.0	5.4	4	2.1 ± 0.1
1eRASS J054446.6-262214	86.1946	-26.3677	0.33 ± 0.15	1.66 ± 0.29	4.0	5.1	2	1.7 ± 0.4
1eRASS J054537.3-311250	86.4068	-31.2112	0.66 ± 0.21	2.78 ± 0.36	5.1	4.2	4	1.8 ± 0.3
1eRASS J054715.8-532340	86.8157	-53.3947	1.82 ± 0.2	0.38 ± 0.09	6.5	4.8	1	2.5 ± 0.2
1eRASS J055023.4-534129	87.5986	-53.6922	0.42 ± 0.1	2.11 ± 0.19	7.8	5.1	2	2.1 ± 0.2
1eRASS J055027.7-580532	87.6154	-58.0928	0.54 ± 0.09	0.11 ± 0.04	4.2	4.8	1	2.1 ± 0.4
1eRASS J055438.6-570336	88.6605	-57.0605	0.71 ± 0.11	0.13 ± 0.05	4.7	5.5	1	1.8 ± 0.3
1eRASS J055648.8-211921	89.2049	-21.3209	0.57 ± 0.21	4.13 ± 0.62	5.4	7.2	2	1.8 ± 0.3
1eRASS J055701.1-451409	89.2554	-45.2361	2.08 ± 0.28	0.19 ± 0.09	6.5	10.7	4	2.1 ± 0.3
1eRASS J060056.2-293922	90.2345	-29.6569	6.1 ± 0.67	1.38 ± 0.34	6.2	4.4	4	2.2 ± 0.2
1eRASS J060232.1-425547	90.6339	-42.9308	1.64 ± 0.3	0.31 ± 0.14	4.0	5.3	4	1.9 ± 0.4
1eRASS J060302.2-490549	90.7592	-49.0977	1.44 ± 0.25	0.25 ± 0.11	4.4	5.7	4	2.5 ± 0.4
1eRASS J060355.2-631007	90.9808	-63.1693	0.46 ± 0.06	0.11 ± 0.04	4.8	4.3	1	1.7 ± 0.3
1eRASS J060449.1-724217	91.2025	-72.7048	0.69 ± 0.09	0.13 ± 0.04	5.6	5.2	4	1.5 ± 0.3
1eRASS J060525.0-574408	91.3543	-57.7357	0.24 ± 0.07	1.04 ± 0.16	4.6	4.4	2	2.4 ± 0.3
1eRASS J060824.5-372649	92.1023	-37.4474	5.12 ± 0.57	$0.64^{\triangledown}$	7.9	8.0	1	1.8 ± 0.2
eRASSU J060829.4-435320	92.1225	-43.8888	$0.41^{\triangledown}$	6.33 ± 0.6	9.8	15.6	2	4.1 ± 0.2
eRASSU J061508.1-445921	93.7836	-44.9892	$0.33^{\triangledown}$	1.92 ± 0.33	4.9	5.9	2	3.2 ± 0.4
1eRASS J061553.4-550846	93.9747	-55.1484	0.21 ± 0.08	1.05 ± 0.18	4.2	4.9	4	2.0 ± 0.4
1eRASS J061710.9-703314	94.2972	-70.5537	2.5 ± 0.12	0.3 ± 0.05	16.6	8.5	4	2.2 ± 0.1
1eRASS J062106.9-711308	95.276	-71.2189	0.07 ± 0.03	1.02 ± 0.09	10.2	15.4	4	1.7 ± 0.2
1eRASS J063300.7-504152	98.2536	-50.6983	1.42 ± 0.23	0.27 ± 0.11	4.4	5.3	4	1.7 ± 0.3
eRASSU J063413.3-713908	98.5555	-71.6522	$0.2^{\triangledown}$	2.39 ± 0.14	15.8	11.7	2	4.2 ± 0.1
eRASSU J063430.2-653701	98.6258	-65.6169	$0.11^{\triangledown}$	0.51 ± 0.07	5.6	4.9	2	1.1 ± 0.3
1eRASS J064157.7-765007	100.4947	-76.8350	0.2 ± 0.06	0.83 ± 0.12	4.8	4.1	2	2.2 ± 0.3
1eRASS J064245.9-541752	100.6944	-54.2983	0.35 ± 0.11	1.66 ± 0.24	5.0	4.7	2	1.8 ± 0.3
1eRASS J064340.0-840006	100.9102	-84.0018	0.18 ± 0.08	0.9 ± 0.15	4.1	4.9	2	2.3 ± 0.5
eRASSU J064402.2-574247	101.0093	-57.7131	$0.32^{\triangledown}$	1.63 ± 0.21	6.3	5.0	2	2.0 ± 0.3
1eRASS J064449.4-603704	101.2053	-60.6176	0.56 ± 0.1	$0.12^{\triangledown}$	4.4	4.7	1	6.1 ± 0.6
1eRASS J064702.4-593705	101.7594	-59.6183	1.21 ± 0.16	0.21 ± 0.07	5.8	5.8	4	1.3 ± 0.3
1eRASS J065027.4-693258	102.6121	-69.5500	0.14 ± 0.04	0.76 ± 0.07	7.8	5.3	2	2.1 ± 0.2
1eRASS J065109.8-555031	102.7907	-55.8423	1.59 ± 0.23	0.31 ± 0.11	5.0	5.2	1	2.1 ± 0.4
1eRASS J065228.7-730534	103.1254	-73.0917	0.17 ± 0.05	0.7 ± 0.09	5.2	4.1	4	3.7 ± 0.4
1eRASS J065708.6-682354	104.2868	-68.3975	0.23 ± 0.05	2.0 ± 0.11	14.3	8.7	4	1.9 ± 0.1
1eRASS J065720.9-602728	104.3373	-60.4578	1.52 ± 0.17	0.15 ± 0.06	7.5	10.4	1	2.3 ± 0.3
1eRASS J065836.2-612103	104.6503	-61.3508	1.07 ± 0.14	0.19 ± 0.07	5.7	5.7	4	2.7 ± 0.3
eRASSU J070709.4-842044	106.7893	-84.3455	$0.4^{\triangledown}$	2.65 ± 0.26	8.7	6.6	2	4.1 ± 0.3
1eRASS J070827.4-562838	107.1141	-56.4772	1.13 ± 0.18	0.16 ± 0.08	4.9	7.3	1	1.3 ± 0.4
1eRASS J070947.6-703231	107.4480	-70.5425	0.98 ± 0.09	0.14 ± 0.04	8.4	7.1	4	2.5 ± 0.3
1eRASS J071217.2-703056	108.0703	-70.5160	3.52 ± 0.17	0.65 ± 0.08	15.2	5.4	4	2.4 ± 0.1
1eRASS J072429.8-672436	111.1249	-67.4100	0.83 ± 0.1	$0.17^{\triangledown}$	6.5	4.8	1	1.5 ± 0.3
1eRASS J072454.2-700254	111.2235	-70.0473	0.08 ± 0.03	0.45 ± 0.07	4.7	5.5	2	2.5 ± 0.4
1eRASS J072531.9-665731	111.3837	-66.9594	0.75 ± 0.1	0.12 ± 0.05	5.6	6.4	4	2.2 ± 0.3
1eRASS J072633.6-784308	111.6436	-78.7183	0.16 ± 0.06	0.77 ± 0.13	4.2	4.8	2	1.9 ± 0.4
1eRASS J073455.3-671725	113.7343	-67.2896	0.45 ± 0.08	2.03 ± 0.18	8.0	4.6	4	2.6 ± 0.2
1eRASS J073850.4-775454	114.7093	-77.9153	1.5 ± 0.17	0.29 ± 0.09	6.2	5.2	4	1.7 ± 0.3
1eRASS J074315.7-671305	115.8149	-67.2178	0.61 ± 0.1	0.14 ± 0.06	4.2	4.5	4	2.9 ± 0.4
eRASSU J074426.3+291606	116.1097	29.2682	$0.89^{\triangledown}$	10.43 ± 1.27	7.5	11.7	2	4.2 ± 0.3
1eRASS J075031.8+093330	117.6327	9.5586	12.67 ± 1.28	0.99 ± 0.39	8.7	12.8	4	1.5 ± 0.2
1eRASS J075526.1-713047	118.8542	-71.5134	0.15 ± 0.05	0.72 ± 0.1	5.3	4.9	2	1.3 ± 0.4

NAME	RA	DEC	FLUX ERASS1	FLUX ERASS2	S	A	LC CLASS	GAMMA
1eRASS J080354.9-734346	120.9785	-73.7296	1.49 ± 0.15	$0.26^{\triangledown}$	8.3	5.6	4	2.4 ± 0.2
1eRASS J080622.8+070247	121.5948	7.0469	0.86 ± 0.35	7.96 ± 1.06	6.4	9.2	2	0.7 ± 0.2
1eRASS J080807.9-775826	122.0348	-77.9737	1.01 ± 0.15	0.16 ± 0.06	5.3	6.3	1	1.4 ± 0.3
eRASSU J082055.8+192538	125.2325	19.4271	$1.17^{\triangledown}$	8.69 ± 1.09	6.9	7.5	2	5.2 ± 0.3
1eRASS J082336.8+042303	125.9033	4.3838	12.4 ± 1.3	75.29 ± 3.16	18.4	6.1	2	4.1 ± 0.1
1eRASS J083748.4-062335	129.4514	-6.3937	4.94 ± 0.74	1.16 ± 0.4	4.5	4.3	1	2.2 ± 0.3
1eRASS J084717.3-751050	131.8271	-75.1808	0.15 ± 0.05	0.78 ± 0.13	4.5	5.1	2	2.8 ± 0.5
eRASSU J084936.6-800247	132.4024	-80.0463	$0.19^{\triangledown}$	0.87 ± 0.16	4.3	4.6	4	1.3 ± 0.4
1eRASS J091329.3-811036	138.3694	-81.1765	1.05 ± 0.17	0.18 ± 0.08	4.5	5.9	4	2.8 ± 0.5
1eRASS J091619.3-821820	139.0841	-82.3043	1.09 ± 0.18	0.25 ± 0.1	4.2	4.3	4	1.6 ± 0.4
1eRASS J091657.8+060955	139.2408	6.1656	6.36 ± 0.91	$1.07^{\triangledown}$	5.8	5.9	1	5.4 ± 0.4
1eRASS J092753.8+162005	141.9746	16.3349	1.64 ± 0.5	7.95 ± 1.03	5.5	4.9	2	2.1 ± 0.2
1eRASS J093546.2-835823	143.9408	-83.9732	1.67 ± 0.23	0.29 ± 0.1	5.5	5.7	1	1.9 ± 0.3
1eRASS J095701.6+002422	149.2563	0.4056	5.09 ± 0.76	1.27 ± 0.43	4.4	4.0	1	1.6 ± 0.3
1eRASS J095836.6+170001	149.6527	17.0006	23.07 ± 1.85	1.63 ± 0.51	11.2	14.2	1	2.7 ± 0.1
1eRASS J100812.4-244044	152.0512	-24.6788	5.33 ± 0.77	0.89 ± 0.39	5.1	6.0	1	1.6 ± 0.3
eRASSU J100813.8-824050	152.0575	-82.6804	$0.28^{\triangledown}$	1.69 ± 0.23	6.2	6.1	4	3.2 ± 0.3
1eRASS J102851.3+251439	157.2143	25.2439	7.5 ± 0.94	0.87 ± 0.34	6.6	8.7	1	2.1 ± 0.2
1eRASS J103210.7-270559	158.0435	-27.0988	0.41 ± 0.22	2.67 ± 0.5	4.1	6.6	4	2.5 ± 0.5
1eRASS J103656.4-144922	159.2352	-14.8231	6.85 ± 0.91	0.82 ± 0.39	6.1	8.4	1	1.8 ± 0.3
1eRASS J104720.4-835045	161.8213	-83.8450	1.1 ± 0.2	0.22 ± 0.09	4.1	4.9	4	2.0 ± 0.4
1eRASS J110240.0-051809	165.6669	-5.3038	3.8 ± 0.7	$0.92^{\triangledown}$	4.1	4.1	1	4.9 ± 0.4
1eRASS J110459.5-135123	166.2481	-13.8574	3.89 ± 0.63	0.8 ± 0.3	4.4	4.9	4	2.4 ± 0.3
1eRASS J110936.6-083725	167.4030	-8.6235	6.62 ± 0.94	1.14 ± 0.36	5.5	5.8	1	3.0 ± 0.3
1eRASS J111110.6-434214	167.7940	-43.7039	4.31 ± 0.54	0.45 ± 0.19	6.8	9.7	4	1.9 ± 0.3
1eRASS J112220.7-102743	170.5866	-10.4629	4.01 ± 0.65	0.84 ± 0.31	4.4	4.8	4	1.6 ± 0.3
1eRASS J113028.2-080612	172.6173	-8.1028	5.95 ± 0.78	1.12 ± 0.37	5.6	5.3	4	3.3 ± 0.3
1eRASS J113306.2+074153	173.2756	7.6987	23.71 ± 1.78	5.69 ± 0.8	9.3	4.2	4	2.1 ± 0.1
1eRASS J114339.2+041547	175.9126	4.2630	0.62 ± 0.27	4.0 ± 0.67	4.7	6.5	2	2.3 ± 0.3
1eRASS J114608.7-760452	176.5322	-76.0809	0.26 ± 0.12	1.53 ± 0.23	4.9	6.0	2	1.6 ± 0.3
1eRASS J115124.5-371554	177.8523	-37.2655	4.0 ± 0.51	0.6 ± 0.23	6.1	6.7	1	1.6 ± 0.3
1eRASS J120703.2+245317	181.7638	24.8878	0.48 ± 0.26	3.76 ± 0.63	4.8	7.8	4	1.8 ± 0.3
1eRASS J121115.1-223501	182.8132	-22.5838	3.27 ± 0.5	$0.77^{\triangledown}$	5.0	4.3	1	1.3 ± 0.3
1eRASS J121309.1-301057	183.2874	-30.1821	0.94 ± 0.26	4.51 ± 0.63	5.2	4.8	4	2.2 ± 0.3
1eRASS J121439.4-045901	183.6631	-4.9846	0.89 ± 0.3	4.94 ± 0.73	5.2	5.6	4	2.1 ± 0.3
1eRASS J121648.6-424818	184.2038	-42.8049	3.03 ± 0.42	0.57 ± 0.17	5.4	5.3	1	1.4 ± 0.3
1eRASS J122157.0-272141	185.4873	-27.3620	3.21 ± 0.48	0.56 ± 0.23	5.0	5.8	4	1.4 ± 0.3
1eRASS J122355.8-051221	185.9828	-5.2062	3.37 ± 0.55	0.69 ± 0.3	4.3	4.9	1	1.9 ± 0.3
1eRASS J122529.2-215250	186.3718	-21.8800	1.5 ± 0.35	11.39 ± 1.02	9.2	7.6	2	2.1 ± 0.2
1eRASS J123250.6-373616	188.2111	-37.6038	0.68 ± 0.22	3.07 ± 0.42	5.1	4.5	4	1.5 ± 0.3
1eRASS J123408.7-161418	188.5369	-16.2385	4.46 ± 0.59	1.08 ± 0.33	5.0	4.1	1	2.5 ± 0.3
1eRASS J123822.2-253210	189.5929	-25.5363	193.58 ± 3.93	$1.12^{\triangledown}$	48.9	172.1	1	1.3 ± 0.0
1eRASS J124027.9-042735	190.1167	-4.4601	9.41 ± 0.95	0.8 ± 0.29	8.7	11.7	4	2.3 ± 0.2
1eRASS J124203.1-211223	190.5128	-21.2070	3.52 ± 0.51	0.69 ± 0.28	4.8	5.1	1	2.4 ± 0.3
1eRASS J124912.0-465534	192.3001	-46.9268	1.77 ± 0.31	0.31 ± 0.14	4.3	5.7	4	1.8 ± 0.4
1eRASS J125002.8-433111	192.5124	-43.5197	4.21 ± 0.48	0.97 ± 0.24	6.1	4.4	4	2.1 ± 0.2
1eRASS J125117.6-252059	192.8237	-25.3497	4.34 ± 0.55	0.99 ± 0.26	5.5	4.4	1	2.5 ± 0.3
1eRASS J125339.4-163430	193.4148	-16.5747	2.43 ± 0.44	0.4 ± 0.2	4.2	6.1	1	1.8 ± 0.4
1eRASS J125844.9-021714	194.6872	-2.2875	3.74 ± 0.55	0.72 ± 0.31	4.8	5.2	4	2.6 ± 0.3
1eRASS J130055.7-423149	195.2322	-42.5310	2.23 ± 0.36	0.42 ± 0.16	4.6	5.3	4	2.5 ± 0.4
eRASSU J130410.9-254525	196.0455	-25.7570	$0.57^{\triangledown}$	2.42 ± 0.38	4.8	4.2	2	1.6 ± 0.3
1eRASS J130535.7+014700	196.3995	1.7835	1.52 ± 0.36	6.73 ± 0.8	6.0	4.4	2	3.7 ± 0.2
1eRASS J130734.9+182333	196.8958	18.3927	5.07 ± 0.63	$1.17^{\triangledown}$	6.1	4.3	4	1.8 ± 0.2
1eRASS J130804.7+040128	197.0200	4.0246	7.7 ± 0.77	$0.99^{\triangledown}$	8.7	7.8	1	2.8 ± 0.2
1eRASS J130834.4-122802	197.1425	-12.4673	0.49 ± 0.21	3.1 ± 0.55	4.4	6.3	2	1.5 ± 0.3
1eRASS J131805.1-242322	199.5216	-24.3908	0.71 ± 0.23	4.67 ± 0.54	6.8	6.6	4	1.7 ± 0.2
1eRASS J131926.2-021228	199.8577	-2.2082	0.66 ± 0.24	3.22 ± 0.57	4.1	4.9	4	1.7 ± 0.3
1eRASS J132252.1+182253	200.7171	18.3813	3.52 ± 0.51	$0.87^{\triangledown}$	5.1	4.0	4	2.7 ± 0.3
1eRASS J132324.3+011829	200.8507	1.3085	5.58 ± 0.66	0.95 ± 0.34	6.3	5.9	1	2.1 ± 0.2
1eRASS J132821.9-341723	202.0916	-34.2902	7.94 ± 0.7	1.17 ± 0.28	9.0	6.8	4	2.2 ± 0.2
1eRASS J133144.6+203541	202.9371	20.5964	0.65 ± 0.23	2.91 ± 0.51	4.1	4.5	2	2.7 ± 0.3
1eRASS J133213.2-404205	203.0543	-40.7005	0.56 ± 0.19	2.74 ± 0.4	5.0	4.9	3	1.8 ± 0.3
1eRASS J133511.5-331720	203.8000	-33.2902	1.08 ± 0.27	5.56 ± 0.57	7.1	5.1	4	2.0 ± 0.2
1eRASS J133647.0-361249	204.1960	-36.2120	0.5 ± 0.19	2.21 ± 0.37	4.1	4.4	4	2.0 ± 0.4

NAME	RA	DEC	FLUX ERASS1	FLUX ERASS2	S	A	LC CLASS	GAMMA
1eRASS J134250.2-374154	205.7095	-37.6990	2.95 ± 0.42	0.49 ± 0.18	5.4	6.1	1	1.9 ± 0.3
1eRASS J134601.8-053857	206.5070	-5.6485	0.76 ± 0.25	3.53 ± 0.47	5.2	4.6	2	1.6 ± 0.3
1eRASS J135051.1-201009	207.7136	-20.1686	2.37 ± 0.41	0.46 ± 0.19	4.2	5.2	4	2.3 ± 0.4
1eRASS J135133.8-761146	207.8923	-76.1967	0.91 ± 0.24	4.06 ± 0.44	6.2	4.5	4	0.8 ± 0.2
eRASSU J135202.9-343706	208.0120	-34.6183	$0.62^{\triangledown}$	3.35 ± 0.45	6.1	5.4	2	2.0 ± 0.3
eRASSU J140158.1+081402	210.4922	8.2340	$0.54^{\triangledown}$	2.71 ± 0.42	5.2	5.1	2	5.2 ± 0.4
1eRASS J140353.4-243210	210.9734	-24.5374	0.44 ± 0.18	2.09 ± 0.37	4.0	4.7	4	0.3 ± 0.2
eRASSU J140702.9-360235	211.7623	-36.0431	$0.85^{\triangledown}$	17.13 ± 0.98	16.6	20.2	2	1.9 ± 0.1
eRASSU J140842.4-100025	212.1769	-10.0070	$0.46^{\triangledown}$	2.73 ± 0.45	5.0	5.9	2	3.5 ± 0.4
1eRASS J141904.3-215330	214.7683	-21.8918	10.62 ± 0.8	2.56 ± 0.4	9.0	4.2	1	2.3 ± 0.2
1eRASS J142140.3-295325	215.4151	-29.8892	1.15 ± 0.28	15.75 ± 0.95	14.7	13.7	2	3.1 ± 0.1
1eRASS J142405.0-164137	216.0215	-16.6942	3.28 ± 0.45	0.31 ± 0.16	6.2	10.6	4	2.4 ± 0.3
1eRASS J142752.8-230425	216.9692	-23.0727	0.4 ± 0.19	2.16 ± 0.37	4.3	5.4	2	1.9 ± 0.4
1eRASS J143045.4-332705	217.6868	-33.4509	0.61 ± 0.22	5.05 ± 0.59	7.0	8.2	3	2.0 ± 0.2
1eRASS J143237.8-245545	218.1578	-24.9292	3.52 ± 0.47	0.46 ± 0.19	6.0	7.6	1	1.6 ± 0.3
1eRASS J143308.1-772938	218.2825	-77.4946	0.43 ± 0.15	4.12 ± 0.43	8.1	9.5	2	2.6 ± 0.2
1eRASS J143330.9+003102	218.3792	0.5177	2.87 ± 0.42	0.45 ± 0.18	5.3	6.4	4	2.3 ± 0.3
1eRASS J143623.9-174103	219.0995	-17.6848	4.46 ± 0.54	0.52 ± 0.2	6.8	8.6	1	4.5 ± 0.3
1eRASS J143915.1-270227	219.8139	-27.0411	4.9 ± 0.59	0.86 ± 0.27	6.2	5.7	1	2.3 ± 0.3
1eRASS J144858.9-790610	222.2418	-79.1036	3.06 ± 0.38	0.7 ± 0.18	5.7	4.4	1	2.3 ± 0.3
eRASSU J145622.8-283853	224.0951	-28.6481	$0.5^{\triangledown}$	6.1 ± 0.65	8.6	12.2	2	5.3 ± 0.3
1eRASS J145629.0-171332	224.1202	-17.2275	0.63 ± 0.21	2.88 ± 0.46	4.4	4.5	2	2.1 ± 0.3
eRASSU J145954.5-260822	224.9772	-26.1396	$0.4^{\triangledown}$	1.99 ± 0.38	4.1	5.0	2	2.9 ± 0.5
1eRASS J150624.6-765958	226.6011	-76.9989	2.16 ± 0.33	0.36 ± 0.14	5.0	6.0	1	1.2 ± 0.3
1eRASS J151734.6-271017	229.3940	-27.1717	10.04 ± 0.81	$1.06^{\triangledown}$	11.1	9.5	1	1.6 ± 0.2
1eRASS J152749.1-793901	231.9520	-79.6498	1.57 ± 0.28	0.23 ± 0.11	4.5	6.9	1	2.1 ± 0.4
1eRASS J153406.2-090332	233.5257	-9.0591	19.75 ± 0.97	$1.08^{\triangledown}$	19.3	18.2	1	4.2 ± 0.1
eRASSU J164649.4-692539	251.7058	-69.4275	$0.43^{\triangledown}$	10.57 ± 0.75	13.4	24.4	2	4.5 ± 0.2
1eRASS J165122.0-843616	252.8431	-84.6053	1.97 ± 0.32	$0.44^{\triangledown}$	4.7	4.5	1	1.8 ± 0.3
1eRASS J173029.5-850501	262.6079	-85.0842	0.3 ± 0.13	1.96 ± 0.35	4.4	6.6	2	3.0 ± 0.4
eRASSU J180242.5-673708	270.6772	-67.6189	$1.22^{\triangledown}$	5.06 ± 0.71	5.4	4.1	2	1.6 ± 0.3
1eRASS J181610.0-654608	274.0413	-65.7720	0.77 ± 0.33	4.64 ± 0.74	4.8	6.1	4	2.0 ± 0.3
1eRASS J184230.2-713519	280.6236	-71.5892	1.44 ± 0.36	6.25 ± 0.78	5.6	4.3	2	1.6 ± 0.2
1eRASS J190146.6-552200	285.4444	-55.3664	9.02 ± 1.01	1.97 ± 0.51	6.2	4.6	1	5.1 ± 0.3
1eRASS J192128.0-502746	290.3677	-50.4655	0.69 ± 0.31	9.98 ± 1.1	8.1	14.4	2	2.8 ± 0.2
1eRASS J200146.6-861201	300.4463	-86.2005	0.59 ± 0.2	2.49 ± 0.42	4.1	4.2	2	2.1 ± 0.4
1eRASS J201206.8-442838	303.0301	-44.4778	0.96 ± 0.36	12.57 ± 1.29	8.7	13.1	2	2.0 ± 0.2
1eRASS J201626.1-790248	304.1099	-79.0466	6.6 ± 0.69	0.59 ± 0.23	8.3	11.2	1	2.6 ± 0.2
1eRASS J203710.7-434641	309.2902	-43.7791	0.85 ± 0.35	5.15 ± 0.84	4.7	6.1	4	2.0 ± 0.3
1eRASS J204112.1-613948	310.3005	-61.6635	6.0 ± 0.77	1.18 ± 0.37	5.7	5.1	1	2.1 ± 0.3
eRASSU J205101.3-743003	312.7555	-74.5008	$0.95^{\triangledown}$	11.06 ± 0.99	10.2	11.7	2	2.1 ± 0.2
1eRASS J210857.6-562835	317.2435	-56.4754	1.55 ± 0.4	6.24 ± 0.83	5.1	4.0	2	3.2 ± 0.3
1eRASS J215334.9-714745	328.3926	-71.7977	0.35 ± 0.18	2.62 ± 0.48	4.4	7.4	4	2.9 ± 0.4
1eRASS J215650.3-473028	329.2098	-47.5079	3.24 ± 0.58	0.62 ± 0.28	4.1	5.2	1	2.4 ± 0.4
1eRASS J223102.3-493705	337.7601	-49.6183	2.22 ± 0.48	10.4 ± 1.07	7.0	4.7	4	2.0 ± 0.2
1eRASS J224831.6-413039	342.1313	-41.5111	4.72 ± 0.75	0.82 ± 0.33	4.8	5.8	4	1.7 ± 0.3
1eRASS J225728.2-753629	344.3685	-75.6080	3.07 ± 0.46	0.68 ± 0.23	4.6	4.5	4	2.2 ± 0.3
1eRASS J225802.9-523647	344.5122	-52.6119	0.62 ± 0.26	3.69 ± 0.65	4.4	5.9	3	2.6 ± 0.3
1eRASS J230453.8-393631	346.2248	-39.6084	11.1 ± 1.04	$0.76^{\triangledown}$	9.9	14.5	1	2.2 ± 0.2
1eRASS J230518.2-481700	346.3262	-48.2834	4.66 ± 0.69	1.0 ± 0.35	4.7	4.7	4	2.4 ± 0.3
1eRASS J230801.5-421556	347.0059	-42.2650	3.56 ± 0.6	0.62 ± 0.29	4.4	5.8	1	1.7 ± 0.3
1eRASS J231004.4-453925	347.5192	-45.6572	6.26 ± 0.77	1.49 ± 0.44	5.3	4.2	4	2.6 ± 0.2
1eRASS J232048.0-603345	350.2001	-60.5626	9.19 ± 0.87	1.46 ± 0.44	7.9	6.3	4	1.9 ± 0.2
1eRASS J232809.3-442238	352.039	-44.3781	0.93 ± 0.31	4.04 ± 0.66	4.2	4.3	3	2.3 ± 0.3
1eRASS J232819.9-605652	352.083	-60.9477	4.59 ± 0.63	1.09 ± 0.32	5.0	4.2	1	1.4 ± 0.3
1eRASS J233109.5-603056	352.7893	-60.5157	4.96 ± 0.65	0.75 ± 0.28	5.9	6.6	1	2.2 ± 0.2
eRASSU J234403.1-352640	356.0130	-35.4446	$1.21^{\triangledown}$	119.84 ± 4.34	27.3	99.3	2	4.6 ± 0.1
1eRASS J234522.8-501854	356.3460	-50.3158	4.52 ± 0.63	0.9 ± 0.31	5.2	5.1	4	1.7 ± 0.2
1eRASS J235154.2-484752	357.9770	-48.7975	7.83 ± 0.82	1.92 ± 0.45	6.3	4.1	4	2.1 ± 0.2
1eRASS J235240.2-350900	358.1681	-35.1499	6.4 ± 0.85	0.42 ± 0.22	6.8	15.1	4	2.0 ± 0.2
1eRASS J235933.8-440243	359.8924	-44.0455	14.7 ± 1.22	2.09 ± 0.48	9.6	7.0	4	2.3 ± 0.2

Appendix B

Additional information for the population of eROSITA TDEs

B.1 X-ray properties of the TDE sample

The eROSITA spectral modeling results for eRASS1-4(5) are provided in Table B.1. The eROSITA eRASS1-4(5) light curves are shown in Fig. B.1.

B.2 J1421 – an optical transient in LS10

In the LS10 scanning strategy, each sky area is not observed simultaneously in *griz* optical bands but rather is covered at different times. In cases of drastic variability, such as the appearance of a new source, images taken at different bands can be used to identify transients. The inspection of the LS10 images revealed that the optical counterpart was detected only in the *g*-band and only in two consecutive epochs in 2019 (MJD 58643.14 and 58643.16, see Fig. B.2). It was not detected in any other bands and epochs between 2015 to 2021[1]. The optical emission of 19.21 mag appeared at least 14 months before the eROSITA peak (MJD 59064) in eRASS2 and has faded to a non-detection during the X-ray decline phase, which was confirmed by a total absence of the source during a follow-up observation with NTT in March 2021.

The source is likely extragalactic and physically associated with a pair of nearby merging galaxies. At their common redshift of z = 0.06, the distance between the center of the closest galaxy and the g-band source is only ≈ 20 kpc. The luminosity ($L_X \approx 1.4 \times 10^{43} \mathrm{ergs}^{-1}$), soft X-ray spectrum (kT $\approx$ 170eV), and flaring light curve would be consistent with an off-nuclear TDE. As the optical flare was detected approximately 1 year before the X-ray peak, this would require the X-ray emission to either be from a repeating event or a delayed late-time response. Other non-TDE extragalactic origins cannot be excluded. However, we point out that soft X-ray spectra would be atypical for standard AGN and/or fast blue

[1] `https://www.legacysurvey.org/viewer/exposures/?ra=215.4154&dec=-29.8895&layer=ls-dr10`

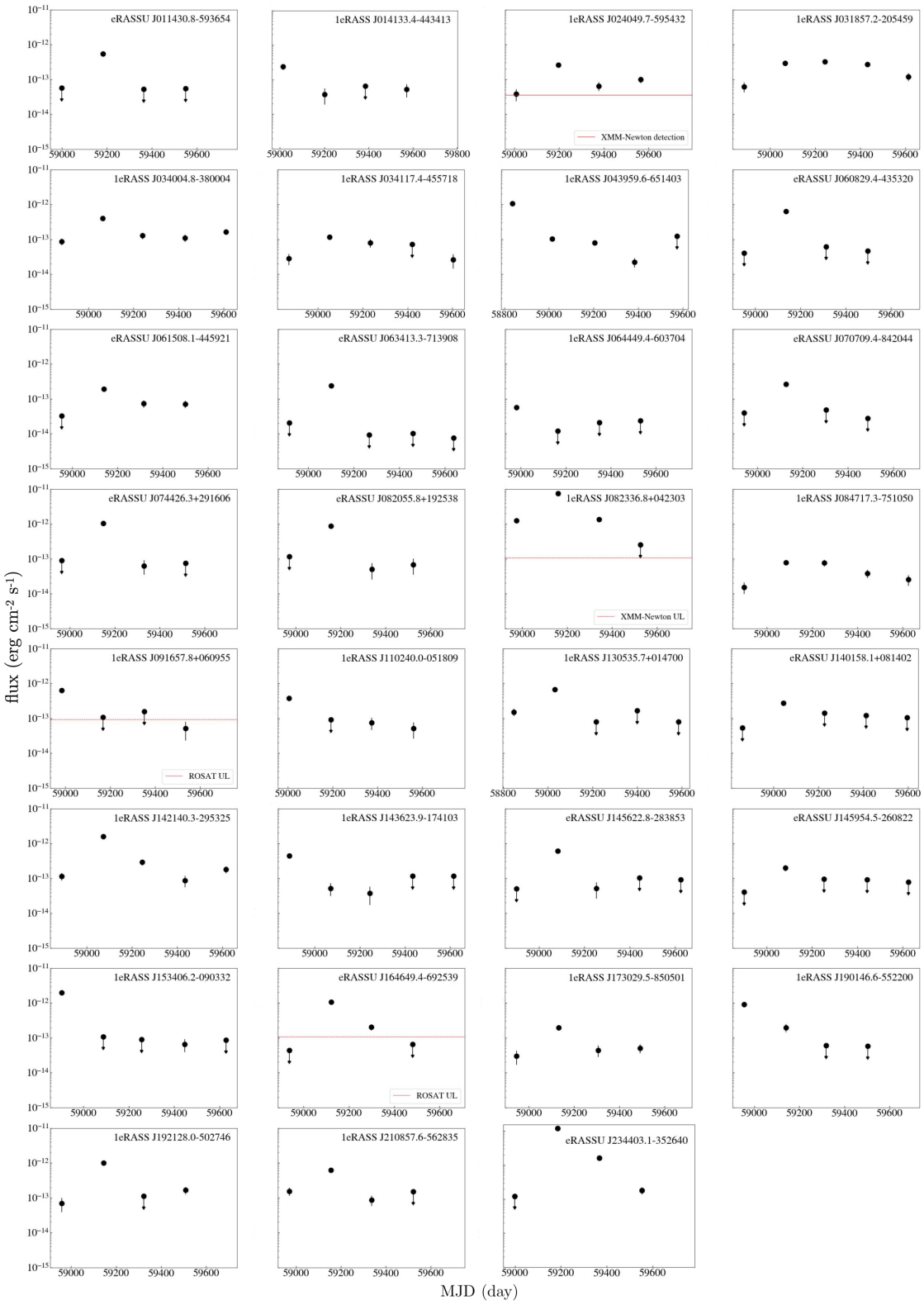

Figure B.1: eRASS1-4(5) eROSITA X-ray light curves for the TDE sample in 0.2–2.3 keV. Red dashed and solid lines denote archival upper limits and detections, respectively.

Table B.1: Spectral modeling results of TDE candidates for eRASS1-eRASS5 in keV. The modeling is performed for all detections with sufficient counts with detection likelihood DET_LIKE>15.

ERO_NAME	kT_{eRASS1}	kT_{eRASS2}	kT_{eRASS3}	kT_{eRASS4}	kT_{eRASS5}
eRASSU J011430.8-593654	-	0.10± 0.01	-	-	-
1eRASS J014133.4-443413	0.08 ± 0.01	-	-	-	-
1eRASS J024049.7-595432	-	0.20 ± 0.02	0.28 ± 0.08	0.27 ± 0.06	-
1eRASS J031857.2-205459	0.05 ± 0.01	0.09 ± 0.01	0.08 ± 0.01	0.08 ± 0.01	0.07 ± 0.01
1eRASS J034004.8-380004	0.24 ± 0.07	0.17 ± 0.01	0.29 ± 0.05	0.58 ± 0.22	0.20 ± 0.03
1eRASS J034117.4-455718	-	0.17 ± 0.04	0.12 ± 0.04	-	-
1eRASS J043959.6-651403	0.081 ± 0.002	0.21 ± 0.02	0.14 ± 0.03	0.35 ± 0.27	-
eRASSU J060829.4-435320	-	0.11 ± 0.01	-	-	-
eRASSU J061508.1-445921	-	0.14 ± 0.02	0.12 ± 0.03	0.14 ± 0.03	-
eRASSU J063413.3-713908	-	0.12 ± 0.01	-	-	-
1eRASS J064449.4-603704	0.08 ± 0.01	-	-	-	-
eRASSU J070709.4-842044	-	0.14 ± 0.01	-	-	-
eRASSU J074426.3+291606	-	0.10 ± 0.01	-	-	-
eRASSU J082055.8+192538	-	0.08 ± 0.01	-	-	-
1eRASS J082336.8+042303	0.09 ± 0.01	0.087 ± 0.002	0.08 ± 0.01	-	-
1eRASS J084717.3-751050	-	0.32 ± 0.06	0.50 ± 0.18	0.33 ± 0.11	-
1eRASS J091657.8+060955	0.06 ± 0.01	-	-	-	-
1eRASS J110240.0-051809	0.08 ± 0.01	-	-	-	-
1eRASS J130535.7+014700	0.09 ± 0.02	0.11 ± 0.01	-	-	-
eRASSU J140158.1+081402	-	0.06 ± 0.01	-	-	-
1eRASS J142140.3-295325	0.17 ± 0.03	0.17 ± 0.01	0.16 ± 0.02	-	0.16 ± 0.03
1eRASS J143623.9-174103	0.10 ± 0.01	-	-	-	-
eRASSU J145622.8-283853	-	0.09 ± 0.01	-	-	-
eRASSU J145954.5-260822	-	0.18 ± 0.04	-	-	-
1eRASS J153406.2-090332	0.118 ± 0.004	-	-	-	-
eRASSU J164649.4-692539	-	0.096 ± 0.004	0.13 ± 0.02	-	-
1eRASS J173029.5-850501	-	0.24 ± 0.03	-	0.52 ± 0.16	-
1eRASS J190146.6-552200	0.09 ± 0.01	0.06 ± 0.01	-	-	-
1eRASS J192128.0-502746	-	0.20 ± 0.02	-	0.29 ± 0.07	-
1eRASS J210857.6-562835	0.19 ± 0.05	0.13 ± 0.01	0.16 ± 0.08	-	-
eRASSU J234403.1-352640	-	0.075 ± 0.002	0.050 ± 0.003	0.04 ± 0.01	-

optical transients (e.g., Bright et al. 2022). The long duration of the X-ray event (J1421 was detected in all five eRASSes) and much earlier optical detection make a Galactic stellar flare origin very unlikely.

This example shows how our view of optical and X-ray TDE candidates depends on the scanning strategy, sensitivity of the instruments and precise timing of observations. If the LS10 observation coincidentally was not taken during the optical brightening phase, the source would be classified as X-ray bright only. Moreover, there would be no evidence to assume that the source is not nuclear.

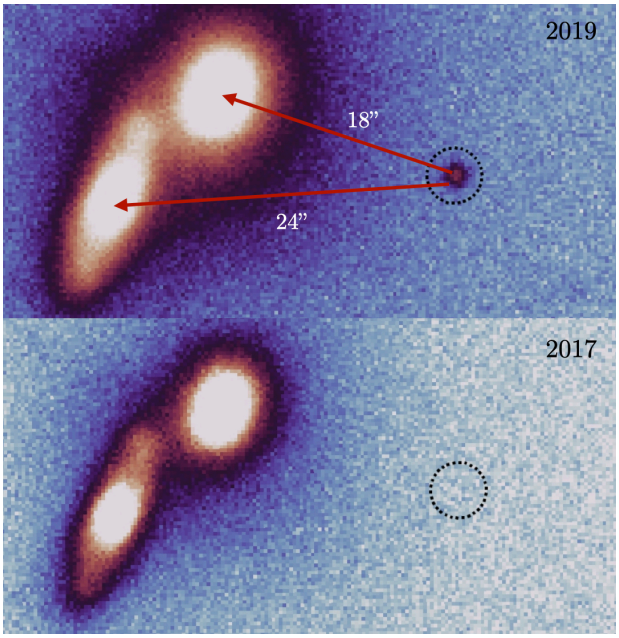

Figure B.2: LS10 images of the optical transient at the location of J1421. Top: the detection of the transient in g-band in 2019 (MJD 58643). The distances from the centers of two merging galaxies at z=0.06 are ≈ 18 arcsec (21 kpc) and ≈ 24 arcsec (28 kpc), respectively. Bottom: the non-detection of the source in g-band in 2017 (MJD 57850).

B.3 Multiwavelength flares of TDEs

This section presents additional mid-IR and optical properties and light curves for the TDE sample. The mid-IR non host-subtracted NEOWISE light curves for all 31 TDEs are shown in Fig. B.3 and B.4. To filter the reliable W1, W2 data points we applied quality indicator factor qi_fact > 0.9. The optical host-subtracted light curves for sources showing a significant flare (see Table 3.5) are shown in Fig. B.5. The summary of used optical data and calculated ATLAS ULs is presented in Table B.2.

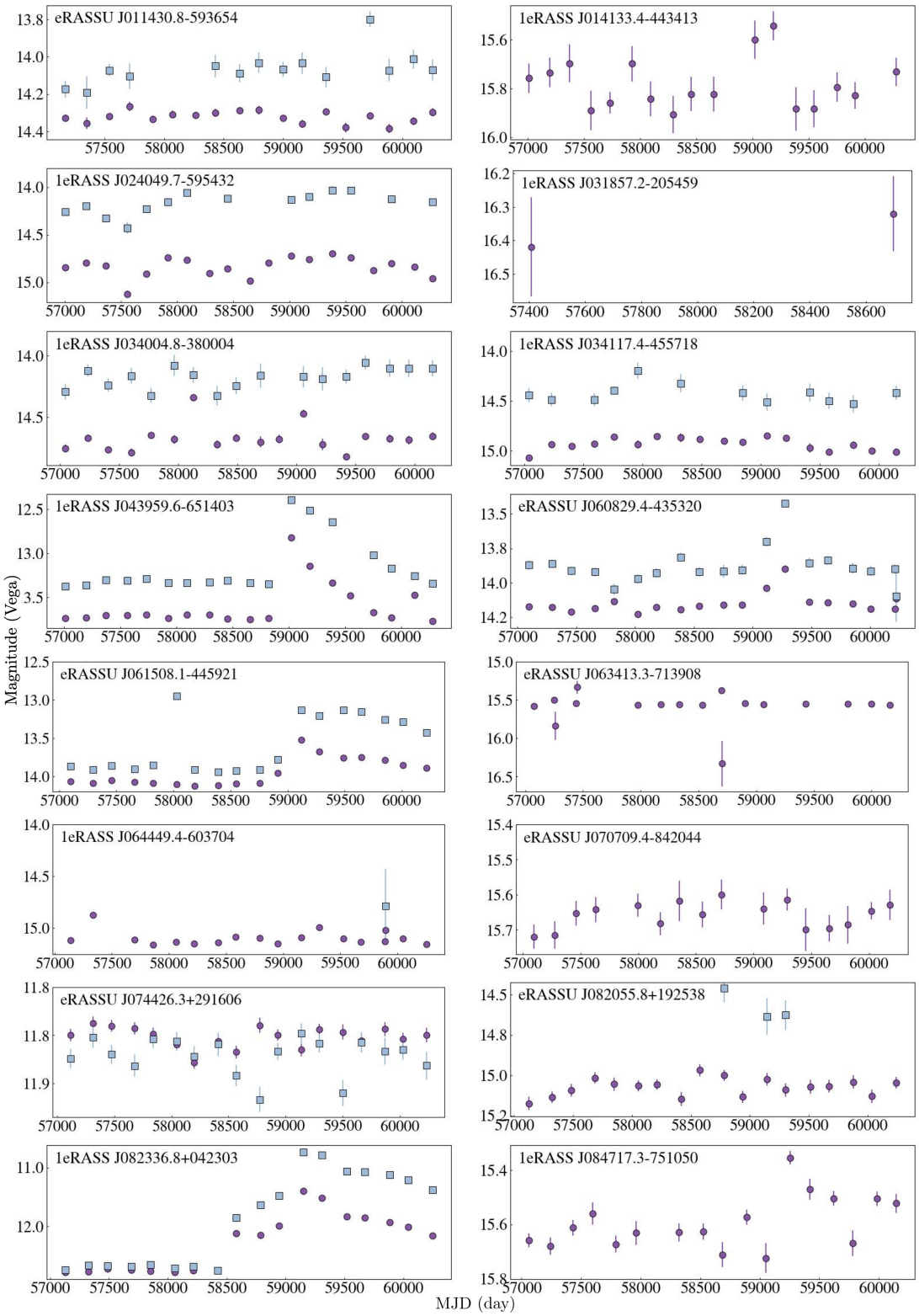

Figure B.3: NEOWISE W1 and W2 light curves, binned in ten-day intervals, for the TDE sample. Purple circles denote W1 data points, and blue squares show W2 data points.

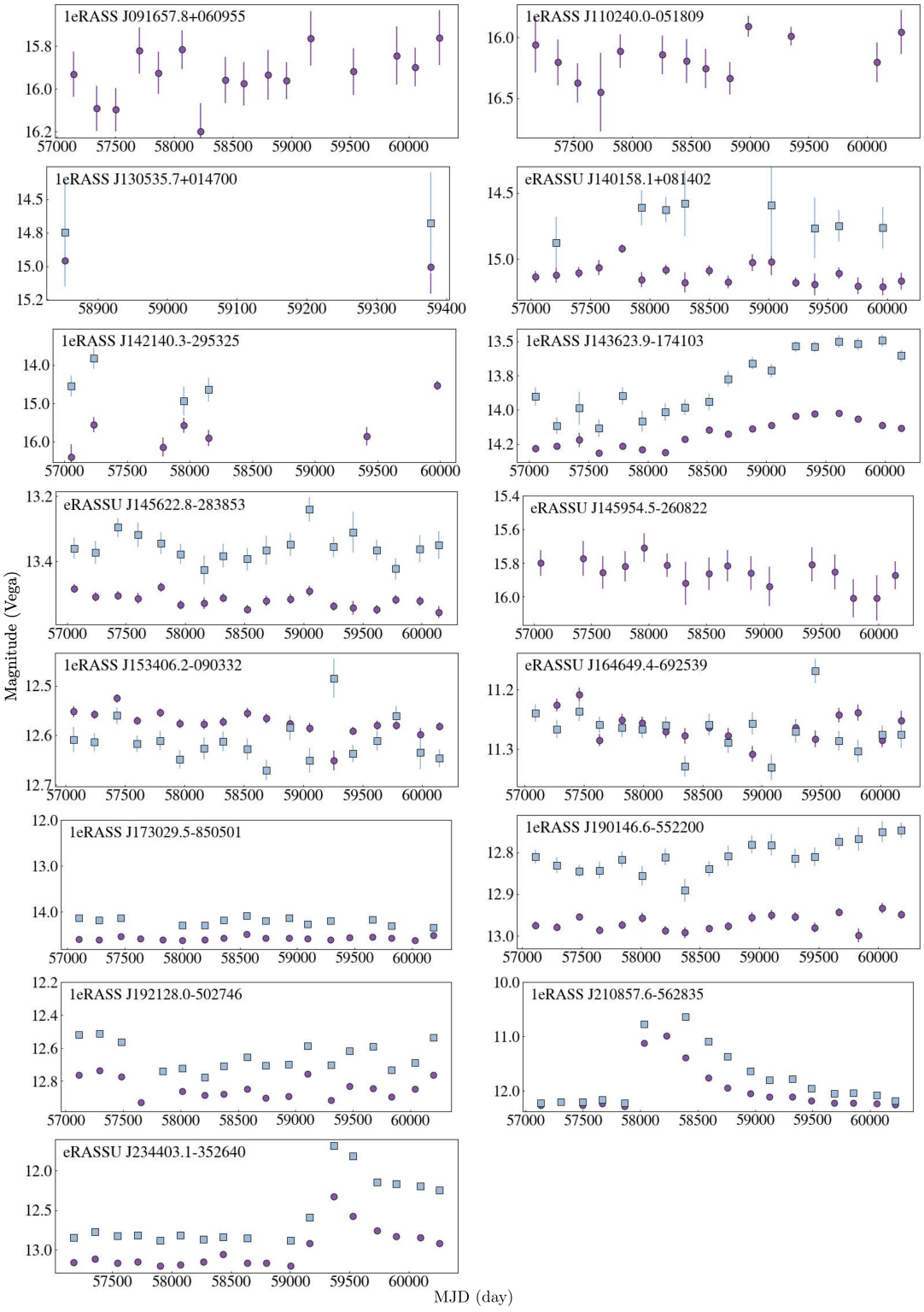

Figure B.4: Continuation of Fig. B.3.

Table B.2: Optical magnitudes at peak for the TDE sample. Detections are provided in the g-band with 1σ errors at the peak time of the optical flare. Triangles represent 5σ ATLAS upper limits in the o-band for sources without detected optical flares.

Name	Survey	Peak magnitude [AB mag]	Transient ID
J0114-59	ATLAS	$19.0^{\triangledown}$	
J0141-44	ATLAS	$18.7^{\triangledown}$	
J0240-59	ATLAS	$19.0^{\triangledown}$	
J0318-20	ZTF	20.3 ± 0.1	
J0340-38	ATLAS	$19.1^{\triangledown}$	
J0341-45	ATLAS	$18.9^{\triangledown}$	
J0439-65	Gaia	18.41 ± 0.12	Gaia20cdq/AT2020jgh
J0608-43	ATLAS	$18.8^{\triangledown}$	
J0615-44	ATLAS	$19.0^{\triangledown}$	
J0634-71	ATLAS	$18.8^{\triangledown}$	
J0644-60	ATLAS	$19.0^{\triangledown}$	
J0707-84	ATLAS	$18.8^{\triangledown}$	
J0744+29	ZTF	19.6 ± 0.1	ZTF20acgrymn
J0820+19	ATLAS	$19.0^{\triangledown}$	
J0823+04	ZTF	17.13 ± 0.04	AT2019avd
J0847-75	ATLAS	$18.9^{\triangledown}$	
J0916+06	ATLAS	$18.9^{\triangledown}$	
J1102-05	ZTF	19.8 ± 0.3	
J1305+01	ATLAS	$19.0^{\triangledown}$	
J1401+08	ATLAS	$19.0^{\triangledown}$	
J1421-29	ATLAS	$18.3^{\triangledown}$	
J1436-17	ATLAS	$19.0^{\triangledown}$	
J1456-28	ATLAS	$18.2^{\triangledown}$	
J1459-26	ATLAS	$18.7^{\triangledown}$	
J1534-09	ATLAS	$18.9^{\triangledown}$	
J1646-69	ATLAS	$18.6^{\triangledown}$	
J1730-85	ATLAS	$18.6^{\triangledown}$	
J1901-55	ATLAS	$18.8^{\triangledown}$	
J1921-50	ATLAS	$18.9^{\triangledown}$	
J2108-56	ATLAS	$18.8^{\triangledown}$	
J2344-35	Gaia	16.50 ± 0.11	Gaia20eub/AT2020wjw

B.4 SED modeling

This section presents SED modeling results in Table B.3.

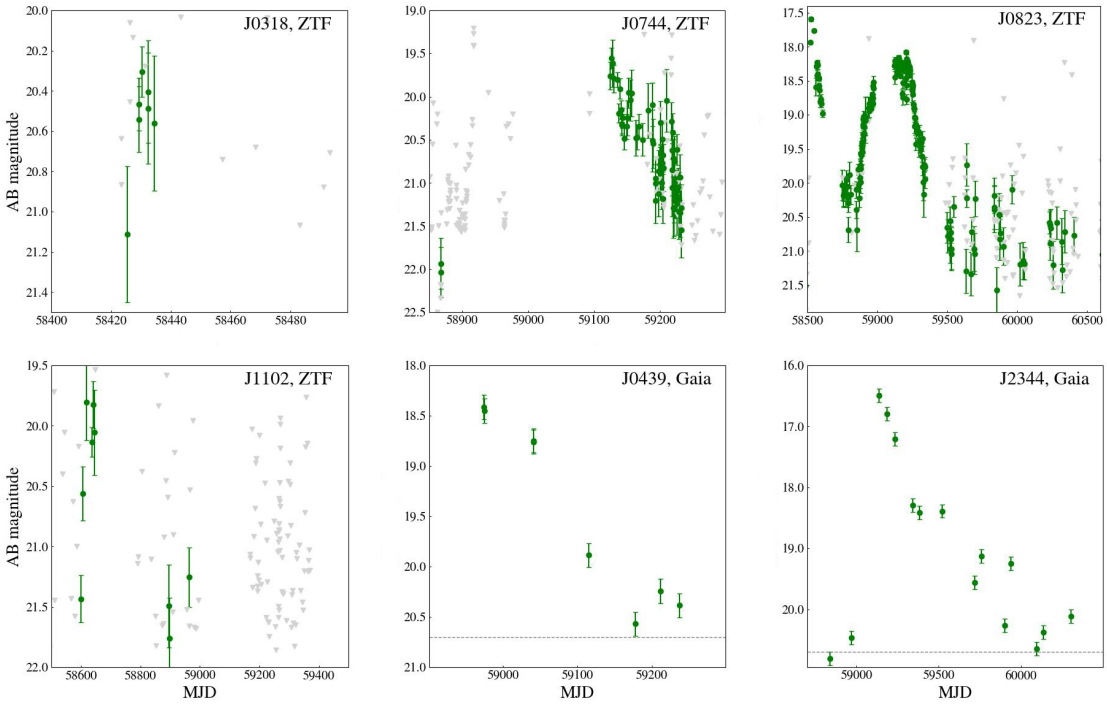

Figure B.5: Host-subtracted light curves of optical flares of six sources from the TDE sample in g-band. The gray triangles denote upper limits in ZTF light curves. The gray dashed lines show the Gaia detection limit of 20.7 mag (Hodgkin et al., 2021).

Table B.3: SED modeling results for 28 sources from eROSITA TDE sample. The mass column lists host stellar masses. The surviving mass, used in this work, is obtained by multiplying the total mass by the coefficient mfrac. The $^{0,0}u-r$ represents the rest frame colors.

Name	Mass $\times 10^{10}\mathrm{M}_{\odot}$	mfrac	$^{0,0}u-r$ [mag]
J0240-59	$6.88^{+3.8}_{-3.76}$	0.62	$1.68^{+0.33}_{-0.25}$
J0340-38	$5.09^{+5.59}_{-1.97}$	0.66	$1.63^{+0.22}_{-0.27}$
J0341-45	$6.52^{+3.64}_{-3.47}$	0.67	$1.31^{+0.32}_{-0.18}$
J0615-44	$5.84^{+6.56}_{-3.32}$	0.62	$2.13^{+0.10}_{-0.14}$
J0707-84	$3.18^{+9.79}_{-1.11}$	0.61	$2.08^{+0.10}_{-0.79}$
J1102-05	$3.01^{+2.05}_{-1.63}$	0.64	$1.58^{+0.42}_{-0.33}$
J1305+01	$3.0^{+1.76}_{-1.36}$	0.61	$1.9^{+0.29}_{-0.37}$
J1730-85	$22.5^{+14.93}_{-8.48}$	0.63	$1.95^{+0.31}_{-0.25}$
J0114-59	$13.43^{+1.91}_{-1.74}$	0.61	$2.31^{+0.05}_{-0.05}$
J0141-44	$0.88^{+0.17}_{-0.16}$	0.6	$2.1^{+0.06}_{-0.06}$
J0318-20	$1.77^{+2.14}_{-0.97}$	0.61	$1.63^{+0.31}_{-0.48}$
J0439-65	$16.35^{+4.0}_{-2.53}$	0.64	$2.21^{+0.06}_{-0.06}$
J0608-43	$2.17^{+0.49}_{-0.32}$	0.64	$1.78^{+0.11}_{-0.11}$
J0634-71	$1.72^{+0.39}_{-0.3}$	0.62	$1.98^{+0.06}_{-0.06}$
J0644-60	$2.12^{+0.44}_{-0.33}$	0.61	$2.0^{+0.06}_{-0.06}$
J0744+29	$0.19^{+0.05}_{-0.03}$	0.62	$2.07^{+0.08}_{-0.08}$
J0820+19	$2.26^{+0.51}_{-0.41}$	0.61	$2.07^{+0.08}_{-0.08}$
J0823+04	$2.29^{+0.57}_{-0.42}$	0.62	$2.25^{+0.08}_{-0.08}$
J0916+06	$1.02^{+0.19}_{-0.17}$	0.57	$2.11^{+0.05}_{-0.05}$
J1401+08	$10.65^{+7.37}_{-4.37}$	0.63	$1.82^{+0.26}_{-0.28}$
J1436-17	$10.92^{+10.67}_{-4.0}$	0.61	$2.14^{+0.16}_{-0.18}$
J1456-28	$17.55^{+4.86}_{-3.81}$	0.61	$2.12^{+0.06}_{-0.06}$
J1459-26	$0.88^{+0.18}_{-0.16}$	0.6	$2.11^{+0.06}_{-0.06}$
J1534-09	$2.31^{+0.32}_{-0.29}$	0.61	$2.15^{+0.07}_{-0.07}$
J1901-55	$4.51^{+1.2}_{-0.94}$	0.61	$2.07^{+0.08}_{-0.08}$
J1921-50	$9.1^{+2.26}_{-1.72}$	0.62	$2.15^{+0.07}_{-0.07}$
J2108-56	$7.85^{+1.84}_{-1.56}$	0.6	$1.97^{+0.10}_{-0.10}$
J2344-35	$2.41^{+0.47}_{-0.33}$	0.65	$2.07^{+0.08}_{-0.08}$

Bibliography

Aartsen M., et al., 2017, Journal of Instrumentation, 12, P03012–P03012

Abdurro'uf et al., 2022, The Astrophysical Journal Supplement Series, 259, 35

Aird J., et al., 2010, Monthly Notices of the Royal Astronomical Society, 401, 2531

Alexander K. D., Wieringa M. H., Berger E., Saxton R. D., Komossa S., 2017, The Astrophysical Journal, 837, 153

Alexander K. D., van Velzen S., Horesh A., Zauderer B. A., 2020, Space Science Reviews, 216, 81

Alp D., Larsson J., 2020, The Astrophysical Journal, 896, 39

Andreoni I., et al., 2022, Nature, 612, 430–434

Arcavi I., et al., 2014, The Astrophysical Journal, 793, 38

Arcodia R., et al., 2021, Nature, 592, 704

Arcodia R., et al., 2024, Astronomy and Astrophysics, 684, A64

Arnaud K. A., 1996, in Jacoby G. H., Barnes J., eds, Astronomical Society of the Pacific Conference Series Vol. 101, Astronomical Data Analysis Software and Systems V. p. 17

Assef R. J., et al., 2013, The Astrophysical Journal, 772, 26

Auchettl K., Ramirez-Ruiz E., Guillochon J., 2018, The Astrophysical Journal, 852, 37

Avakyan A., et al., 2023, Astronomy and Astrophysics, 675, A199

Babel J., North P., 1997, Astronomy and Astrophysics, 325, 195

Bachetti M., et al., 2014, Nature, 514, 202

Bade N., Komossa S., Dahlem M., 1996, Astronomy and Astrophysics, 309, L35

Baldwin J. A., Phillips M. M., Terlevich R., 1981, Publications of the Astronomical Society of the Pacific, 93, 5

Ballet J., Bruel P., Burnett T. H., Lott B., The Fermi-LAT collaboration 2023, arXiv e-prints, p. arXiv:2307.12546

Barrows R. S., Mezcua M., Comerford J. M., 2019, The Astrophysical Journal, 882, 181

Baskill D. S., Wheatley P. J., Osborne J. P., 2005, Monthly Notices of the Royal Astronomical Society, 357, 626

Basko M. M., Sunyaev R. A., 1976, Monthly Notices of the Royal Astronomical Society, 175, 395

Becker R. H., White R. L., Helfand D. J., 1995, The Astrophysical Journal, 450, 559

Becker W., et al., 2021, Astronomy and Astrophysics, 648, A30

Bell E. F., McIntosh D. H., Katz N., Weinberg M. D., 2003, The Astrophysical Journal Supplement Series, 149, 289

Bellm E. C., et al., 2019, Publications of the Astronomical Society of the Pacific, 131, 018002

Berger E., 2014, Annual Review of Astronomy and Astrophysics, 52, 43

Bernardini F., et al., 2017, Monthly Notices of the Royal Astronomical Society, 470, 4815

Best P. N., Heckman T. M., 2012, Monthly Notices of the Royal Astronomical Society, 421, 1569

Bhatt H., Pandey J. C., Singh K. P., Sagar R., Kumar B., 2014, Journal of Astrophysics and Astronomy, 35, 39

Blagorodnova N., et al., 2017, The Astrophysical Journal, 844, 46

Blanchard P. K., et al., 2017, The Astrophysical Journal, 843, 106

Blandford R., Meier D., Readhead A., 2019, Annual Review of Astronomy and Astrophysics, 57, 467

Bloom J. S., et al., 2011, Science, 333, 203–206

Bogensberger D., Nandra K., Buchner J., 2024, Astronomy and Astrophysics, 687, A21

Boller T., Brandt W. N., Fink H., 1996, Astronomy and Astrophysics, 305, 53

Boller T., et al., 2021, Astronomy and Astrophysics, 647, A6

Boller T., et al., 2022, Astronomy and Astrophysics, 661, A8

Boller T., et al., 2025, Astronomy and Astrophysics, 700, A61

Bonnerot C., Rossi E. M., Lodato G., Price D. J., 2015, Monthly Notices of the Royal Astronomical Society, 455, 2253

Bonnerot C., Rossi E. M., Lodato G., 2017, Monthly Notices of the Royal Astronomical Society, 464, 2816

Bortolas E., Ryu T., Broggi L., Sesana A., 2023, Monthly Notices of the Royal Astronomical Society, 524

Bradley Cenko S., et al., 2012, The Astrophysical Journal, 753, 77

Bright J. S., et al., 2022, The Astrophysical Journal, 926, 112

Brockamp M., Baumgardt H., Kroupa P., 2011, Monthly Notices of the Royal Astronomical Society, 418, 1308

Brown T., et al., 2013, Publications of the Astronomical Society of the Pacific, 125

Brown G. C., et al., 2015, Monthly Notices of the Royal Astronomical Society, 452, 4297

Brunner H., et al., 2022, Astronomy and Astrophysics, 661, A1

Buchner J., 2021, J. Open Source Softw., 6, 3001

Buchner J., et al., 2014, Astronomy and Astrophysics, 564, A125

Buckley D. A. H., Swart G. P., Meiring J. G., 2006, in Stepp L. M., ed., Society of Photo-Optical Instrumentation Engineers Conference Series Vol. 6267, Ground-based and Airborne Telescopes. p. 62670Z

Bulbul E., et al., 2024, Astronomy and Astrophysics, 685, A106

Burgh E. B., et al., 2003, in Iye M., Moorwood A. F. M., eds, Society of Photo-Optical Instrumentation Engineers Conference Series Vol. 4841, Instrument Design and Performance for Optical/Infrared Ground-based Telescopes. pp 1463–1471

Burrows D. N., et al., 2005, Space Science Reviews, 120, 165

Burrows D. N., et al., 2011, Nature, 476, 421

Buzzoni B., et al., 1984, The Messenger, 38, 9

Calzetti D., et al., 2000, The Astrophysical Journal, 533, 682

Capetti A., Massaro F., Baldi R. D., 2017, Astronomy and Astrophysics, 601, A81

Cappelluti N., et al., 2009, Astronomy and Astrophysics, 495, L9

Cash W., 1976, Astronomy and Astrophysics, 52, 307

Cendes Y., et al., 2024, The Astrophysical Journal, 971, 185

Cenko S., et al., 2012, The Astrophysical Journal, 753, 77

Chabrier G., 2003, Publications of the Astronomical Society of the Pacific, 115, 763

Chakraborty J., et al., 2021, The Astrophysical Journal Letters, 921, L40

Chan C.-H., Piran T., Krolik J. H., Saban D., 2019, The Astrophysical Journal, 881, 113

Chang Y. L., Arsioli B., Giommi P., Padovani P., Brandt C. H., 2019, Astronomy and Astrophysics, 632, A77

Chen J.-H., Dou L.-M., Shen R.-F., 2022, The Astrophysical Journal, 928, 63

Chevalier R. A., Fransson C., 1994, The Astrophysical Journal, 420, 268

Childress M. J., Vogt F. P. A., Nielsen J., Sharp R. G., 2014, Astrophysics and Space Science, 349, 617

Condon J. J., et al., 1998, The Astronomical Journal, 115, 1693

Conroy C., Gunn J. E., 2010, The Astrophysical Journal, 712, 833

Coppejans D. L., et al., 2016, Monthly Notices of the Royal Astronomical Society, 456, 4441

Cordes J. M., Lazio T. J. W., 2002, arXiv e-prints, pp astro–ph/0207156

Costa E., et al., 1997, Nature, 387, 783

Coughlin E. R., Nixon C. J., 2019, The Astrophysical Journal Letters, 883, L17

Crawford S. M., et al., 2010, in Silva D. R., Peck A. B., Soifer B. T., eds, Society of Photo-Optical Instrumentation Engineers Conference Series Vol. 7737, Observatory Operations: Strategies, Processes, and Systems III. p. 773725

Cropper M., et al., 2004, Monthly Notices of the Royal Astronomical Society, 349, 39

Cruise M., et al., 2025, Nature Astronomy, 9, 36

Czerny B., 2006, in Gaskell C. M., McHardy I. M., Peterson B. M., Sergeev S. G., eds, Astronomical Society of the Pacific Conference Series Vol. 360, AGN Variability from X-Rays to Radio Waves. p. 265

D'Abrusco R., et al., 2019, The Astrophysical Journal Supplement Series, 242, 4

D'Avanzo P., et al., 2012, Monthly Notices of the Royal Astronomical Society, 425, 506

Dai Z. G., Wang X. Y., Wu X. F., Zhang B., 2006, Science, 311, 1127

Dai L., McKinney J. C., Miller M. C., 2015, The Astrophysical Journal, 812, L39

Dai L., McKinney J. C., Roth N., Ramirez-Ruiz E., Miller M. C., 2018, The Astrophysical Journal Letters, 859, L20

Dey A., et al., 2019, The Astronomical Journal, 157, 168

Dezalay J. P., Lestrade J. P., Barat C., Talon R., Sunyaev R., Terekhov O., Kuznetsov A., 1996, The Astrophysical Journal Letters, 471, L27

Di Matteo T., 1998, Monthly Notices of the Royal Astronomical Society, 299, L15

Donley J. L., Brandt W. N., Eracleous M., Boller T., 2002, The Astronomical Journal, 124, 1308

Dopita M., et al., 2010, Astrophysics and Space Science, 327, 245

Dou L., et al., 2017, The Astrophysical Journal Letters, 841, L8

Dressler A., et al., 2011, Publications of the Astronomical Society of the Pacific, 123, 288

Duchesne S. W., et al., 2023, Publications of the Astronomical Society of Australia, 40, e034

Duchesne S. W., et al., 2024, Publications of the Astronomical Society of Australia, 41, e003

Dwarkadas V. V., Gruszko J., 2011, Monthly Notices of the Royal Astronomical Society, 419, 1515

Dykaar H., et al., 2024, The Astrophysical Journal, 973, 104

Eckart A., et al., 1986, Astronomy and Astrophysics, 168, 17

Esquej P., et al., 2008, Astronomy and Astrophysics, 489, 543–554

Evans C. R., Kochanek C. S., 1989, The Astrophysical Journal Letters, 346, L13

Evans D. A., Worrall D. M., Hardcastle M. J., Kraft R. P., Birkinshaw M., 2006, The Astrophysical Journal, 642, 96

Evans P. A., et al., 2023, Nature Astronomy, 7, 1368–1375

Fabbiano G., 1989, Annual Review of Astronomy and Astrophysics, 27, 87

Fabrika S., Ueda Y., Vinokurov A., Sholukhova O., Shidatsu M., 2015, Nature Physics, 11, 551–553

Fanaroff B. L., Riley J. M., 1974, Monthly Notices of the Royal Astronomical Society, 167, 31P

Fang K., Metzger B. D., Vurm I., Aydi E., Chomiuk L., 2020, The Astrophysical Journal, 904, 4

Feng H., Soria R., 2011, New Astronomy Reviews, 55, 166–183

Flesch E. W., 2023, The Open Journal of Astrophysics, 6, 49

Foreman-Mackey D., Hogg D. W., Lang D., Goodman J., 2013, Publications of the Astronomical Society of the Pacific, 125, 306

Fotopoulou S., et al., 2016, Astronomy and Astrophysics, 587, A142

Franchini A., et al., 2023, Astronomy and Astrophysics, 675, A100

Frank J., King A., Raine D. J., 2002, Accretion Power in Astrophysics: Third Edition

French K. D., Arcavi I., Zabludoff A., 2016, The Astrophysical Journal Letters, 818, L21

French K. D., Wevers T., Law-Smith J., Graur O., Zabludoff A. I., 2020a, Space Science Reviews, 216, 32

French K. D., et al., 2020b, The Astrophysical Journal, 891, 93

Freudling W., et al., 2013, Astronomy and Astrophysics, 559, A96

Fuhrmeister B., Schmitt J. H. M. M., 2003, Astronomy and Astrophysics, 403, 247

Fürst F., et al., 2016, The Astrophysical Journal Letters, 831, L14

Gaia Collaboration et al., 2016, Astronomy and Astrophysics, 595, A1

Gaia Collaboration et al., 2023, Astronomy and Astrophysics, 674, A1

Galeev A. A., Rosner R., Vaiana G. S., 1979, The Astrophysical Journal, 229, 318

Galloway D. K., et al., 2020, The Astrophysical Journal Supplement Series, 249, 32

Gehrels N., Ramirez-Ruiz E., Fox D. B., 2009, Annual Review of Astronomy and Astrophysics, 47, 567

Gezari S., 2021, Annual Review of Astronomy and Astrophysics, 59, 21

Gezari S., et al., 2006, The Astrophysical Journal Letters, 653, L25

Gezari S., et al., 2008, The Astrophysical Journal, 676, 944

Gezari S., et al., 2009, The Astrophysical Journal, 698, 1367

Gezari S., et al., 2012, Nature, 485, 217

Gezari S., Cenko S. B., Arcavi I., 2017, The Astrophysical Journal, 851, L47

Giacconi R., Gursky H., Kellogg E., Schreier E., Tananbaum H., 1971, The Astrophysical Journal Letters, 167, L67

Giacconi R., et al., 1972, The Astrophysical Journal, 178, 281

Giustini M., Miniutti G., Saxton R. D., 2020, Astronomy and Astrophysics, 636, L2

Gomez S., et al., 2020, Monthly Notices of the Royal Astronomical Society, 497, 1925–1934

Goodwin A. J., et al., 2023, Monthly Notices of the Royal Astronomical Society, 522, 5084–5097

Goodwin A. J., Arcodia R., Miniutti G., Miller-Jones J. C. A., van Velzen S., 2025a, Publications of the Astronomical Society of Australia, 42, e130

Goodwin A. J., et al., 2025b, The Astrophysical Journal Supplement Series, 278, 36

Grandi P., Torresi E., Macconi D., Boccardi B., Capetti A., 2021, The Astrophysical Journal, 911, 17

Greene J. E., 2012, Nature Communications, 3

Greiner J., Schwarz R., Zharikov S., Orio M., 2000, Astronomy and Astrophysics, 362, L25

Grotova I., Liu Z., Malyali A., Rau A., Merloni A., 2021, The Astronomer's Telegram, 14668, 1

Grotova I., et al., 2025a, Astronomy and Astrophysics, 693, A62

Grotova I., et al., 2025b, Astronomy and Astrophysics, 697, A159

Grupe D., Thomas H. C., Leighly K. M., 1999, Astronomy and Astrophysics, 350, L31

Güdel M., 2004, Astronomy and Astrophysics, 12, 71

Güdel M., Nazé Y., 2009, Astronomy and Astrophysics, 17, 309

Guillochon J., Ramirez-Ruiz E., 2013, The Astrophysical Journal, 767, 25

Guillochon J., Ramirez-Ruiz E., 2015, The Astrophysical Journal, 809, 166

Guillochon J., Manukian H., Ramirez-Ruiz E., 2014, The Astrophysical Journal, 783, 23

Guo H., et al., 2025, The Astrophysical Journal, 979, 235

Guolo M., et al., 2024, The Astrophysical Journal, 966, 160

Günther H. M., Frost J., Theriault-Shay A., 2017, The Astronomical Journal, 154, 243

HI4PI Collaboration: et al., 2016, Astronomy and Astrophysics, 594, A116

Haemmerich S., et al., 2025, arXiv e-prints, p. arXiv:2510.25589

Haisch B., Strong K. T., Rodono M., 1991, Annual Review of Astronomy and Astrophysics, 29, 275

Hammerstein E., et al., 2021, The Astrophysical Journal Letters, 908, L20

Hammerstein E., et al., 2022, The Astrophysical Journal, 942, 9

Hammerstein E., et al., 2023, The Astrophysical Journal, 957, 86

Harrison F. A., et al., 2013, The Astrophysical Journal, 770, 103

Hawkins M., 2002, Monthly Notices of the Royal Astronomical Society, 329, 76

Hickish J., et al., 2018, Monthly Notices of the Royal Astronomical Society, 475, 5677

Hillebrandt W., Niemeyer J. C., 2000, Annual Review of Astronomy and Astrophysics, 38, 191–230

Hills J. G., 1975, Nature, 254, 295

Hodgkin S. T., et al., 2021, Astronomy and Astrophysics, 652, A76

Holoien T. W.-S., et al., 2015, Monthly Notices of the Royal Astronomical Society, 455, 2918

Homan D., et al., 2023, Astronomy and Astrophysics, 672, A167

Hotan A. W., et al., 2021, Publications of the Astronomical Society of Australia, 38

Igo Z., et al., 2024, Astronomy and Astrophysics, 686, A43

Immler S., Lewin W. H. G., 2003, in Weiler K., ed., Lecture Notes in Physics, Vol. 598, Supernovae and Gamma-Ray Bursters. Springer, pp 91–111

Immler S., et al., 2006, The Astrophysical Journal Letters, 648, L119

Israel G. L., et al., 2016, Monthly Notices of the Royal Astronomical Society: Letters, 466, L48

Itoh R., et al., 2020, The Astrophysical Journal, 901, 3

Ivezić Ž., et al., 2019, The Astrophysical Journal, 873, 111

Iwasawa K., et al., 2024, Astronomy and Astrophysics, 684, A153

Jagoda N., Austin G., Mickiewicz S., Goddard R., 1972, IEEE Transactions on Nuclear Science, 19, 579

Janka H.-T., 2012, Annual Review of Nuclear and Particle Science, 62, 407

Jansen F., et al., 2001, Astronomy and Astrophysics, 365, L1

Jiang Y.-F., Guillochon J., Loeb A., 2016, The Astrophysical Journal, 830, 125

Johnson B. D., Leja J., Conroy C., Speagle J. S., 2021, The Astrophysical Journal Supplement Series, 254, 22

Jones D. H., et al., 2004, Monthly Notices of the Royal Astronomical Society, 355, 747

Kaaret P., Feng H., Roberts T. P., 2017, Annual Review of Astronomy and Astrophysics, 55, 303

Karas V., Šubr L., 2007, Astronomy and Astrophysics, 470, 11–19

Kellermann K. I., Pauliny-Toth I. I. K., 1969, Astrophysical Journal Letters, 155, L71

Kennicutt R. C. J., 1983, The Astrophysical Journal, 272, 54

Khabibullin I., Sazonov S., 2014, Monthly Notices of the Royal Astronomical Society, 444, 1041

King A., 2022, Monthly Notices of the Royal Astronomical Society, 515, 4344

Klebesadel R. W., Strong I. B., Olson R. A., 1973, The Astrophysical Journal Letters, 182, L85

Kochanek C. S., et al., 2017, Publications of the Astronomical Society of the Pacific, 129, 104502

Komossa S., 2015, Journal of High Energy Astrophysics, 7, 148

Komossa S., Bade N., 1999, Astronomy and Astrophysics, 343, 775

Komossa S., Greiner J., 1999, Astronomy and Astrophysics, 349, L45

Komossa S., et al., 2004, The Astrophysical Journal, 603, L17

König O., et al., 2022a, Astronomy and Computing, 38, 100529

König O., et al., 2022b, Nature, 605, 248

Kormendy J., Ho L. C., 2013, Annual Review of Astronomy and Astrophysics, 51, 511

Kosec P., Pinto C., Fabian A. C., Walton D. J., 2018, Monthly Notices of the Royal Astronomical Society, 473, 5680

Kouveliotou C., Meegan C. A., Fishman G. J., Bhat N. P., Briggs M. S., Koshut T. M., Paciesas W. S., Pendleton G. N., 1993, The Astrophysical Journal Letters, 413, L101

Kozieł-Wierzbowska D., Stasińska G., 2011, Monthly Notices of the Royal Astronomical Society, 415, 1013

Kraft R. P., Burrows D. N., Nousek J. A., 1991, The Astrophysical Journal, 374, 344

Krishnan S., et al., 2024, Astronomy & Astrophysics, 691

Kumar P., Granot J., 2003, The Astrophysical Journal, 591, 1075

Lacy J. H., Townes C. H., Hollenbach D. J., 1982, The Astrophysical Journal, 262, 120

Lacy M., et al., 2020, Publications of the Astronomical Society of the Pacific, 132, 035001

Laing R. A., Jenkins C. R., Wall J. V., Unger S. W., 1994, in Bicknell G. V., Dopita M. A., Quinn P. J., eds, Astronomical Society of the Pacific Conference Series Vol. 54, The Physics of Active Galaxies. p. 201

Lanzuisi G., et al., 2014, The Astrophysical Journal, 781, 105

Lasota J.-P., 2001, New Astronomy Reviews, 45, 449–508

Lasota J. P., Alexander T., Dubus G., Barret D., Farrell S. A., Gehrels N., Godet O., Webb N. A., 2011, The Astrophysical Journal, 735, 89

Law-Smith J., Ramirez-Ruiz E., Ellison S. L., Foley R. J., 2017, The Astrophysical Journal, 850, 22

Levi M., et al., 2019, in Bulletin of the American Astronomical Society. p. 57 (arXiv:1907.10688), doi:10.48550/arXiv.1907.10688

Lewin W. H. G., van Paradijs J., van den Heuvel E. P. J., 1995, Cambridge Astrophysics Series, 26

Lin D., et al., 2018, Nature Astronomy, 2, 656–661

Linial I., Metzger B. D., 2024, The Astrophysical Journal Letters, 963, L1

Liu R.-Y., Xi S.-Q., Wang X.-Y., 2020, Physical Review D, 102, 083028

Liu T., et al., 2022a, Astronomy and Astrophysics, 661, A5

Liu X.-L., Dou L.-M., Chen J.-H., Shen R.-F., 2022b, The Astrophysical Journal, 925, 67

Liu Z., et al., 2023, Astronomy and Astrophysics, 669, A75

Liu Z., et al., 2024, Astronomy & Astrophysics, 683, L13

Lodato G., Rossi E. M., 2010, Monthly Notices of the Royal Astronomical Society, 410, 359–367

Loeb A., Ulmer A., 1997, The Astrophysical Journal, 489, 573

Long K. S., Dodorico S., Charles P. A., Dopita M. A., 1981, The Astrophysical Journal Letters, 246, L61

Lu W., Bonnerot C., 2019, Monthly Notices of the Royal Astronomical Society, 492, 686

Lu W., Kumar P., Evans Neal J. I., 2016, Monthly Notices of the Royal Astronomical Society, 458, 575

Lynden-Bell D., 1969, Nature, 223, 690

Lyubarskii Y. E., 1997, Monthly Notices of the Royal Astronomical Society, 292, 679

MacLeod M., Guillochon J., Ramirez-Ruiz E., 2012, The Astrophysical Journal, 757, 134

Mageshwaran T., Mangalam A., 2015, The Astrophysical Journal, 814, 141

Maguire K., Eracleous M., Jonker P. G., MacLeod M., Rosswog S., 2020, Space Science Reviews, 216

Mainzer A., et al., 2011, The Astrophysical Journal, 731, 53

Maksym W. P., Lin D., Irwin J. A., 2014, The Astrophysical Journal Letters, 792, L29

Malyali A., Rau A., Nandra K., 2019, Monthly Notices of the Royal Astronomical Society, 489, 5413

Malyali A., et al., 2021, Astronomy and Astrophysics, 647, A9

Malyali A., et al., 2023a, Monthly Notices of the Royal Astronomical Society, 520, 3549

Malyali A., et al., 2023b, Monthly Notices of the Royal Astronomical Society, 520, 4209

Markowitz A., et al., 2024, Astronomy and Astrophysics, 684, A101

Marocco F., et al., 2021, The Astrophysical Journal Supplement Series, 253, 8

Martin D. C., et al., 2007, The Astrophysical Journal Supplement Series, 173, 342

Masci F. J., et al., 2019, Publications of the Astronomical Society of the Pacific, 131, 018003

Massaro E., et al., 2015, Astrophysics and Space Science, 357, 75

Masterson M., et al., 2024, The Astrophysical Journal, 961, 211

Matt G., et al., 2000, Astronomy and Astrophysics, 358, 177

Matt G., Guainazzi M., Maiolino R., 2003, Monthly Notices of the Royal Astronomical Society, 342, 422

Mayer M. G. F., Becker W., Predehl P., Sasaki M., 2023, Astronomy and Astrophysics, 676, A68

McConnell D., et al., 2020, Publications of the Astronomical Society of Australia, 37, e048

McHardy I. M., Papadakis I. E., Uttley P., Page M. J., Mason K. O., 2004, Monthly Notices of the Royal Astronomical Society, 348, 783

McHardy I. M., Koerding E., Knigge C., Uttley P., Fender R. P., 2006, Nature, 444, 730

Medvedev P., Gilfanov M., Sazonov S., Sunyaev R., Khorunzhev G., 2023, Astronomy Letters, 48, 735

Mendel J. T., Simard L., Palmer M., Ellison S. L., Patton D. R., 2014, The Astrophysical Journal Supplement Series, 210, 3

Merloni A., et al., 2024, Astronomy and Astrophysics, 682, A34

Metzger B. D., Stone N. C., 2016, Monthly Notices of the Royal Astronomical Society, 461, 948

Metzger B. D., Stone N. C., Gilbaum S., 2022, The Astrophysical Journal, 926, 101

Miles P. R., Coughlin E. R., Nixon C. J., 2020, The Astrophysical Journal, 899, 36

Miller M. C., 2015, The Astrophysical Journal, 805, 83

Miller J. M., Fabbiano G., Miller M. C., Fabian A. C., 2003, The Astrophysical Journal, 585, L37

Mingo B., et al., 2022, Monthly Notices of the Royal Astronomical Society, 511, 3250

Miniutti G., et al., 2019, Nature, 573, 381

Miniutti G., et al., 2023, Astronomy and Astrophysics, 670, A93

Molina M., et al., 2009, Monthly Notices of the Royal Astronomical Society, 399, 1293

Mummery A., 2021, Monthly Notices of the Royal Astronomical Society, 504, 5144

Mummery A., Balbus S. A., 2020, Monthly Notices of the Royal Astronomical Society, 497, L13

Mummery A., van Velzen S., 2025, Monthly Notices of the Royal Astronomical Society, 541, 429

Mummery A., et al., 2023, Monthly Notices of the Royal Astronomical Society, 527, 2452

Murphy E. J., et al., 2011, The Astrophysical Journal, 737, 67

Nabizadeh A., Balman , 2020, Advances in Space Research, 66, 1139–1146

Nandra K., Pounds K. A., 1994, Monthly Notices of the Royal Astronomical Society, 268, 405

Nandra K., George I. M., Mushotzky R. F., Turner T. J., Yaqoob T., 1997, The Astrophysical Journal, 476, 70

Navarro Navarro N., Piran T., 2025, The Astrophysical Journal, 983, 177

Noda H., Done C., 2018, Monthly Notices of the Royal Astronomical Society, 480, 3898

Nomoto K., Thielemann F. K., Yokoi K., 1984, The Astrophysical Journal, 286, 644

Nousek J. A., et al., 2006, The Astrophysical Journal, 642, 389

Oda M., et al., 1971, The Astrophysical Journal Letters, 166, L1

Ok S., Schwope A., Buckley D. A. H., Brink J., 2024, Astronomy and Astrophysics, 686, A175

Orio M., Covington J., Ögelman H., 2001, Astronomy and Astrophysics, 373, 542

Osterbrock D. E., 1989, Astrophysics of gaseous nebulae and active galactic nuclei

Paggi A., et al., 2020, Astronomy and Astrophysics, 641, A62

Pan X., Li S.-L., Cao X., 2023, The Astrophysical Journal, 952, 32

Panagiotou C., et al., 2023, The Astrophysical Journal Letters, 948, L5

Pandel D., Córdova F. A., Howell S. B., 2003, Monthly Notices of the Royal Astronomical Society, 346, 1231

Paolillo M., et al., 2017, Monthly Notices of the Royal Astronomical Society, 471, 4398

Parkinson E. J., et al., 2022, Monthly Notices of the Royal Astronomical Society, 510, 5426

Pavlinsky M., et al., 2021, Astronomy and Astrophysics, 650, A42

Piran T., Svirski G., Krolik J., Cheng R. M., Shiokawa H., 2015, The Astrophysical Journal, 806, 164

Planck Collaboration et al., 2016, Astronomy and Astrophysics, 594, A13

Polzin A., et al., 2023, The Astrophysical Journal, 959, 75

Poutanen J., Lipunova G., Fabrika S., Butkevich A. G., Abolmasov P., 2007, Monthly Notices of the Royal Astronomical Society, 377, 1187

Predehl P., et al., 2021, Astronomy and Astrophysics, 647, A1

Prevot M. L., Lequeux J., Maurice E., Prevot L., Rocca-Volmerange B., 1984, Astronomy and Astrophysics, 132, 389

Prieto J. L., et al., 2016, The Astrophysical Journal Letters, 830, L32

Pringle J. E., Savonije G. J., 1979, Monthly Notices of the Royal Astronomical Society, 187, 777

Prokhorenko S. A., et al., 2024, Monthly Notices of the Royal Astronomical Society, 528, 5972

Pye J. P., Rosen S., Fyfe D., Schröder A. C., 2015, Astronomy and Astrophysics, 581, A28

Quintin E., et al., 2023, Astronomy and Astrophysics, 675, A152

Quirola-Vásquez J., et al., 2022, Astronomy and Astrophysics, 663, A168

Raj A., Nixon C. J., 2021, The Astrophysical Journal, 909, 82

Rees M. J., 1988, Nature, 333, 523

Reeves J. N., Turner M. J. L., 2000, Monthly Notices of the Royal Astronomical Society, 316, 234

Reiners A., 2012, Living Reviews in Solar Physics, 9, 1

Reines A. E., Volonteri M., 2015, The Astrophysical Journal, 813, 82

Remillard R. A., McClintock J. E., 2006, Annual Review of Astronomy and Astrophysics, 44, 49–92

Reusch S., et al., 2022, Physical Review Letters, 128, 221101

Rhodes L., et al., 2023, Monthly Notices of the Royal Astronomical Society, 521, 389

Ricarte A., Tremmel M., Natarajan P., Quinn T., 2021, The Astrophysical Journal Letters, 916, L18

Ricci C., et al., 2016, The Astrophysical Journal, 820, 5

Ricci C., et al., 2020, The Astrophysical Journal Letters, 898, L1

Risaliti G., Elvis M., Nicastro F., 2002, The Astrophysical Journal, 571, 234

Roming P. W. A., et al., 2005, Space Science Reviews, 120, 95

Roth N., Kasen D., Guillochon J., Ramirez-Ruiz E., 2016, The Astrophysical Journal, 827, 3

Roth N., van Velzen S., Cenko S. B., Mushotzky R. F., 2021, The Astrophysical Journal, 910, 93

Ruiz A., et al., 2022, Monthly Notices of the Royal Astronomical Society, 511, 4265

Russell B. R., Immler S., 2012, The Astrophysical Journal, 748, L29

Saglia R. P., et al., 2016, The Astrophysical Journal, 818, 47

Salvato M., et al., 2018, Monthly Notices of the Royal Astronomical Society, 473, 4937

Salvato M., et al., 2022, Astronomy and Astrophysics, 661, A3

Salvato M., et al., 2025, arXiv e-prints, p. arXiv:2509.02842

Saxena A., et al., 2024, Astronomy and Astrophysics, 690, A365

Saxton R. D., et al., 2008, Astronomy and Astrophysics, 480, 611

Saxton C. J., Soria R., Wu K., Kuin N. P. M., 2012a, Monthly Notices of the Royal Astronomical Society, 422, 1625–1639

Saxton R. D., et al., 2012b, Astronomy and Astrophysics, 541, A106

Saxton R. D., et al., 2017, Astronomy and Astrophysics, 598, A29

Saxton R., Komossa S., Auchettl K., Jonker P. G., 2020, Space Science Reviews, 216, 85

Saxton R. D., et al., 2022, Astronomy and Computing, 38, 100531

Sazonov S., et al., 2021, Monthly Notices of the Royal Astronomical Society, 508, 3820

Schmidt M., 1968, The Astrophysical Journal, 151, 393

Schober J., Schleicher D. R. G., Klessen R. S., 2014, Monthly Notices of the Royal Astronomical Society, 446, 2

Schwope A. D., et al., 2024, Astronomy and Astrophysics, 690, A243

Seppi R., et al., 2022, Astronomy and Astrophysics, 665, A78

Sfaradi I., et al., 2024, Monthly Notices of the Royal Astronomical Society, 527, 7672

Shakura N. I., Sunyaev R. A., 1973, Astronomy and Astrophysics, 24, 337

Shappee B. J., et al., 2014, The Astrophysical Journal, 788, 48

Shiokawa H., Krolik J. H., Cheng R. M., Piran T., Noble S. C., 2015, The Astrophysical Journal, 804, 85

Simard L., Trevor Mendel J., Patton D. R., Ellison S. L., McConnachie A. W., 2011, The Astrophysical Journal Supplement Series, 196, 11

Simmonds C., Buchner J., Salvato M., Hsu L. T., Bauer F. E., 2018, Astronomy and Astrophysics, 618, A66

Soldi S., et al., 2014, Astronomy and Astrophysics, 563, A57

Stein R., et al., 2021, Nature Astronomy, 5, 510

Stelzer B., Flaccomio E., Montmerle T., Micela G., Sciortino S., Favata F., Preibisch T., Feigelson E. D., 2005, The Astrophysical Journal Supplement Series, 160, 557

Stern D., et al., 2012, The Astrophysical Journal, 753, 30

Stone N. C., Metzger B. D., 2016, Monthly Notices of the Royal Astronomical Society, 455, 859

Stone N. C., Generozov A., Vasiliev E., Metzger B. D., 2018, Monthly Notices of the Royal Astronomical Society, 480, 5060

Strubbe L. E., Quataert E., 2009, Monthly Notices of the Royal Astronomical Society, 400, 2070–2084

Subrayan B. M., et al., 2023, The Astrophysical Journal Letters, 948, L19

Sunyaev R., et al., 2021, Astronomy and Astrophysics, 656, A132

Svirski G., Piran T., Krolik J., 2017, Monthly Notices of the Royal Astronomical Society, 467, 1426

Swartz D. A., Ghosh K. K., Tennant A. F., Wu K., 2004, The Astrophysical Journal Supplement Series, 154, 519

Tadhunter C., Spence R., Rose M., Mullaney J., Crowther P., 2017, Nature Astronomy, 1, 0061

Tanaka Y., Shibazaki N., 1996, Annual Review of Astronomy and Astrophysics, 34, 607

Taylor B. G., Andresen R. D., Peacock A., Zobl R., 1981, Space Science Reviews, 30, 479

Teboul O., Perets H. B., 2025, The Astrophysical Journal, 984, 12

Thomsen L. L., et al., 2022, The Astrophysical Journal Letters, 937, L28

Tonry J. L., et al., 2018, Publications of the Astronomical Society of the Pacific, 130, 064505

Truemper J., 1992, Quarterly Journal of the Royal Astronomical Society, 33, 165

Tubín-Arenas D., et al., 2024, Astronomy and Astrophysics, 682, A35

Turner T. J., Miller L., 2009, Astronomy and Astrophysics, 17, 47

Untzaga J., Bonoli S., Izquierdo-Villalba D., Mezcua M., Spinoso D., 2024, Monthly Notices of the Royal Astronomical Society, 535, 3293

Urry C. M., Padovani P., 1995, Publications of the Astronomical Society of the Pacific, 107, 803

Valenti S., et al., 2013, The Astronomer's Telegram, 4958, 1

Voges W., et al., 1999, Astronomy and Astrophysics, 349, 389

Waddell S. G. H., et al., 2024, arXiv e-prints, p. arXiv:2401.17306

Wang X.-Y., Liu R.-Y., Dai Z.-G., Cheng K. S., 2011, Physical Review D, 84, 081301

Wang J., et al., 2022, The Astrophysical Journal, 930, 18

Wang M., Ma Y., Wu Q., Jiang N., 2023, The Astrophysical Journal, 960, 69

Warner B., 1995, Cataclysmic Variable Stars. Cambridge Astrophysics, Cambridge University Press

Warner B., 2003, Cataclysmic Variable Stars. Cambridge University Press

Waxman E., Katz B., 2017, in Alsabti A. W., Murdin P., eds, , Handbook of Supernovae. p. 967

Weisskopf M. C., Tananbaum H. D., Van Speybroeck L. P., O'Dell S. L., 2000, in Truemper J. E., Aschenbach B., eds, Society of Photo-Optical Instrumentation Engineers Conference Series Vol. 4012, X-Ray Optics, Instruments, and Missions III. pp 2–16

Wenger M., et al., 2000, Astronomy and Astrophysicss, 143, 9

Wevers T., et al., 2017, Monthly Notices of the Royal Astronomical Society, 471, 1694–1708

Wevers T., et al., 2021, The Astrophysical Journal, 912, 151

Wevers T., et al., 2023, The Astrophysical Journal, 942, L33

Wheatley P. J., Mauche C. W., Mattei J. A., 2003, Monthly Notices of the Royal Astronomical Society, 345, 49–61

White N. E., et al., 1986, The Astrophysical Journal, 301, 262

Wilkins D. R., Gallo L. C., 2015, Monthly Notices of the Royal Astronomical Society, 449, 129

Wilms J., et al., 2020, The Astronomer's Telegram, 13416, 1

Wolff M. T., Becker P. A., Ray P. S., Wood K. S., 2005, The Astrophysical Journal, 632, 1099

Woosley S. E., Bloom J. S., 2006, Annual Review of Astronomy and Astrophysics, 44, 507

Woosley S. E., Weaver T. A., 1986, Annual Review of Astronomy and Astrophysics, 24, 205

Wright E. L., et al., 2010, The Astronomical Journal, 140, 1868

Wu H.-J., Mou G., Wang K., Wang W., Li Z., 2022, Monthly Notices of the Royal Astronomical Society, 514, 4406

Yan Z., Yu W., 2015, The Astrophysical Journal, 805, 87

Yao Y., et al., 2023, The Astrophysical Journal Letters, 955, L6

Yao Y., et al., 2025, Transient Name Server AstroNote, 13, 1

Yuan W., et al., 2016, in Meiron Y., Li S., Liu F. K., Spurzem R., eds, IAU Symposium Vol. 312, Star Clusters and Black Holes in Galaxies across Cosmic Time. pp 68–70

Yuan W., Zhang C., Chen Y., Ling Z., 2022, in Bambi C., ed., , Handbook of X-ray and Gamma-ray Astrophysics. Springer Nature Singapore, p. 86

Zwart J. T. L., et al., 2008, Monthly Notices of the Royal Astronomical Society, 391, 1545

de Pasquale M., et al., 2006, Astronomy and Astrophysics, 455, 813

di Matteo T., 1998, Monthly Notices of the Royal Astronomical Society, 299, L15

van Velzen S., Falcke H., Körding E., 2015, Monthly Notices of the Royal Astronomical Society, 446, 2985

van Velzen S., Mendez A. J., Krolik J. H., Gorjian V., 2016, The Astrophysical Journal, 829, 19

van Velzen S., et al., 2019, The Astrophysical Journal, 878, 82

van Velzen S., Holoien T. W. S., Onori F., Hung T., Arcavi I., 2020, Space Science Reviews, 216, 124

van Velzen S., Pasham D. R., Komossa S., Yan L., Kara E. A., 2021, Space Science Reviews, 217, 63

van Velzen S., et al., 2024, Monthly Notices of the Royal Astronomical Society, 529, 2559

van der Meer A., et al., 2005, Astronomy and Astrophysics, 432, 999

Acknowledgements

I am deeply grateful for the eventful and inspiring PhD journey I have experienced at MPE: years full of growth, learning, and memorable moments.

First and foremost, I would like to express my sincere thanks to my supervisors, Arne and Paul, for their support and belief in me. I am deeply grateful for the time, effort, and guidance you invested in my development as a scientist, and I could not have wished for better supervisors. Thank you for being caring, encouraging, and motivating – not only during moments of success, such as my first conferences and publications, but also through more challenging periods, including remote work during the pandemic and the inevitable obstacles along the way.

I would also like to thank the MPE High Energy Group for providing such a welcoming and stimulating environment to grow and explore. Your encouragement and challenges have always pushed me to improve. Special thanks to Mara and Andrea for their detailed feedback on my publications and their insightful ideas, and to the other members of the TDE group – Adam, Zhu, and Pietro – for their support and camaraderie. I am also grateful to Johannes for being a great mentor and helping me navigate various challenges. I would also like to thank my Master's supervisor, George, for teaching me so much during my first steps in research and for laying the foundation for my academic path.

Finally, I am thankful to my family, who have always believed in me and supported my journey in astrophysics for over a decade. Your encouragement made it possible for me to move abroad and build a home from scratch, and I will always be grateful for that.